# Studies on Structural Configurations for Vehicular Crash Energy Absorption

**THESIS**

Submitted in partial fulfilment of the
requirements for the degree of

**DOCTOR OF PHILOSOPHY**

by

**T JANARDHANA REDDY**

ID. No. 2013PHXF0117H

Under the Supervision of

**Prof. VENKATA DASESWARA RAO YENDLURI**

**&**

**Dr. VIJAYABASKAR NARAYANAMURTHY**

**RESEARCH CENTRE IMARAT, DEFENCE R & D ORGANISATION, HYDERABAD, INDIA**


**BIRLA INSTITUTE OF TECHNOLOGY AND SCIENCE - PILANI**

**HYDERABAD, TELANGANA, INDIA**

**2018**

# CERTIFICATE

This is to certify that the thesis entitled "**Studies on Structural Configurations for Vehicular Crash Energy Absorption"** submitted by **T JANARDHANA REDDY**, ID No. **2013PHXF0117H** for award of Ph.D. of the Institute embodies original work done by him under our supervision.

Signature of the Supervisors:

1) **Dr. VENKATA DASESWARA RAO YENDLURI**
   **Associate Professor**
   Department of Mechanical Engineering
   BITS-Pilani Hyderabad Campus, Jawahar Nagar
   Shameerpet (Mandal), Hyderabad – 500 078
   Telangana, India.

2) **Dr. VIJAYABASKAR NARAYANAMURTHY**
   Scientist-'E', Directorate of Systems Integration (Mechanical)
   Resarch Center Imarat – Defence R&D Organisation,
   Vignyana Kancha P.O., Hyderabad – 500 069.
   Telangana, India.

## ACKNOWLEDGEMENT

I feel very fortunate to have an opportunity to acknowledge various persons involved in my research work and for their help in one way or the other.

First of all, I would like to thank the *Almighty* for giving me the opportunity to do the research work with good health and prosperity.

My deep sense of gratitude to **Prof. Souvik Bhattacharyya**, Vice Chancellor, BITS-Pilani for permitting me to carry out my doctorial work in the institute.

My heart-felt gratitude to **Prof. G. Sundar**, Director, BITS-Pilani, Hyderabad Campus, for permitting me to carry out my research work in the campus.

I wish to express my earnest gratitude and heartfelt thanks to my **research supervisors, Prof. Venkata Daseswara Rao Yendluri**, Department of Mechanical Engineering, BITS-Pilani, Hyderabad Campus and **Dr. Vijayabaskar Narayanamurthy**, Scientist, RCI-DRDO, Hyderabad for their excellent guidance, constant encouragement, enormous patience and good advice throughout my research work. I would like to acknowledge them for their moral support by standing by me during all situations with their constructive criticism throughout my research work and dissertation, without which, this work would not have been completed.

My sincere and heart-felt gratitude to my employer M/s **Satyam Venture Engineering Services Pvt. Ltd, Mr. Srinivasa Rao Vadlamudi,** CEO, **Mr. Sridhar Lakshminarayanan,** Vice-President & Global Delivery Head – CAE and **Mr. Devdutta Sarma,** Vice-President – Human Resources of Satyam Venture Engineering Services Pvt. Ltd., Hyderabad for permitting and encouraging me to carry out this research work.

I am thankful to **Prof. Srinivasa Prakash Regalla** and **Prof. Sabareesh Geeta Rajasekaran**, Doctoral Advisory Committee members, Department of Mechanical

Engineering, BITS-Pilani, Hyderabad Campus, for their valuable time in reviewing this thesis and suggestions.

I am thankful to **Prof. Vamsikrishna Venuganti,** Associate Dean, ARD, BITS-Pilani, Hyderabad Campus and **Prof. Vidya Rajesh,** former Associate Dean, ARD for their support to my research work.

I wish to express my thanks to **Prof. N Suresh Kumar Reddy** for providing the required facilities at central workshop and take immense pleasure in acknowledging all the **faculty and support staff** of Department of Mechanical Engineering, BITS-Pilani, Hyderabad Campus for their kind support.

My special thanks to **Prof. Amit Kumar Gupta**, HOD, Department of Mechanical Engineering, BITS-Pilani, Hyderabad Campus, for permitting me to carry out my research work in the Department of Mechanical Engineering.

I would like to thank my research group, my friends in and out of the department who have made the last few years an exciting and memorable experience.

Last, but not least, I place my deep sense of gratitude and thanks to my **family** and **parents** for their unconditional support and loving encouragement throughout my life.

Date: T Janardhana Reddy

# ABSTRACT

Human safety in transportation is given a paramount priority across the globe in the design, development and qualification of passenger cars and other road vehicles. Different research and surveys reveal that on an average about 1.3 million people die in road accidents every year and frontal collision is observed to be the major cause. Extensive research in vehicle crashworthiness, occupant protection, safety and bio-mechanics of occupants in road vehicles attributed the severe fatalities in frontal collisions to the high intensity decelerations that causes severe damage to internal organs of the human occupants. Therefore, the transportation industry had come with injury criteria for various vital parts of the human body. These criteria recommend the limiting values of deformations, velocities, decelerations (accelerations) and forces a human body can tolerate. These standards triggered the need for controlled energy absorption to attenuate the intensity of decelerations in frontal collisions. Widely accepted and proven method of energy absorption is through irreversible plastic deformation of materials /structures. The crash energy is absorbed axially by the energy absorbing (EA) structures such as crush cans or crush tubes within the frontal portion of the vehicle known as crumple zones. Although considerable research is carried out so far in developing EA structures, major limitation in most structures is that they exhibit high initial peak crush forces and low stroke efficiencies. Stroke efficiency (SE) is the ratio between the deformed and the original lengths of an EA structure.

In phase-1 of current research, methodologies are developed for numerical simulation of crash energy absorption behaviour of EA structures based on non-linear explicit finite element analysis (FEA). The simulation methods are established and finalised after comparison with experimental results available in literature for crash behaviour of certain standard EA structures.

The FEA procedure thus established is extended to analyse and understand the crash behaviour of crush tubes having cross-sections with different standard shapes ranging from triangle to circular through polygons of increasing sides, in phase-2, before attempting to develop new EA structural configurations in the next phase. This research revealed that as the number of sides increase in the polygon, crush force behaviour tends to move towards circular cross-sections which exhibited best crash performance amongst all basic shapes but all cross-sections have high fluctuations in the crush forces. Appropriate crush-triggering mechanisms can control the initial peak forces in all cross-sections. For effective design of

EA structures, cross-sections with an optimum combination of straight edges and curves may be considered.

In phase-3, various EA structural configurations are proposed through numerical simulations based on two major design strategies such as i) circular tube-in-tube, and ii) hybrid cross-sections and their relative performances are evaluated based on different crashworthiness assessment parameters. It is reiterated that the crashworthiness is not only assessed by the total amount of energy absorbed, but also through a comprehensive and quantitative evaluation of crash performance parameters such as SE, crush force efficiency (CFE, ratio between mean and initial peak crush forces) and equivalent induced-deceleration or 'g' levels. This study presented a deeper understanding on the effect of mutual interactions between cross-sectional geometries and topologies on their plastic deformation modes, crush force and crash EA behaviours. This research demonstrated that the tube-inversion mode of deformation observed in tube-in-tube set of designs possesses the potential for a practical choice for EA applications with its superior crash performance. Even, few existing research have demonstrated that the circular tubes referred to as *invertubes* can absorb maximum crash energy through plastic inversion phenomena.

Notwithstanding significant research on date on tube inversion concept and invertubes, gaps exist in literature with respect to the relationship between geometric parameters such as diameter, thickness and knuckle radius, geometric imperfections and their influence on the inversion process of the tube and the material involved. Available knowledge is inadequate in exploring the feasibility of medium strength grade steels for tube inversion. Therefore, the phase-4 of the present research is focused on these gaps and series of attempts are made to evolve a new invertube's geometric profile and cross-section with stainless steel SS304 material to achieve desirable inversion characteristics for an ideal energy absorption based on numerical simulations and experiments. The proposed invertube profile addresses anomalies in existing literature. The deformation characteristics and process in developing this new invertube profile are explained in detail.

Although phase-4 of research demonstrated that the inversion phenomena controls high initial peak crush force and helps in achieving nearly 100% SE and CFE due to its near-ideal crush force behaviour, the combination of invertube's geometric profile and material ductility significantly limit the specific energy absorption (SEA, energy absorbed per unit mass), a critical crash performance parameter that influences the selection of an EA structure. Detailed

studies revealed that this reduction in SEA of invertube is due to underutilization of material in the plastic inversion deformation process. Therefore, in phase-5 of present research, invertubes with multi-material (using hybrid composites and fiber metal laminates) structural configurations are proposed to achieve higher SEA.

Further, in phase-6 of research, few more EA structural concepts are proposed with multi-material combinations involving conventional steel/aluminium sheets sandwiching aluminium foams and these structural and hybrid material combinations exhibited near-ideal crush force behaviours during the crush stroke and increased the total crash energy absorption through unique bending and inversion deformation mode.

Even though, FEA simulations are used extensively in the design of EA structures, the damage criterion is often ignored for the sake of simplicity or unavailability of data, which leads to substantial differences between FEA predictions and experiments. Therefore, phase-7 i.e. the final stage of present research demonstrated the importance and effect of damage modelling in numerical simulation of crash EA structures. This study is illustrated with crush tubes made of aluminium alloy H30 in WP condition and stainless steel SS304 grades. It is shown that the damage modelling improves the accuracy of predictions irrespective of the magnitude of loading, loading rates and plastic strains in crush tubes. Finally, it is recommended to limit the deformation induced plastic strains within the damage initiation limit as the onset of damage alters the deformation mechanisms and crush force behaviour compromising the amount of crash energy absorbed.

*Keywords:* energy absorption, impact decelerations, crush force behaviour, plastic deformation, numerical methods and ABAQUS®.

# Table of Contents

# LIST OF TABLES

# LIST OF FIGURES

## LIST OF ABBREVIATIONS

| | |
|---|---|
| FMVSS | Federal Motor Vehicle Safety Standards |
| NHTSA | National Highway Traffic Safety Administration |
| NCAP | New Car Assessment Program |
| HIC | Head Injury Criteria |
| NIC | Neck Injury Criteria |
| BrIC | Brain Injury Criteria |
| TTI | Thoracic Trauma Index |
| EA | Energy absorbing / Energy absorption |
| TEA | Total energy absorbed |
| CFE | Crush force efficiency |
| SE | Stroke efficiency |
| SEA | Specific energy absorption |
| ASTM | American Society for Testing and Materials |
| FEA | Finite element analysis |
| CFRP | Carbon fiber reinforced polymer |
| GFRP | Glass fiber reinforced polymer |
| FML | Fiber metal laminate |
| SHM | Strain hardening modulus |
| J-C | Johnson-Cook |

## LIST OF SYMBOLS

| | |
|---|---|
| $A_t$ | Cross-section area of tube |
| $b$ | Curvature parameter (initial knuckle radius) |
| c | side of square |
| $C_t$ | cross-section area of square tube |
| $D$ | diameter of tube (outer diameter in chapter till chapter 5 and mean diameter from chapter 6) |
| $D_0$ | Mean diameter of tube after inversion |
| $E_p$ | Strain hardening modulus of the material |
| $F_{peak}$ | Initial peak crush force |
| $F_{mean}$ | Mean crush force |
| $L$ | Total length of tube |
| $P$ | Inversion load |
| $R$ | Mean radius of tube |
| $R_i$ | Mean intermediate radius of tube (during inversion) |
| $R_0$ | Mean radius of tube after inversion |
| $t$ | Thickness of tube |
| $\sigma_0$ | Initial yield stress of material |
| $\beta$ | Non-dimensional strain hardening parameter = $E_p$ / $Y_0$ |
| $\varepsilon_\varphi$ | Strains along circumferential (hoop) direction |
| $\varepsilon_l$ | Strains along meridional (axial) direction |
| $\varepsilon_t$ | Strains along thickness direction |
| $\rho$ | Density of material |
| $\sigma_p$ | Perfect plastic stress of material |
| $E_1$ | Elastic modulus in fiber direction |

| | |
|---|---|
| $E_2$, $E_3$ | Elastic moduli in directions perpendicular to fiber direction |
| $G_{12}$ | Shear modulus in the first principal plane |
| $G_{13}$ | Shear modulus in the second principal plane |
| $G_{23}$ | Shear modulus in the third principal plane |
| $X_T$ | Tensile strength in the longitudinal direction |
| $X_C$ | Compressive strength in the longitudinal direction |
| $Y_T$ | Tensile strength in the transverse direction |
| $Y_C$ | Compressive strength in the transverse direction |
| $S_{12}$ | Shear strength |
| $G_{fc}^{1+}$ | Fracture energy of the lamina in the longitudinal tensile direction |
| $G_{fc}^{1-}$ | Fracture energy of the lamina in the longitudinal compressive direction |
| $G_{fc}^{2+}$ | Fracture energy of the lamina in the transverse tensile direction |
| $G_{fc}^{2-}$ | Fracture energy of the lamina in the transverse compressive direction |

# Chapter 1

# Introduction

This chapter presents the background of vehicular crash impacts, need for occupant safety in road vehicles, motivation for the present research and an overview of the organization of thesis.

## 1.1 Background

### 1.1.1 Road accidents

The invention of automobile at the dawn of the 20$^{th}$ century created a progressive impact than any other invention in the modern world. Being the most recognized means of transportation, automobiles have altered the way people lived all over the world and have become an integral part of human lives. They have affected many aspects of society such as family life, the economy, and even the environment. Over the past century, with advances in various fields of engineering, automobiles became affordable and reached millions of users across the globe. Developments in various aspects of the society have impelled the need for increase in number and speed of the vehicles. This increased speed and the number of vehicles are posing a big threat to human safety and lives in the form of accidents (collisions in various forms) due to various reasons. Road accidents are broadly classified as shown below in Figure 1.1.

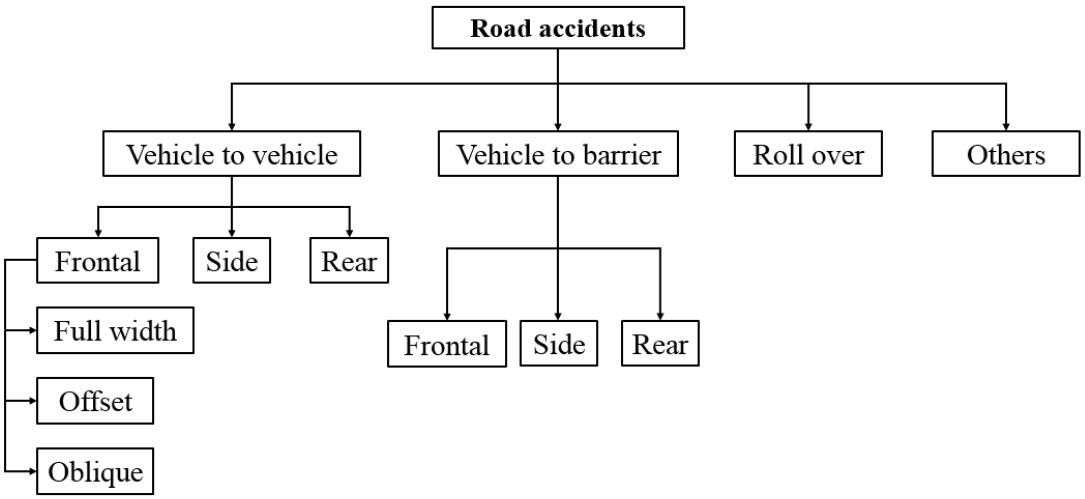


Figure 1.1: Classification of road accidents [1]

In a series of surveys conducted by the world health organization (WHO) [2, 3], the reports revealed that about 1.3 million people die in road accidents every year across the globe. The reports also highlighted that people with predominantly middle-income groups and in countries with emerging economies are the most vulnerable population. This is due to rapid motorization which is not backed by appropriate infrastructure, transportation policies and legislation for road safety [2, 4, 5]. The Figure 1.2 shows the distribution of human deaths by different types of road accidents based on the survey by National Centre for Statistics and Analysis (NCSA) [5, 6]. It is understood that accidental deaths by frontal impact mode of collision between vehicles is the major cause across all age groups of drivers from 18 years to above 70 years [7, 8].

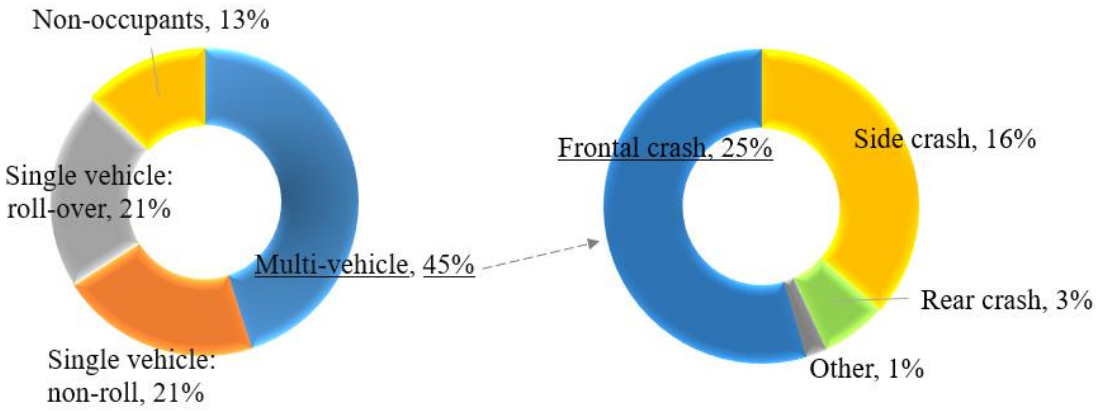


Figure 1.2: Distribution of mortalities by type of accident [5]

### 1.1.2 Vehicular safety and crash energy management

As the human life is invaluable, the transportation industry has been taking adequate engineering measures to ensure that occupant safety is given the paramount priority and was made an integral and uncompromising aspect of vehicle engineering since about 1950s. The US department of transportation led this road safety mission by empowering National Highway Traffic Safety Administration (NHTSA) department to frame guidelines and regulations to all vehicle manufacturers. These regulations covered every critical component of the vehicle to cover all aspects of the vehicle safety in the form of standard guidelines which became popular as Federal Motor Vehicle Safety Standards (FMVSS) [9]. Other industrially developed countries followed this trend and established their own regulations which the vehicle manufacturers adhered to conform and certify for compliance. These standards and regulations became mandatory for every new car assessment program (NCAP).

The occupant safety standards and regulations presently followed across globe which cover all vital systems of the vehicle are shown in Figure.1.3.

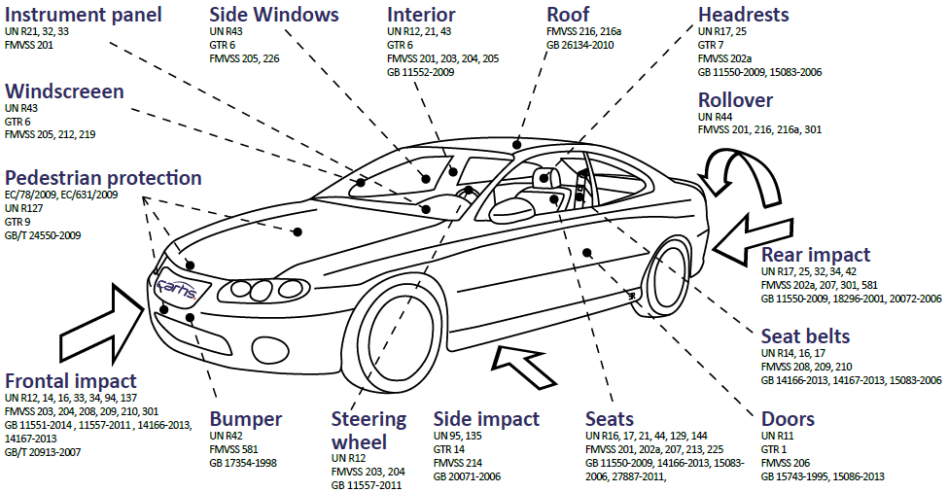


Figure 1.3: Automotive safety regulations across the world [1]

In the early years of motorized transportation, vehicle manufacturers believed in stronger front structure for protection against frontal collisions. This approach helped in minimizing the intrusions into the passenger cabin, but the stiffer front structures only ensured direct transfer of impact-induced decelerations (crash energy) to the occupants resulting in external injuries and internal failures of human body elements (head, chest, tissues and bones, etc) [8-10] due to impact on the vehicle interiors and impact-induced decelerations. Over the years, automotive engineers understood the concept of impact mitigation by controlled energy absorption through plastic deformation method, where the front structures deform plastically in a controlled manner over a certain length under the action of impact forces. In 1952-53, Béla Barényi [11], an engineer working for Mercedes Benz is believed to have first designed and patented the concept for the collapsible (plastically deformable) type frontal energy absorbing member and assembled in the serial production vehicle for Mercedes model series W120 [11, 12]. This plastically deformable type of energy absorbing (EA) element enabled the vehicle to reduce impact-induced decelerations thereby helping the occupants cope better with the impact scenario by providing them with a few extra milli seconds for the impact wave reaching the occupants and reduce the intensity of injuries [13].

Later through continuous and combined research efforts in engineering and medicine, the science of impact energy absorption has become more organized and brought forth the limiting values of decelerations and forces which different organs and parts of a human body can withstand from the injury perspective. These recommendations which have been

quantified in the engineering terms evolved as fundamentals for the design of frontal energy absorbing structures. These guidelines have been legalized and evolved as the statutory standards for all vehicle manufacturers for compliance and certification [9]. Research in the field of occupant safety has gained immense priority since then and the vehicle manufacturers have come up with various active and passive safety systems such as seat belts, airbags, anti-lock braking systems (ABS), stability control systems (SCS) and traction control systems (TCS) to name a few [1].

As the frontal impact mode of accidents were found to be more frequent and a major cause of fatalities in road accidents, research efforts towards attenuating the intensity of impact has gained a lot of importance [5]. Frontal impact has become the widely studied topic in the field of occupant safety. Multiple ways of mechanical methods to absorb the impact energy have been tried in the past which were based mostly on friction and plastic deformation. Few examples are axial splitting by tube expansion [14], energy absorption by plastic deformation through tearing a thin sheet [15] and a friction and hydraulic brakes based novel adaptive design [16]. But plastic deformation based methods are preferred over the other modes and are widely practiced till today.

The very first innovative design of front deformable EA structure [11] sparked a new trend in the design of frontal structures. Extended research in vehicle collisions, crashworthiness and biomechanics of occupants, over the years, led to the evolution of several injury criterion such as head injury criterion (HIC) [17, 18], brain injury criterion (BrIC) [19, 20], neck injury criterion (NIC) [21] and chest compression levels, etc. These criterion are expressed as functions of decelerations (accelerations) and have helped in assessment and evaluation of injury levels for different collision scenarios and to arrive at the limiting values of decelerations (converted into equivalent crush forces) and forces [22] a human body can tolerate without undergoing serious injuries. Over the past few years it has been a standard engineering practice with all the vehicle manufacturers to design the front EA structures such that their crush forces are within these allowable magnitudes to comply with statutory safety regulations.

Today's vehicle manufacturers are following an all-inclusive and comprehensive approach to the extent of building the complete human model representing all the vital parts in terms of stiffness, mass and failure characteristics with the maximum possible accuracy using numerical methods as shown in Figure 1.4. This practice was pioneered by the Japanese auto major Toyota Motor Corporation for an accurate estimation of responses of occupants in a

collision scenario [23]. It demonstrates the importance of safety and commitment shown by the transportation industry towards building safer vehicles.

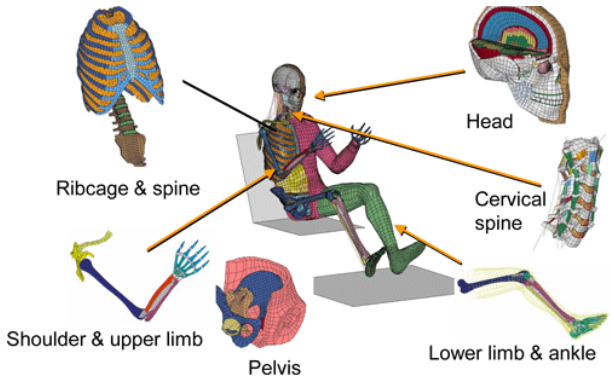


Figure 1.4. Detailed FE models of human body for advanced safety studies [23]

Further, the following can be clearly understood from detailed studies on existing practices on vehicle safety.

- New road safety laws have been passed in 35 countries – but only 7% of the world's population is covered by comprehensive legislation for the major risk factors [2].
- Automotive crashworthiness is still not enforced as a statutory regulation in major developing countries such as India [24] and majority of vehicles do not comply with safety standards for frontal collisions even for medium range speed.
- Compact vehicles are getting more popular in emerging markets but there is no enough space available for fitment of frontal EA structures which is a concern for passenger safety.

## 1.2 Motivation

Most EA structural configurations are characterized by high initial peak crush forces (often beyond the limiting values) which are transferred into the occupant compartment. As the frontal EA structure has a mission-critical role in the first defense against all forms of frontal collisions, there is a need for designing these structures to be in strict compliance with the standard regulations to protect the occupants from being exposed to higher magnitudes of crash forces (higher decelerations). Importance of human safety in frontal vehicular collisions and research gaps evidenced in existing literature in design of frontal EA structures have

provided the necessary thrust and motivation for selecting this subject of controlled energy absorption by frontal EA structures for the current research work.

In all, passenger safety is the sole motivation factor behind this research on the study of development of EA structural configurations through energy absorption by plastic deformation with an aim to contribute an incremental knowledge in improving the occupant safety in the transportation vehicles.

### 1.3 Organization of the Dissertation

This thesis is organized into 10 chapters. A brief introduction to the contents of each chapter is as given below.

***Chapter-1*** discusses the background of this research with respect to the need for crash energy absorption in the context of occupant safety in road vehicles, motivation for this research, and organization of the thesis.

***Chapter-2*** covers a comprehensive review of the literature in the area of impact energy absorption with focus on the evolution of the concept of impact energy absorption with application to occupant safety in road vehicles, definition of several injury criterion for occupants and their relationships with impact decelerations and impact forces during collision. Mathematical definitions of various performance parameters for assessment of crashworthiness of EA structures are formalized as the basis for evaluation of new EA structural concepts. The requirements of an ideal EA structure are detailed. Different structural configurations with respect to their geometry, materials and modes of plastic deformations and their influence on the crush force behavior are studied in detail and summarized. Objectives of the present research work and the research methodology are discussed.

***Chapter-3*** presents development of methodologies for non-linear explicit finite element analysis (FEA) for numerical simulation of crash energy absorption behaviour of certain standard EA structures under axial impact and their validation with experimental results available in literature.

***Chapter-4*** discusses the crash energy absorption behaviour of crush tubes with various basic geometric shapes with a closer attention to their plastic deformation patterns and their influence on the crush force behavior using FEA methods.

***Chapter-5*** proposes various novel EA structural configurations through numerical simulations based on two major design strategies such as i) circular tube-in-tube, and ii) hybrid cross-sections and evaluation of their relative performances based on standard crashworthiness assessment parameters.

***Chapter-6*** details the evolution of the design of a new invertube's geometric profile and cross-section for inversion-based mode of plastic deformation to achieve desirable inversion characteristics for a near-ideal energy absorption based on numerical simulations, their fabrication and experimental validation. It also critically examines the vital parameters of inversion process and deformation characteristics.

***Chapter-7*** proposes EA structures based on invertubes with multi-material (using hybrid composites and fiber metal laminates) structural configurations to achieve higher SEA using high specific strength materials such as composites and low density material magnesium.

***Chapter-8*** presents a few more multi-material (metals and metallic foams) EA structural configurations based on a unique combination of bending and inversion deformation modes.

***Chapter-9*** demonstrates the importance and effect of damage modelling in numerical simulation of crash EA structures. This study is illustrated with crush tubes made of aluminium alloy H30 in WP condition and stainless steel SS304 grades.

***Chapter-10*** presents the overall summary of the research, investigations carried out, contributions specific to this research area and conclusions drawn from this work. It also suggests the recommendations for further future work in this area.

# Chapter 2

# Literature Review, Research Objectives and Research Methodology

This chapter initially presents a comprehensive review of literature in the area of vehicular collisions, concepts, and crash energy absorption and its assessments. Certain research gaps are identified in existing literature and are reported. The detailed literature review and the identified research gaps led to the formulation of research objectives for the present research, which are subsequently outlined. Finally, the methodology adopted to achieve the research objectives are provided with a detailed summary at the end.

## 2.1 Introduction

Crashworthiness and occupant safety have been given a top priority in automobiles since the introduction of Highway Safety Act in the second half of the 20$^{th}$ century by the US Government. This law triggered the formulation of guidelines for vehicle manufacturers in several aspects of the vehicle for passenger safety. These safety regulations later came into existence as Federal Motor Vehicle Safety Standards (FMVSS) in USA and soon the other countries also started enforcing similar standards and guidelines, as appropriate to their regions. Vehicle safety systems are designed to protect the occupants during various collision scenarios involving frontal collision, side impact, roll-over crashes or any other incident. Each of these events can occur in several ways and each incident is unique in its nature by virtue of the damage to the vehicle and the intensity of injuries to its occupants [25, 26]. Crashworthiness with reference to the common frontal crash impact may be understood as the measure of vehicle's frontal energy absorbing (EA) structure capability to absorb the impact energy by allowing the controlled plastic deformation while possessing enough strength to avoid intrusion of engine block into the passenger cell and to keep the impact induced deceleration levels within the human tolerance limits (crush forces should be within the allowable limits) [27].

## 2.2 Background

In the earlier years of automobile history, engineers believed that stiffer frontal structures provide a better resistance against the impact due to frontal collisions from the intrusion perspective. These structures being stiff helped in preventing the intrusions into the occupant cell, but the occupants received severe injuries due to the effect of inertia of motion as the rigid structure ensured a direct transfer of impact-induced decelerations into the occupant cell and hence to the occupants. These injuries were both internal (within the body as the sensitive tissues of vital parts tear off resulting in internal damage and bleeding; head, brain, neck, bones and other important organs) and external (due to primary and secondary impacts on the vehicle interiors) in nature.

## 2.3 Collision Physics

### 2.3.1 Momentum, Impulse and Kinetic Energy (understanding the fundamentals)

In the 1950s, the automotive industry with its increasing focus on human safety shifted the design paradigms of vehicle's front structures. The concept of impact energy absorption was introduced in the vehicle's architecture with a softer front structure and a relatively stiffer occupant cell. The front structures were tuned to have an optimum stiffness and deform in an axial mode over a defined distance in a controlled manner instead of exhibiting a stiff behaviour. This controlled axial stiffness helped in delaying the impact-induced decelerations into the passenger compartment. The inertia effects were controlled and hence the decelerations. The occupant cell was strengthened further to prevent the intrusion of heavy masses (engine and the front part) [25, 26]. This can be understood easily from the first principles of engineering mechanics as explained below [27, 28].

Let $m$ = mass, v = velocity, F = force, $a$ = acceleration, $t$ = time, $I$ = impulse, and $P$ = Momentum. Momentum of a body having mass $m$ and moving with a velocity $v$ is given by

$$P = mv \tag{2.1}$$

Change of momentum in the body is

$$dP = mdv \tag{2.2}$$

Force $F$ on the body is the rate of change of momentum given by

$$F = m\,\frac{dV}{t} \tag{2.3}$$

Impulse *I* is a vector quantity related to this force and it is the product of force and the duration of the time *t* it acts on a body. Generally this time period is very short in vehicle impacts and impulse on the body is

$$I = Ft \tag{2.4}$$

From Eqs (2.3) and (2.4), impulse is also nothing but the change in momentum in the body

$$Ft = mv \tag{2.5}$$

This is known as the impulse-momentum change theorem.

For example, if a car of mass 1000 kg travels with a velocity of 10 m/s and crashes into a rigid barrier and stops in 1 second.

Initial momentum, $P_i$ = 1000 x 10 = 10000 kg m/s

Final momentum, $P_f$ = 1000 x 0 = 0 (final velocity is zero as the car stops completely).

Change of momentum, $P_f - P_i$ = -10000 kg m/s (negative sign indicates that momentum is lost).

Using Eq. (2.5) and taking *t* =1 s, Impact force transmitted to the car upon impact on rigid barrier in 1 second = -10000 N

If the car crashes into the wall and stops in 2 seconds, then from Eq. (2.5),

Impact force transmitted to the car = -5000 N.

The kinetic energy of the moving car is given by

$$\text{KE} = \frac{1}{2}mv^2 \tag{2.6}$$

From the above example, KE possessed by the car at the impact is 50000 J.

To absorb this KE completely, the vehicle front structure has to deform plastically by a distance *x*.

Work done by the impact is given by

$$\text{W} = Fx \tag{2.7}$$

Equating the KE to the plastic work done by the front structure (i.e. equating Eqs. (2.6) and (2.7)) assuming the impact duration as 1 s, we get deformation length needed as *x* = 5 m.

It may be understood that to minimize the impact forces, deformation should happen over a long distance. Generally, the acceptable impact crush forces are derived based on the mass of the vehicle and the allowable decelerations. Thought it is not possible to conserve the kinetic energy completely in inelastic collisions, the amount of energy absorbed by the vehicular structure can be maximized without crossing the allowable crush force limits. In the context of vehicular crash energy absorption, the following inferences can be made from this study.

i) Lesser the impact forces, lesser the decelerations induced into the vehicle body due to the impact

ii) The duration of impact should be prolonged to the maximum possible extent to minimize the magnitude of decelerations.

iii) To maximize the amount of kinetic energy being absorbed, deformation distance should tend to maximum and the impact forces should be within the allowable limits.

### 2.3.2 Biomechanics and Injury Mechanisms

In a car collision, all parts of the human body from head to toe are vulnerable to injuries and the location and the intensity of the injury depends on the type of collision and the kinematics it induces on occupants. The major sources of injury of an occupant during an accident are [5]:

i) high decelerations;

ii) crushing of the occupant compartment and intrusion of heavy masses;

iii) primary and secondary impacts with the vehicle interiors; and

iv) ejection from the vehicle if the occupant is not belted

The occupant kinematics in a typical frontal crash scenario and the acceptable limits of injury criterion are shown in Figure 2.1. Based on the plausible kinematics of occupants in the vehicle for different collision scenarios and the limiting values of mechanical parameters (deformation, moment, velocity and acceleration) a human body can withstand, injury criterion for several parts of the human body have been formulated as the guidelines [26]. A few of such criterion are discussed here.

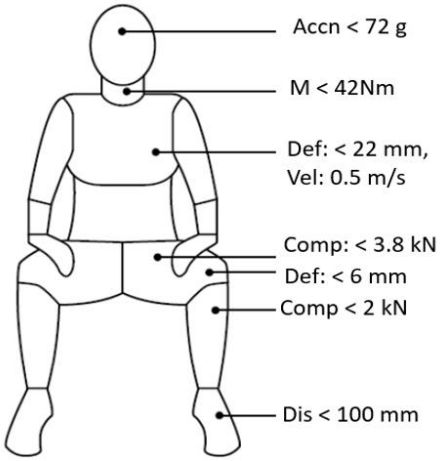


Figure 2.1: Acceptable levels of injury criterion [1]

2.3.2.1 Combined injury criterion for the whole human body

According to Gadd criterion, a single parameter (acceleration of head) represents the tolerance levels for the whole body and it is represented as Gadd Severity Index (GSI) [6, 29];

$$GSI = \int_0^t a^{2.5}\, dt < 1000 \tag{2.8}$$

where *a* is the acceleration (or deceleration) level of the head which causes concussion and skull fracture. The total duration of the pulse is *t* in milliseconds over which the acceleration is applied.

2.3.2.2 Head injury criterion (HIC)

Subsequent to GSI, head injury criterion (HIC) [30, 31] was formulated for specific assessment of injuries related to head alone

$$\text{HIC} = \max\left\{\left[\frac{1}{(t_2 - t_1)}\int_{t_1}^{t_2} a(t)dt\right]^{2.5}(t_2 - t_1)\right\} < 1000 \tag{2.9}$$

where $t_1$ and $t_2$ are the two time instances between which the acceleration *a(t)* is measured. The current standard suggests that the HIC values above 1000 will induce an irrecoverable damage on head or brain [8, 9].

2.3.2.3 Brain injury criterion (BrIC)

Brain injury criterion is expressed as

$$BrIC = \sqrt{\left(\frac{\omega_x}{\omega_{xC}}\right)^2 + \left(\frac{\omega_y}{\omega_{yC}}\right)^2 + \left(\frac{\omega_z}{\omega_{zC}}\right)^2} \tag{2.10}$$

where $\omega_x$, $\omega_y$ and $\omega_z$ are angular velocities along the principal directions and $\omega_{xC}$, $\omega_{yC}$ and $\omega_{zC}$ are the critical angular velocities along their respective directions [19, 20].

2.3.2.4 Neck injury criterion (NIC)

The neck injury criterion (NIC) is given as

$$NIC = \frac{F_z}{F_{int}} + \frac{M_Y}{M_{int}} \tag{2.11}$$

where $F_Z$ is the vertical force (tensile/compressive) on the neck and $M_Y$ is the moment for forward/rearward rotation of the neck. The $F_{int}$ and $M_{int}$ are the critical intercept values of vertical force and moments [1, 21].

2.3.2.5 Chest injury criterion

According to NHTSA [31], the current regulation mandates a limit of 60g for chest acceleration and a chest deflection of 76 mm as the safe allowable limits.

2.3.2.6 Thoracic trauma index (TTI)

TTI measure deals with the risk of organs within the thoracic cage (ex: liver, kidneys, spleen, etc.). An extensive study on the physiological responses to certain collision scenarios led to the evolution of this injury index, TTI [32]. It is expressed as

$$TTI = 0.5(G_r + G_{ls}) < 100 \quad (2.12)$$

where $G_r$ is greater of the peak acceleration of either lower or upper rib expressed in 'g's and $G_{ls}$ is the peak acceleration of the lower spine expressed in 'g's. The TTI value should be below 100 to avoid life threatening injuries.

## 2.4 Emergence of Crashworthiness

To ensure proper protection to occupants from various collision scenarios as discussed before, the automotive industry in the second half of the 20$^{th}$ century came with a comprehensive safety program. This program termed as 'Crashworthiness' laid guidelines for vehicle's architecture from the occupant safety perspective. A section of crashworthiness subject which is related to the frontal energy absorbing members is discussed in this research.

### 2.4.1 What is Crashworthiness?

The term 'crashworthiness' was first used in the aviation industry as a measure to assess a structure's ability to protect its occupants in survivable crashes. In the automotive context, it may be related as the vehicle's structural aptitude to deform plastically at the front and yet retain a survivable occupant space in the event of collisions which involve reasonable decelerations. The lesser the damage to the vehicle and/or its occupants and contents after the collision event, the higher the crashworthiness of the vehicle or the better its crashworthy performance [26].

### 2.4.2 Characteristics of an Effective EA structure

The literature suggests three important characteristics for an effective impact EA structure. They are (1) EA structure should be characterised by low initial crush force, (2) it should delay the transfer of impact-induced decelerations into the passenger compartment, (3) it should exhibit a uniform crush force during the entire crush stroke and (4) it should induce irreversible impact energy conversion to plastic deformation. The detailed explanation of these characteristics are given here.

i) Low initial crush force

If the vehicle's front structure is stiff, it induces short-duration and high-intensity decelerations; and if the front structure is soft, the response is characterized by low to moderate intensity decelerations for relatively longer duration. Tolerance limits for deceleration in the longitudinal direction during a frontal impact have been formulated. They also provided an empirical formula for the head injury criterion given in Eq. (2.9) as a guideline for the design of safety systems [33-35]. Equation (2.9) for the HIC shows that the acceleration (i.e. deceleration) induced during the impact is directly related to the probability of head injuries; and the initial peak crush force being the source of high intensity deceleration is a very critical factor from the occupant safety perspective. Further, an EA structure should always be characterised by crush forces within the human tolerance limits. The maximum allowable deceleration [34] for a serious injury but not life-threatening injury is 20g. On the contrary, a softer front structure may lead to an early intrusion into the passenger cell thereby jeopardizing the fundamental safety aspects. To counter this, the ideal approach would be to build an optimally soft front structure to attenuate the intensity of deceleration and a strong structure around the passenger cell to defy the intrusions.

ii) Delay the transfer of impact-induced decelerations into the passenger compartment

This is possible when the EA structure has a long crush stroke. With the longer crush stroke, the impact process takes a few additional milli seconds to reach the passenger compartment, which is a very vital factor from the occupant safety perspective [34]. Longer crush stroke helps in maximizing stroke efficiency (SE) and the energy absorbed by plastic deformation.

iii) Exhibit uniform crush force during the entire crush stroke

The crush force behaviour should tend to be nearly uniform throughout the crush stroke to maximise the total energy absorbed (TEA) by the EA structure. The crush force should not drop drastically after triggering the plastic deformation in the structure and the plastic deformation should progress gradually with uniform crush force that increases the crush force

efficiency (CFE).

The three important characteristics of an effective EA structure thus discussed can be summarily stated that the fundamental responsibility of an EA structure is to absorb the maximum possible energy with crush forces within the human tolerable limits and utilize the entire length of the EA structure in plastic deformation. For such an ideal performance, it requires a combination of (i) a carefully engineered structural configuration which allows its complete volume to deform plastically, (ii) an optimum grade of material that allows such plastic deformation while possessing the required resistive strength and (iii) a controlled trigger mechanism to keep the initial peak crush force within the limits. It is a challenge to achieve such a combination of geometric configuration and ductile material. It is also equally important to minimize the mass of EA structure as today's automotive industry is serious in pursuit of light weight structures [2].

iv) Irreversible energy conversion

For effective absorption of impact kinetic energy, the process should be irreversible. The structure or the material involved in the process should convert the input kinetic energy into inelastic energy by plastic deformation instead of storing it in the elastic form [6].

If the kinetic energy is converted into elastic strain energy, as the deformation reaches its maximum elastic limit, the elastic strain energy will be released and it results in further damage as the rebound causes an impulsive reversal of accelerations occupants as explained in the Figure 2.2.


(a) (b)

Figure 2.2: A car collides with an elastic spring: it is (a) decelerated by the compressed spring; b) subsequently accelerated by the recovery of the spring [5].

### 2.4.3 Crashworthiness Assessment Parameters

The amount of energy absorbed (i.e. TEA) by an EA structure alone is not the direct measure of its crashworthiness, there are several other underlying parameters that are critical to the occupant safety. These parameters as given below are quantifiable, help in assessing

crashworthiness and provide a deeper understanding of the crashworthiness of an EA structure [1, 5, 24, 29-31]. In summarising the crashworthiness performance evaluation parameters, it is said that no single parameter can decide the efficacy of an EA structure. An ideal EA structure should absorb maximum energy with higher SE and CFE with a minimum mass.

2.4.3.1 Initial peak crush force ($F_{peak}$)

$F_{peak}$ is the peak impact crush force that is required to trigger the plastic deformation in the structure. It should be within the threshold limits (equivalent acceleration levels $\leq$ 20g to avoid serious injuries from the passenger safety perspective). If it is too low, the structure will not be stiff enough to resist low speed impacts and compromises the total energy absorbed. The structure will also deform at low speed impacts. If it is high, it results in the early transfer of high intensity decelerations into the passenger cell. The structure should exhibit an optimum initial peak force whose accelerations are within the human tolerance limits and with a smooth time gradient to reach the first peak force.

$$\mathrm{F_{peak}} = \max\ [\mathrm{F}(l)] \qquad (2.13)\ [36]$$

where $F(l)$ is the instantaneous crush force at a crush distance of $l$.

2.4.3.2 Stroke efficiency (SE)

SE is the ratio of length of the EA structure crushed by plastic deformation to the total length of the EA structure. It is a fundamental performance indicator which influences other measures. Higher SE maximises the area under the crush force versus crush stroke curve and thus the TEA. An ideal EA structure should involve the complete available length in crushing (plastic deformation) thereby enabling the structure to utilize the entire length to absorb the impact energy over a long distance. Higher stroke efficiency also helps in delaying the transfer of impact-induced decelerations into the passenger cell by offering a few vital extra milliseconds to the occupant before reaching the state of higher decelerations which is a very critical aspect of occupant safety. Stroke efficiency is quantified as given below;

$$\mathrm{SE} = \frac{l}{L}\mathrm{x}100 \qquad (2.14)\ [36]$$

where $l$ is the length of the EA structure crushed by plastic deformation and $L$ is the total length of the EA structure.

2.4.3.3 Total energy absorbed (TEA)

TEA is the total energy absorbed by the structure by plastic deformation during the impact. It is the area under the crush force versus crush stroke curve. Theoretically, an EA structure with nearly 100% CFE and SE can maximize TEA. The objective here is to maximize TEA while keeping the magnitude of crush force within the human tolerance limits. The total energy absorbed during plastic deformation of the EA structure is expressed as

$$\mathrm{TEA} = \int_0^l \mathrm{F(x)dx} \qquad (2.15)\ [36]$$

where $l$ is the effective crush stroke and $F(x)$ is the instantaneous axial crush force.

2.4.3.4 Crush force efficiency (CFE)

CFE is the ratio of mean crush force $F_{\mathrm{mean}}$ to the initial peak force $F_{peak}$. The crush force curve generally drops after the initial peak and follows a series of fluctuations. For effective energy absorption, the crush force should tend to be uniform around the threshold value (equivalent acceleration levels ≤ 20g) without much fluctuation as the crush progresses. The TEA by the structure will be maximum if CFE approaches unity. The CFE is calculated as

$$\mathrm{CFE} = \frac{F_{mean}}{F_{peak}}\mathrm{x100} \qquad (2.16)\ [36]$$

where $F_{mean}$, the mean crush force is expressed as

$$F_{mean} = \frac{\mathrm{TEA}}{l} \qquad (2.17)\ [36]$$

For an ideal EA structure, the CFE should tend to unity. Lower CFE indicates drop in the crush force after the first peak which will result in the loss of TEA. It is not a direct measure of crashworthiness, but is a measure of stability of crush force that maximizes the total energy absorbed.

2.4.3.5 Specific energy absorption (SEA)

SEA is the ratio of total energy absorbed (TEA) by the structure through plastic deformation to the total mass $m$ of the structure. The ideal requirement is to absorb a maximum amount of impact energy with a minimum possible mass of the EA structure. In today's automotive industry, structures with superior performance-to-weight ratio are highly appreciated. The SEA is expressed as

$$\mathrm{SEA} = \frac{\mathrm{TEA}}{\mathrm{m}} \qquad (2.18)\ [36]$$

2.4.3.6 Energy absorption efficiency

It is the ratio of the TEA by the structure to the initial kinetic energy available with the impacting body. This parameter indicates the effectiveness of the energy absorption.

As a summary of all the crashworthiness assessment parameters, an ideal EA structure's crashworthiness performance may be represented in a graphical form as shown in Figure 2.3

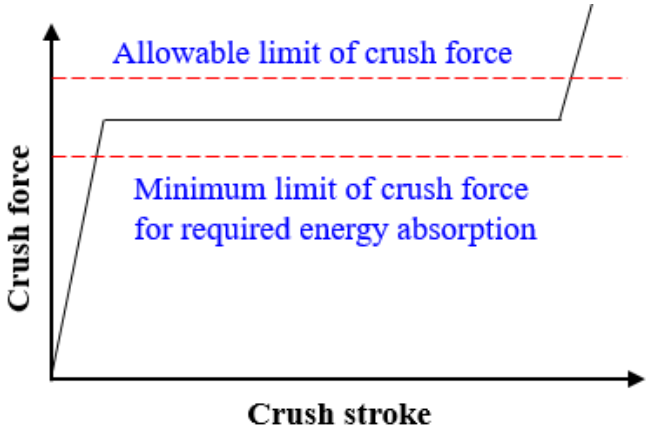


Figure 2.3: Crush force Vs crush displacement of an ideal energy absorbing structure [36]

## 2.5 Crash Energy Absorption

### 2.5.1 Types of Energy Absorption

Absorption of impact energy in simple words is the process of conversion of kinetic energy into different forms. In simple terms, the kinetic energy is converted into some forms of work. In case of a collision involving two vehicles or a vehicle and a barrier, the kinetic energy is converted into i) deformation work, ii) heat, iii) friction, iv) elastic work due to rebound kinematics based on the collision, and v) other miscellaneous effects. The options for kinetic energy absorption that have been tried in the past are based on i) elastic deformation, ii) plastic deformation, iii) friction and iv) hydraulic or viscous damping effects [5] and this classification is as shown in Figure 2.4.

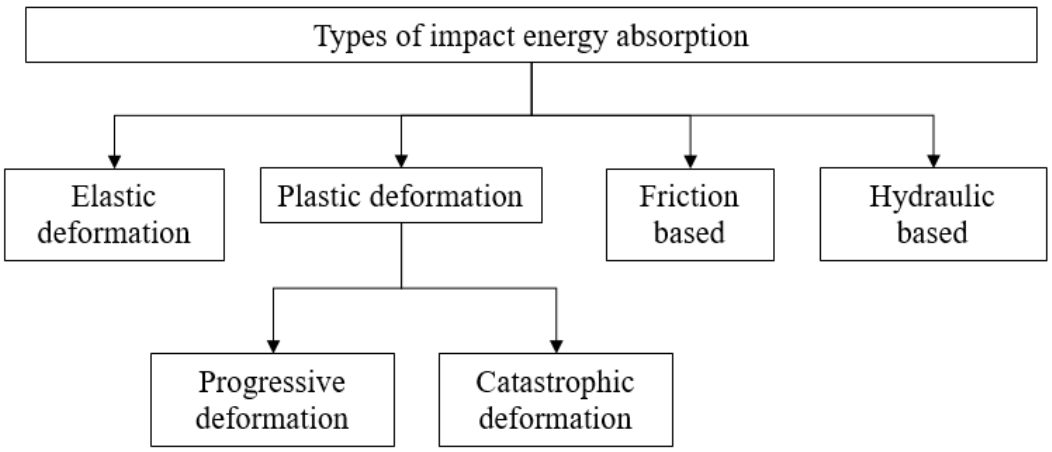

Figure 2.4: Classification of impact energy absorption modes [5]

2.5.1.1 Elastic deformation

This type of energy absorption process is not discussed as it involves the sudden release of strain energy after the impact and the rebound induces reversing accelerations which is an undesired trait of an energy absorbing structure as explained in Figure 2.2.

2.5.1.2 Plastic deformation

Intensive attention is given to the study of plastic deformation based energy absorbing structures as plastic deformation is the most efficient means of irreversible energy absorption with ductile materials and is a widely accepted practice. Structural configurations with different cross-sections, their plastic deformation patterns and crush force behaviours under pure axial crushing scenarios and material trends are discussed in detail in this chapter.

### 2.5.2 Existing Structural Configurations for Energy Absorption

The existing structural configurations for crash energy absorption uses circular tubes, inversion of tubes, axial splitting of tubes, tube expansions, foam filled tubes, tubes with multi-cornered cross sections (i.e square, or polygonal tubes), tubes with multi-cell configurations, frusta and conical tubes, composite tubes, etc. The EA structural configurations with above geometries are discussed in this section.

2.5.2.1 Circular tubes

i) Axial crushing

Energy absorption using thin-walled circular tubes is a widely researched subject due to simplicity in fabrication of circular tubes and the amenability of circular geometry for plastic deformation. Circular tubes exhibit a variety of deformation patterns in axisymmetric and asymmetric forms under axial crushing and they are classified as: i) sequential concertina (series of concentric ring folds), ii) sequential diamond, iii) Eulerian buckling, iv) alternate concertina and diamond, v) simultaneous concertina, vi) simultaneous diamond, and v) tilting of tube axis [37]. These deformation modes are governed by geometric parameters of the tube (diameter-*D*, thickness-*t*, and length-*L*) and material parameter $\sigma_0$/E ratio (ratio of yield strength to modulus of elasticity) [38]. Observations from numerous experiments [39]

suggest that thick cylinders with D/t ratio in the range of 50-60 deform in axisymmetric concertina mode while cylindrical tubes with higher D/t ratios deform in asymmetric diamond mode. As the D/t ratio goes high, the number of asymmetric lobes also increases. On the crush force behaviour front, the tubes with axisymmetric concertina deformation modes exhibit a high initial peak force followed by a series of peaks and valleys around a mean value with the magnitude of force going up for each successive peak. The difference between each peak and valley on the force-displacement curve increases with each round of rise and fall in the crush force. However, due to a gradual and regular deformation pattern, stroke efficiencies around 80% are common in this kind of structures. In the case of circular tubes with asymmetric diamond mode of deformation, the crush force behaviour is not predictable as in the case of concertina kind of deformation and as a result moderate stroke efficiencies are observed as the uncrushed material gets densified quickly leading to a compromise in the total energy absorbed compared to circular tubes with concertina folding modes. A typical concertina and diamond type of deformation modes and their corresponding crush force behaviours are shown in Figure 2.5.

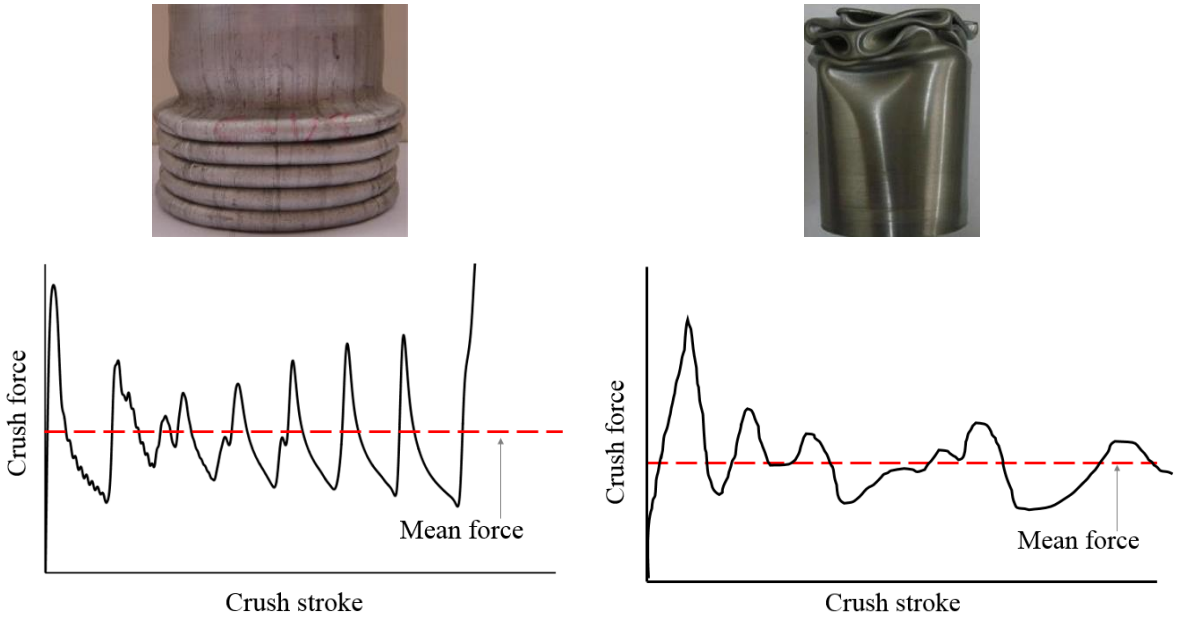


a) Concertina deformation b) Diamond deformation

Figure 2.5: Comparison of typical concertina and diamond deformation modes of circular tubes and corresponding crush force behaviours [36]

There are also some empirical formulae for prediction of average crushing force of cylindrical tubes for concertina mode with D/t < 30 [40, 41], diamond mode of deformation with large D/t values [42] in terms of tube geometry parameters and material's flow stress.

In addition to axial crushing, circular tubes are also deformed in some other modes such as i) inversion, ii) splitting, iii) tube expansion, iv) lateral indentation, and v) lateral flattening. Of these methods, only inversion deformation is observed to be efficient for energy absorption applications [43].

ii) Inversion of tubes

Inversion is a peculiar mode of continuous plastic deformation where the inner surface of the tube comes outside and vice versa [6]. Inversion can be achieved with or without using a guiding die. Inversion can be achieved on straight circular tubes or conical frusta [44 - 46]. Constant crushing force is the salient feature of inversion mode of deformation. Typical modes of inversion are shown in Figure 2.6. Available knowledge is very limited on the underlying principles, geometry and material requirements of inversion of tubes in literature. However, inversion of tubes may be considered as an excellent choice for energy absorption with nearly ideal crush force behaviour [46].

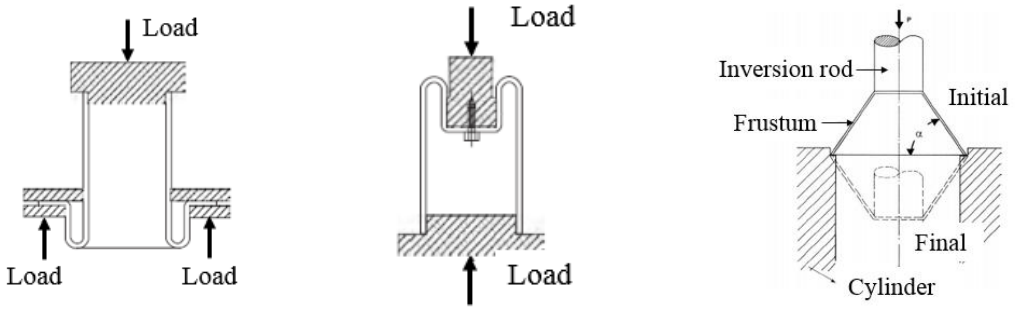


a) Inside-out [6] b) Outside-in [6] c) Inside-out inversion of a frusta [45]

Figure 2.6: Different types of tube inversion

iii) Axial splitting

Splitting and curling of circular tube is another novel method employed in the energy absorption process [47, 48] where a longitudinally pre-grooved tube is pushed against a conical die to initiate the tearing and splitting exploiting the ductile behaviour of the material. Longer crush strokes and uniform crush forces help in achieving the near-ideal crush force

behaviour. A tube splitting set up and crush force behaviour of a typical tube splitting and curling is shown in Figure 2.7.


a) Tube splitting setup b) Axially split specimen c) Crush force behaviour

Figure 2.7: A typical tube splitting process and the corresponding crush force behaviour [47]

Though the splitting method demonstrates the ideal crush force behaviour, its sensitivity to axial alignments and structural integrity issues in the assembly state forbid the prospects of axial splitting method for energy absorption applications.

iv) Tube expansion

Yang *et al'*s [49] demonstrated energy absorption through tube expansion which is a novel method of energy absorption based on the combination of friction and plastic deformation with friction playing the dominant role. The work done here is based on plastic deformation by tube expansion process with friction contributing majorly to the crush force. Friction is observed to play a major role as observed in Figure 2.8. The crush force behaviour is observed to be nearly ideal with a constant force playing throughout the stroke, but this kind of structure pose challenges in terms of structural integrity in the normal working conditions.


a) Schematic layout of expandable tube system b) Tube expansion process c) crush force behaviour

Figure 2.8: Energy absorption by tube expansion process [49]

2.5.2.2 Multi-cornered cross-sections

Tubes with cross-sections consisting of different number of corners have been investigated in the past for energy absorbing applications. In this family, only square tubes were widely studied with emphasis on deformation modes and crush force behaviours.

i) Square tubes

Tubes with square cross-sections are also the widely adapted choice for energy absorption applications in cars, railways and ships. Their deformation modes are different to that of circular tubes because of their shape. However not much difference of crush force behaviour is reported in the literature as both the cross sections undergo progressive axial crushing. Under axial crushing, square tubes undergo a combination of inward and outward plastic bending on each successive surface of the tube with an appropriate stretching. Similar to circular tubes, geometric parameters play an influencing role in the plastic deformation pattern and the crush force behaviour. Crush force against crush displacement of typical square tubes is shown in Figure 2.9. Thin square tubes with high c/t ratio (where *c* is the side of the square and *t* is the thickness of the tube) higher than 50-60 are said to undergo non-compact collapse mode. The folding is not continuous and may tend to undergo Euler-type buckling, which is fundamentally an undesirable trait for an energy absorbing structure [50]. On the other hand, square tubes with smaller c/t ratios (thick tubes) tend to deform with gradual and regular alternate inward and outward folds on successive faces of the tube.


a) Compact deformation b) Non-compact deformation c) Crush force behaviour of square tube

Figure 2.9: Plastic deformation pattern and crush force behaviour of typical square tubes [5]

Generally the crush force behaviour of square tubes is characterized by high initial peak forces followed by fluctuations around a mean value in a narrow band. Stroke efficiencies are observed to be moderate in comparison to circular tubes [51 - 53].

ii) Multi-cornered sections

Some structural configurations with up to twelve numbers of corners are also used for energy absorbing applications. It is observed that as the number of sides in the polygon increases, the crush force and plastic deformation pattern also appear to be similar to those of circular tubes where crush force fluctuates in a wide band around a mean value. If the cross-section is made to be unconventional such as the shape of the mathematical operator 'plus' (+), the crush force behaviour is observed to be completely in contrast to a regular polygon with an initial high peak force followed by fluctuations in a narrow band as observed in the case of square tubes. However, the stroke efficiency continues to be an issue with a premature densification [54, 55].

2.5.2.3 Multi-celled configurations

Multi-celled configurations are also investigated with an objective of achieving the uniform crush force in literature. Majority of such structural configurations are made of square cross-sections [56 - 58] with square grid inside the main square as shown in Figure 2.10.

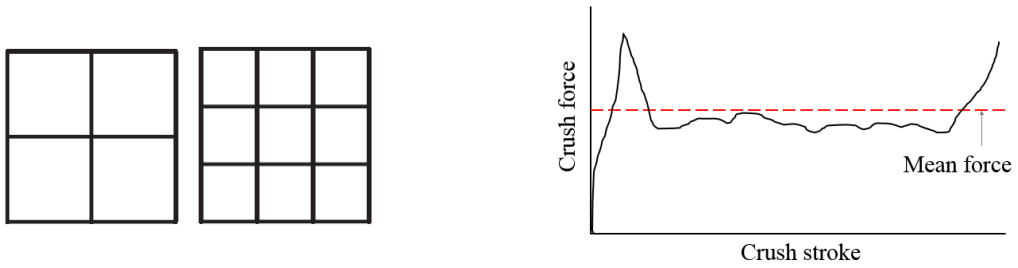


a) Multi-cell configurations b) Crush force behaviour

Figure 2.10: Cross-sections and crush force behaviour of typical multi-cell configurations [59]

Multi-celled configurations generally exhibit a near-ideal crush force behaviour after the initial peak with fluctuations in a very narrow band. However, a major drawback with such configurations is observed to be the stroke efficiency with an earlier or premature densification of material of the crushed part with a compromise in the fundamental requirement of energy absorption [56 - 58]. There are some empirical formulae available for crush force predictions which are expressed in terms of side of the square, thickness of tube, number of cells and the material's flow stress [60, 61].

2.5.2.4 Frusta and conical geometries

Circular and polygonal tubes with varying cross-sections (tapered) are widely studied for assessing the suitability for energy absorption applications [62-64]. In comparison to their straight counterparts, tapered sections demonstrated some improvements in stroke efficiency

as the varying geometry accommodates more material during the deformation process delaying the event of densification and also in minimizing the fluctuations in the crush force levels after the initial peak force.

2.5.2.5 Foam-filled metal tubes

Some attempts have been made in the past to improve the total energy absorbed by filling the metal tubes with metal or polymer foams [65]. Compressive strength of foams can be controlled by tuning the relative density and crush force behaviours can be customized to an extent. Several research studies suggest that filling the metallic tubes with foams increases the total energy absorbed. It has been observed that pure axial compression, uniform crush force and higher crush forces (higher TEA) are the major advantages for using foams as a crush force enhancing medium for metallic tubes. A typical arrangement of foam-filled tubes and the effect of interaction on the crush force is shown in Figure 2.11.

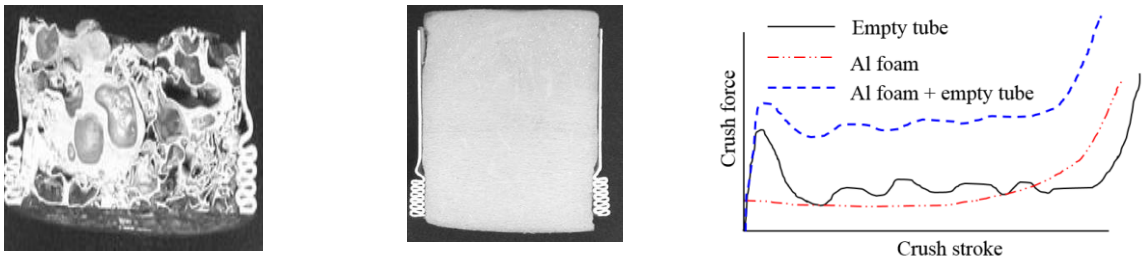


a) Metal tube filled with aluminium foam

b) Metal tube filled with polystyrene foam

c) Influence of foam on the crush force behaviour

Figure 2.11: Typical metal tubes filled with foams for energy absorption applications [65]

However, early densification of metallic foams and interaction effects of foam with the main tube during the axial compression results in moderate stroke efficiency leading to low TEA and SEA which work against the foams in energy absorbing applications [66-68].

2.5.2.6 Novel structural configurations

Some attempts have been made to stiffen the regular tubes axially with ribs and beads and corrugations to increase the crush force levels and hence TEA [69-71]. Zhang *et al*'s [72] kagome type sandwich cellular configuration; Yang *et al'*s [73] circular tube with ellipsoidal dimples for controlling the initial peak force and stabilizing the crush force behaviour after the initial peak; Zahran *et al'*s [74] novel 3D cellular configuration for improving the crush

force efficiency; Esa *et al'*s [75] piecemeal energy absorption (PEA) strategy for adaptive control of energy absorbing elements based on the impact velocity; Xu *et al'*s [76] investigation on the suitability of tailor-welded blanks and precise combination of different grades of materials are some of the case studies of novel approaches in the research of impact energy absorption. Outlines of such designs are shown in Figure 2.12.

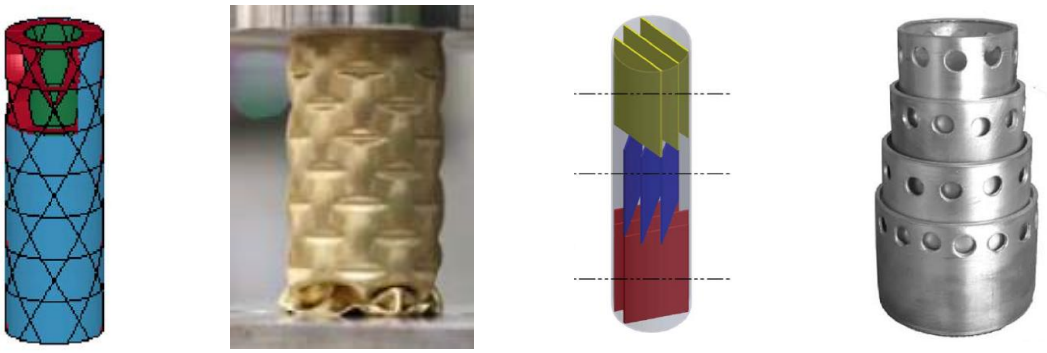

a) Kagome honeycomb [72] b) Ellipsoidal dimples [73] c) 3D cellular [74] d) Adaptive circular tubes [75]

Figure 2.12: Various novel designs of energy absorbing structures

2.5.2.7 Composite tubes

In the recent past, composite materials are being explored as a mainstream choice for energy absorbing applications. If the material properties in terms of damage initiation and evolution are tuned properly in all the three principal directions, composite materials with their characteristic tendency to deform and fail progressively can be ideal candidates for energy absorption applications. So far, carbon-fibre and glass-fibre family of composites have been widely explored for automotive applications [77]. Effect of fibre orientation [78], fibre thickness [79] and triggering mechanisms [77] are being studied extensively for achieving the near-ideal crush force behaviour. Composites in the form of truncated cones are also being explored for better control over the initial peak crush force [80]. In certain cases, composites are also being filled with polymer foams for better stability and improving the total energy absorbed [81]. Composites in the form of fibre metal laminates as both metal-intensive and composite-intensive [79, 82] forms are being studied to combine the benefits of metals and composites. Microscopic and macroscopic deformation and failure effects, inter-laminar fractures and delamination effects are widely exploited for controlled crush force behaviour [77-82]. In general, uniform crush forces and high stroke efficiencies are the salient features

of composites in energy absorption applications. However structural integrity issues and cost work against the composites for wide range energy absorption applications. Typical progressive failure and the corresponding crush force behaviour of composites is shown in Figure 2.13.

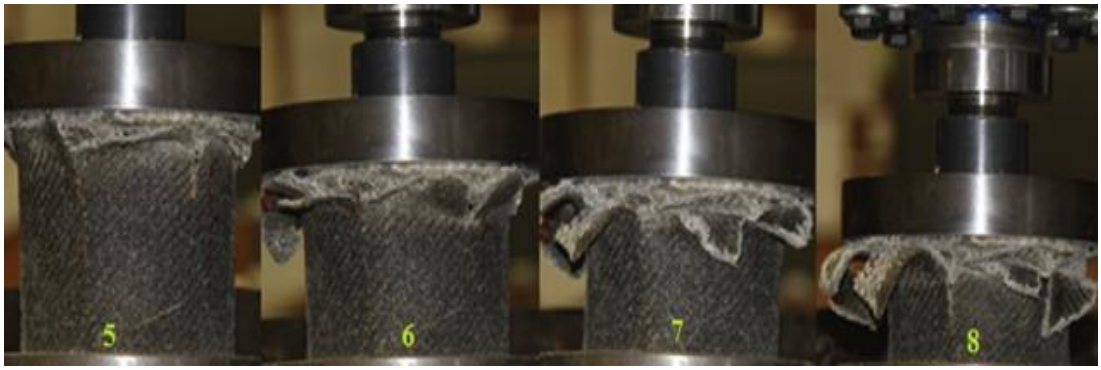


a) Progressive deformation in composite materials

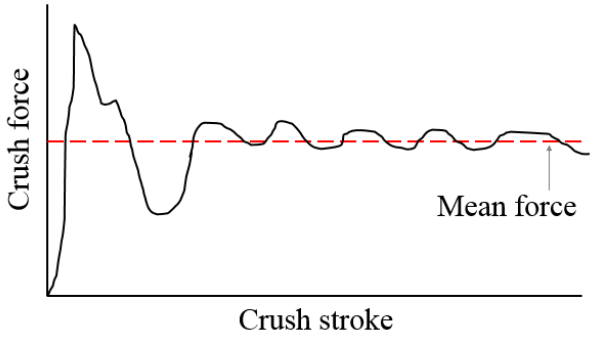


b) Crush force behaviour

Figure 2.13: Progressive deformation mode and crush force behaviour of a typical composite material [55]

### 2.5.3 Special Modes of Energy Absorption (using Hydraulics and Friction)

Special modes of energy absorption are the innovative concepts that work on the combination of friction, hydraulic effects and plastic deformation [83]. This concept as shown in Figure 2.14 consists of telescopic hydraulic tube system which is supported by two longitudinal members on either side. These members run under the longitudinal frame of the vehicle. A master cylinder controls the hydraulic fluid to the telescopic system which regulates the supply of fluid volume based on the impact velocity. At the instance of impact, the longitudinal members offer some resistance by undergoing plastic deformation. Major

contribution comes from the hydraulic system, where the impact resistance comes in the form of friction in the telescopic system and hydraulic effects.

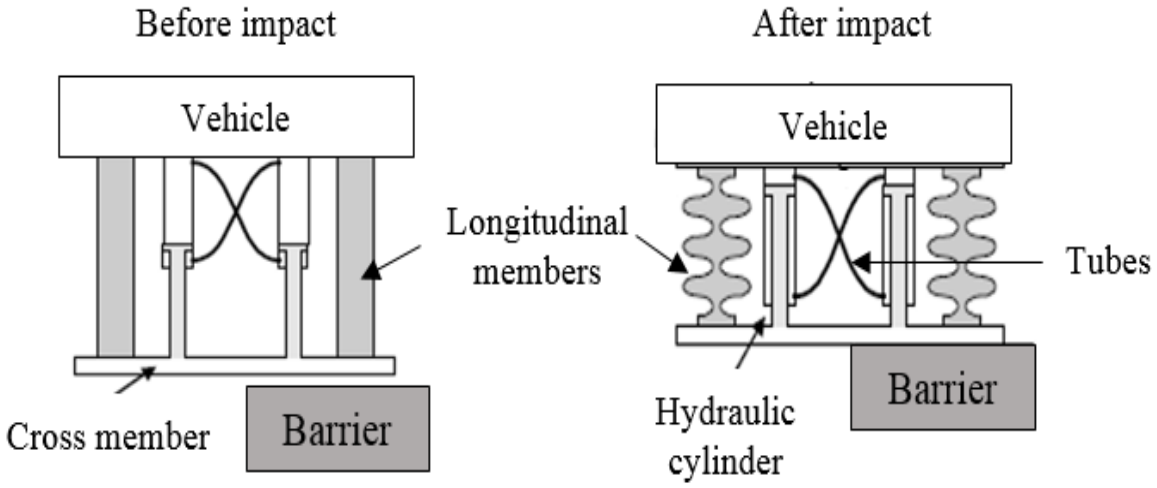


Figure 2.14: Innovative adaptive hydraulic energy absorbing system [83]

One major advantage of this system is its adaptability to all scenarios of frontal collision. As the whole system is integrated together, oblique impacts also get the same resistance as the pure axial scenario and this is a major advantage over the conventional deformation-based structures. But a limitation is the challenge in achieving compactness in the frontal compartment of the vehicle.

### 2.6 Materials

Different materials are used for energy absorbing structures either individually or in combination. Most common materials are as given below.

#### 2.6.1 Metals

Alloys of steels and aluminium have been the primary choice for energy absorption applications. Materials with high degree of ductility are generally ideal for these applications as large deformation plasticity is involved. High strength materials with moderate degree of ductility may help achieve crush forces in the initial phase, but eventually fall behind as the crushing progresses due to cracking. An optimum combination of strength and a high degree of ductility is a prerequisite for the materials used for crash energy absorption.

### 2.6.2 Foams

Foams with their porosity, grain structure and low Poission's ratio are ideal for crushing mode of deformation and exhibit near-ideal crush force behaviour. Relative density can be controlled by latest manufacturing methods for optimizing the weight. Aluminium and polymer foams are widely used in energy absorption applications. Densification of foams which leads to loss in stroke efficiency is a major drawback in foam materials.

### 2.6.3 Composites

The widely used composite materials are carbon or glass fibre reinforced polymer composites. An optimum combination of fibre material, matrix material, fibre/matrix interface strength, fibre stacking sequence, fibre orientation and fibre form (unidirectional, woven fabric or braided fabric), cross-sectional shape (square, rectangular or circular) and lengthwise shape (tapered or constant) and triggering system can be tuned for the required crush force behavior. Composite materials with precise control over all these parameters and direction-specific strengths are an ideal choice for crash energy absorption applications.

## 2.7 Research Gaps

After an extensive survey of literature, it is understood that control over the initial peak force, higher stroke efficiency, and crush force efficiency together with simplicity in structural integrity are the primary and essential requirements of an energy absorbing structure. Certain gaps exist in the literature which led the path for the present research and these gaps can be summarized as given below.

1. **Initial peak crush force:** There are very limited structural configurations that possess good control over the initial peak crush force (impact induced decelerations) which is a fundamental requirement from the occupant safety perspective as the decelerations are directly related to several injury criterion of occupants. Most of the structural configurations are observed to exhibit crush forces with equivalent deceleration levels beyond 30g which are considered unsafe from the occupant safety perspective.
2. **Crush force efficiency:** The crush force behaviour after the first yield is observed to be unstable for most configurations and the crush forces fluctuate over a wide range. Most of

the existing configurations are observed to possess CFE of around 50% and even 40% in case of structures with multi-celled cross-sections. Though stability is observed in some cases such as multi-cell and multi-cornered configurations, it is not retained for a long portion of the crush stroke. Stable crush force is an enabler for maximizing the TEA within the allowable range of crush forces.

3. **Stroke efficiency:** Moderate stroke efficiency is another drawback in most existing configurations and SE is driven by cross-section shape, ratio of geometric parameters (cross-section size to thickness ratio) and its plastic folding pattern. Crush tubes with circular shapes are observed to exhibit higher SE from 80% to 85% in concertina type of deformation and around 75% or less in circular tubes with D/t ratios beyond 70. Tubes with polygonal, multi-cornered and multi-cellular cross sections are observed to exhibit SE of around 70%. Not many structural configurations were observed which utilized the entire available stroke in the plastic deformation.
4. **Specific energy absorption:** Specific energy absorption was affected in many structural configurations due to limitations in the stroke efficiency which deterred the utilization of entire stroke and material of the structure. Very few structural configurations were observed to have demonstrated specific energy absorption factor greater than 15 kJ/kg.
5. **Challenges in practical applications:** Challenges in the structural integrity and assembly aspects have been observed in certain configurations which exhibited near-ideal crush force behaviour such as tube expansion, axial splitting and tearing and some cases of composite materials.
6. **Limited research information on tube inversion:** Tube inversion method, which seems to possess nearly-ideal crashworthy behaviour has very limited research outcome on the intricacies of the underlying aspects of inversion. Knowledge on geometric parameters of tubes, inversion-favourable materials and the cross-section profile of tube that are conducive to inversion process are not available in literature.

These gaps provided the motivation and impetus for the current research work to study the intrinsic aspects of plasticity mechanics and deformation patterns as they form the basis for the energy absorption phenomenon. It is observed that there is an excellent scope for arriving at structural configurations that fulfil the requirements of ideal crashworthiness of energy absorbing structures.

## 2.8 Research objectives

The primary objective of this research to develop energy absorbing structural configurations that exhibit a near-ideal crush force behavior such as i) uniform crush forces throughout the crush stroke, ii) magnitude of crush forces within the human tolerance limits, iii) moderate initial peak crushing forces, and iv) utilization of entire axial length in plastic deformation. These primary objectives aid in maximizing the total energy absorbed by the energy absorbing structure. The secondary objective is to ensure that the new structural configurations exhibit higher values of specific energy absorption (SEA) factor i.e. utilizing the minimum possible mass while maximizing the energy being absorbed by the structure.

The detailed objectives of the current research are listed as follows.

1. A comprehensive review of research from existing literature covering vehicular collisions, mechanics of collision, occupant safety, concept of impact energy absorption through different modes, criterion for assessment of crashworthiness of EA structures, existing structural configurations of energy absorption, and different kinds of materials used in EA structures.
2. Formulation of methodologies for numerical simulation of crash energy absorption behaviour of EA structures based on non-linear explicit finite element analysis (FEA) and validation with experimental results available in literature.
3. Investigation of the crush force behaviour of crush tubes having basic geometric cross-sections through established FEA simulations before attempting to develop novel EA structural configurations in the next phase.
4. Development of various EA structural configurations through numerical simulations based on i) circular tube-in-tube, and ii) hybrid cross-sections and evaluation of their relative performances based on different crashworthiness assessment parameters with crush force and stroke efficiencies around 85%.
5. Evolution of a new invertube's geometric profile and cross-section with stainless steel SS304 material to achieve desirable inversion characteristics for a near-ideal energy absorption based on numerical simulations and experiments.

6. Enhancement in specific energy absorption of invertubes with multi-material structural configurations in the form of hybrid composites and fiber metal laminates to achieve specific energy absorption factor greater than 25 kJ/kg.
7. Development of EA structural concepts through a unique combination of bending and inversion deformation modes with multi-material combinations involving metals and metallic foams to increase the total crash energy absorption.
8. Demonstration of the importance and effect of damage modelling in numerical simulation of crash EA structures

## 2.9 Research Methodology

In the current research work, the principal objective is to arrive at structural configurations that exhibit plastic deformation pattern with controlled initial peak crush forces, uniform crush forces throughout the crush stroke and higher crush force and stroke efficiencies for maximizing the amount of energy absorbed. The methodology adopted in present research in developing EA structural configurations to meet near-ideal crashworthiness requirements is broadly outlined in the form of a flow chart as shown in Figure 2.15.

1. The existing literature in the area of energy absorption has been studied in detail with attention to plastic deformation patterns, their influence on the crush force behaviour and the overall energy absorption process and the material trends.
2. Finite element analysis (FEA) procedures are extensively used for developing various concepts for energy absorbing structures. To validate the accuracy of the FEA methodology and procedures, a few experiments reported in existing literature have been reproduced in the commercial FEA code ABAQUS and FEA simulation results are correlated with the experimental results. These FEA methodologies have been utilized to understand the intricate aspects of the relationship between the plastic deformation modes and the crush force behaviour.
3. Several structural concepts have been formulated and they have been assessed on the standard crashworthiness parameters using FEA methods. The concept (tube inversion) with the plastic deformation which is ideal for energy absorption has been chosen for further steady.

4. Detailed FEA simulation works have been carried out to design a tube cross-section profile that is amenable to tube inversion and the final profile has been validated experimentally in the quasi-static environment.
5. To improve the specific energy absorption factor, a few multi-material concepts involving composites and metal foams have been proposed and they have been assessed on the standard crashworthiness parameters using FEA procedures.

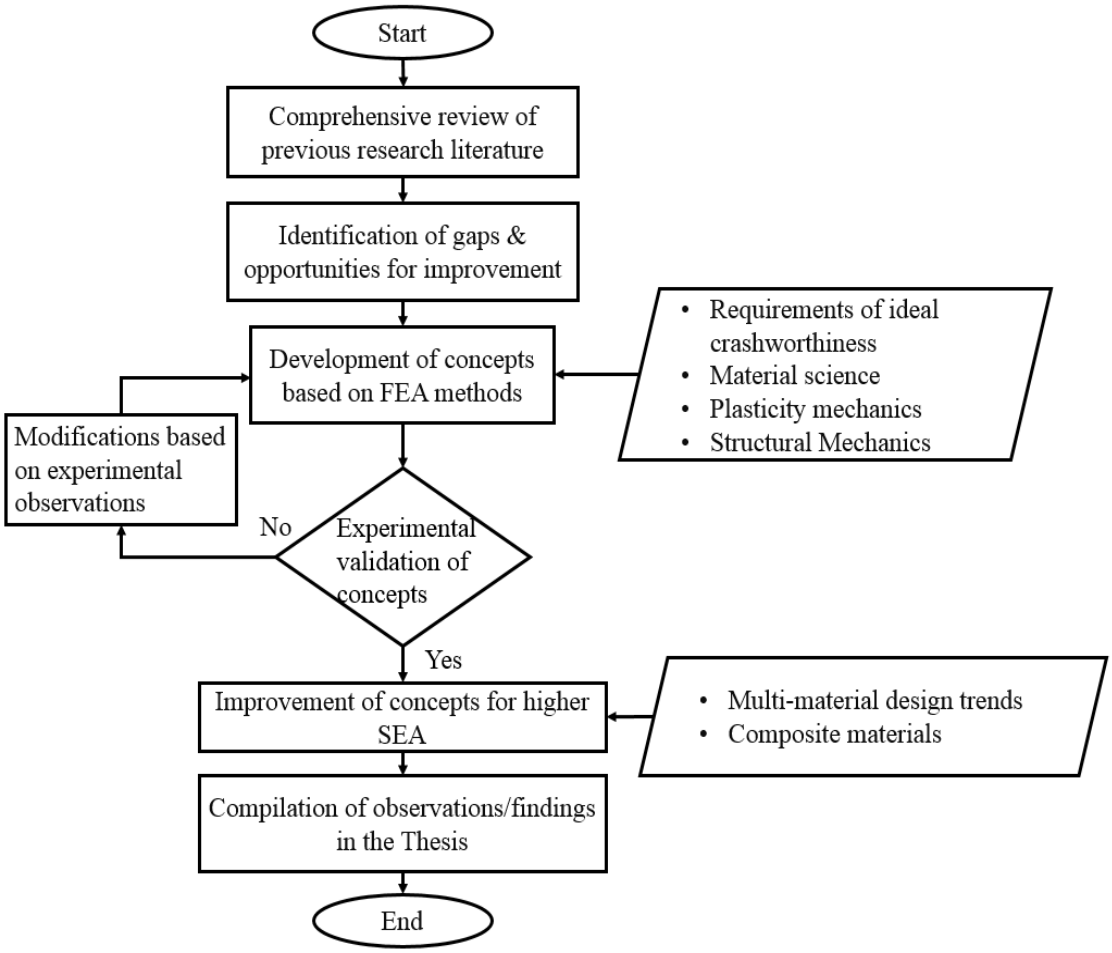


Figure 2.15: General methodology adopted in present research

## 2.10 Summary

A comprehensive review of the research literature has been done on the fundamental aspects of impact energy absorption process from the perspective of occupant safety in road vehicles. This review presented an insight into various methods of energy absorption, their intricate aspects and the requirements of an ideal energy absorbing structure. Plastic deformation is observed to be more efficient and widely accepted mode of crash energy absorption. It has

been observed that plastic deformation mode influences the crush force behaviour of the energy absorbing structure. Plastic deformation mode is governed by the geometry (cross-section) of the structure in general and relation between each geometric parameter in particular (eg. D/t ratio and c/t ratio in case of circular tubes and square tubes respectively).

High initial peak crushing force is a common trait in most of the existing structural configurations which is undesirable from the occupant safety perspective. Crush force and stroke efficiencies are conflicting with each other in most cases while they are expected to be in harmony for an efficient energy absorption process. Tapered geometries exhibited slightly higher stroke efficiencies. Multi-cornered and multi-celled configurations exhibited good trends of uniform crush forces albeit for shorter plastic crush strokes.

Some special deformation mechanisms such as tube expansion and axial splitting exhibited near-ideal crush force behaviour but have challenges in terms of alignments and structural integrities. Some structural configurations with composite materials which exhibited progressive deformation and damage with proper triggering mechanisms have displayed almost an ideal crush force behaviour. Some hybrid configurations which combined porous materials (metal foams and polymer foams) with metals and composites were found to be enablers for enhancing the total energy absorbed, but had some limitations in stroke efficiencies. A material with a good combination of high degree of ductility and strength is preferred as large plastic strains are involved in the deformation process.

Gaps in the existing research which provided impetus for this research, objectives of the current research and the research methodology being followed to meet the said objectives have been discussed.

# Chapter 3

# Formulation of Finite Element Analysis (FEA) Methodology and Its Experimental Validation

This chapter presents development of finite element analysis (FEA) simulation procedure using ABAQUS FEA code [84] to simulate the vehicular crash impact on frontal energy absorbing (EA) structures. The adopted FEA methodology is validated by simulating three energy absorbing structures experimented in previous literature. The discussions in the development of FEA procedure and validation with experiments are elaborated in this chapter and summarized at the end.

## 3.1 Introduction

It is understood that the total energy absorption is no more a single and direct measure of performance of an energy absorbing structure. Crush force behaviour plays a vital role in energy absorption as it is linked to several injury criterion for occupants. With several factors such as geometric parameters (shape, cross-sectional area, thickness and ratio of cross-section size to thickness, and so on) and material holding a significant and decisive influence on the crush force and plastic deformation behaviours, the complexity of mechanics of energy absorption by plastic deformation mode gets compounded. Conventional structural mechanics is inadequate to provide straight forward solutions to such extremely complex and sensitive problems involving nonlinearity of large plastic strains. Numerical simulations based on FEA are commonly adopted due to their growing acceptance and the abundance of computing power and are widely used in the engineering design and research areas to understand the intricacies of several aspects of structural mechanics and to save time and cost on prototyping and testing. FEA simulations help to study the effect of different material, geometry, structural configuration and deformation mechanism on crash energy absorption behaviour of crush tubes. It facilitates proper assessment of crashworthiness of energy absorbing structures based on different performance parameters highlighted in previous chapter. These advanced FEA simulations and their predictions offer reliable solutions which otherwise are not easily and economically possible based on conventional methods.

## 3.2 FEA Simulation of EA Structures

In the present research, FEA methods are proposed to be used to develop new structural concepts for EA applications that exhibit a near-ideal crush force behaviour. The procedure thus formulated in present research is validated by numerically simulating three different EA structures which were subjected to crash impact experiments and reported in previous literature. Three standard EA structures with different geometrical cross sections, made of aluminium and steel alloys from three different literatures for which experimental results are available, are modelled and numerically simulated using the commercial FEA code ABAQUS [84]. The results of present simulations are compared with their experimental results available in literature to ascertain the accuracy of FEA procedure and its methodology. This simulation and experimental validation helps to establish the FEA simulation procedure and build confidence in its correctness before adopting this simulation methodology for developing new structural configurations proposed in latter part of this research work.

### 3.2.1 FEA Simulation of EA Specimen-1 and Validation with Experiment

#### 3.2.1.1 Specimen Geometry and Material Property

This experimental study was conducted on a specimen of square cross section with dimension 200 x 75 x 75 mm and thickness 1.3 mm as shown in Figure 3.1. Crush initiation triggers are introduced at the front end of the structure at a distance of approximately half the width of the crush fold with a depth of 0.3 mm as per the experimental specimen [85]. This EA structure is made of AA6061-O grade with Young's modulus = 69 GPa, Poisson's ratio = 0.3, yield strength = 71 MPa and density = 2580 kg/m$^3$. The material's elasto-plastic stress-strain curve obtained from the uniaxial test conducted [85] as per the standard is shown in Figure 3.2 and is considered for this study.

a) EA specimen-1 [85]

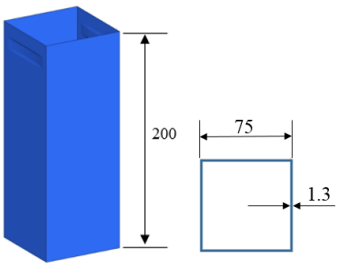


b) FE model of EA specimen

Figure 3.1: EA specimen-1 considered for experiment [85] and present FE model (all dimensions in mm)

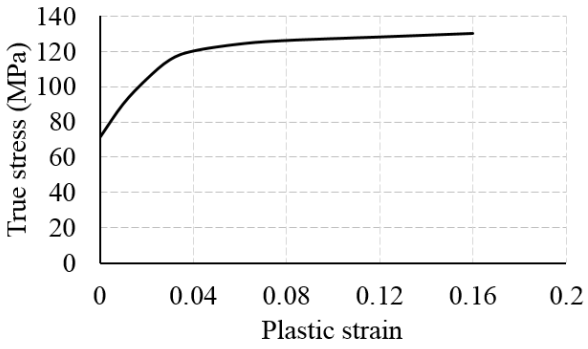


Figure 3.2: True stress – plastic strain curve of Aluminum AA6061-O [85]

3.2.1.2 Experimental Setup

In the experimental setup [85], the bottom face of the specimen was fixed to a rigid block. Another rigid block which is attached to the machine's loading head was used to impact the specimen at the top end with a constant axial velocity of 1 mm/s as shown in the Figure 3.3 (a).

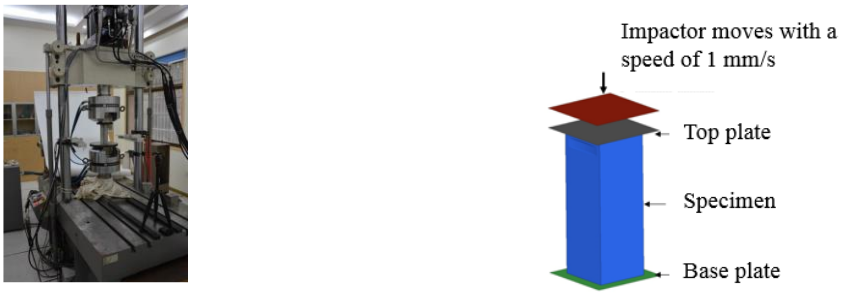


a) Experimental setup [85] b) FEA setup

Figure 3.3 Experimental and FEA setups for EA specimen -1

3.2.1.3 Numerical Simulation

This axial impact simulation is performed as per the FE model set up shown in Figure 3.3 (b). The EA structure is discretized using first order shell elements (S4R) in ABAQUS/Explicit 6.14-3 [84]. The top and bottom plates are modelled as rigid elements (R3D4). Top face of the specimen is rigidly fixed to the top plate and bottom face to the base rigid plate using *TIE option in ABAQUS [84] in accordance with the experimental setup. The rear rigid base plate is completely constrained in all degrees of freedom to represent the ground in the

physical test. The rigid impactor impacts the EA structure in the axial direction with a steady velocity of 1 mm/s. All other degrees of freedom of the impactor are constrained. Explicit dynamic solution methodology [84] with general contact algorithm is activated to capture the folding modes in detail. Reaction forces in the axial direction at the reference node of the base rigid plate are recorded as axial crush forces. After a convergence study, the element size is finalised at 1.4 mm, optimum enough to capture plastic deformation and self-contact effects.

3.2.1.4 Comparison of experimental and present FEA results

A comparison of plastic deformation and crush force behaviours from the experiment [85] and present FEA is shown in Figure 3.4 at the end of active 120 mm crush. Comparison of axial crush force and energy absorption behaviours between the experiment [85] and the present FEA is shown in Figure 3.5. As the structure is stiff due to a stiff square cross-section, $F_{peak}$ of 23.5 kN is required to initiate the plastic folding in the structure and the crush force falls drastically down to around 6 kN as the fold gets completed. Then, the crush force fluctuates around a mean force of approximately 8 kN until a crush stroke of 120 mm. This comparison is done till the crush stroke of 120 mm as the test results are available [85] until 120 mm only. Due to stiffer corners, the structure densifies and it resists further plastic deformation. Prediction of initial peak crush force of 23.56 kN from FEA is observed to be in good agreement with that of the test [85] with 22.48 kN (obtained after digitizing the crush force versus crush displacement of the test). The crush force from FEA after the initial peak also followed the similar trend as that of the test until a crush stroke of 100 mm. The crush force in FEA increased from a crush stroke of 100 mm onwards as densification of the crushed material contributed to increase in stiffness.

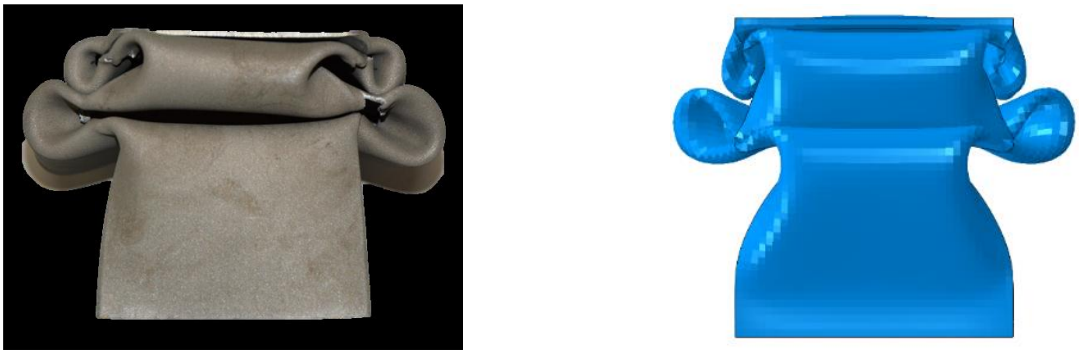

a) Experiment [85] (b) Present FEA

Figure 3.4: Comparison of deformation modes at a crush stroke of 120 mm: EA Specimen-1

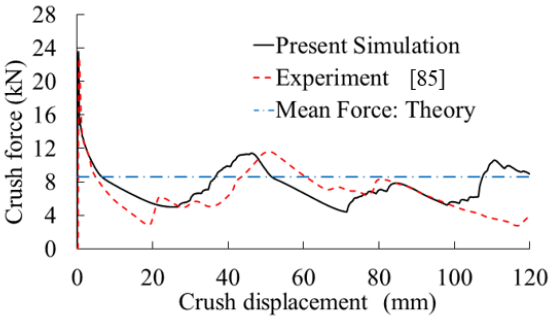


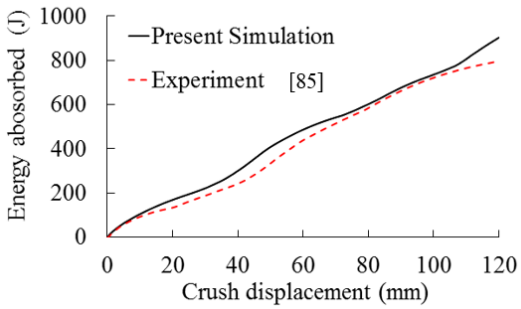


(a) Crush force versus axial displacement (b) Energy absorption versus axial displacement

Figure 3.5: Crush force and energy absorption behaviours of EA specimen-1: Comparison between present simulation and experiment [85]

It is observed from Figure 3.4 (a) that cracks appeared at the square corners during the folding process. This might have contributed to drop in crush resistance of the structure and hence the decreasing trend in the crush force at around 100 mm of crush stroke, though the exact instance of cracking can't be inferred from the available test results. If a damage criteria of the material (threshold plastic strain which triggers cracking through element kill algorithm) is specified in the numerical program, correlation of FEA results with those from the physical test may be closer at this instant. The energy absorbed by EA structures is determined by calculating the area under crush force versus crush displacement i.e. ($F - d$) curves from both present FEA and experiment [13] for a crush stroke of 120 mm which resulted in 900 and 816 joules respectively with a difference of 12.5% in prediction w.r.t. [85]. This comparison is shown in Figure 3.5 (b).

Additionally, the $F_{mean}$ from FEA is compared with theoretical formula as shown in Figure 3.5 (a). There are no straight-forward solutions for prediction of $F_{mean}$ from theory but researchers have proposed some empirical formulae for standard geometrical cross-sections. Chen *et al* [86] with their simplified theory proposed an empirical formulae for $F_{mean}$ of various cross-sections. Accordingly, $F_{mean}$ of a square cross section based EA structure is expressed as

$$F_{mean} = 6.68\ \sigma_p\ c^{1/2} t^{3/2} \tag{3.1}$$

where $\sigma_p$ is the flow stress of the material, $c$ is length of side of square cross-section and $t$ is the thickness of cross-section. In the present study, c = 75 mm and t = 1.3 mm. Assumption

of a value for flow stress $\sigma_p$ is not a straight forward procedure as the value changes with accumulation of strain in the material. Few researchers [87, 88] suggested this as an average of yield strength and ultimate strength of the material. Abramowicz *et al* [89] proposed it as 0.92 times the ultimate strength. In this study, flow stress is considered as the average of yield (71 MPa) and ultimate strength (130 MPa) which is 100.5 MPa. Substituting these values in Eq. (3.1), we get theoretical $F_{mean}$ as 8.6 kN.

$F_{mean}$ from FEA is about 7.5 kN (TEA = 900 joules for a crush stroke of 120 mm), while the $F_{mean}$ from experimental data [13] is about 6.8 kN (TEA = 816 joules for 120 mm) for the same effective crush stroke. The $F_{mean}$ from present FEA closely match with that from the experiment [85] while being offset from the theoretical value by about 12.8%. It may still be considered as a fair correlation. Comparison of this standard EA structure-1 between the present FEA, experiment [85] and theory based on the crashworthiness performance parameters is discussed in Table 3.1.

Table 3.1: Crashworthiness performance of EA specimen-1- present simulation versus experiment [85]

| Parameter | Mass (kg) | Peak force (kN) | Mean force (kN) | TEA (kJ) | Crush stroke (mm) | CFE (%) | SE (%) | SEA (kJ/kg) |
|---|---|---|---|---|---|---|---|---|
| Present simulation | 0.2 | 23.6 | 7.5 | 0.9 | 120 | 31.8 | 60.0 | 4.5 |
| Experiment [85] | 0.2 | 22.5 | 6.8 | 0.8 | 120 | 30.2 | 60.0 | 4.0 |
| Theory [86] | 0.2 | - | 8.6 | 1.0 | 120 | - | - | 5.2 |
| % Difference in present simulation w.r.t. [85] | 0 | 4.9 | 10.3 | 12.5 | 0 | 5.3 | 0 | 12.5 |

### 3.2.2 FEA Simulation of EA Specimen-2 and Validation with Experiment

#### 3.2.2.1 Specimen Geometry and Material Property

In this study, EA specimen-2 with a multi-celled (four cells) column is considered for second level experimental validation of present FEA simulation. This column was also made of aluminium alloy AA6061-O which was used in the previous experimental validation study of EA specimen-1 [85]. The engineering stress-strain curve of AA6061-O from two different

tests [85, 90] is same as the one shown in Figure 3.2. The experimental specimen and the geometry and cross-section of this standard EA structure-2 are shown in Figure 3.6. The structure is 120 mm long with 36 mm width for major square cross section. The thickness of each outer wall and internal webs is 1.2 mm. The bottom of the column is welded to a 6 mm thick aluminium plate.

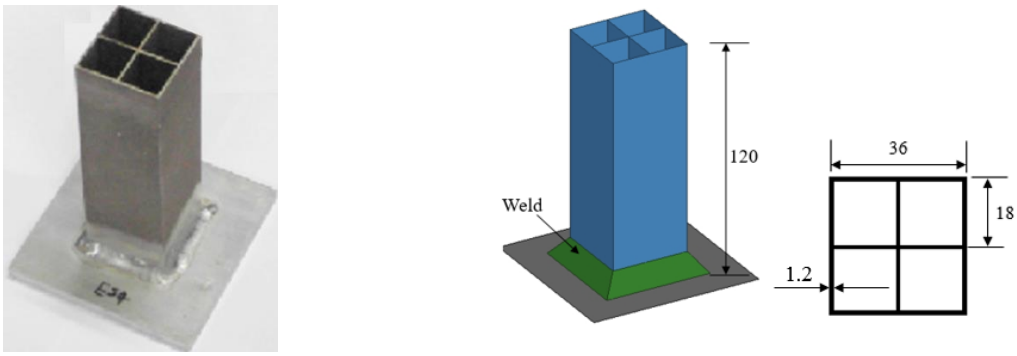


a) Experimental EA specimen-2 [90]

b) FE model of EA specimen-2

Figure 3.6: EA specimen-2 and its present FE model (all dimensions in mm)

3.2.2.2 Experimental Setup

The experimental [90] and FE model setups for EA specimen-2 are shown in Figure 3.7. This axial compression on the specimen is simulated in FEA in a quasi-static environment as per the setup shown in Figure 3.7 (a). As the experimental setup is similar to that of the previous one, the same FEA method is followed here.

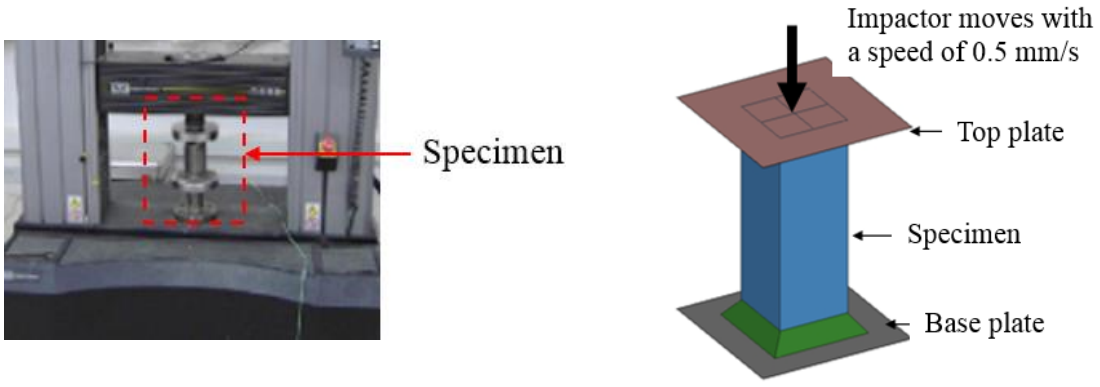


a) Experimental setup [90]

b) FEA setup

Figure 3.7: Experimental setup [90] and present FEA setup for EA specimen-2

3.2.2.3 Numerical Simulation

The structure was discretized using first order shell elements (S4R) [84] with an element size of 1.2 mm (finalized after a mesh convergence study) sufficient enough to capture plastic deformation and self-contact effects. The weld connection of specimen to the thick base plate is modelled with 8-node solid hexahedral elements (C3D8R) as shown in Figure 3.6 (b). The base plate and the impactor are modeled as rigid bodies using rigid shell (R3D4) and the specimen is rigidly fixed to the base rigid plate and the top plate using *TIE option in ABAQUS [84]. The base rigid plate is completely constrained in all degrees of freedom. The impactor is prescribed with a constant axial velocity boundary condition of 0.5 mm/s as shown in the Figure 3.7 (b). All other translations and rotations of impactor are completely constrained. General contact algorithm was activated to capture the self-contact phenomenon during crush folding. Axial compression is simulated in a quasit-static environment using ABAQUS/ Explicit [84].

3.2.2.4 Comparison of experimental and present FEA results

A comparison of plastic deformation modes from the experiment [90] and present FEA is shown in Figure 3.8. Axial crush force pattern of this EA structure-2 from present FEA is compared with experimental results [90] in Figure 3.9 (a).

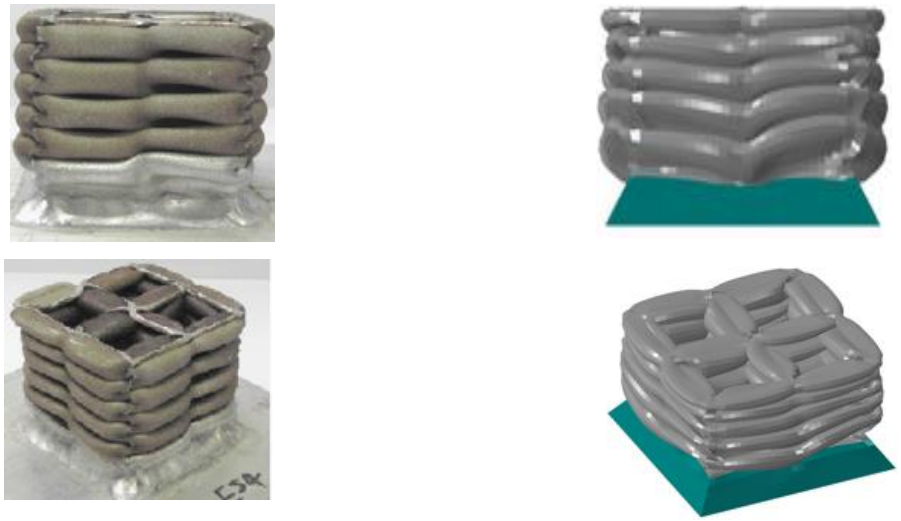

No. of uniform folds = 5

(a) Experiment [90] (b) Present FEA

Figure 3.8: Comparison of deformation modes at a crush stroke of 90 mm for EA specimen-2

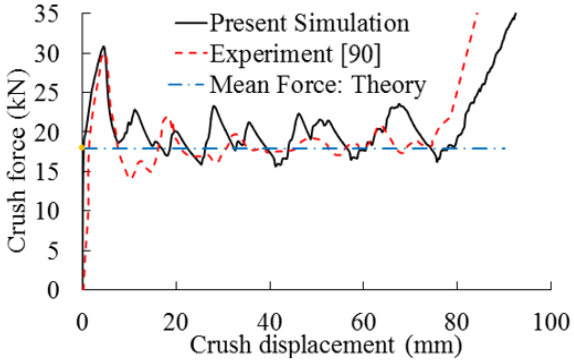


(a) Crush force versus axial displacement

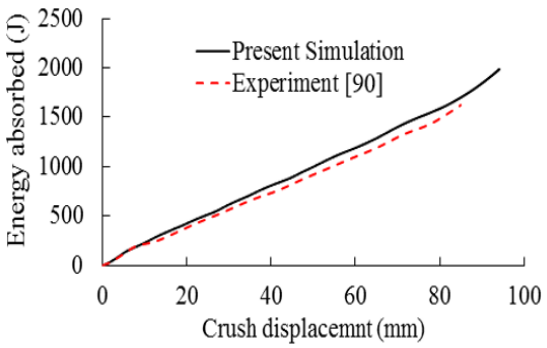


(b) Energy absorption versus axial displacement

Figure 3.9: Crush force and energy absorption behaviours of EA specimen-2: Comparison between present simulation and experiment [90]

Present FEA predicted an $F_{peak}$ for this multi-cell structure as 30.8 kN at a crush stroke of 5 mm, while the $F_{peak}$ from the test is 29.9 kN. The crush force then drops to 20 kN at around 10 mm of crush stroke and fluctuates between 16 kN and 22 kN until a stroke of 82 mm. At 82 mm of stroke, the structure densifies due to a stiff core and resists further plastic crushing. From the crush force versus axial crush displacement i.e. ($F$ – δ) graph [90], densification is observed at a stroke of 78.6 mm and the crush force curve maintains nearly a steady plateau around an average force of 17.5 kN. From the ($F$ – δ) graph shown in Figure 3.9 (a), it can be understood that there is a good correlation between experiment [90] and present FEA result.

The TEA by the specimen calculated from present FEA and experiment [90] at the end of their corresponding crush strokes is around 1628 joules (for 82 mm) and 1448 joules (for 78.6 mm) respectively with a difference of 12.4 % *w.r.t.* the latter [90]. The difference in TEA is due to loss of crush stroke in case of experiment; and $F_{mean}$ from FEA is slightly higher than that of the experiment. Accurate representation of material details would have improved experiment and FEA correlation. Comparison of TEA between experiment [90] and FEA is shown in Figure 3.9 (b).

Chen *et al* [86] suggested a simplified theoretical formula for prediction of $F_{mean}$ for multi-cell cross sectional columns and as per this theory, the $F_{mean}$ for 4-celled column is expressed as

$$F_{mean} = 14.18\ \sigma_p\ c^{1/2} t^{3/2} \quad (3.2)$$

Substituting the values of $\sigma_p$ = 100.5 MPa as discussed previously, c = 36 mm and $t$ = 1.2 mm, the $F_{mean}$ is predicted as 11.28 kN. Based on the super folding element theory, Zhang *et al* [91] proposed different formula for multi-cell columns by dividing the cross-section into corners, criss-cross junctions and T-junctions. According to this theory, the $F_{mean}$ of 4-cell cross-sections is expressed as

$$F_{mean} = 1.3\ \sigma_p\ t \sqrt{(N_c + 4N_o + 2\ N_t)\ \pi\ LC_t t}. \quad (3.3)$$

where $N_C$ = number of corners = 4; $N_O$ = number of criss-cross junctions = 1; $N_t$ = number of T-junctions = 4; $C_t$ = perimeter of total cross-section = 216 mm (6 x 36 mm i.e. 6 equal sides of 36 mm each) as shown in Figure 3.6. By substituting the appropriate values, the $F_{mean}$ is 18.0 kN, which is close to both present FEA and experiment [90]. Detailed comparison of crashworthiness assessment parameters between experiment [90], FEA and theory is given in Table 3.2.

Table 3.2: Crashworthiness performance - present FEA versus experiment [90] of EA specimen-2

| Parameter | Mass (kg) | Peak force (kN) | Mean force (kN) | TEA (kJ) | Crush stroke (mm) | CFE (%) | SE (%) | SEA (kJ/kg) |
|---|---|---|---|---|---|---|---|---|
| Present simulation | 0.11 | 30.8 | 19.8 | 1.6 | 82.0 | 64.3 | 68.3 | 14.8 |
| Experiment [90] | 0.11 | 29.9 | 18.4 | 1.5 | 78.6 | 61.5 | 65.5 | 13.2 |
| Theory [91] | 0.11 | - | 18.0 | 1.5 | 82.0 | - | | 16.5 |
| % Difference in present simulation w.r.t. [90] | 0 | 3.01 | 7.61 | 12.4 | 4.32 | 4.55 | 4.27 | 12.1 |

### 3.2.3 FEA Simulation of EA Specimen-3 and Validation with Experiment

*3.2.3.1 Specimen Geometry and Material Property*

In the third round of FEA validation exercise, EA specimen-3 with a multi-cornered structure studied experimentally by Reddy *et al* [92] is considered. The cross-section of this configuration is made of 12 corners and 12 sides. The structure is made of two sheet metal profiles each with 1.6 mm thick and 350 mm long and welded together with an overlap of

around 8 mm between the two opposite sheets as shown in the Figure 3.10. The material considered for this study is mild steel HA3 having 235 MPa as the yield stress, UTS of 340 MPa and density of $7.8 \times 10^{-6}$ kg/mm$^3$. The material's non-linear stress-strain curve [92] obtained from the uniaxial test conducted as per AS1391-2007 standard and shown in Figure 3.11 is considered for this FEA.

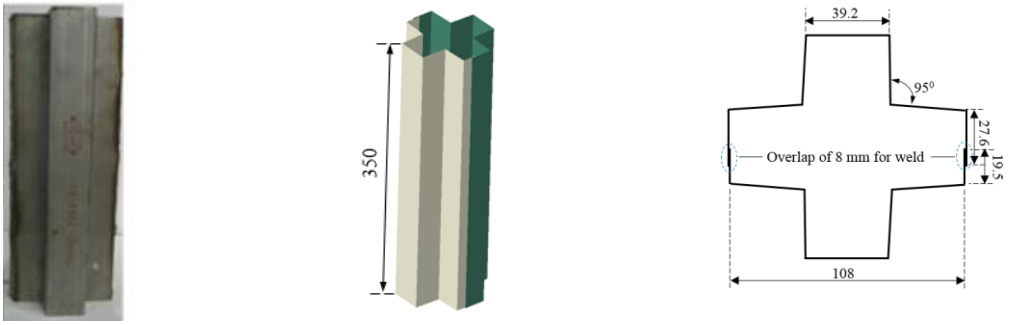


a) Experimental specimen-3 [92] b) FE model c) Cross-section

Figure 3.10: Experimental EA specimen-3 and present FE model (all dimensions in mm)

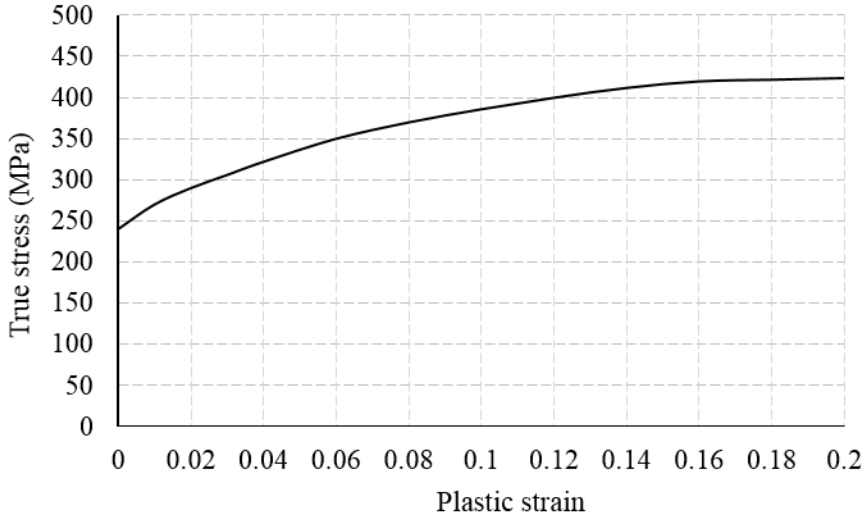


Figure 3.11: Stress-strain response of mild steel HA3 [92]

*3.2.3.2 FE model setup and analysis*

The geometric model is discretized using the first order shell (S4R) elements with an optimum average element size of 2.0 mm, fine enough to capture all details for plastic folding of the column during axial crush. General purpose commercial FEA solver ABAQUS 6.14-3 [84] with explicit solution methodology is chosen for this simulation. The general contact algorithm feature in ABAQUS [84] has been activated to capture the entire contact phenomenon related to plastic folding of the EA structure during the axial crush.

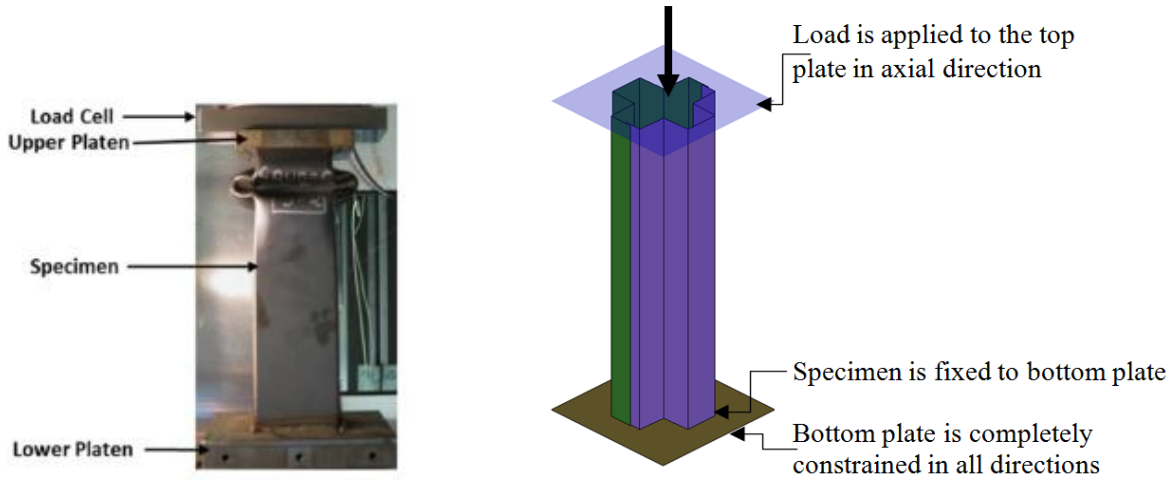


a) Experimental set up [92] b) Present FE model

Figure 3.12: Experimental setup [92] and FEA setup for EA specimen - 3

In the FE model, the bottom end of the EA structure is fixed to a rigid base plate which is constrained completely in all degrees of freedom. Top end of EA structure is fixed to another rigid plate. In the loading setup, EA structure is crushed axially by applying an enforced constant velocity to the top rigid plate in quasi-static mode in the axial direction towards the bottom end of the structure. The actual experimental set up [92] and the present FE model are shown in Figure 3.12. All other degrees of freedom of the top rigid plate are arrested to ensure pure axial motion. This experiment [92] was performed in a quasi-static environment and the speed of impactor was not mentioned in the literature. A series of iterations have been performed with various impact speeds to achieve a good agreement in crush force-vs-crush displacement curve of the present FEA with that of the experiment [92]. An impact speed of 8 mm/s yielded a good correlation.

3.2.3.3 Comparison of results between present FEA simulation and experiment

The crush folding patterns from the experiments and the present simulation are shown in Figures 3.13 (a) and 3.13 (b) respectively, where the stable crushing patterns in both the studies are very similar. The axial crush force and energy absorption behaviours of experiment [92] and the present FEA are shown in Figure 3.14 (a) and 3.14 (b) respectively. Due to high initial stiffness of the structure, an initial peak crush force of around 200 kN is observed to initiate the plastic deformation followed by a steep fall in the crush force. The crush force oscillates about an average force of 98 kN with the progress of plastic deformation in a series of regular outward folds. This stable crush continued until a crush stroke of about 251 mm and the structure resisted further plastic deformation. This is evident

from the crush force – displacement curve (Figure 3.14 (a)) where the curve takes a sudden ascent after 251 mm signifying that the structure has become rigid and plastic folding is no longer possible. The TEA by this standard EA structural configuration is measured as 23.5 kJ in experiment as compared to 24.6 kJ predicted in the present FEA with a difference of 4%.

(a) Present simulation at 260 mm crush (b) Experiment [92]

Figure 3.13: Comparison of deformation modes at a crush stroke of 250 mm for EA specimen-3.

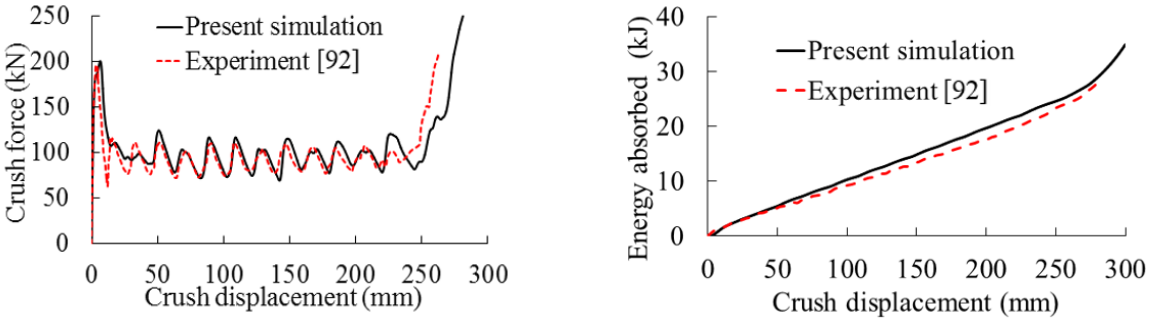


(a) Crush force versus axial displacement (b) Energy absorption versus axial displacement

Figure 3.14: Crush force and energy absorption behaviours of EA specimen-3: Comparison between present simulation and experiment [92]

The crashworthiness performance parameters such as $F_{peak}$, $F_{mean}$, TEA, crush distance, CFE, SE and SEA of the considered EA specimen-3 predicted from the present simulation are compared with that of experimental results [92] in Table 3.3. The percentage difference in these parameters between prediction and experiment with respect to that of experiment is very less and shows very close agreement between the two studies as given in Table 3.3.

Table 3.3: Crashworthiness performance of EA specimen-3- present simulation and experiment [92]

| Parameter | Peak force (kN) | Mean force (kN) | TEA (kJ) | Crush distance (mm) | CFE (%) | SE (%) | SEA (kJ/kg) |
|---|---|---|---|---|---|---|---|
| Present simulation | 202 | 98 | 24.6 | 251 | 49 | 72 | 12.9 |
| Experiment [92] | 196 | 93 | 23.6 | 248 | 48 | 71 | 12.4 |
| % difference with respect to experiment [92] | 3.06 | 5.38 | 4.24 | 1.21 | 2.08 | 1.41 | 4.03 |

The results from present FEA simulation are in very good agreement with those of experiment [92] in terms of observed plastic deformation modes, crush force and energy absorption versus displacement characteristics, and other crashworthiness performance indicators. It can be concluded that the adopted FEA procedure in present simulation has demonstrated an acceptable order of accuracy in predicting axial compressive deformation behaviour of standard EA specimens/structure. It shall be noted here that the strain rate effect on metals under impact speeds observed in vehicular collisions is negligibly less [93] and adopting the material response evaluated under quasi-static condition still produces agreeable results. Further, the difference in the impact velocity between the present FEA validation studies (which is inferred as 8 m/s) discussed above and the latter FEA (at 15 m/s) of the proposed EA structural configurations, in terms of strain rate of loading is insignificant. Therefore, the present FEA approach thus validated is adopted in analysing the newly proposed EA structural configurations for enhanced crashworthiness in latter chapters.

### 3.3 Observations from the Present FEA Validation Studies

Three FEA methodology validations with experimental results i.e. on three standard EA structures with simple square, 4-celled square cross-section and twelve-cornered were performed to establish the present simulation procedure and develop confidence in the FEA methodology. From FEA results of all the three EA specimen, it may be observed that the results of the present FEA method correlated with the experimental results reasonably well (Figures 3.4, 3.5, 3.8, 3.9, 3.13 and 3.14; and Tables 3.1 - 3.3) and also with the theoretical predictions. Some deviation from theoretical predictions is observed, but those formulae have been derived with assumptions and approximations which was evident with the case of 4-cell cross-section specimen discussed above. Though these FEA validation studies are quasi-static in nature, good correlation with the experimental results brings confidence in the application of this established FEA methodology for the development of new EA structural configurations. It shall be noted here that the strain rate effect on metals under impact speeds observed in vehicular collisions is insignificant [93] and adopting the material response evaluated under quasi-static condition still produces agreeable results. The present FEA methodology can be applied for the numerical assessment of crashworthiness of the new EA deformable structural configurations proposed subsequently.

### 3.4 Summary

It may be observed from the validation studies that the present FEA methodology correlates well with all the three experiments with a maximum difference of 10% and 12% for the mean force and the total energy absorbed demonstrating the reliability of FEA procedures. The FEA methodology thus developed brings confidence to developing new structural configurations that can exhibit a near-ideal crush force behaviour.

# Chapter 4

# Numerical investigations on energy absorption behavior of crush tubes with basic geometric shapes

This research aims to arrive at structural configurations of energy absorbing structures that exhibit a near-ideal crush force behavior. In this chapter, energy absorption behavior of different standard and basic geometries are studied exhaustively through FEA simulations. This study is very essential in understanding the behaviour of basic geometries before attempting to propose new EA structural geometries or configurations which exhibit near-ideal crush force behaviours. The FEA simulation procedure established and validated by comparison with experiments in previous chapter is adopted in the numerical simulations of basic geometries in this chapter. This chapter gives a brief observations from the existing energy absorbing structures, introduces the basic geometric shapes to be analyzed, explains FEA setup and methodology to be followed and discusses the crash performance i.e. plastic deformation trends and crush force behaviors of all the geometric shapes. All observations from this present study are summarized at the end which are vital for development of new EA structural configurations to be discussed in Chapter 5.

## 4.1 Introduction

The plastic deformation pattern of the EA structure significantly influences the crush force behavior. Precise control over the crush force behavior both at the initiation of crushing and during the stabilization after the initial phases is observed to be a vital factor and a key enabler for maximizing the amount of energy absorbed while keeping the crush forces within the allowable limits as governed by several injury criterion mentioned in Chapter-2 [29-31]. It may be noted from the previous research studies that the same geometric cross-section of the structure with different ratios of geometric parameters (for example, D/t ratio in case of a circular tube) exhibit completely contrasting crush force and deformation behaviors making the subject even more complex to understand. Achieving a uniform crush force all along the crush stroke is a challenging exercise from many perspectives as it requires a material with a high degree of ductility besides an optimum combination of geometric shape and parametric ratio. Though the trends of deformation patterns are known for axial crushing of some standard geometric shapes, a detailed numerical simulation is carried out on various standard

cross-sections of tube starting from triangular cross-section to circular cross-section with an objective of understanding intricacies of the influence of each geometric shape on the crush force behavior.

### 4.2 Crush Tubes with Basic Geometric Shapes

Axial crushing of tubes with cross sections of the following basic geometric shapes is studied using the FEA methodology that has been established and validated in the Chapter 3 using the commercial FEA code ABAQUS [84]. The geometries considered are Triangle, ii) Square, iii) Rectangle, iv) Pentagon, v) Hexagon, vi) Octagon and vii) Circle.
The geometry of these cross-sections with dimensions are shown in Figure 4.1.

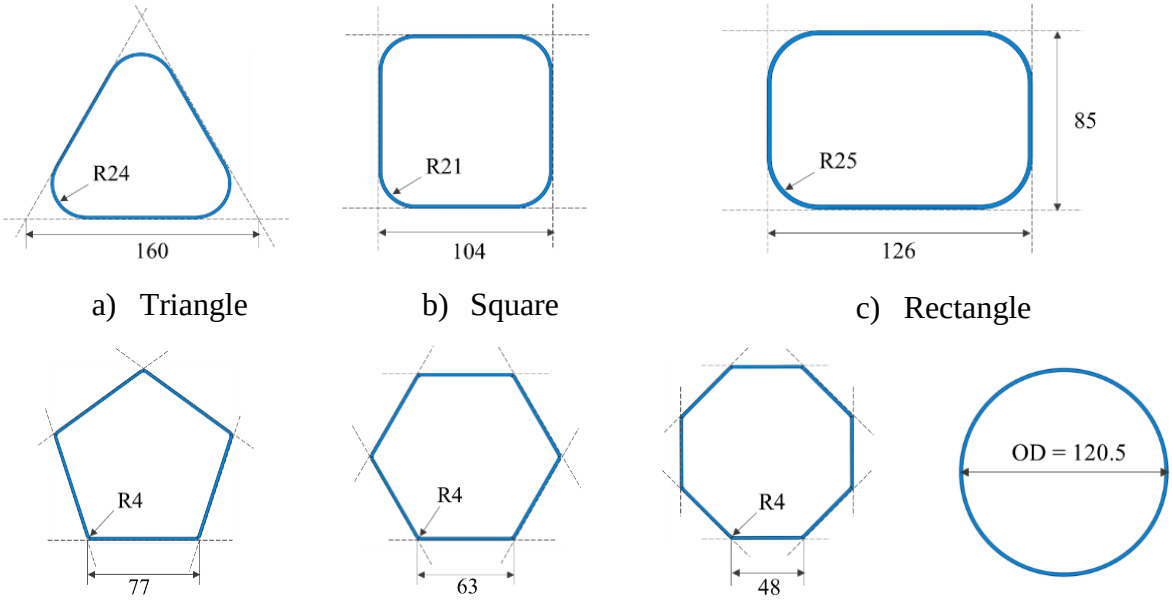


a) Triangle b) Square c) Rectangle

d) Pentagon e) Hexagon f) Octagon g) Circle

Figure 4.1. Crush tubes with different basic geometric shapes (all dimensions in mm)

Uniformity is maintained across all the specimens in terms of length and cross-sectional areas so that the volume and mass are consistent. The common dimensional parameters are given as follows: length = 240 mm, thickness = 2.0 mm, perimeter = 745 mm and cross-sectional area = 380 $mm^2$. Aluminum alloy AA 7005 in T6 condition from a similar work on energy absorption [94] is considered as the common material for all the specimens and the mass of each specimen is maintained as 0.5 kg. Basic material properties of the chosen aluminum alloy are as follows: Young's modulus = 70 GPa; Poisson's ratio = 0.33; yield strength = 330

MPa; tensile strength = 440 MPa; and 8% elongation at break. These material properties are obtained from the standard tensile test conducted according to ASTM E8 specification in [94] and its stress-strain curve as shown in Figure 4.2.

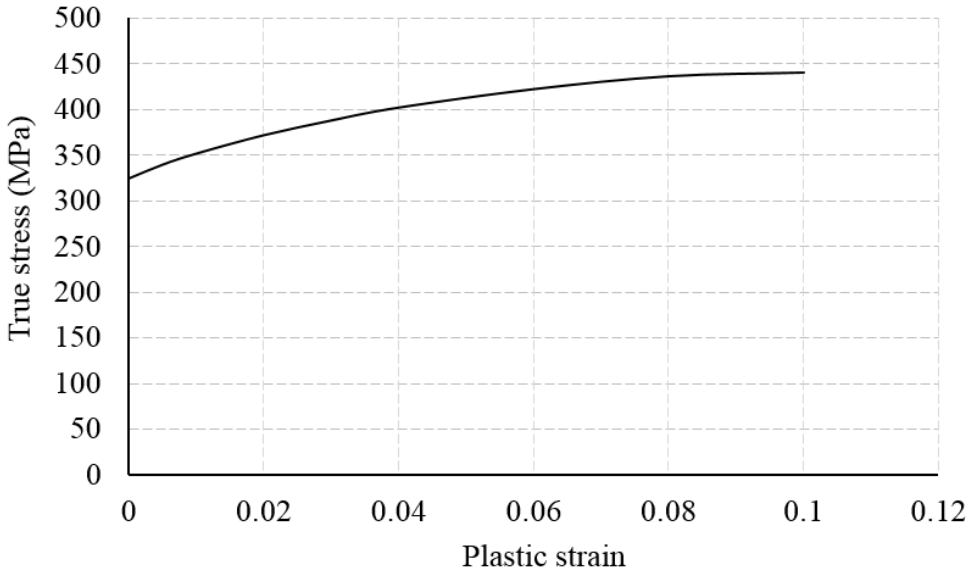


Figure 4.2. Stress-strain curve of aluminum alloy AA 7005 [94]

### 4.3 FEA Simulation

The FEA methodology which has been established and validated in Chapter 3 is adapted here. The difference is only the impact velocity with which the impacting body strikes the tube specimen. In the present research, an impact velocity of 15 m/s is considered to be in line with the Federal Motor Vehicle Safety Standard (FMVSS) speed of 56 kmph (35 mph) for frontal collision [5]. The FEA simulation setup is shown in Figure 4.3. All specimens are analyzed for plastic deformation patterns and crush force behavior required for assessment of their crashworthiness.

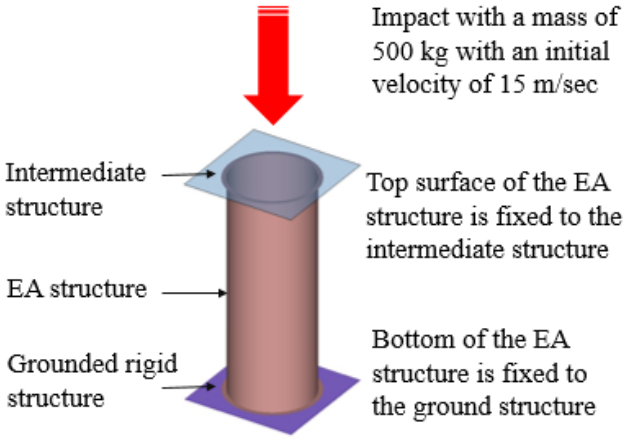


Figure 4.3. FEA simulation set up

### 4.4 Plastic Deformation and Crush Force Behaviour of Basic Geometries

The plastic deformation pattern and crush force behaviour of crush tubes with different basic geometric shapes (shown in Figure 4.1) resulted from present FEA simulations are discussed in detail here.

#### 4.4.1 Crush tube with triangular cross-section

The plastic deformation starts with a steep initial peak crush force of 215 kN to initiate the plastic deformation in the structure and it is observed at a crush stroke of around 4 mm. The crush force then falls rapidly to 40 kN at around a stroke of 26 mm. During this period the triangular section undergoes an inward fold on all the three longitudinal faces of the tube. Further crushing brings an outward folding on all the three faces, but this fold covers a longer envelope as it requires a longer longitudinal space to reverse the plastic folding pattern from inner to outer face and this process happens over a crush stroke of around 60 mm. During this period the crush force fluctuates between 40 kN and 90 kN (range of 50 kN) with an equally spaced peak in the middle. Further crushing brings up another inward fold which spans over a stroke of 45 mm with crush force fluctuating between 50 kN and 80 kN (range of 30 kN). The next outward fold brings the fluctuations further down within a range of 15 kN and as the crush force starts stabilizing around 65 kN, the tube gets densified at a stroke of 193 mm and resists further plastic crushing indicated by a steep rise in the crush force. Progress of plastic deformation and crush force behavior of triangular specimen are shown in Figures 4.4 (a) and

4.4(b) respectively. Total energy absorbed by this specimen until 193 mm of crush stroke is 13.5 kJ.

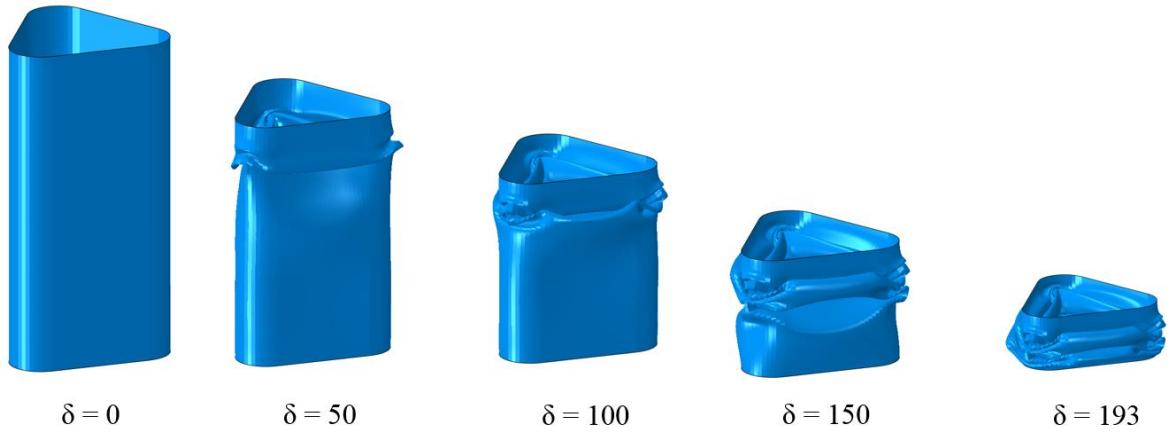


a) Progress of deformation at different crush strokes

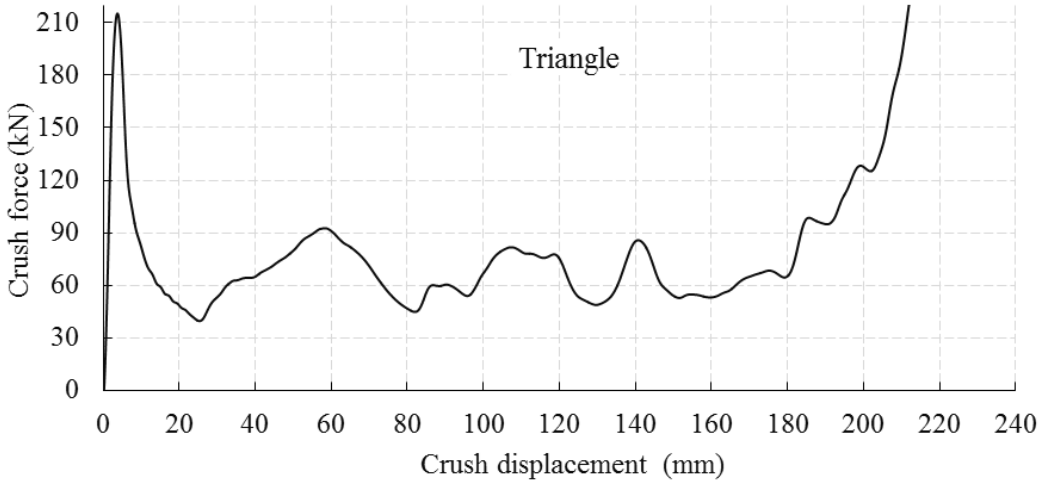


b) Crush force behavior

Figure 4.4. Axial crushing of triangular specimen: a) progress of deformation b) crush force behavior

### 4.4.2 Crush tube with square cross-section

In the case of square profile, the plastic deformation starts with an initial peak crush force of 218 kN with outward folding on all faces of the tube and drops to 40 kN at a stroke of around 24 mm at the end of the first fold. The second fold is observed to be inwards on all four faces of the tube. This transition between inward and outward folds demands higher crush forces of up to 130 kN and the second fold spans over a stroke of 80 mm. The third fold is a combination of outward and inward movement on alternate faces of the tube. This

combination of folding spans over a long distance and the crush force drops to around 40 kN, but some stability is observed in the crush force at around 45 kN for the remainder of the plastic crush stroke up to 195 mm. Resistance to plastic crushing is observed at this point due to densification of the uncrushed material. Progress of deformation and crush force behavior are shown in Figures 4.5 (a) and 4.5 (b) respectively. Total energy absorbed up to 195 mm is 13.2 kJ.

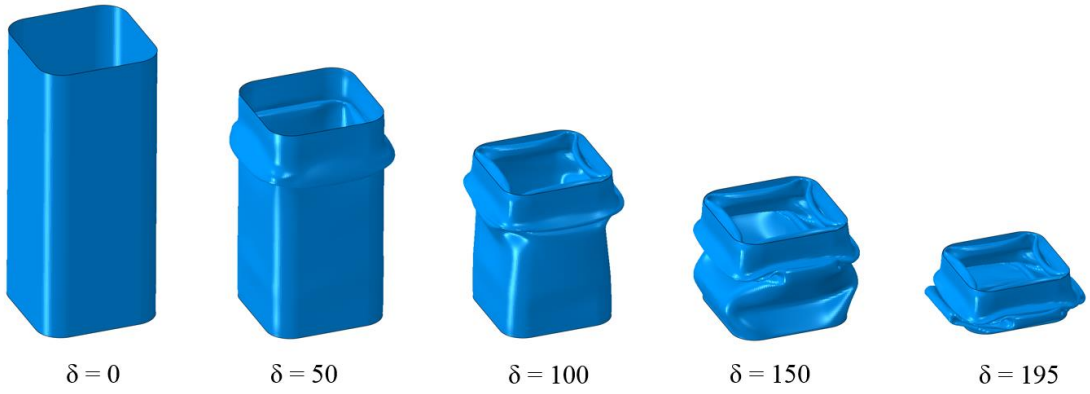


a) Progress of deformation at different crush strokes

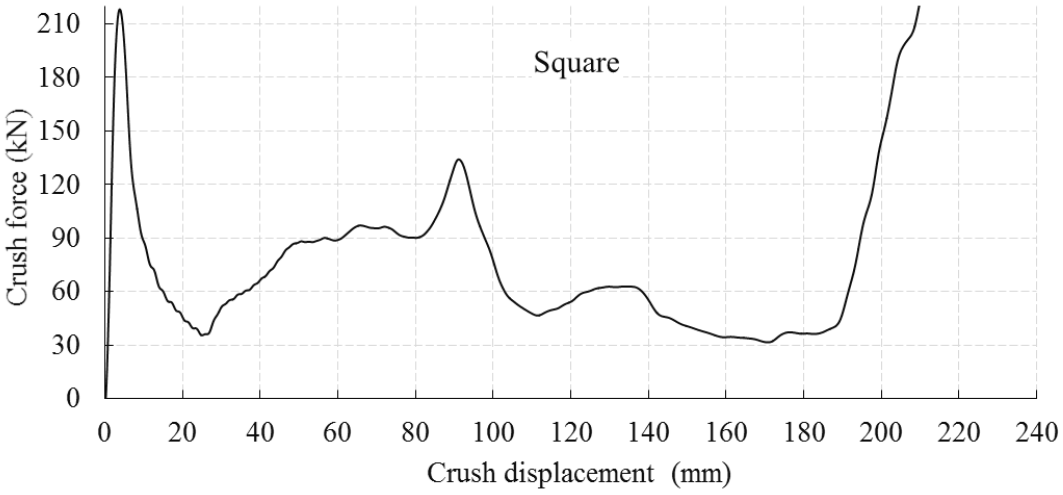


b) Crush force behavior

Figure 4.5. Axial crushing of square specimen: a) progress of deformation b) crush force behavior

### 4.4.3 Crush tube with rectangular cross-section

In the case of rectangular specimen, the first folding is observed to be outwards with an initial peak force of 215 kN followed by a steep fall to about 30 kN at a stroke of 36 mm at the end of the first fold. The second fold though resembles the folding trend of a square profile but is slightly different. Due to unequal lengths of the adjacent sides in the cross-section, the longer side tends to flex a little bit easily in the outward direction as it is the most stable configuration. To balance this deformation, the shorter side tends to move inwards with the folding length larger than its original length by interfering with the outward folding envelope of the longer side. This conflicts results in a longer span of the fold making the structure weak in axial crushing resistance and the crush force drops to below 20 kN during the formation of this longer fold. This pattern of low crush forces is completely in contrast to the earlier profiles. Excessive outward movement of the longer side offers a little more space for internal crushing taking the active crush stroke to 200 mm. The crush force behavior appears to be stable for longer stroke but the forces are low resulting in the drop of energy absorption to 10.3 kJ for a stroke of 200 mm. Plastic deformation and crush behavior are shown in Figures 4.6 (a) and 4.6 (b) respectively.

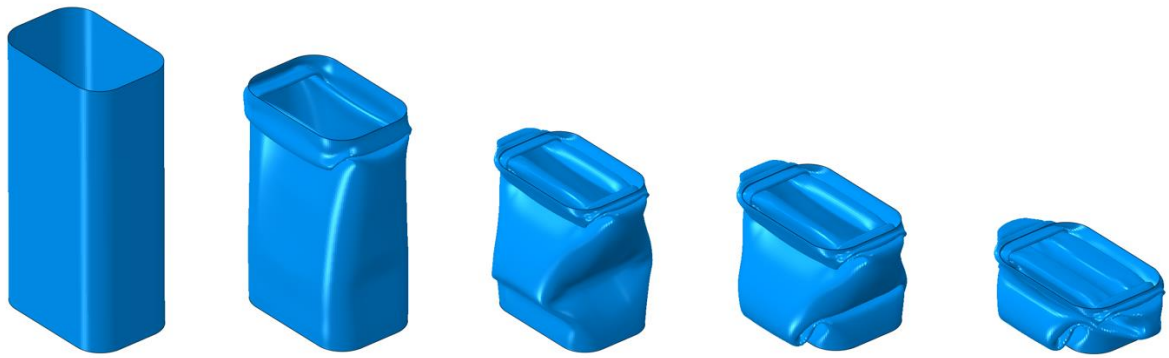


a) Progress of deformation

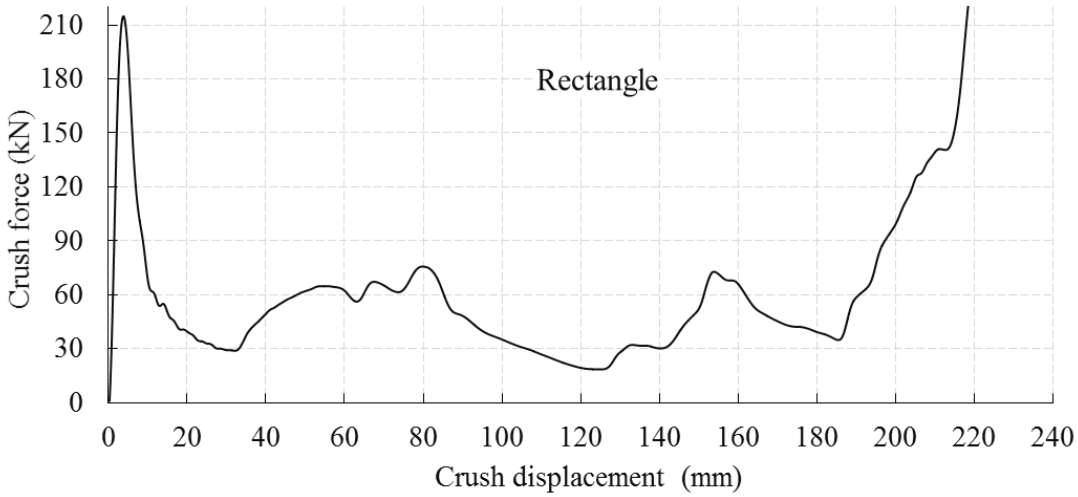


b) Crush force behavior

Figure 4.6. Axial crushing of rectangular specimen: a) progress of deformation b) crush force behavior

### 4.4.4 Crush tube with pentagonal cross-section

In this profile, the first fold is observed to be outside with an initial peak force of 220 kN followed by a drop to 38 kN at a stroke of 25 mm. The second fold follows the trend of square profile with an alternate inward and outward movements on each successive face of the pentagon. As the cross-section has equal sides, the conflict between each successive face for the additional width of the fold is reasonably balanced resulting in a nearly stable crush force for a longer part of crush stroke for about 140 mm after the initial peak force. This interactive folding between each successive face tries to keep the crush forces at a nearly constant level for a longer duration (i.e. longer stroke). This is a contrasting feature in comparison to the earlier geometric shapes. However, uneven folding patterns caused a lot of internal contacts during the second fold limiting the active crush stroke to a moderate 191 mm. Plastic deformation and crush behavior are shown in Figures 4.7 (a) and 4.7 (b) respectively. Total energy absorbed by this specimen over a stroke of 191 mm is about 12.9 kJ.

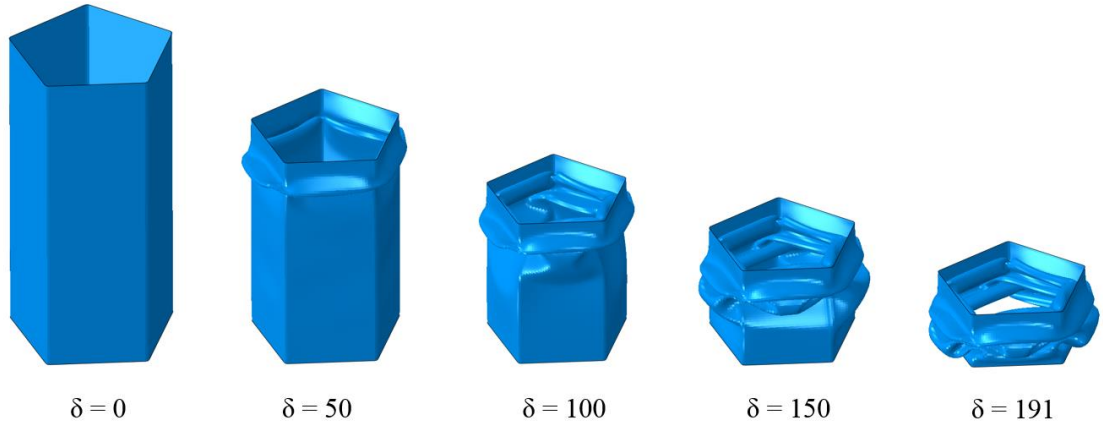


a) Progress of deformation

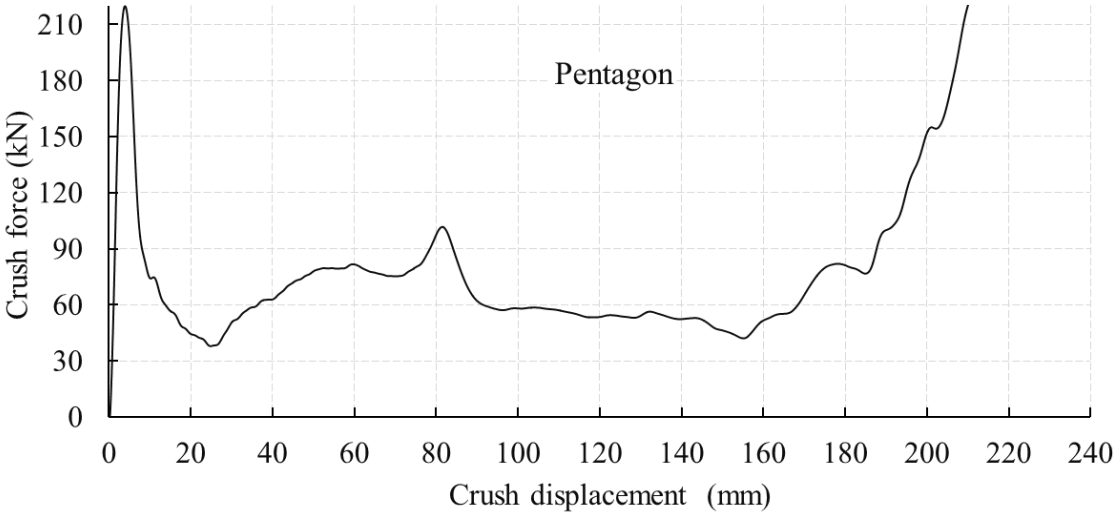


b) Crush force behavior

Figure 4.7. Axial crushing of pentagonal specimen: a) progress of deformation b) crush force behavior

### 4.4.5 Crush tube with hexagonal cross-section

This profile required an initial peak force of 214 kN to initiate the first fold followed by a drop to 37 kN at about 31 mm of crush stroke. First fold progresses inwards on all the six faces of the tube. During the second round of plastic deformation, simultaneous outward folds are initiated immediately next to the first fold region and almost symmetrically at the other end of the tube. This is characterized by a rise in crush force to around 90 kN. The crush force doesn't maintain its plateau, but the fall and rise are gradual until a stroke of 175 mm. During this period the uncrushed middle portion of the tube tends to follow an alternate inward-outward folding on successive faces of the tube with a conflict between the adjacent faces for attaining an equilibrium position between inward and outward folds. This excessive

movement on either side of the cross-section occupies a lot of crushable space limiting the active crush stroke to a mere 184 mm. Plastic deformation and crush force behavior are shown in Figures 4.8 (a) and 4.8 (b) respectively. Total energy absorbed by this specimen over a stroke of 184 mm is about 13.2 kJ as the crush force operates at slightly higher levels in comparison to the earlier versions.

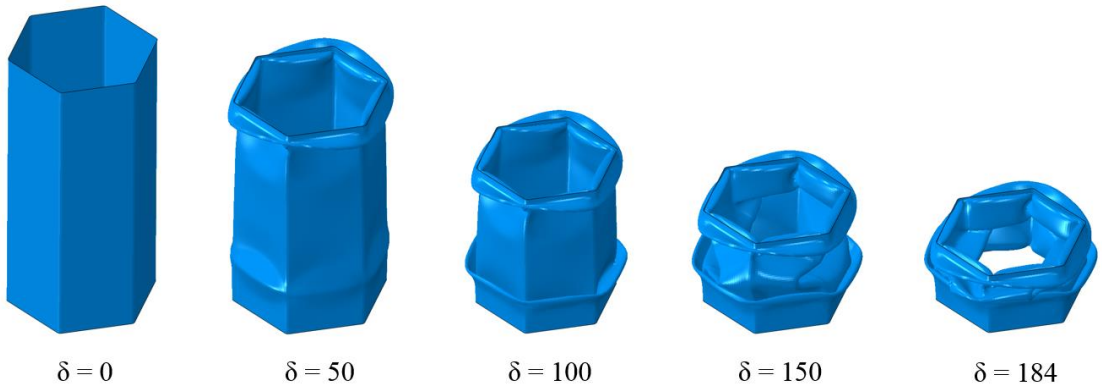


a) Progress of deformation

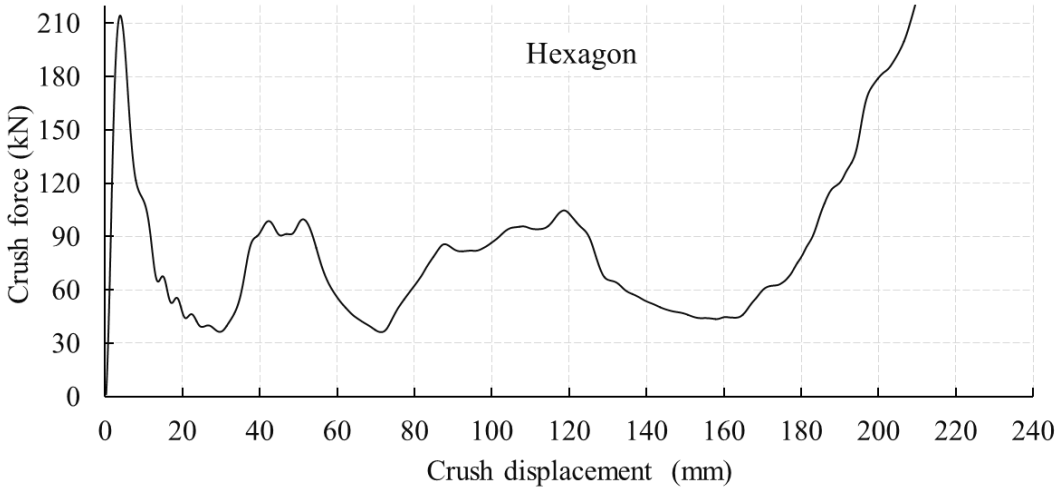


b) Crush force behavior

Figure 4.8. Axial crushing of hexagonal specimen: a) progress of deformation b) crush force behavior

### 4.4.6 Crush tube with octagonal cross-section

This specimen required an initial peak force of 211 kN to initiate the formation of the first fold which moves inwards and the fold is completed at a crush stroke of 27 mm. Second fold is also observed to be inward but at the other end of the tube. This deformation pattern continues as a series of outward folds similar to concertina rings in the crushing of a circular

tube [36-39]. The crush force fluctuates in a wide range between 40 kN and 110 kN. Active plastic crushing continues until a stroke of 201 mm as no conflicts are observed between successive faces of the tube. Progress of plastic deformation and crush force behavior are shown in Figures 4.9 (a) and 4.9 (b) respectively. As the crush forces operate at higher levels and because of slightly longer crush stroke, the total energy absorbed by this specimen up to a stroke of 201 mm is 15.1 kJ.

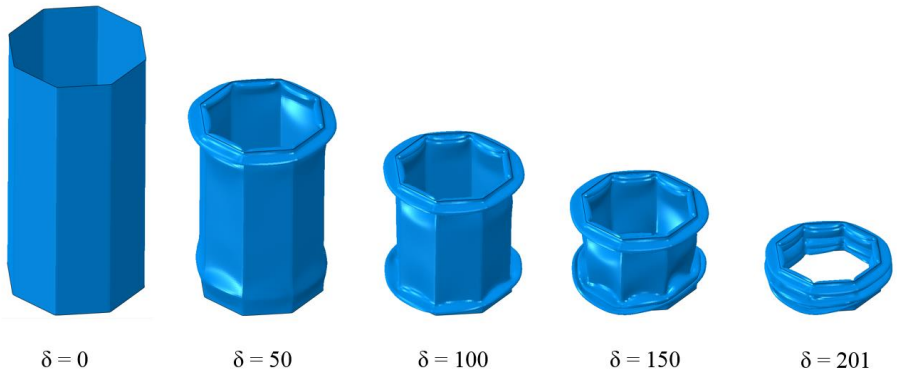


a) Progress of deformation

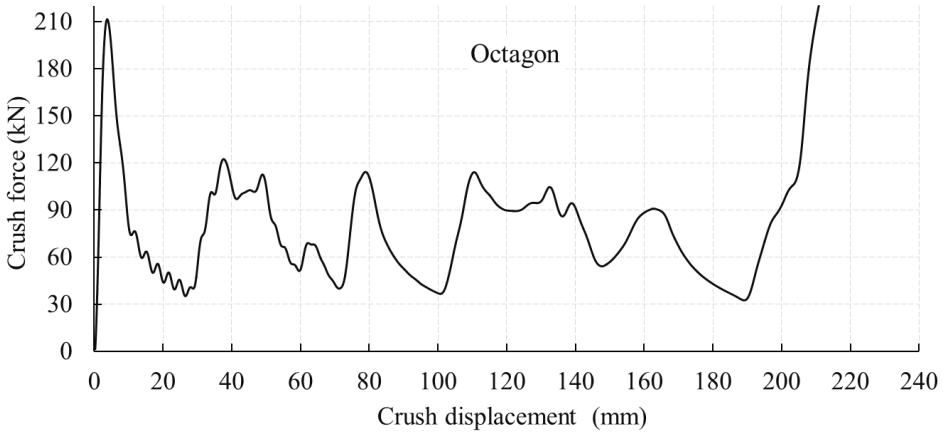


b) Crush force behavior

Figure 4.9. Axial crushing of octagonal specimen: a) progress of deformation b) crush force behavior

### 4.4.7 Crush tube with circular cross-section

Circular specimen required an initial force of 187 kN for the first plastic fold, which is less in comparison to the previous specimens, which may be due to continuity in cross-section and the absence of corners normally contributed to the crushing resistance. Plastic deformation progresses in a series of concentric rings with folds in the outward direction. Each fold is

characterized by a steep rise and fall in the crush force with a peak crush force in the middle of each ring fold with a wide range fluctuation in crush force for each ring fold. The peak force of each ring fold keeps increasing for the successive folds as crushing progresses. Active crushing is observed until a stroke of 202 mm. The total energy absorbed by this specimen up to 202 mm of stroke is about 14.8 kJ. Progress of deformation and crush force behavior are shown in Figures 4.10 (a) and 4.10 (b) respectively.

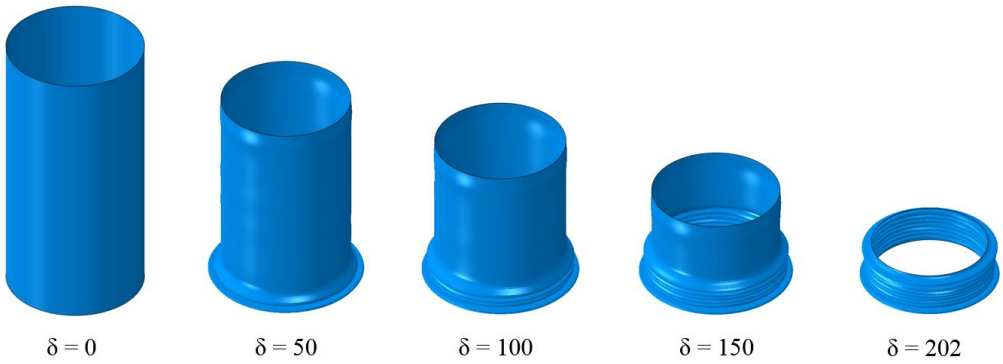


a) Progress of deformation

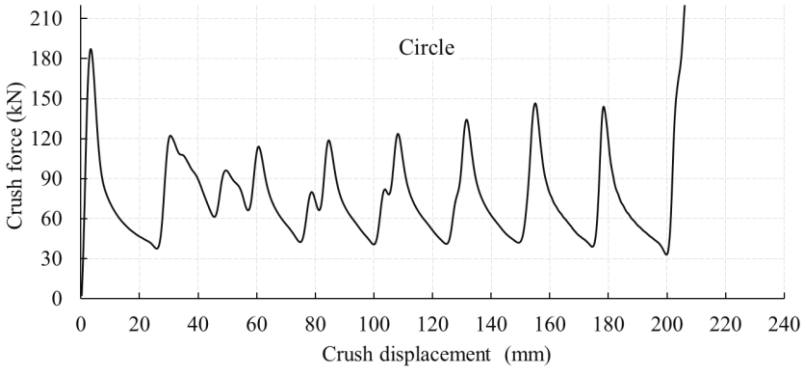


b) Crush force behavior

Figure 4.10. Axial crushing of circular specimen: a) progress of deformation b) crush force behavior

### 4.5 Comparison of Crush Behaviour of All Geometric Cross-Sections

The crush behaviour of crush tubes with all geometric cross-sections studied so far are compared here to assess their relative crush performance. Crush force versus crush displacement of crush tubes with all geometric shapes is shown in Figure 4.11 and energy absorption curves of all the specimens is shown in the Figure 4.12. Detailed crashworthiness summary of all the specimens is shown in the Table 4.1.

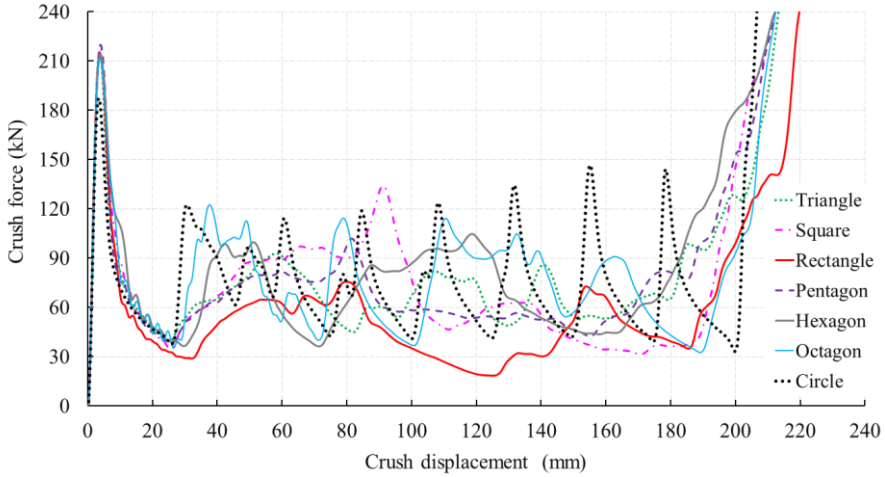


Figure 4.11. Crush force versus crush displacement of crush tubes with all geometries

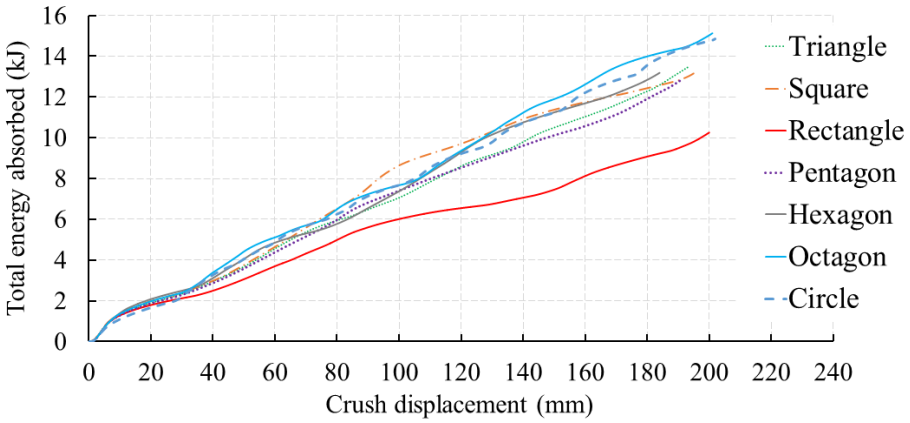


Figure 4.12 Total energy absorbed by all the specimens

Table 4.1. Crashworthiness summary of all the specimens

| Cross-section | Peak force (kN) | Mean force (kN) | TEA (kJ) | Crush distance (mm) | CFE (%) | SE (%) | SEA (kJ/kg) |
|---|---|---|---|---|---|---|---|
| Triangle | 215 | 69.9 | 13.5 | 193 | 32.5 | 80.4 | 27.0 |
| Square | 218 | 67.7 | 13.2 | 195 | 31.0 | 81.3 | 26.4 |
| Rectangle | 215 | 51.5 | 10.3 | 200 | 23.9 | 83.3 | 20.6 |
| Pentagon | 220 | 67.5 | 12.9 | 191 | 30.7 | 79.6 | 25.8 |
| Hexagon | 214 | 71.7 | 13.2 | 184 | 33.5 | 76.7 | 26.4 |
| Octagon | 211 | 75.1 | 15.1 | 201 | 35.6 | 83.8 | 30.2 |
| Circle | 187 | 73.3 | 14.8 | 202 | 39.2 | 84.2 | 29.6 |

## 4.6 Summary

The perimeters and cross-sectional areas of all the specimens are equal but no two specimens exhibited the same crush force behavior or the plastic deformation pattern and there is a variation of 50% in the total energy absorbed across all the specimens. This diversity adds complexity to the subject of plastic deformation based energy absorption. This understanding and knowledge helps in development of energy absorbing structures discussed in subsequent chapters. The following observations and conclusions can be drawn from this study on crush tubes with different geometric shapes.

1. Generally, cross-sections with equal areas exhibit almost the same initial peak crush force.
2. Cross-sections made of polygonal shapes are favourable for stability in the crush force behavior than the curved ones. Tapering may improve the stroke efficiency of polygonal sections.
3. Polygonal cross-sections should be regular (equal sides) for achieving higher stroke efficiencies.
4. Circular or curved cross-sections are favorable for higher stroke efficiencies, but have high fluctuations in the crush forces.
5. Appropriate crush-triggering mechanisms should be employed for all cross-sections to control the initial peak forces.
6. As the number of sides increase in the polygon, crush force behavior tends to move towards circular cross sections.
7. For effective design of energy absorbing structures, cross-sections with an optimum combination of straight edges and curves may be considered.

# Chapter 5

# Development of New Structural Configurations for Frontal Crash Energy Absorption

The importance of controlled energy absorption in frontal collisions of road vehicles is elucidated in previous chapters. Although considerable research is carried out till date in developing a variety of energy absorbing (EA) structures, major limitations in most structures is that they exhibit high initial peak force ($F_{peak}$) and low stroke efficiency (SE). In this chapter, a few structural configurations for enhanced crashworthiness have been developed in two parts with two different approaches using the FEA methodology which has been developed and validated in Chapter 3. This chapter gives a brief note on the strategy being followed for development of new structural configurations, explains the development of EA structural configurations based on two different approaches with discussion on relative merits and limitations and finally the observations from the numerical study on structural arrangements are summarized with pointers to the subsequent part of research work.

## 5.1 Introduction

The systematic numerical studies on crush tubes with cross-sections made of different basic geometric shapes for assessment of crashworthiness has provided vital clues on the relationship between geometric shape, plastic deformation mode and the crush force behaviour. Based on these hints, a few EA structural configurations have been developed with an objective of enhancing the crashworthiness (with respect to the standard crashworthiness assessment parameters) using the numerical procedures. These configurations have been developed based on two different structural approaches (type-A and type-B) or arrangements. The first approach is based on conventional circular tubes in a *tube-in-tube* (type-A) kind of setup in four different ways. The second approach is based on a non-conventional arrangement with cross-sections made of *combination of curved and straight line segments* (type-B) with precise distribution of stiffness at specified locations along the axial length. Relative merits and demerits of each approach are discussed in detail.

### 5.1.1 Material

Aluminium alloy is considered as the material for all the proposed EA structural configurations in the present work as the current trend in the automotive industry is to build light weight vehicles. Aluminium alloy has many merits as EA structure due to its i) superior strength to weight ratio, ii) steady plastic deformation with less rebound which is a vital factor for EA structures, and iii) growing acceptance in the automobile industry with increased application in load-intensive structures in the vehicle [95]. Simhachalam *et al* [94] conducted studies on circular tubes for impact EA applications with aluminium alloy (AA) grades in AA6xxx series and AA7xxx series. A very few studies in literature had the use of AA7005 in T6 (solution heat treated and aged) for impact energy applications. Selection of this material grade and condition in the present study for new EA structural configurations is due to its high yield strength and good post yield behaviour that helps in achieving higher SEA. The mechanical properties of this material are: Young's modulus = 70 GPa; Poisson's ratio = 0.33; yield strength = 330 MPa; tensile strength = 440 MPa; and 8% elongation at break. Simhachalam *et al* [94] conducted standard tensile test according to ASTM E8 specification on this material samples and obtained the stress-strain curve as shown in Figure 4.2.

### 5.1.2 FE modelling and solution methodology

The objective of this study is to evaluate the crashworthiness of conceptual EA structural configurations using FEA methods. A schematic layout of vehicle front structure and chassis is shown in Figure 5.1 and the FE model of the crash simulation setup on EA structure with boundary conditions is shown in Figure 5.2. The bottom end of the specimen is attached to the rigid fixed base using the TIE option in ABAQUS/Explicit software v 6.14-3 [84]. The top end of the specimen is fixed to a thick intermediate plate which is assumed to be steel with linear elastic material property (Young's modulus: 210 GPa and Poisson's ratio: 0.29). The intermediate plate is introduced to represent the front attachment to the EA member. The rear rigid plate represents the chassis frame which acts as a ground for the EA structure. To simulate the impact scenario, an impactor of mass 500 kg impacts the specimen through the front intermediate plate with an initial velocity of 15 m/s which is equivalent to a standard frontal crash impact speed of 54 kmph [9].

Explicit numerical integration solution methodology is chosen for numerically simulating the impact dynamics of the crash event. The duration of this axial impact event is taken as 20 milli seconds based on a series of solution trials. The general contact algorithm is invoked to capture the entire self-contact phenomenon in the EA structural specimen during the axial crush. The reaction forces at the rear rigid plate are monitored during the axial crush and are recorded as crush forces.

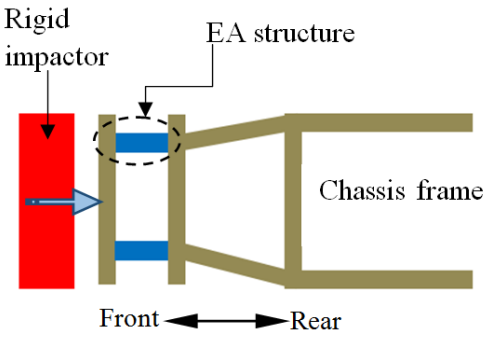


Figure 5.1. Schematic layout of chassis frame, EA structure and front bumper

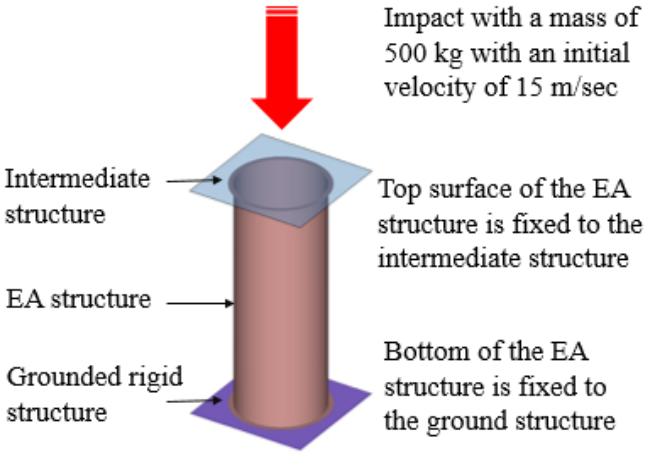


Figure 5.2. FE model setup with boundary conditions

## 5.2 Development of New Structural Configurations Based on Tube-In-Tube (Type-A) Approach

The proposed new EA structural configurations are as shown in Figure 5.3. The length of all these configurations is maintained at 240 mm based on the average length of most of EA members in most mid-range passenger cars. The mass of each EA structural configuration is

kept at around 0.5 kg for uniformity among all the configurations.

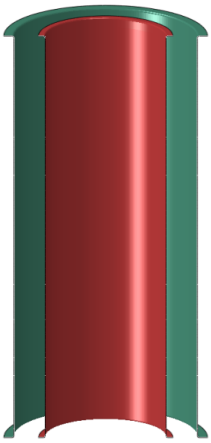

(a) Configuration-A1

(Sectional view of a tube-in-tube)

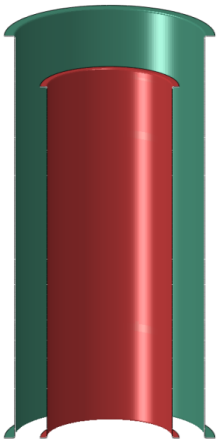

(b) Configuration-A2

(Sectional view of a tube-in-tube with shorter inner tube)

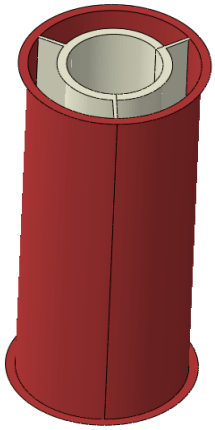

(c) Configuration-A3

(Tube-in-tube with 3 longitudinal ribs at $120^0$)

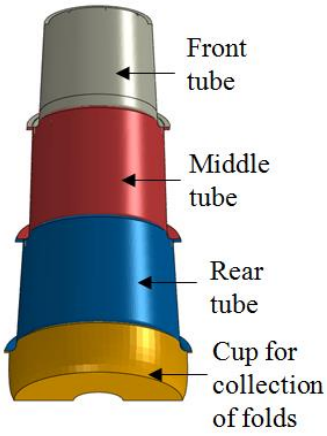


(d) Configuration-A4

(Sectional view of conical tubes in series)

Figure 5.3. Proposed configurations for EA structure based on type-A approach

### 5.2.1 Configuration-A1

The conceptual development is based on simple straight cylindrical tubes in different arrangements with a uniform circular cross section as shown in Figure 5.3(a). In an attempt to bring down the $F_{peak}$ associated with circular tubes, the cylindrical tube is split into two coaxial tubes. The thickness of the outer tube is kept at 2.0 mm and the thickness of core tube is kept at 0.8 mm, the mean diameters of outer and inner tubes are 90 mm and 60 mm respectively while maintaining the mass at 0.5 kg. A series of FEA iterations were performed

to arrive at the optimum combination of thicknesses and radii of tubes. Other EA structural configurations (Figure 5.3) proposed in this study are extended from this basic configuration-A1. This configuration-A1 is then subjected to an axial impact by a rigid block of mass 500 kg according to the FEA setup shown in Figure 5.2 as discussed in the previous chapter.

5.2.1.1 Analysis of crash performance

Axial crush force against axial crush displacement of configuration-A1 is shown in Figure 5.4(a). This configuration exhibited an initial peak force of 231 kN (equivalent to an acceleration of 47 g). The crush force drops down to about 60 kN at a displacement of 24 mm signifying the completion of first loop of plastic fold on both the tubes. Various stages of plastic deformation are shown in Figure 5.5(a). The crush fold pattern is not as regular as standard tube. Folding starts at the rear end of the inner tube and only four regular ring shaped folds are observed. The folding pattern loses circularity from the second fold onwards due to instability. Folding pattern at the top end of the inner and outer tubes loses stability from the second fold onwards and the fold pattern transforms from circular to polygonal form. As the crushing progresses, stiffer folds of both the tubes interact with each other advancing the end of plastic deformation. As a result, the structure becomes stiffer resulting in relatively low SE. The average fluctuation in crush force after the initial peak is observed to be around 60 kN, reducing the mean force which results in a drop in the CFE. Though this configuration is inferior compared to a simple circular tube one in many aspects, it gives clues on the relationship between the geometric configuration, stability during the course of axial crush, plastic deformation patterns and the overall crashworthiness.

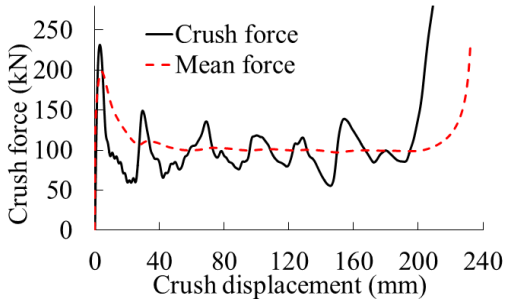


(a) Configuration-A1

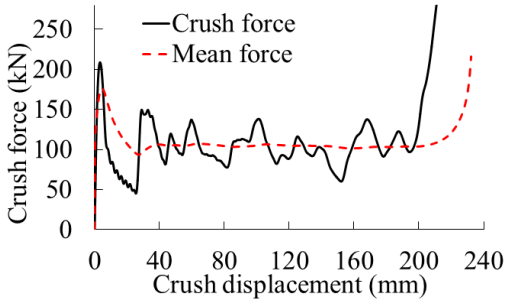


(b) Configuration-A2

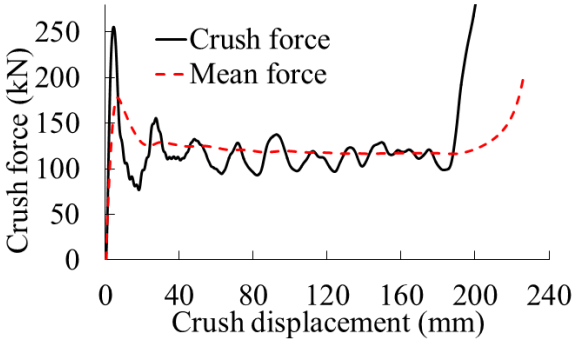


(c) Configuration-A3

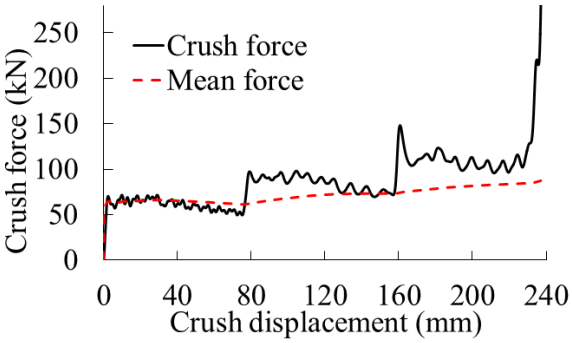


(d) Configuration-A4

Figure 5.4. Crush force and mean force with respect to crush displacement for four EA structural configurations based on type-A approach

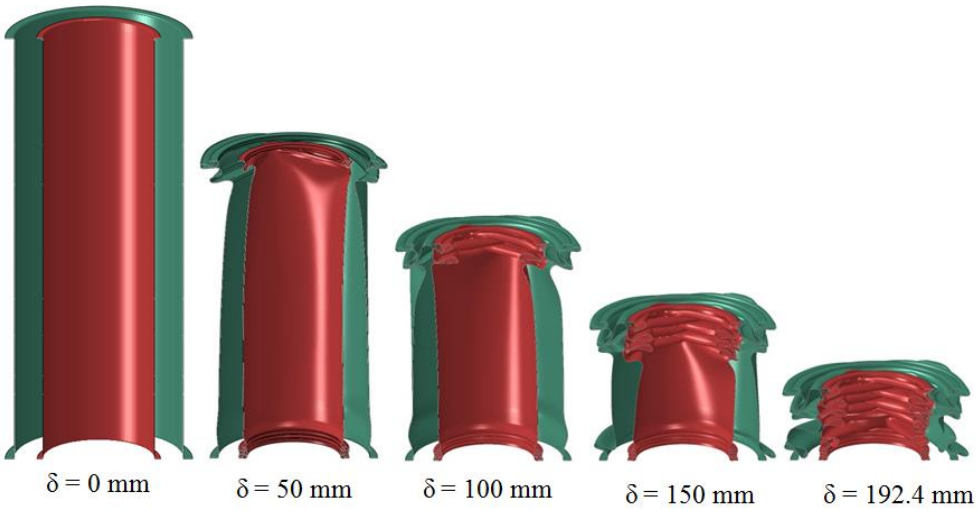


(a) Configuration-A1

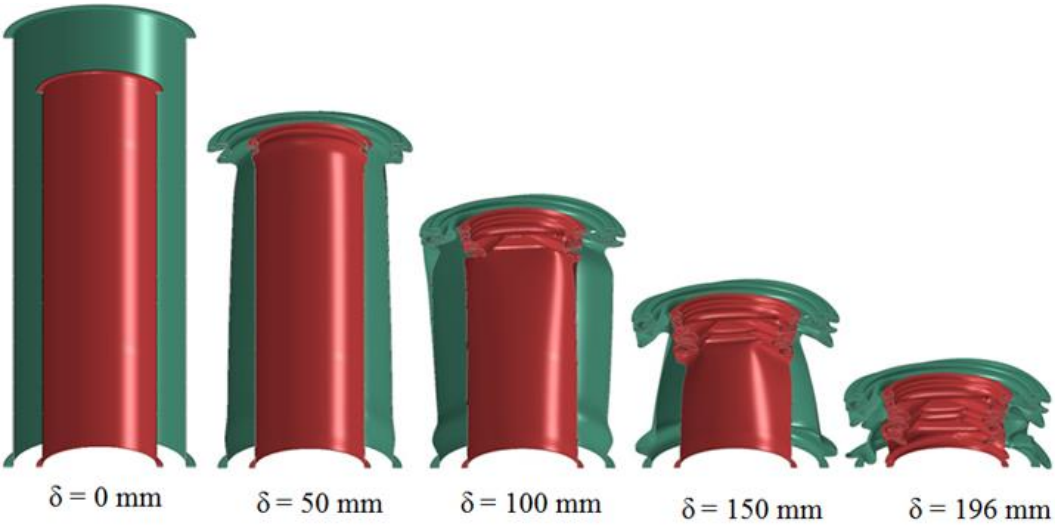


(b) Configuration-A2

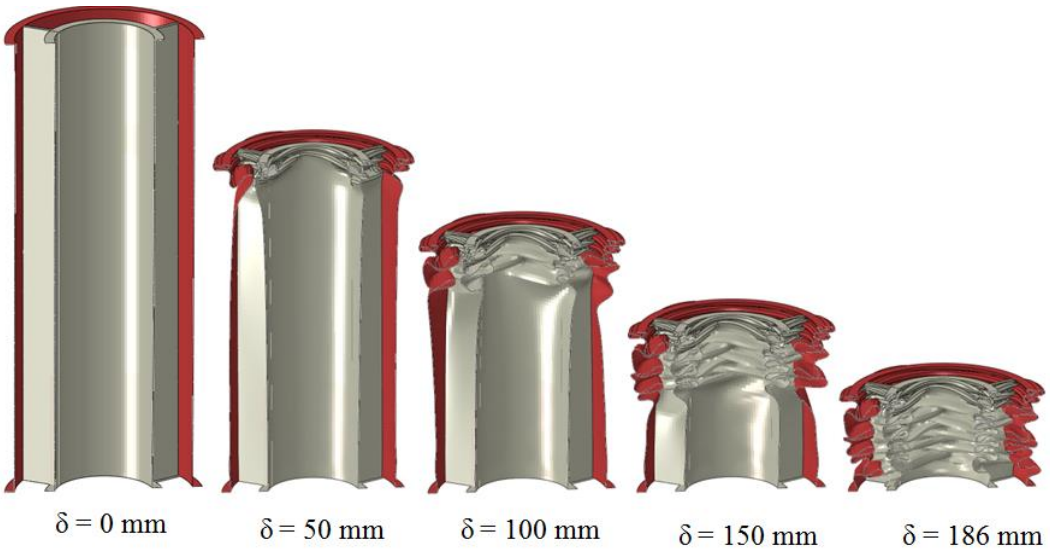


(c) Configuration-A3

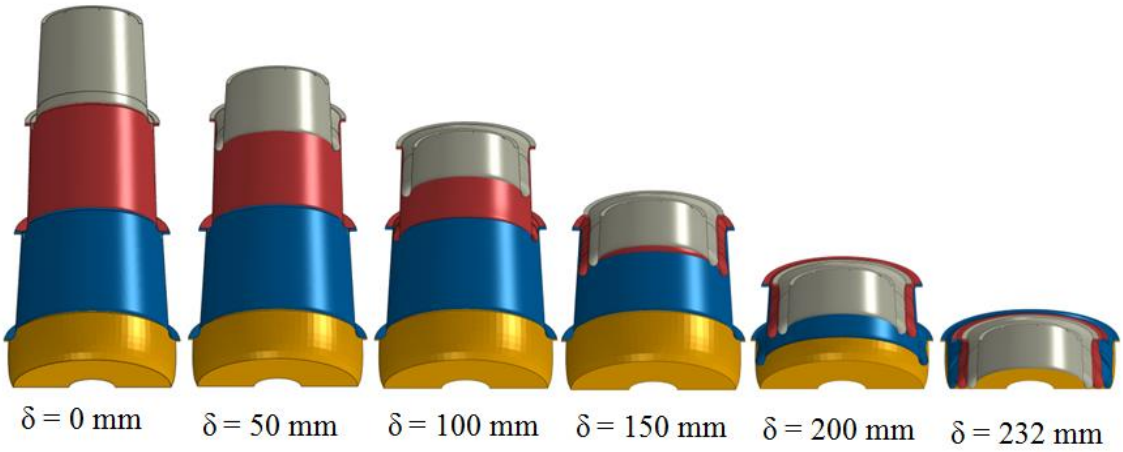


(d) Configuration-A4

Figure 5.5. Sectional view of crushing stages of four EA structural configurations

### 5.2.2 Configuration-A2

Configuration-A1 is modified to address the major drawbacks of high $F_{peak}$ and steep fluctuations. Coaxial tubes could not bring down the $F_{peak}$ as expected. The cross sectional view of Configuration-A2 is shown in Figure 5.3(b) and is obtained by shortening the length of the inner tube by 30 mm at the front end. This is mainly to reduce the $F_{peak}$ so that the outer tube alone takes the initial impact for the first 30 mm of crush stroke. Mean diameters of outer and inner tubes are 90 mm and 60 mm respectively. Thicknesses of outer and inner tubes are 2.0 mm and 0.85 mm respectively. The mass is maintained at 0.5 kg and the mass of the trimmed portion of the tube is added to the inner tube to improve its stability during the

course of the axial crush. Reducing the thickness of the tubes may also be considered as an option to reduce the initial $F_{peak}$, but few iterations in FEA shown that it induces instability in the model as the crush progresses resulting in low SE and TEA.

5.2.2.1 Analysis of crash performance

Numerical simulation of configuration-A2 predicted a drop in the initial $F_{peak}$ to 206 kN (equivalent to 42g) as the outer tube alone takes first impact for the first 30 mm of crush stroke. Crush force - crush displacement graph is shown in Figure 5.4(b). The crush force drops down to 50 kN at around 25 mm of crush stroke. The drop is steep as compared to the previous configurations due to reduced strength in the structure in the initial part of the crush stroke. The crush force then picks up quickly due to addition of strength through inner tube. The average fluctuations in the crush force also reduced to 55 kN. Out-of-phase folding patterns of coaxial tubes also might have contributed to the stabilization of crush force behaviour. Plastic crush continues for a stroke of 196 mm, 4 mm more than the configuration-1 scoring better in terms of both SE and CFE (Tables 5.1-5.2). Circular folds begin at the front end for both the tubes and thereafter the folding pattern loses circularity due to inadequate stability after the second fold, similar to that of configuration-1. Progress of plastic deformation and crushing are shown in Figure 5.5(b). Though the improvement in SE and CFE is marginal compared to configuration-1, reduction of initial $F_{peak}$ provides clues and possibilities to develop structural configurations that can absorb reasonable amount of impact energy with reduced initial $F_{peak}$ (as it is still high) which is very vital from the safety perspective.

### 5.2.3 Configuration-A3

Based on observations from configurations 1 and 2, on how the distribution of the same mass in different parts can affect the initial $F_{peak}$ and CFE, some more modifications are brought in to develop configuration-A3 as shown in Figure 5.3(c). This configuration-A3 is made of two coaxial tubes reinforced by three longitudinal ribs spaced at $120^0$. After a series of FEA iterations, outer tube thickness is fixed at 1.6 mm while the thickness of inner tube and longitudinal ribs is kept at 1.2 mm. Mean diameters of outer and inner tubes are 90 mm and 50 mm respectively. The mass is maintained at 0.5 kg. The objective of introducing the longitudinal ribs between the two tubes is to understand the effect of interaction between folding modes of tubes and ribs on the stability of crush force. In an axial crush, cylindrical tubes are observed to fold in circular mode while the ribs try to bend in zig-zag mode in a

different plane. The interaction between folding of tubes and ribs in different planes is expected to minimize the fluctuations in the crush force and stabilize after the initial peak.

5.2.3.1 Analysis of crash performance

Due to high initial stiffness in the structure due to reinforcement by longitudinal ribs, this configuration exhibits high initial $F_{peak}$ of around 256 kN (equivalent to an acceleration of 52g) at a crush stroke of 4 mm as shown in Figure 5.4(c). The crush force then drops to 75 kN before 20 mm of crush stroke and tends to stabilize from 35 mm of crush stroke onwards. The crush force oscillates between 100 kN and 135 kN till the end of crush stroke at 186 mm. This behaviour of crush force with reduced fluctuations in the crush force is in contrary to the earlier versions. The tubes follow an alternate folding pattern throughout the circumference, while the folding plane of the rib is normal to that of the tube. These two orthogonal folding patterns of tube and ribs compete with each other and prevent the fluctuations in the crush force. This configuration differentiates itself from the earlier ones with a nearly stable crush force pattern for a reasonable crush stroke and the curve tends to be flat for about 40 mm before becoming rigid (Figure 5.5(c)). Progress of axial crush is shown in Figure 5.5(c). The structure starts to resist folding at 186 mm. Crush stroke is a little shorter compared to the earlier configurations due to stiffer interactions between the two tubes and the ribs leading to densification of the structure. This configuration scores well in SEA, TEA and SE aspects of crashworthiness (Tables 5.1-5.2). However CFE is below 50% due to high initial $F_{peak}$. This EA structure gave some more clues on the relationship between geometric configuration and the crush force pattern. To make this configuration a favourable choice for EA applications, the structural arrangement has to be improved to minimize the initial $F_{peak}$ and extend the crush stroke. Similar attempts have been tried previously by Zhang *et al* [96] through honeycomb kind of structures.

### 5.2.4 Configuration-A4

It is learnt from the first three configurations that high initial $F_{peak}$ is the prime limitation of EA structures, a parameter directly related to the occupant safety as the impulsive high intensity accelerations are highly undesirable. The second limitation is the structure's inherent nature to resist plastic deformation after a certain crush stroke. An extensive literature survey was done to get some base for the design of EA structures with moderate initial $F_{peak}$ and SE beyond 90%. Zhang *et al's* [96] provoked clues with their cylindrical sandwich structures with kagome core which yielded moderate initial $F_{peak}$ and followed a

stable crush behaviour. But the structure couldn't sustain the longer crush stroke and yielded a low SE of 66%. Works of Reid [97] on stable plastic deformation mechanisms and Alghamdi's [43] elaborate overview on various collapsible configurations for impact EA provided some impetus for the development of proposed configuration-A4 as shown in Figure 5.3(d).

This configuration-A4 is based on the tube inversion concept [6, 44-46] which suggests that longer and unidirectional folds yield much stable and constant crush force, and such a folding pattern additionally enables a sustained plastic deformation that improves the SE which in turn improves TEA. These two aspects when viewed from the occupant safety perspective may be understood as a gradual reach to the initial $F_{peak}$ that translates into a smoother gradient of acceleration pulse and sustenance of those acceleration levels over a longer period of time during the impact. This is very much a desirable feature of an EA structure.

Configuration-A4 has three conical tubes arranged in series. Tube inversion concepts from [43, 97] have been attempted on a single tube. In the proposed configuration, the available stroke length is divided into 3 segments to ensure stability during the axial crush and to control the crush force in a controlled manner. Segment based arrangement also helps in easily accommodating the folded part of the tube during crushing, compared to that of a single tube. In this concept, each tube is 80 mm long and the thickness of the tubes increases from the front to the rear. As the front tube initially faces the impact, it is given the smallest thickness of all the tubes to have a lower initial $F_{peak}$. The middle tube is slightly thicker than the front to support the front tube as the ground and to take the crush force to the next rear tube segment. The rear tube is thicker than the middle tube as it has to act as the ground for the front and the middle tubes. The rear part of the rear tube is fixed to a cup shaped rigid structure which is part of the chassis frame. The base radii and the top radii of each conical tube and fillet radii at the base of each tube are carefully optimized for a stable and a smooth folding of the tubes during the crush. The front tube is 2.0 mm thick with 74 mm and 81 mm as the mean diameters at the small and the big ends respectively. The middle tube is 2.2 mm thick with 90 mm and 94.4 mm as the mean diameters at the small and the big ends respectively. The rear tube is 2.4 mm thick with 102.4 mm and 112.4 mm as the mean diameters at the small and the big ends respectively. The thicknesses and diameters of conical sections have been arrived after a series of FEA iterations such that each conical tube after undergoing the folding process goes into the next section without interfering with its folding process. Big-end diameter which fits within the bounding box of 120 mm is taken as the starting point and smooth passage of each section into its following one is ensured while

deciding diameters of both ends of each conical section.

#### 5.2.4.1 Analysis of crash performance

The crush force with respect to crush displacement is shown in Figure 5.4(d) and various stages of progressive deformation of conical tubes in configuration-A4 are shown in Figure 5.5(d). At the onset of impact, the front conical tube begins inward inversion with a stable and unidirectional fold pattern. This folding which yields a low initial peak force of 70 kN which is equivalent to an acceleration of 14.2 g is within the allowable limits from the safety perspective [34]. The folding progresses gradually until the length of the front tube becomes half. At this stage, the intermediate front structure comes in contact with the middle tube and the crush force reaches the next level at around 90 kN (equivalent to an acceleration of 18.3g). The middle tube begins to invert internally with a gradual folding until its length becomes half. At the end of the inward inversion of the second tube, the intermediate structure comes into contact with the rear and the final tube initiating the inward fold. The crush force reaches the next level in the range of 120 kN (equivalent to an acceleration of 24g) and continues there until the crush fold reaches the bottom of the cup shaped structure in the chassis frame at around 232 mm of the crush stroke. The structure starts resisting the plastic deformation as the double folds of all the tubes are accumulated in the cup shaped structure becomes rigid. The differentiating merits of this configuration are i) low initial peak force i.e. low acceleration level which is vital from the occupant safety perspective, ii) stable deformation pattern with nearly uniform crush force that helps in maximizing the TEA by the structure, and iii) plastic deformation for the entire stroke leading to higher SE. These aspects enable this configuration to distribute the crush energy over the entire length of the crush stroke. The TEA by this configuration-A4 is comparable to that of the other configurations in spite of the low initial $F_{peak}$ and the crush force operating within the allowable limits. It exhibits an all-round performance in every aspect of the crashworthiness assessment criteria.

### 5.2.5 Analysis of energy absorption

The overall performance assessment of all the four EA structural configurations is provided in Tables 5.1 and 5.2. Energy absorption curves of all configurations are shown in Figure 5.6. Here, the energy absorbed by any configuration refers to the energy absorbed by the structure till the end of active crush stroke. There is no common reference point (w.r.t. the crush

stroke) at which the total energy absorbed is measured. The TEA by each configuration is measured at the corresponding end point of crush stroke for each configuration. For example, TEA for configuration-A1 is measured at 192.4 mm which is the end of active crush stroke while it is measured at 232 mm for configuration-A4. The objective here is to consider the EA by pure plastic deformation only, as the crush force curve beyond the end of active crush stroke has no significance. Quantitatively, configuration-A3 is found to absorb maximum amount of impact energy as its axial crush is represented by higher crush forces much beyond the acceptable levels. Configurations A2 and A3 also exhibit a similar trend of energy absorption. These configurations absorbing higher amounts of impact energy within a shorter crush stroke is not favourable from the occupant safety perspective. On contrary, configuration-4 with closely comparable value of TEA distinguishes itself by absorbing the impact energy almost throughout the entire length of the EA structure. This is possible because of higher SE (97%) and nearly uniform crush force in each conical segment of the structure. These peculiar features of configuration-4 exhibits a superior performance in comparison to other configurations.

The total initial (kinetic) energy available with the impacting body in this study is 56.25 kJ (mass = 500 kg and initial velocity = 15 m/s). The amount of energy absorbed by each configuration as a fraction of the initial energy available with the impacting body is calculated as energy absorption factor (EAF) and is provided in Table 5.2 for all configurations.

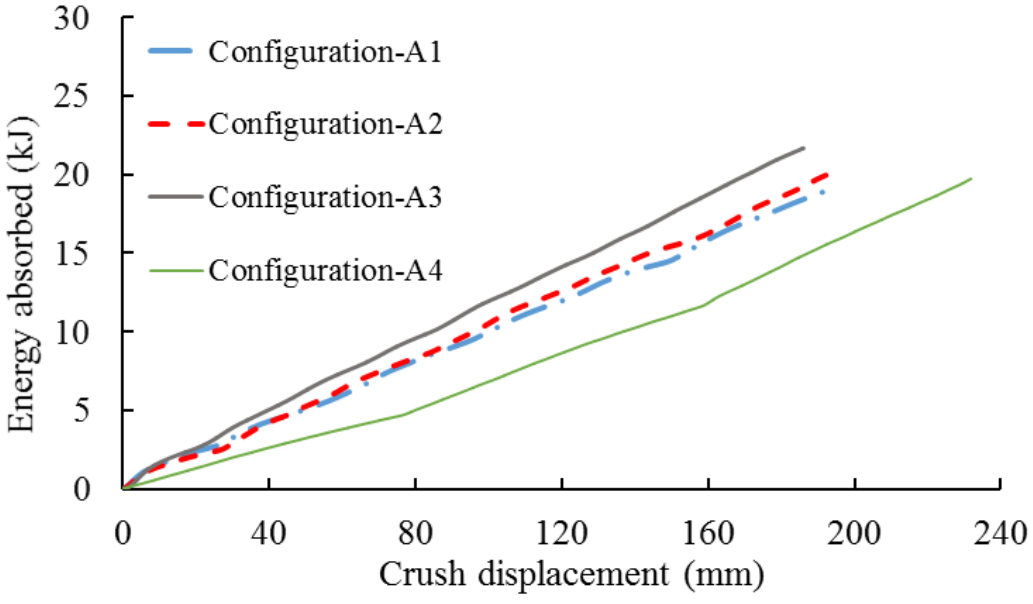


Figure 5.6. Energy absorption versus axial crush for all four EA structural configurations

Table 5.1: Crashworthiness assessment of all configurations in terms of primary parameters

| Configuration | Mass (kg) | Initial peak crush force (kN) | TEA (kJ) | Crush stroke (mm) | Energy per unit crush (kJ/mm) |
|---|---|---|---|---|---|
| A1 | 0.502 | 231.6 | 18.95 | 192.4 | 98.5 |
| A2 | 0.499 | 206.5 | 20.25 | 196.0 | 103.3 |
| A3 | 0.492 | 255.6 | 21.63 | 186.0 | 116.3 |
| A4 | 0.494 | 69.9 | 19.70 | 231.8 | 85.0 |

Table 5.2: Crashworthiness assessment of all configurations in terms of secondary parameters

| Configuration | Mean force (kN) | CFE (%) | SEA (kJ/kg) | SE (%) | Acceleration level (g) | EAF (%) |
|---|---|---|---|---|---|---|
| A1 | 98.6 | 43 | 37.8 | 80 | 47 | 34 |
| A2 | 103.4 | 51 | 40.6 | 82 | 42 | 36 |
| A3 | 116.4 | 46 | 44.0 | 78 | 52 | 38 |
| A4 | 85.1 | 122 | 39.9 | 97 | 14.2 | 35 |

### 5.2.6 Discussion of Results: Tube-in-tube concepts

It is understood from literature [5, 22, 34] that crashworthiness of a frontal protective structure doesn't go by the TEA alone, but an effective EA structure should absorb the targeted amount of impact energy by utilizing the crush forces within the human tolerance limits. In the present study, configurations A2 and A3 exhibited higher TEA and SEA quantitatively. As the energy absorbed is the area under the crush force – crush displacement curve, higher crush forces normally yield higher TEA values giving a false impression about crashworthiness of the structure. Such structures are not a favourable choice from the safety perspective. Under this guideline, configurations A2 and A3 are not considered a good choice for impact mitigation as crush forces are far outside the tolerance levels. Configuration-A3

demonstrated that crush folding modes of tubes and ribs competing with each other in orthogonal planes ensured stability in the crush force behaviour for major part of the crush stroke. Limited crush stroke and high initial $F_{peak}$ have to be addressed to make these configurations a choice for EA applications. Configuration-A4 with its unique structural arrangement in three segments and a unique unidirectional folding behaviour ensured a benchmark performance in all aspects of crashworthiness assessment. Conical shape helped in achieving a stable folding which in turn resulted in a nearly uniform crush force in each segment. This shape also helped in involving the entire length in plastic deformation, a step towards achieving nearly 100% SE. Dividing the structure into multiple segments without any interaction between their folding patterns ensured 97% of SE for the entire length of the structure. Simple fillets at the big end of each conical section acted as controllable crush force triggers. These three factors helped configuration-A4 achieve reasonably good TEA and SEA with acceleration levels within the allowable limits of 20 to 23 g. Benchmark performance in all the aspects of crashworthiness assessment criteria helped configuration-A4 as the favourable choice from the first kind of EA structural configuration with tube-in-tube arrangement in the current study.

## 5.3 Development of new structural configurations based on combination of standard shapes (Type-B approach)

In this section, structural concepts with cross sections based on the combination of arcs and straight lines and tapered columns have been proposed and assessed for crashworthiness. The axial lengths (240 mm), mass (0.5 kg) and the material (Aluminum AA7005 T6) of all these configurations is maintained in the similar lines as those of the tube-in-tube sections. The individual elements (ribs, semi-circular tubes, joining strips and inner core) of all the structural configurations are proposed to be joined together by appropriate welding procedure.

### 5.3.1 Configuration-B1 (base configuration)

The motivation for this kind of base configuration stems from observations from the previous studies [38, 39, 43, 98, 99] on the circular cross section based EA structures which exhibit progressive plastic folding modes and higher SE; and polygonal, multi-cell and multi-cornered column structures [86, 89, 90, 92, 96] which offer stable crush forces. While the circular EA structures have the drawback of fluctuations in crush force, multi-cell columns

exhibit low SE and both of these configurations possess poor CFE due to high $F_{peak}$. An attempt is made to develop five EA configurations that have the combined advantages of circular and straight sided columns (yielding progressive crush, high SE and stable crush forces) while trying to keep the safety-critical $F_{peak}$ within the limits and improve CFE to maximize the TEA by utilizing the crush forces which are within the allowable limits.

With this back ground, the base configuration is obtained by splitting a circular tube into two semi-circular tubes (mean diameter 70 mm and thickness 2 mm), and elongate the circular cross section such that the end-to-end distance is 110 mm as shown in Figure 5.7(a). The purpose of straight-edged side profile is to add more strength to the semi-circular tubes during crushing and to decrease the intensity of fluctuation in the crush force thereby offering stability to the crush force. This configuration is constructed to understand the effect of these geometric changes on the basic crashworthiness assessment parameters such as $F_{peak}$, SE, CFE and the acceleration level. The front flange corners of both the semi-circular tubes are rounded with a fillet radius of 12 mm to minimize the initial $F_{peak}$. The FE model is built and analysed with an axial impact using a 500 kg mass impacting the EA structure with an initial velocity of 15.5 m/s as discussed in Section 5.1.2.

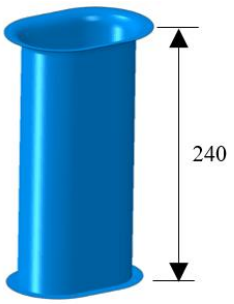


(i) Geometry

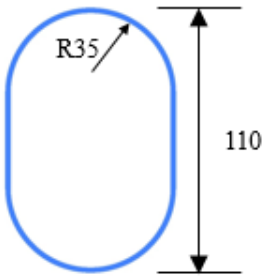


(ii) Cross-section

(a) Configuration-B1 (base configuration)

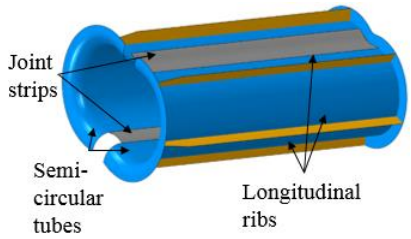


(i) Geometry

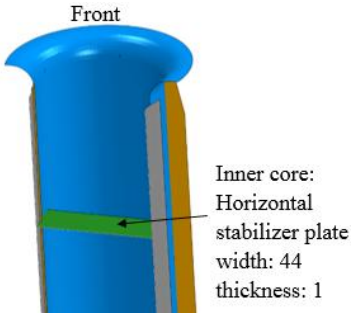

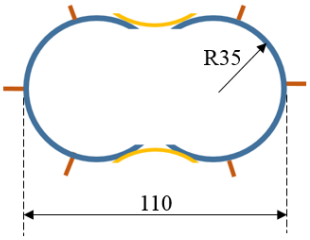


(ii) Cross-section

(iii) Cross-section view at the plane of symmetry

(b) Configuration-B2

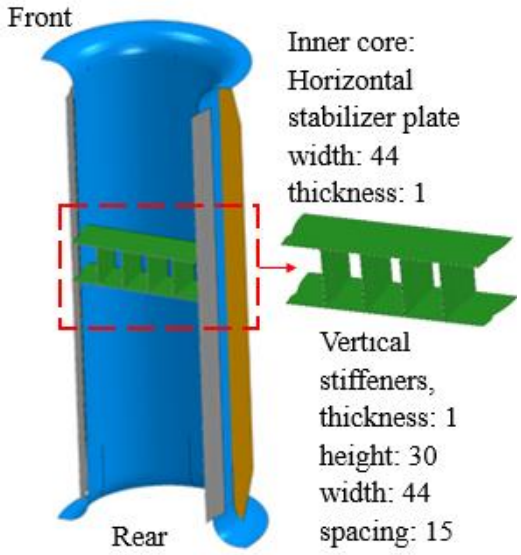


(c) Configuration-B3: Cross-sectional view at the plane of symmetry

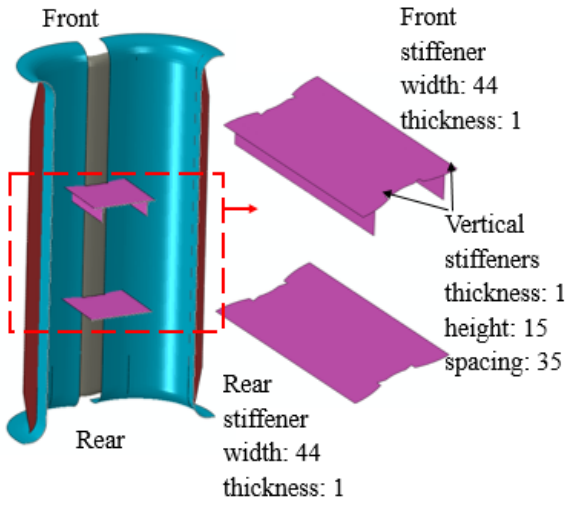


(d) Configuration-B4: Cross-sectional view at the plane of symmetry

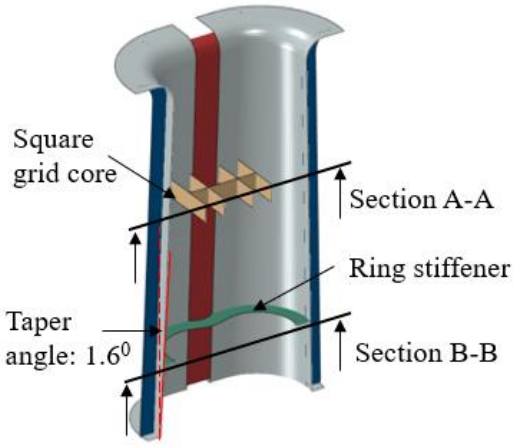


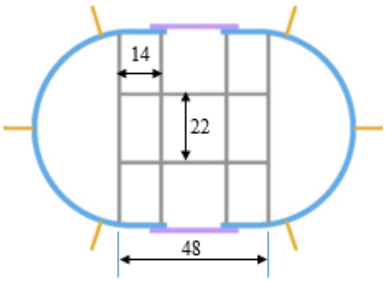


Height of grid core: 15

(ii) Section A-A: Square grid location

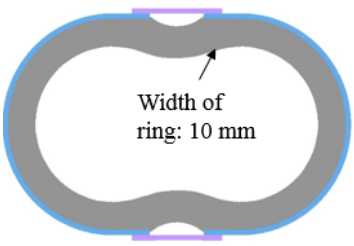

(i) Cross-sectional view at the plane of symmetry (iii) Section B-B: Ring stiffener location

(e) Configuration-B5

Figure 5.7. Proposed configurations for EA structure based on type-B approach (all dimensions in mm)

5.3.1.1 Analysis of crash performance:

Different stages of plastic deformation of this base configuration under different progressive axial crush (δ) is shown in Figure 5.8(a) and axial crush force against the crush displacement ($F$ - δ) curve is shown in Figure 5.9(a). This configuration required an initial $F_{peak}$ of around 153 kN which is equivalent to an acceleration of 31.2g to initiate the crushing deformation. This is followed by a series of fluctuations in the crush force. A close look at the crush force curve and the progress of crush deformation shows that the crush force drops from 153 kN at 14 mm stroke to 60 kN at a stroke of 29 mm. The crush force then fluctuates in cycles with a wavelength of around 24 mm for the first two cycles and the wavelength of fluctuation increases as the crushing progresses. The magnitude of fluctuation also tends to stabilize with the crush stroke. From the crush stroke of 140 mm onwards, the crush force drops to 60 kN due to change in cross-section as the semi-circular parts of the structure push inwards resulting in loss of stability. However, crush force settles at 60 kN for the remaining active crush stroke until 210 mm. At this point, due to densification of crushed part and reduction in uncrushed length, the structure resists further plastic deformation and becomes much stiffer. As the plastic crushing is active until a stroke of 210 mm, the SE of this EA structure is 84.2 % (total length is 240 mm).

High initial $F_{peak}$, instability in the curve till 130 mm are the major limitations of this configuration. This results in the loss of energy absorbed as the area under the ($F$ - δ) curve is minimized. However, this configuration gives some hints for improvement in i) crush force stability in contrast to pure circular columns, and ii) SE in comparison to regular polygonal and multi-cell based configurations. The structure needs some core support between the two semi-circular tubes to resist the fall at 60 mm crush and to stabilize the crush-force curve. Geometry of the core support and its location along the axis are the key factors in improving the stability in the structure and thereby the crush-force behaviour. The optimization of core

topology and its distribution along the length of the structure are discussed in detail in the next four new configurations.

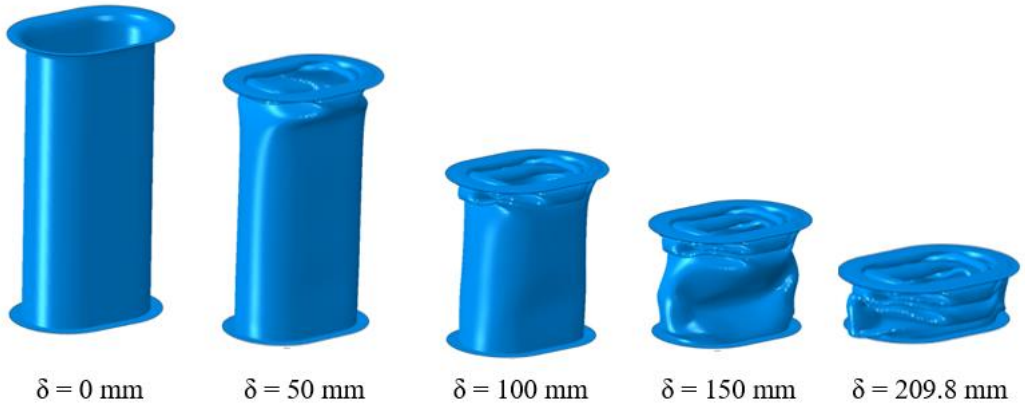


(a) Configuration-B1 (base configuration)

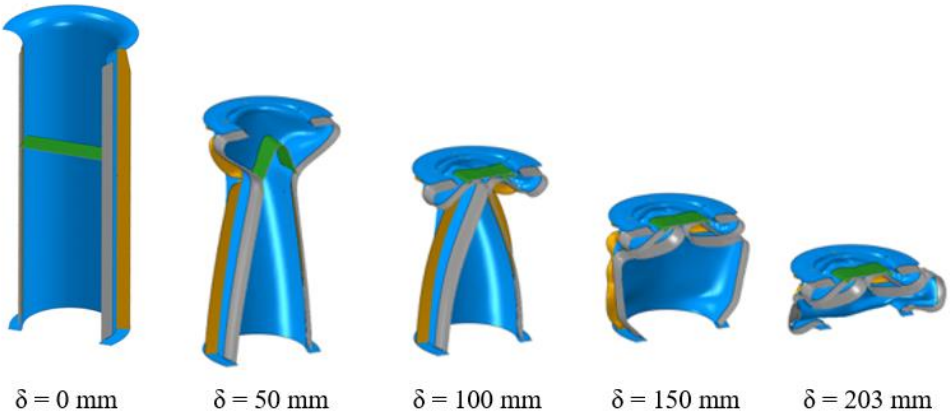


(b) Configuration-B2 (Sectional view)

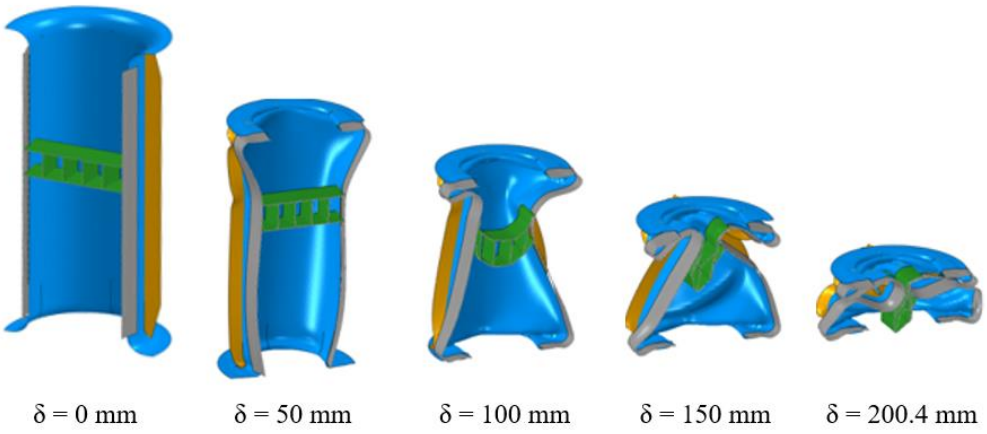


(c) Configuration-B3 (Sectional view)

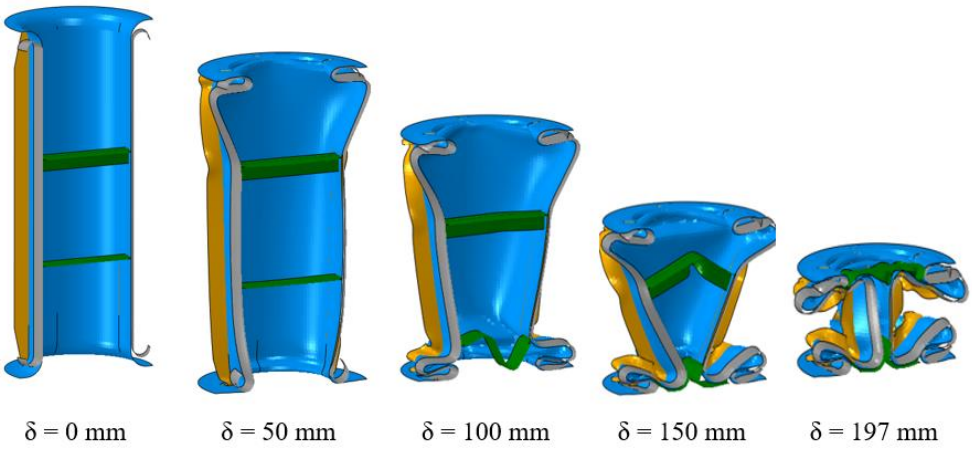


(d) Configuration-B4 (Sectional view)

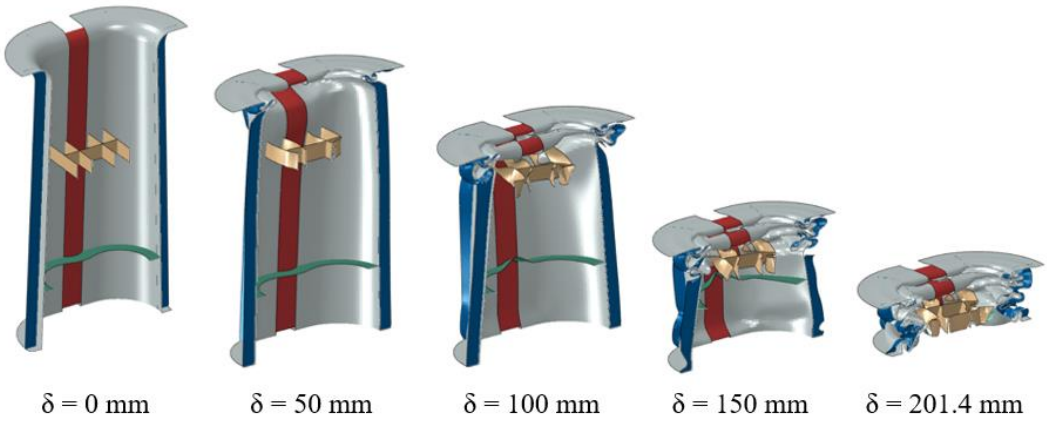


(e) Configuration-B5 (Sectional view)

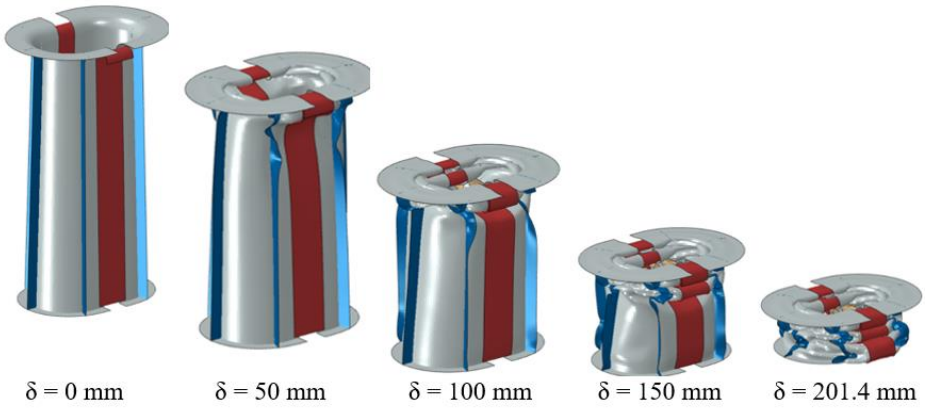


(f) Configuration-B5 (Full view)

Figure 5.8. Different stages during deformation of proposed EA structures based on type-B approach

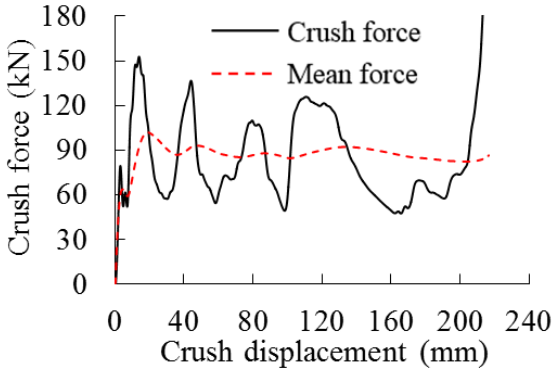


(a) Configuration-B1 (base configuration)

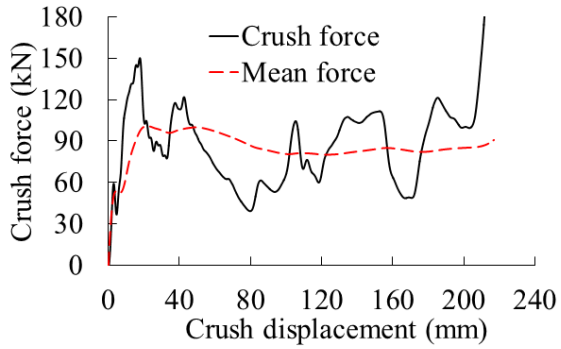


(b) Configuration-B2

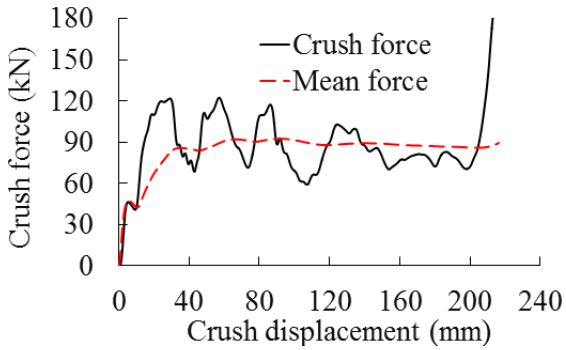


(c) Configuration-B3

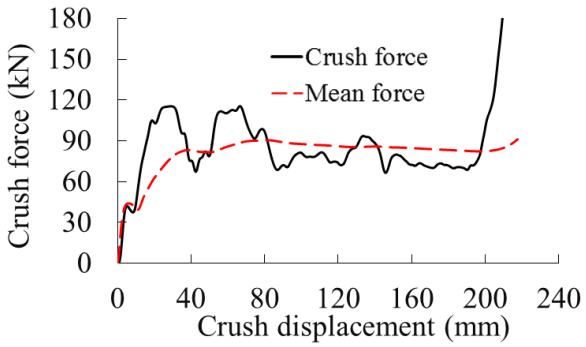


(d) Configuration-B4

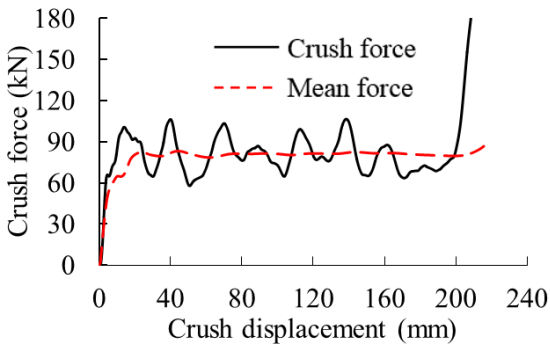


(e) Configuration-B5

Figure 5.9 Crush force and mean force with respect to crush displacement for proposed EA structural configurations based on type-B approach

### 5.3.2 Configuration-B2

Based on the observations from the performance of base configuration-B1, configuration-B2 as shown in Figure 5.7(b) is obtained by combining two semi-circular tubes (mean diameter 70 mm and thickness 2 mm) using two longitudinal strips (each 1.8 mm thick). The purpose of these two strips is to stiffen the semi-circular tubes during crushing and to decrease the intensity of fluctuation in the crush force. Front end flanges of semi-circular tubes are

provided with fillet radii of 12 mm to control the initial $F_{peak}$. Semi-circular tubes are reinforced by three longitudinal ribs of 1 mm thick and 10 mm wide on the outer circumference. As the semi-circular tube and ribs deform plastically in two different planes, it helps minimize the fluctuations in the crush force during the crush, as observed in the crush behaviour of multi-cell columns [90, 96] where the inner reinforcement ribs and the circular tubes deform plastically in two orthogonal plane walls and try to negotiate with each other thereby offering stability to the crush force. These ribs have been placed outside to improve the SE which is a drawback in the multi-cell columns due to densification of crushed material and lack of space.

To address the issues with respect to stability of semi-circular tubes which were observed during axial crushing of base configuration, a few reinforcements are introduced. A horizontal stiffener plate of width 44 mm and thickness 1 mm is placed at a distance of 90 mm from the front end to control the loss of crush force due to change of cross-section. The dimensions and placement of this horizontal stiffener have been decided after a few iterations based on the deformation behaviour of the base configuration. This configuration has been constructed to understand the effect of these geometric changes to the base configuration.

#### 5.3.2.1 Analysis of crash performance

Different stages during plastic deformation of configuration-B2 are shown in Figure 5.9(b). The crush force versus crush displacement i.e. ($F$ - $\delta$) is shown in Figure 5.10(b). Dynamic $F_{mean}$ shown in the $F$ - $\delta$ graph is represented as the ratio of cumulative energy absorbed to the corresponding crush stroke. This configuration required an initial $F_{peak}$ of around 150 kN to initiate the crushing deformation, equivalent to an acceleration of approximately 30.6 g which is high from the human tolerance limits [34]. This is followed by a series of fluctuations in the crush force and this results in the loss of the TEA. The structure being wide and not adequately strong in the inner core could not sustain its crush force for a longer period due to its unstable crush. The horizontal stiffener plate could not provide enough strength to resist the change of cross section which results in an uneven folding mode leading to a drastic drop in the crush force. The crush force fluctuates between 120 kN and 46 kN altering the state of accelerations to a great extent limiting the CFE to 57 %. A total crush stroke of 203 mm is achieved that gave a SE of 84.6 % and TEA is 17.25 kJ. The crush performance of configuration-B2 is observed to be similar to that of base configuration-B1 in many aspects.

The horizontal stiffener plate could not help improve stability of the structure after the initial peak and the overall crush-force behaviour, but it has given enough clues that the presence of

core structure between the semi-circular tubes does improve the stability as the range of fluctuations in the crush-force is reduced slightly and the minimum crush force is around 46 kN (against 38 kN with base configuration-B1). Further improvements to the core support are discussed in configuration-B3.

### 5.3.3 Configuration-B3

Configuration-B2 is slightly modified to address its shortcomings i.e., high initial $F_{peak}$ and fluctuating crush force (low CFE). Thickness of the semi-circular tubes is reduced to 1.8 mm and fillets are introduced at the rear flange of the semi-circular tubes to reduce the initial $F_{peak}$. For better stability during the crush, inner horizontal stiffener plate is reinforced by adding i) another parallel plate of 1.0 mm thickness and width of 44 mm, at a distance of 30 mm towards the rear end (at 120 mm from the front end), and ii) four equally spaced vertical members connecting these two horizontal plates with a spacing of 15 mm between each vertical member. The resulting Configuration-B3 is shown in Figure 5.7(c). The objective of distributing the stiffness along the axis of the structure is to provide controlled stiffness at the critical locations along the length of the semi-circular tubes to improve stability (resist the drastic and uneven change of cross section) during the crush process after studying the crush force patterns of the previous configurations. It was evident that the inner core topology could not sustain the crush-force for a longer stroke. The placement of the second stiffener and its location with respect to the first plate are decided after a few iterations by altering the distance between the two horizontal plates. As the stiffness in the plane normal to the axis of the structure alone was not enough to resist the inward folding, four vertical members between the two horizontal plates have been added to improve bending resistance of the horizontal plates and to improve the stability after the initial $F_{peak}$.

5.3.3.2 Analysis of crash performance:

Different stages of plastic deformation of configuration-B3 are shown in Figure 5.8(c) and crush force versus crush displacement i.e. ($F$ - $\delta$) is shown in Figure 5.9(c). Configuration-B3 reduced the initial $F_{peak}$ to 121 kN, which is equivalent to an acceleration of 24.8 g, due to reduction of thickness of main semi-circular tubes by 0.2 mm. However, this structure also experienced a series of fluctuations in the crush force before attaining a stable crush force from a crush stroke of 110 to 120 mm onwards. In earlier versions, inadequate core strength was resulting in an uneven change of cross section of semi-circular continuous tubes which was triggering instability in the structure leading to a sudden drop of crush force. The

improved core topology with increased bending resistance of horizontal plates retained the stability of the structure by providing stiff support to the front part during the early stage of the crush stroke. The cross section of semi-circular continuous tubes changed slightly but the intensity is not significant and the inner surfaces do not touch each other. The improvement is evident from the crush-force behaviour as the crush force continued to sway between 70 kN and 120 kN during the first 90 mm of crush. From 90 mm onwards, change of cross section is also more stabilized as the crush force remained between 80 kN and 95 kN after 120 mm of crush. The crush force never reduced below 60 kN. The stability of the crush force is observed to be better in comparison to that of configuration-B2, hence the CFE has improved to 71 % from 57 %. There is a slight drop in the crush stroke to 200.4 mm leading to SE of 83.5% due to early densification of the structure owing to the thick inner core structure. But this did not affect the TEA which is at 17.18 kJ as the crush forces were above 60 kN enlarging the area under $F$ - $\delta$ curve.

### 5.3.4 Configuration-B4

To address the concerns associated with configuration-B3 *i.e.*, initial $F_{peak}$ of 121 kN and fluctuations in the crush force until 110 mm of crush stroke, some more modifications are made to configuration-B3. Thickness of semi-circular tubes is further reduced to 1.7 mm, as it is evident from configuration-B3 that the thickness of semi-circular tubes influences the initial $F_{peak}$. Integrated inner core of configuration-B3 is further optimized to provide stability during the crush in the rear part of the structure. Horizontal stiffener plate which is placed at a distance of 90 mm from the front plane is reinforced by only two vertical members of thickness 1.0 mm and height 15 mm with a spacing of 35 mm between them, as shown in Figure 5.7(d). Rear horizontal plate is separated from the vertical members and moved further towards the rear end. It is placed at a distance of 76 mm from the rear end plane. After observing the crush force behaviour of configuration-B3, it may be noted that the stability is slightly lost between 90 – 110 mm of crush stroke and there is not enough support in the rear part of the structure. A few iterations have been performed in the background to optimally distribute the stiffness in the rear part of the structure. Finally the second horizontal stiffener plate is placed at a distance of 76 mm from the rear end. Vertical members have not been attached to the rear horizontal member as just a planar support was observed to be enough and not much of the crushable part of the structure is left towards the rear end.

5.3.4.2 Analysis of crash performance

Different stages during plastic deformation of configuration-B4 are shown in Figure 5.8(d) and its $F$ - $\delta$ response is shown in Figure 5.9(d). It may be observed that the reduced thickness of semi-circular tubes helped in bringing the initial $F_{peak}$ to 115 kN which is equivalent to an acceleration of 23.5 g. The modified inner core improved the stability during the crush. The magnitude of fluctuation in the crush force reduced slightly and the crush force became stable from the crush stroke of 80 mm onwards, improving the CFE further to 71.4 %. The crush stroke dropped to 197 mm from 200 mm as the crushed material densified early due to crushing happened from both the ends. This uneven crush folding limited the SE to 82.1%. As the crush force curve was fluctuating around at a slightly lower crush force of 70 kN, the TEA came down to 16.2 kJ. Decrease in $F_{peak}$ and fluctuations in the crush force behaviour are major findings from this configuration. Improvements are required in SE and TEA.

### 5.3.5 Configuration-B5

Performance of configuration-B4 is better than configuration-B3 in many aspects, but there is a short fall in crush stroke and the TEA. It is observed that the fillet radii at the rear end of the semi-circular tubes was interfering with the progress of axial crush from the front to the rear portion. This interruption altered the folding process and also limited the crush stroke of configuration-B4. The two semi-circular tubes are tapered by $1.6^0$ with bigger radius at the rear end and smaller radius at the front end. This taper is expected to address the stability issues during crushing due to change of cross-section of semi-circular tubes by uneven inward movement which is observed during the previous four configurations. Fillets at the rear end of the tubes are removed to add more stability during the crush. Cross-section of semi-circular tubes is modified such that circularity is maintained for exactly $180^0$ and the profile is straightened tangentially after $180^0$. Updated cross-sectional view is shown in Figure 5.7(e) as configuration-B5. As the horizontal stiffener plates are observed to be not strong enough to resist the uneven inward folding of semi-circular tubes, square grid type of core structure with axial height of 15 mm is introduced in place of the core configuration available in configuration-B4. The thickness of strips used for this core support is 1.2 mm. Square grid core is placed at an axial distance of 90 mm from the front end of the structure. Horizontal plate type stiffener at the rear end of the structure is also replaced by a flat ring of

width 10 mm and thickness of 1.0 mm that runs through the entire internal cross-section of the structure. It is placed at an axial distance of 65 mm from the rear end of the structure. Dimensions and location of these modified core structures have been decided after a series of FEA iterations. The resulting configuration-B5 is shown in Figure 5.8(e).

5.3.5.2 Analysis of crash performance

Different stages during plastic deformation of configuration-B5 are shown in Figure 5.8(e-f). Introduction of taper to the structure with reduced radius at the front end helped in bringing down the initial $F_{peak}$ to 99.8 kN which is equivalent to an acceleration of 20.3g which is the threshold limit from the safety perspective [34]. Crush force versus crush displacement of configuration-B5 is shown in Figure 5.9(e).

There is an improved crush force behaviour as the crush force continues to stay within the range of 65 kN to 100 kN with significant part of crushing happening at a crush force of 80 kN. Tapering of semi-circular tubes allowed progressive crush while flattening side portion along with the modified core structure prevented the inward folding and change of cross-section of semi-circular tubes. This is evident from $F$ - $\delta$ curve where steep falls in the crush force is not observed. Optimized ring shaped stiffener placed at the rear part of the structure helped in offering just the enough support to the semi-circular tubes to prevent inward folding and retain the cross-section. This factor along with the taper in the tubes helped in shifting the folding mode to a proper and progressive folding resulting in a stable crush force and an improved crush stroke. New modifications in this configuration helped in improving the crush stroke to 201.4 mm improving the SE to 83.9 %. Optimum initial $F_{peak}$ and a stable crush force during the crush improved the CFE to 80.6 %. Post stabilization, the crush force curve swayed around 80 kN and helped in improving the TEA to 16.2 kJ. In this configuration, as discussed earlier in this section, major issues observed with cylindrical and multi-cell columns i.e., initial $F_{peak}$, low SE and low CFE have been addressed considerably based on the results and observations from FEA studies. Comparison of energy absorption of all the five type-B configurations are shown in Figure 5.10.

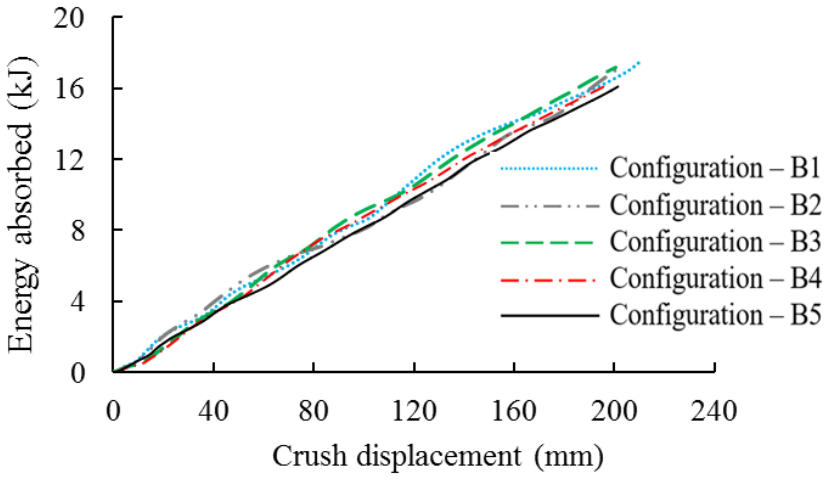


Figure 5.10. Energy absorbed versus axial displacement of all proposed EA structural configurations

### 5.3.6 Discussion of Results of type-B Configurations

Base configuration-B1 has provided the impetus to the conceptualisation of proposed EA structures that combine the merits of familiar EA structures available in literature while addressing their limitations to form a constructive basis for this study. Configuration-B2 with inappropriate structural arrangement resulted in high initial $F_{peak}$ (higher 'g' levels from the human injury criteria perspective) and low crashworthy performance in terms of SE and CFE. It was highly susceptible to instabilities during crush due to excessive changes in cross sections leading to sudden and drastic drops in the crush forces. The performance was inadequate in many parameters barring the SE. Configuration-B3 with stiffened and optimized core support was able to bring the crush force down to 122 kN while maintaining other assessment parameters almost at the same levels as that of configuration-B2. Drop in equivalent acceleration levels from 30.6 g to 24.8 g was a major accomplishment of configuration-B3. Though the deviations of cross sections have not been eliminated completely, their effect on the stability of the structure and crush force behaviour has been controlled significantly. Absorbing the same amount of energy by utilizing an $F_{peak}$ which is 80% of that of configuration-B2 and with the same mass was a notable improvement as the performance parameters tend to be in line with the safety requirements.

Configuration-B4 with an optimally distributed stiffness addressed the stability issues in the rear part of the structure and a smoothened collapse trigger gave a better performance in all the assessment parameters except the SE. Equivalent acceleration levels came down to 23.5 g which is an encouraging factor from the safety point. Introduction of fillets at the rear end of the structure interfered with the progress of crush and disturbed the folding modes which in

turn limited the crush stroke to 197 mm resulting a compromise in the overall objective of energy absorption. However, further drop in the initial crush with comparable performance in the remaining parameters was a major takeaway.

Configuration-B5 was able to fill the gaps of configuration-B4 with a tapered structural arrangement. It was able to absorb nearly the same amount of energy as that of configuraton-B2 with peak crush forces that are 65% of those of configuration-B2. Configuration-B5 with its all-round performance in all the assessment parameters is close to the target performance of achieving the crush forces with acceleration levels close to 20g which is the threshold limit for the probability of serious injury. In general, it has been understood from this study that for impact mitigation applications by plastic deformation, structural configurations that exhibit stable and progressive folding which lasts for the majority of the length of the EA structure is the most preferred choice. In view of the industry's exploration for light-weight structures, achieving SEA measures above 35 kJ/kg though based on a numerical study is an encouraging point for further developments. A detailed performance summary of all five EA structural configurations based on type-B approach is presented in Table 5.3. Configuration-B5 performs better in all aspects of crashworthiness amongst all the five proposed EA structural configurations under this category.

Table 5.3: Crashworthiness assessment of all proposed EA structural configurations (Type-B)

| Configuration | Mass (kg) | Peak force (kN) | Mean force (kN) | Equivalent acceleration (g) | TEA (kJ) | Crush stroke (mm) | CFE (%) | SE (%) | SEA (kJ/kg) |
|---|---|---|---|---|---|---|---|---|---|
| 1 (base) | 0.50 | 153.0 | 84.2 | 31.2 | 17.7 | 209.8 | 55.0 | 87.5 | 35.4 |
| 2 | 0.50 | 150.0 | 84.9 | 30.6 | 17.2 | 203.0 | 56.6 | 84.6 | 34.2 |
| 3 | 0.48 | 121.5 | 85.7 | 24.8 | 17.2 | 200.4 | 70.6 | 83.5 | 35.9 |
| 4 | 0.46 | 115.1 | 82.2 | 23.5 | 16.2 | 197.0 | 71.4 | 82.1 | 35.2 |
| 5 | 0.44 | 99.8 | 80.4 | 20.3 | 16.2 | 201.4 | 80.6 | 83.9 | 37.2 |

### 5.4 Summary

Crashworthiness of structural configurations based on both type-A (i.e. tube-in-tube arrangements) and type-B (combination of standard shapes and profiles) approaches has been assessed on all the standard crashworthiness parameters. It has been learnt that quantitative TEA alone is not the measure of crashworthiness of an EA structure. The effect of material distribution and stiffness on the crush force behaviour has been understood to a large extent. Energy absorption by utilizing the crush forces which are within the allowable limits is a

positive trait of an EA structure. This is possible only with configurations where CFE and SE tend to reach unity while keeping the crush forces below the equivalent acceleration levels of 20g. In the current study, from the tube-in-tube series, configuration – A4 with conical tube arrangement exhibited an all-round crashworthiness with near-ideal performance in every parameter. Configuration-A3 with near-uniform crush force trend also has the potential if proper crush triggering mechanisms are employed to control the $F_{peak}$.

From the second set of concepts i.e. type-B configurations with hybrid cross-sections, configuration-B5 with precisely optimized distribution of stiffness at key locations along the axial length also has the potential to be a choice of EA applications with a reasonably good control over the peak crush forces and the overall crush force behaviour.

Configuration-A4 with conical tubes which is based on the tube inversion concept with its superior crashworthiness has been chosen for further studies in the subsequent phases of the current research work.

# Chapter 6

# Evolution of a New Geometric Profile for Proper Tube Inversion for Crash Energy Absorption

Circular tubes under axial load undergoing deformation through inversion mode are referred to as *invertubes.* Inversion phenomena controls high initial peak crush force which is a fundamental requirement of an energy absorbing (EA) structure in road vehicles and helps in achieving nearly 100% stroke and crush force efficiencies. This rare combination of these three features offers a good potential for *invertubes* to be an ideal choice for impact crash energy absorption. This chapter presents 1) a brief history of tube inversion process, 2) an overview of theory of tube inversion and the knowledge gaps, 3) objectives of this part of research, 4) methodology for development of geometries for tube inversion, 5) the evolution process of tube geometries for tube inversion, 6) a detailed discussion of different variants, and 7) summary of all the observations.

## 6.1 Introduction

Impact energy absorption through plastic deformation of an energy absorbing (EA) structure is a well proven concept and is widely accepted in practice. An effective EA structure should absorb impact energy by controlled plastic deformation which is characterized by uniform crush forces through the entire crush stroke to maximize the area under crush force versus crush displacement curve [100] as shown in Figure 6.1. Previous researchers have proposed certain measurement criteria for evaluation of crashworthiness of EA structures through certain vital parameters such as (i) initial peak crush force ($F_{max}$, maximum force required to induce plasticity in an EA structure), (ii) stroke efficiency (SE, ratio of plastically deformed length to the total length of an EA structure), and (iii) crush force efficiency (CFE, ratio of mean crush force to initial peak crush force). Total energy absorbed (TEA) will be maximum as CFE and SE tend to unity within the allowable limits of crush forces [22]. This allowable limit of crush forces are governed by the acceptable deceleration limits ($\leq$ 20g) which a human being can withstand in a standard frontal collision at the specified vehicle speed. As the deceleration levels are directly related to head injury criteria (HIC) of occupants, keeping the initial peak crush forces within this deceleration limit is a fundamental requirement of an EA structure [5].

Literature on crash energy absorption suggests that structural configurations with circular cross-sections exhibit relatively higher SE and moderate CFE with little control on initial peak crush forces [39]. Structural configurations with multi-cornered cross sections (polygons) generally exhibit high crush forces leading to low CFE and SE due to densification, but maintain stable crush forces after the initial high peak [92]. Multi-cell cross-sections also exhibit similar behavior to that of multi-cornered sections with more stability in the crush force and observed to be more versatile for axial and oblique impact scenarios [86]. Filling of circular and multi-cornered sections with different kinds of foam materials were explored to maximize TEA, but at the cost of high initial peak crush forces and low CFE and SE [101]. Some novel configurations with kagome honeycomb sandwich arrangement were attempted, but SE could not exceed 75% [72]. Composite materials in the standard geometric cross-sections and controlled triggers show some promise in terms of CFE and SE, but still seem a little far from being a mainstream option for energy absorbing applications [102]. Tube inversion method addresses most of these shortcomings because of its unique method of plastic deformation.

Circular tubes under axial load undergoing deformation through inversion mode are referred to as *invertubes.* Inversion phenomena controls high initial peak crush force which is a fundamental requirement of an EA structure in road vehicles and helps in achieving nearly 100% stroke and crush force efficiencies. The concept of circular tube inversion has been in existence since 1960s and has shown possibilities in meeting the requirements of an ideal EA structure. Guist *et al* [103] provided theoretical formulations for prediction of inversion load of a circular tube along with experimental validation using selected material grades. Inversion mode of plastic deformation may be encouraged as an ideal mechanism for energy absorption in the road vehicles where controlled peak crush forces (impact induced deceleration levels) are critical for occupant safety and higher SE and CFE are key for maximizing the energy absorption. Reddy *et al* [104] proposed various structural configurations for energy absorption involving telescopic, conical-tubes-in-series kind of arrangement and suggested that inversion of conical tubes offers better control over the initial peak crush force, SE and CFE. Zhang *et al* [105] in their numerical study on similar works observed that multi-stage inversions can accommodate the deformed material within the minimum axial space while maintaining the uniform crush forces.

Researchers have always attempted to predict inversion forces in invertubes in terms of geometrical and material parameters through empirical relations and often ignored the geometric imperfections on plastic deformation and their influence on the inversion process.

Limited knowledge exist on inversion using stainless steel SS304 material. With this motivation, the present research is focused on understanding the intricacies of inversion with respect to geometric parameters in the design of invertubes and their effect on the inversion process as a step towards studying the feasibility of invertubes for EA applications in road vehicles. In this chapter, series of attampts are made to evolve a new invertube profile with SS304 material to achieve desirable inversion charecteristics for an ideal energy absorption. In this process, the effect of geometric parameters and their imperfections that contribute to effective inversion of invertubes have been studied in detail through finite element analysis (FEA) and experiments. A new invertube profile has been proposed that addresses anamolies in existing literature and inversion characteristics of this profile have been validated experimentally in a quasi-static environment.

### 6.2 Tube Inversion

Basically there are two types of inversions, inside-out and outside-in. In each of these procedures, inversion without any external guide (die) is known as free inversion and the inversion with the help of a guide is referred to as guided inversion. Schematics of these variations in inversion are shown in Figure 6.1 [5]. Only inside-out free inversion method is discussed here due to its relevance with the present research.

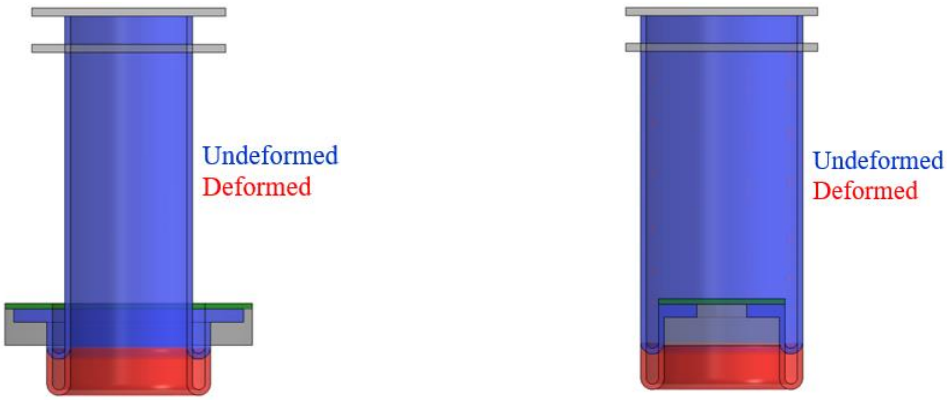


(a) Inside - Out: Free inversion (b) Outside - In: Free inversion

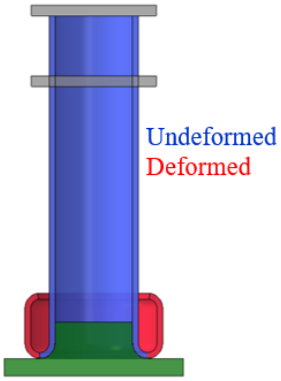


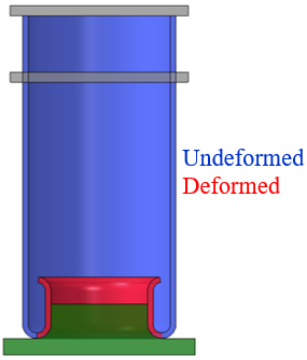


(c) Inside - Out: Guided inversion (d) Outside - In: Guided inversion

Figure 6.1: Different modes of tube inversion [5]

### 6.2.1 Theory of tube inversion

Literatures reveal that the impetus for tube inversions came from the need for soft landing systems for space vehicles in 1960s. Guist *et al* [103] pioneered in proposing the theory of tube inversion with detailed insights into the mechanics of plasticity during the inversion process. This process is characterized by turning one side of the tube to the other (inside-to-outside or outside-to-inside). Limitation in this process is the feasibility of inversion with only a few materials having a required degree of ductility with a controlled combination of tube geometric parameters (tube thickness to diameter ratios).

A schematic geometrical representation of an invertube is shown in Figure 6.2. In theoretical formulation of inversion, every increment of inversion stroke involves three stages of plastic deformation: i) plastic bending at the inner radius, $R$ at a point $A$, ii) hoop extension from radius $R$ to $R_i$, which follows the arc $A$ - $C$ to reach point $B$, and iii) plastic strengthening of the expanded material at point $B$ at radius $R_o$. The following assumptions were considered in this fundamental theory of tube inversion.

1. Material is perfectly plastic;
2. Work done during the inversion process is completely dissipated as internal plastic work by the three aforementioned phases of inversion process;
3. Thickness and axial length of the tube are constant;
4. Outer diameter attains an equilibrium state governed by curvature parameter, $b$; and
5. Inversion occurs at a constant load.

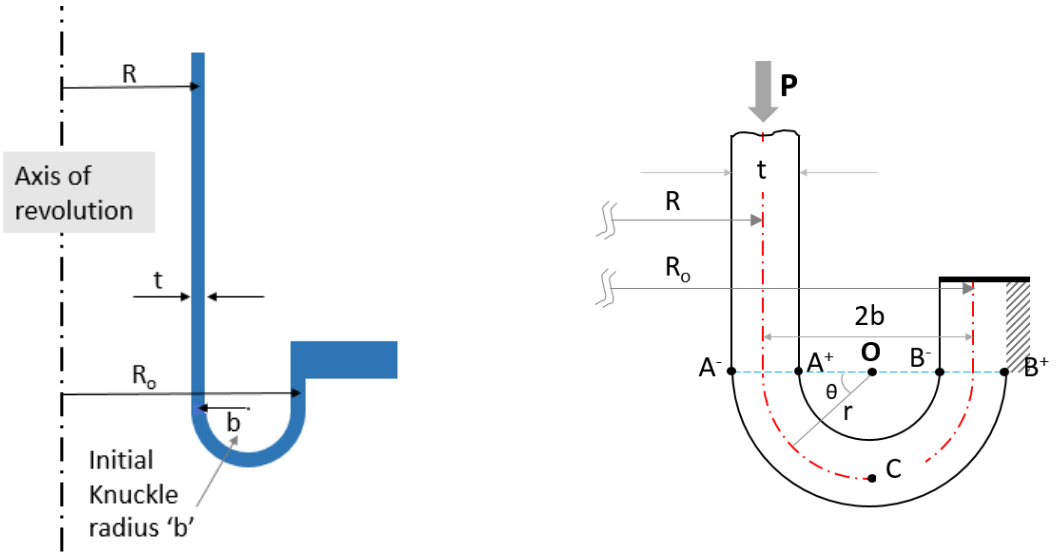


a) Schematic layout b) Nomenclature

Figure 6.2. Geometrical representation of an invertube

Based on Guist *et al* [103] theory, fundamental principle of inversion is based on equating the external work done by inversion force to the internal work of plastic deformation, and as a result, the force required to invert the tube, *P* is given by

$$P = \pi D t \sigma_p \sqrt{\left(\frac{2t}{D}\right)} = 4.44\, \sigma_P t^{1.5} D^{0.5} \quad (6.1)$$

As the initial knuckle radius *b* is observed to be critical in the inversion process, an empirical formula has been provided as

$$b_{min} = \sqrt{\left(\frac{D}{2t}\right)} \quad (6.2)$$

Kinkead *et al* [106] further improved the theoretical formulation proposed by Guist *et al* [103] by considering the sub-structural elements involved in the inversion process i.e. strains in i) tube expansion, ii) meridional bending, iii) normal-to-meridian reversed bending, iv) normal-to-meridian bending, and v) rotational process. This theory [106] is based on engineering strain in the material and the inversion force is expressed as

$$P = \frac{A_t \sigma_P}{\sqrt{3}} \left[\frac{t}{2b} + \frac{4b}{D} + \frac{t(D+2b)^2}{\{D^2(D+4b)\}} + \frac{\pi t}{2D}\right] \quad (6.3)$$

Kinkead *et al* [106] suggested the requirement for an in-depth study considering all aspects of plasticity to improve reliability in this theoretical prediction.

Reddy *et al* [107] focused on the differences between knuckle radii from theory and experiment, and slightly modified the material model by adopting i) true strains in the material model instead of engineering strains, ii) linear strain-hardening material model in place of rigid perfectly plastic (RPP) model, and iii) Tresca's yield criterion. Option for

adjusting the strain hardening parameter also provided better opportunities for matching experimental and theoretical values while obeying the law of conservation of volume.

$$d\mathcal{E}_{\varphi} + d\mathcal{E}_{l} + d\mathcal{E}_{t} = 0 \tag{6.4}$$

where $\varepsilon_{\varphi}$, $\varepsilon_{l}$ and $\varepsilon_{t}$ are strains along circumferential (hoop), meridional (axial) and thickness directions respectively. Equating external work and internal work of plastic deformation, the inversion force [107] is expressed as

$$P = 2\pi R\sigma_0 t\left[\frac{t}{4b} + \frac{1}{\sqrt{3}}\ln Z\left(1 + \frac{E_p}{2\sigma_0}\ln Z\right)\right] \tag{6.5}$$

where $z = 1 + \frac{2b}{R}$. (6.6)

They also proposed an empirical relation between knuckle radius *b*, tube radius *R* and thickness *t* for a minimum inversion load *w.r.t. b* as

$$b = \sqrt{\left(\frac{Rt}{2}\right)} \tag{6.7}$$

This model is observed to have a good correlation with experimental values for certain combination of material's strain hardening modulus to yield stress ratio ($E_p/Y_o$) and tube geometries ($t/R$ ratio) only.

Colokoglu *et al* [108] made an attempt to understand the inertial and strain rate effects on the tube inversion process. They conducted a detailed experimentation on pre-formed samples of mild steel specimens under quasi-static and dynamic conditions at different impact velocities and analysed the differences with the theoretical predicitons of inversion load. They considered the effect of thickness changes in the tube at plastic hinges and changes in curvature of the neutral fibre of the tube. They expressed the inversion load in terms of tube geometric parameters, yield stress and strain-hardening parameters of the material as

$$P = 2\pi R\sigma_0 t\left[\left(1 + \frac{3b}{2R} + \beta\frac{t}{16b}\right)\frac{t}{Z\,4b} + \frac{1}{\sqrt{3}}\ln Z\left(1 + \frac{\beta}{2}ln\,Z\right)\right] \tag{6.8}$$

Qiu *et al* [109] attempted to improve the theoretical prediction of inversion load by including the axial stretching phenomena of tube with an assumption that the external work done is equal to the sum of internal plastic work in bending and stretching modes. Their model captures the inversion process into 3 stages: i) axial bending at the internal diameter, ii) stretching in the hoop direction, and iii) straightening of bent portion at the external diameter position. Their model was built on Reddy *et al's* [107] theory and the expression for inversion load is given as

$$P = \pi R\sigma_0 t\,\frac{(R+2b)}{(R+b)}\left[\frac{t}{2b} + \frac{2}{\sqrt{3}}\,ln\left(1 + \frac{2b}{R}\right)\right] \tag{6.9}$$

Qiu *et al* [110] further improved the theory by working on a 3D model using a simple RPP material with von-Mises yield criterion and volume conservation rule. They introduced the changes in thickness of tube along the knuckle arc and strain variations through the thickness in their formulation. Their expression for inversion load is too complex. They have improved the predictions of steady state inversion load without much improvement in prediction of knuckle radius.

Yu *et al* [111] adopted a simplified 2D theoretical model and included the effect of energy dissipation through axial stretching as exclusion of this effect was leading to over-estimation of knuckle radius. Their model is based on initial and final states of geometry considering all the three stages of inversion process. They proposed three different concepts based on three different mechanisms as given below.

i) Constant velocity – material travels from inner diameter position to outer diameter position during the inversion process with constant velocity (thickness decreases with formation of knuckle radius).

ii) Constant thickness – material velocity varies during the deformation process (thickness is constant). But this theory has been observed to hold good for $t/R$ values between 0.02 and 0.12.

iii) Two-stage assumption – which is a combination of Reddy *et al* [107] and Colokogulu *et al* [108] models with thickness being constant in one half of the deformation process involving knuckle radius formation and velocity being constant in the other half.

This approach rules out influence of knuckle radius on the inversion force.

Qiu *et al* [112] proposed another model by considering a practical aspect of changes in curvature of knuckle radius which was ignored in the previous studies and also considered the interaction of bending and tension in the deformation process. The expression for inversion load included only the tube geometric parameters and yield stress of the material and is given as

$$P = 2\,\pi\,\sigma_0\,R\,t\left(\frac{1.144}{\sqrt{R}} + \frac{0.303}{R}\right) \tag{6.10}$$

### 6.2.2 Knowledge gaps

It may be understood from all these previous research that the natural knuckle radius is a key factor in the inversion process although theoretically it is not observed to have any significant

influence on the magnitude of inversion force. Optimum knuckle radius can be calculated from theoretical formulations and can be incorporated in the preformed geometry of the tube, but cannot be retained during the process of inversion. During the inversion process in experiments, the tube geometry tries to attain an equilibrium configuration making the knuckle radius smaller. At this instant, inversion process becomes difficult as the progressive knuckle radius becomes smaller than the natural minimum bending radius [113] of the tube with the resulting thickness. These natural aspects of mechanics of plastic deformation have not been considered while formulating theoretical models for inversion. This is because the focus of previous researchers was more on arriving at an empirical formula for prediction of inversion load in terms of tube geometry and material yield limit, and guidelines for optimum initial knuckle radius in terms of initial radius and thickness of the tube. These gaps have contributed to the differences between theoretical simplifications and experiments for inversion forces and knuckle radii.

It may be noted here that the existing literature do not provide any information related to geometry of preformed shapes of tubes, a central feature that drives the inversion phenomenon. Very limited experimental evidence is available on the deformation patterns of inverted tubes, failures during the process of attaining the tube inversion and reasons behind such failures. Information with respect to transition from 'initial' knuckle radius to final 'natural' knuckle radius and how this final equilibrium state has been achieved is also not available. As very few materials have been tried so far in experiments, existing knowledge is insufficient to choose a suitable material for the given $t/R$ ratio and knuckle radius of the tube. Theoretical formulations in the existing literature are largely based on perfectly plastic material formulation. Some parametric studies conducted by Reddy [107] on geometric and material parameters may not qualify highly ductile materials like SS304 grade (known for its high ductility) with low $E_p/\sigma_0$ ratio.

## 6.3 Present research

The present scope of research is focused on developing tube geometric profile which is ideal for inversion using stainless steel grade SS304. This material is chosen because of its considerable yield and ultimate strengths coupled with an excellent degree of ductility. A material with high ductility is an ideal choice for energy absorption applications in general and inversion phenomenon in particular. Most materials studied in literature are of low

strength (aluminum alloys and mild steel). High ductility and tensile strength of SS304 can contribute to tube inversion and improvements in specific energy absorption (SEA) factor.

### 6.3.1 Evaluation of Material Properties

Tensile test specimens of SS304 were prepared according to ASTM E8 [114] standard in the rod form as all the tube geometries studied in the current research were machined from rods of different diameters. Tensile tests were performed on two specimens as per the standard procedure on an *MCS* universal testing machine. The setup is shown in Figure 6.3(a) and the standard dimensions of the test specimen are shown in the Figure 6.3(b). Average true stress versus plastic strain derived from the test data is shown in Figure 6.3(c). Material properties obtained from tension tests are: Young's modulus = 210 GPa; Poisson's ratio = 0.29; yield strength = 280 MPa; ultimate tensile strength = 600 MPa; and elongation at break = 55%. The stress-strain curve (Figure 6.3(c)) derived from this test is considered for numerical simulations using FEA.

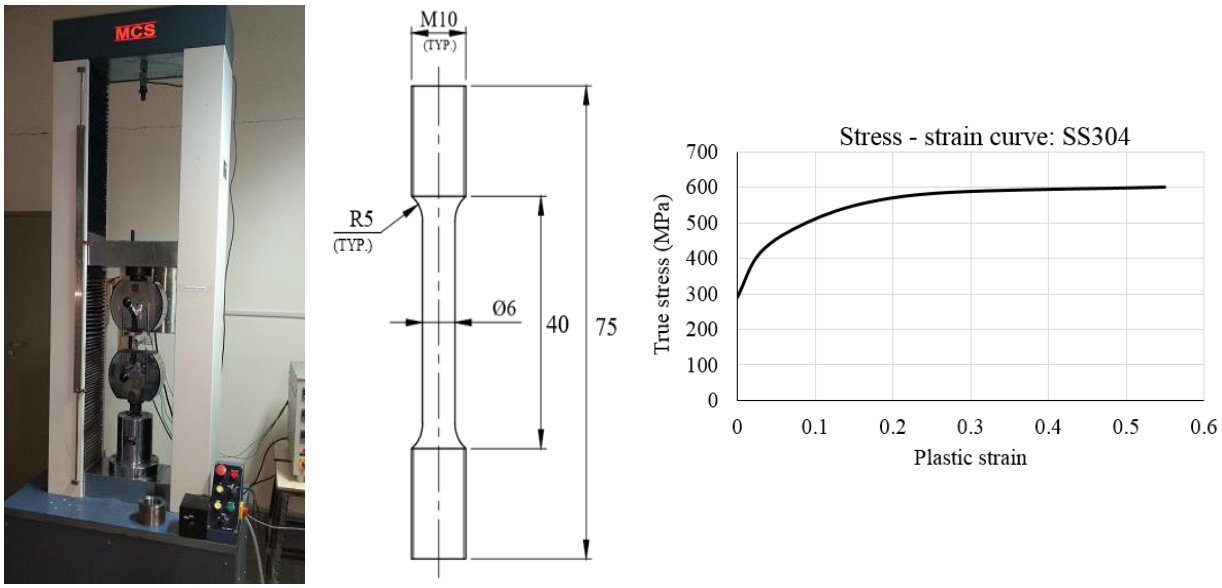


a) Tensile test setup b) Test specimen c) Stress-strain curve

Figure 6.3. Tensile test setup, tensile specimen and stress-strain curve of stainless steel SS304 (all dimensions in mm)

## 6.4 Development of Tube Geometries for Tube Inversion

### 6.4.1 Methodology

In the present research, FEA is chosen to develop the tube geometries as it helps in deeper understanding of plastic deformation phenomena and formation of natural knuckle radius in the process of inversion. Tube geometries are arrived based on detailed FEA and are validated experimentally to ascertain their accuracies. The inversion phenomenon are studied numerically and experimentally on tube geometries with different $t/R$ ratios 0.1, 0.06, 0.04 and 0.01. These ratios are selected based on the existing literature. Values of initial knuckle radii have been calculated based on the empirical formula given in Eq. (6.2). Axial length of all these tubes is maintained at 90 mm.

### 6.4.2 FEA and Experimental setups

A schematic layout of FEA along with the quasi-static experimental setup is shown in Figure 6.4 for a typical invertube.

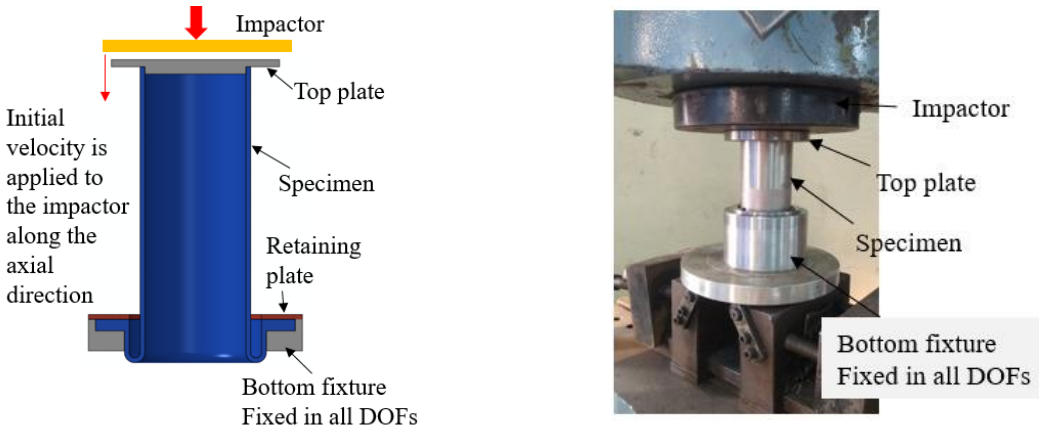


a) FEA setup b) Experimental setup

Figure 6.4. FE analysis and experimental setups

#### 6.4.2.1 FE model setup

A 2D axisymmetric FEA formulation is followed here to save the computational effort as the geometry and loading are rotationally symmetric. This method also gives the opportunity to use finer element sizes which helps in precisely capturing the plastic deformation effects. The cross section of the tube is idealized using first order 4-node axi-symmetric 2D elements

(CAX4) using the FE modeling tool Altair/HyperMesh [115]. After studying the mesh sensitivity with various element sizes, an average element edge length of 0.1 mm is adopted for capturing the finer details of plastic deformation during the inversion process. The bottom fixture has been modeled as a rigid body surface using *analytical surface* option in ABAQUS [116]. The reference node of bottom fixture is completely fixed in all degrees of freedom. The bottom surface of the flange portion of the test specimen is fixed to the top surface of the bottom fixture using *tie* option [116]. A guide plate is placed on top of the test specimen as an intermediate structure to transfer the loading. An impactor which is represented as a rigid body is placed on top of the intermediate structure at a distance of 1 mm. Contact surfaces are defined between all the parts at their respective interfaces to capture all possible contact scenarios. Impactor body is allowed free in the axial direction of the tube and constrained in all other degrees of freedom. ABAQUS/Explicit 2017 [116] solver is used as the solver for the entire numerical simulation. FEA setup is shown in Figure 6.4(a). Enforced velocity boundary condition of 5 mm/s is applied to the impactor body in the axial direction towards the test specimen to simulate quasi static compressive loading.

#### 6.4.2.2 Experimental set up

The tube specimen for inversion is manufactured by machining the tube profile out of an SS304 rod. This is accomplished by turning on a CNC lathe. A thick flange is provided at the bottom of the tube for fastening the tube to the bottom fixture using four numbers of M6 screws. An intermediate support plate is placed on top of the specimen for transferring the load. By introducing this intermediate top plate member, i.e. a stepped collar that fits snugly inside the top cylindrical portion of tube and by selection of tube dimensions it is ensured that the tube doesn't buckle at the top cylindrical portion and the deformation happens only at the preformed trigger at the bottom.

Test setup is shown in Figure 6.4(b). The specimen assembly is placed on the support platform in the universal testing machine (UTM). The test setup used for this experiment is an UTM with a compression load capacity of 650 kN with a maximum loading rate of 50 mm/min. An axial compressive load is applied on the specimen through the intermediate top plate member at a quasi-static loading rate of 5 mm/min. UTM's integrated computer gives a real-time display of crush force against the axial crush displacement.

## 6.5 Progressive Evolution of Tube Geometries for Tube Inversion

Tube geometries ideal for the tube inversion are evolved progressively through numerical and experimental investigations on different successive variants of invertubes. The process of evolution of tube geometries for tube inversion is discussed in this section.

### 6.5.1 Variant-1

This development started with a pre-formed tube of thickness 2.0 mm and initial mean radius of 20.0 mm ($t/R$ = 0.1) and with an initial annular gap of 4.4 mm (initial knuckle radius of 2.2 mm) between initial outer radius and final inner radius of the tube. The cross-section of this pre-formed tube assumed the shape of reversed English alphabet 'J' as shown in Figure 6.5(a). The inversion tube machined with these dimensions is shown in Figure 6.5(b).The value of initial knuckle radius is calculated based on Eq. 6.2). The tube geometry for this Variant-1 is finalized after calculating the buckling force from Wierzbicki *et al* [117] and inversion force from Guist *et al* [103]. These analytical calculations ensured that the buckling force is much higher than the inversion force.

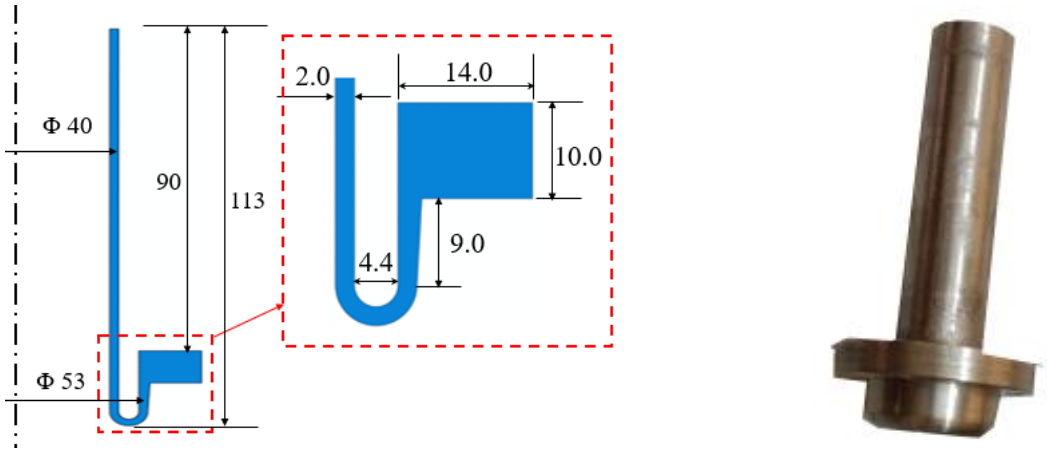


a) Cross section profile b) Test specimen

Figure 6.5. Inversion tube geometry and test specimen of Variant -1 (dimensions in mm)

The buckling load for cylindrical tube as given by Wierzbicki *et al* [117] is expressed as

$$F_{mean} = 7.935\ \sigma_p D^{0.5} t^{1.5} \quad (6.11)$$

where $D$ and $t$ are diameter and thickness of tube and $\sigma_p$ is the flow stress of the material. Substituting the appropriate values of tube geometry for Variant-1 in Eq. (6.11) results in 62.5 kN as circular tube's buckling resistance. Average inversion force of this variant is

about 34.9 kN as predicted from Eq. (6.1) given by Guist *et al* [103]. Thus it is ensured that the buckling mode of deformation is eliminated as the buckling resistance is much higher than the inversion force.

Various stages of deformation during inversion process as predicted from FEA simulations are shown in Figure 6.6(a). It may be understood that after the preformed semicircular shape (initial knuckle region) completes its inversion, the immediate following segment of the tube tries to find its equilibrium position between its initial (inner diameter) and final (outer diameter) configurations and doesn't follow the path shown by initial knuckle radius. As the inversion travel reaches around 5 mm, plastic strains (equivalent plastic strain, PEEQ in ABAQUS [116]) cross the material's limit of elongation and the preformed groove region tends to lose its circularity and radius of curvature signifying the deviation in deformation path from its ideal path as shown in Figure 6.6(a) as a dashed (grey) line. The inversion process continues as the damage criterion of SS304 is not modelled in FEA simulations.

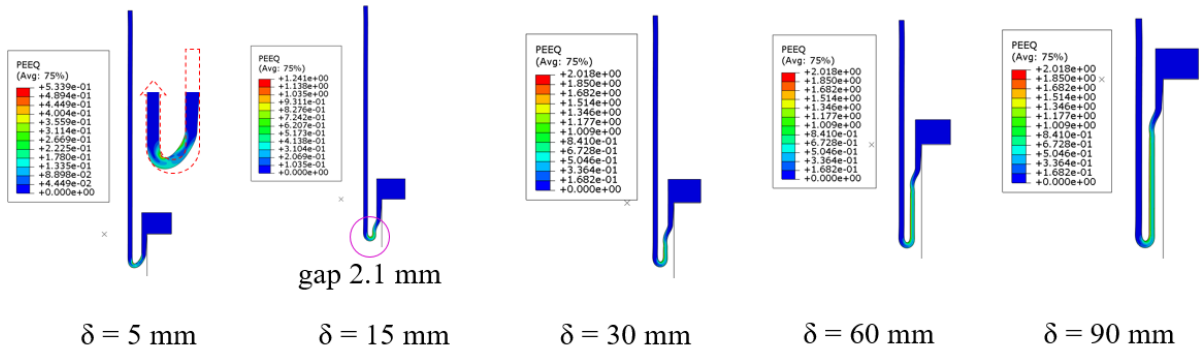


(a) Progress of inversion deformation predicted from FEA simulation

(b) Deformed test specimen

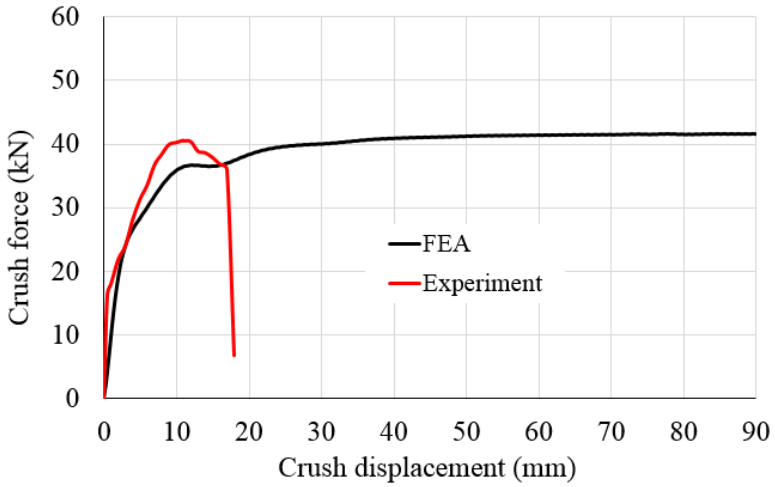


(c) Crush force versus axial displacement

Figure 6.6. Inversion deformation of Variant – 1: a) FEA, b) Experiment, and c) Crush force-axial displacement

Knuckle radius continues to close in, following its own path to find an equilibrium position between the inner and the dynamic outer diameter of the invertube. As the inversion travel reaches around 15 mm, the gap between inner and outer segments of the invertube drops down to 2.1 mm and it reaches a stage where the plastic folding of the invertube is no longer practically possible as the available radius is inadequate. In this configuration, the load shifts to the immediate segment of the cross section towards the recently deformed side (flange side) forcing it to stretch in the axial direction as the axial stretch is the only permissible kinematic configuration to resist the continuing load. This gap of 2.1 mm (knuckle radius of 1.05 mm) is below the minimum bending diameter of steel sheets as per the standard [113] which suggests that the minimum bending radius should be more than approximately 1.5 times the sheet thickness for comfortable bending, which in this case is less than half of the sheet thickness. However in FEA, the inversion continues to happen until the entire crush stroke is completed though at the cost of excessively high and unrealistic plastic strains exceeding its failure limit. Observations from FEA may be considered insignificant beyond this point. Crush force is recorded as the reaction force at the bottom fixture in the axial direction.

The tube specimen for inversion is machined from SS304 rod of diameter 90 mm. Preformed shape of induced knuckle radius is carefully machined by maintaining an annular gap of 4.4 mm. In crush experiment conducted as per the test setup shown in Figure 6.4(b), the specimen exhibited a uniform crushing force up to a stroke of 12 mm. The crush force goes through a steep fall due to a crack in the specimen owing to closing of the knuckle radius as

the inversion happens. Failed specimen is shown in Figure 6.6(b). A comparison of crush force versus crush displacement curves between FEA and the experiment is shown in Figure 6.6(c). It may be observed that curves from FEA and experiment exhibit a good correlation up to an inversion travel of 15 mm and the experimental curve drops suddenly due to failure by cracking. This is due to increase in plastic strain in knuckle radius region due to closing-in effect of the progressive knuckle radius. It can be concluded from this study on Variant-1 that the assumed combination of $t$, $R$ and $b$ ($t/R$ = 0.1) is not favourable for inversion.

### 6.5.2 Variant - 2

Taking clues from Variant-1, another variant is tried with a small modification to the tube geometry. The $t/R$ ratio is changed to 0.066 with mean diameter of the tube as 60 mm and thickness at 2.0 mm. Clamping support area in flange is slightly changed as shown in Figure 6.7(a) by introducing a fillet at the corner with an idea to add more strength during the axial stretch phase of inversion. The machined invertube specimen of Variant -2 is shown in Figure 6.7(b).

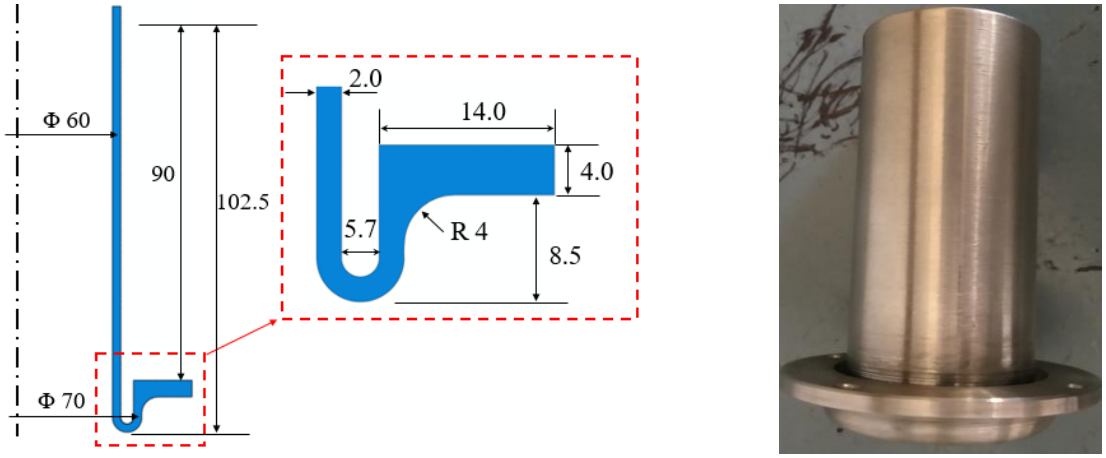


a) Cross section profile b) Test specimen

Figure 6.7. Inversion tube geometry and test specimen of Variant -2 (dimensions in mm)

Numerical simulations using FEA is performed with the same idealization and setup as adopted for Variant-1. The FEA predicted an average inversion force of 55 kN. However, at an inversion travel of 6.0 mm, the tube profile in its initial knuckle region loses its original radius of curvature and tends to form a sharp closing in the shape of a narrow parabola with a gap of 2.3 mm between the inner and the outer diametric segments. Further increments of inversion resulted in a small outward throwing of the profile as a unit instead of small

segments of the tube showing a visible outward bulge in the deformation pattern of the tube. At this stage, the plastic strains cross the limit of elongation making the observations beyond this stage insignificant. However, the FEA predicted a steady trend of inversion force at around 55 kN. Progress of inversion deformation of Variant -2 predicted from FEA is shown in Figure 6.8(a).

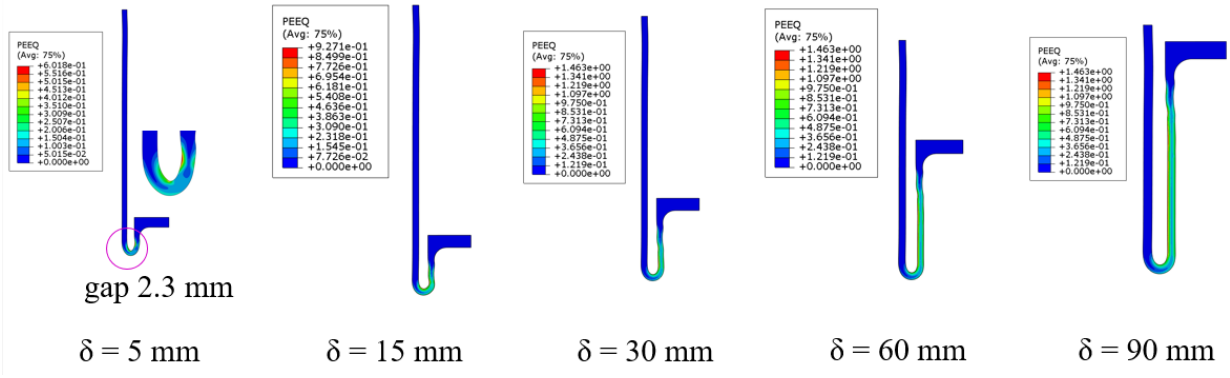


(a) Progress of inversion deformation predicted from FEA simulation

(b) Deformed test specimen

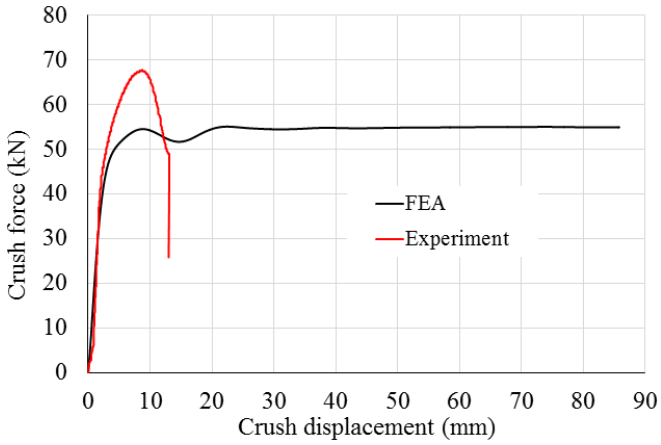


(c) Crush force versus axial displacement

Figure 6.8. Inversion deformation of Variant – 2: a) FEA, b) Experiment, and c) Crush force-axial displacement

Even in Variant-2, a crack is observed after an initial inversion travel of 12 mm. Failed specimen is shown in Figure 6.8(b). A comparison of crush force curves between FEA and the experiment is shown in Figure 6.8(c). Though the graphs are showing different trends, it may be observed that both of them depict good correlation up to an inversion travel of about 5 mm, where the plastic strain in FEA crosses the limit of elongation. Beyond this point, sharp closing-in and outward bulging of the profile in the experiment showed a different trend as the curve showed a steep rise till the stroke of 8 mm followed by a drastic fall. The closing-in phenomenon seems to have a slightly different effect on the axial force behavior. But this deviation was observed only for a small stroke of 2 mm which strongly complements the observations from FEA. The failure of Variant-2 in experiment proved that the assumed *t*/*R* ratio is ineffective for a proper tube inversion.

### 6.5.3 Variant - 3

Variant -2 is further modified by changing the depth of annular space between initial and final radius positions (knuckle radius) with an objective to give more initial length for a better start and stability of inversion. The *t*/*R* ratio also is changed to 0.04 with a mean diameter of 70 mm and thickness of 1.4 mm. An initial knuckle radius of 8.4 mm is used in this variant. A chamfer of 2x2 mm is added at the base of clamping block to add more strength as shown in Figure 6.9(a). The fabricated tube specimen of Variant -3 is shown in Figure 6.9(b).

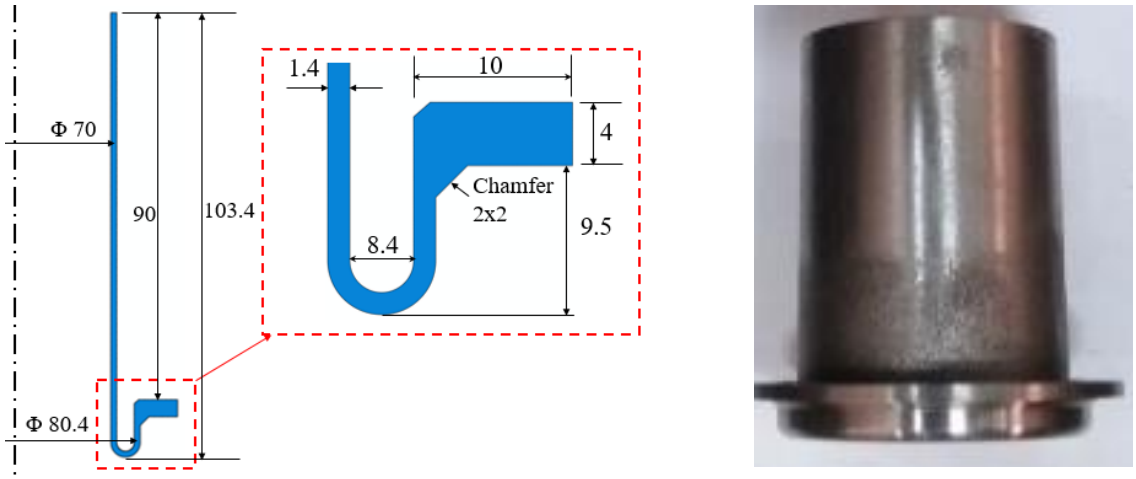


a) Cross section profile b) Test specimen

Figure 6.9. Inversion tube geometry and test specimen of Variant -3 (dimensions in mm)

The FEA of this variant predicted an average inversion force of 38 kN. Even for this *t*/*R* ratio, there is no considerable difference in the decreasing tendency of the knuckle radius during

the inversion process as it closed in with a gap of 3.4 mm. Plastic strains are observed to cross the limit of elongation after an inversion travel of 15 mm. Small outward bulges are observed in this variant as well due to change in radius of curvature of knuckle radius region in the initial stages. Progress of inversion deformation is shown in Figure 6.10(a). Experiment was conducted on Variant-3 as per the experimental setup shown in Figure 6.4(b). In Variant-3 also, a crack is observed after an initial travel of 34 mm. The inversion progressed for a distance of 34 mm in contrast to the earlier two variants. Failed specimen is shown in Figure 6.10(b). The deformation pattern was observed to be different from the first two variants with a bigger outward bulge of the tube profile during the initial stages of inversion. Good agreement between FEA and experiment existed only up to a travel of 6 mm and crush force behaviors exhibited a completely different trend.

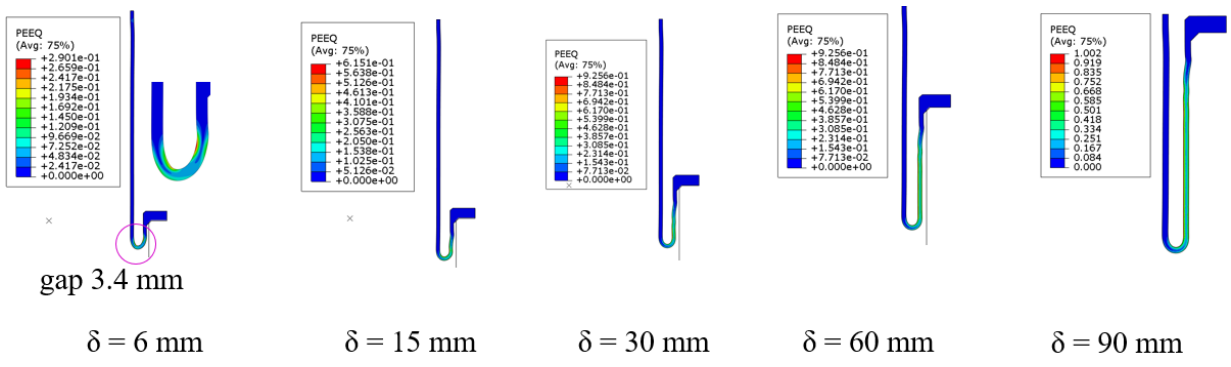


(a) Progress of inversion deformation predicted from FEA simulation

(b) Deformed test specimen

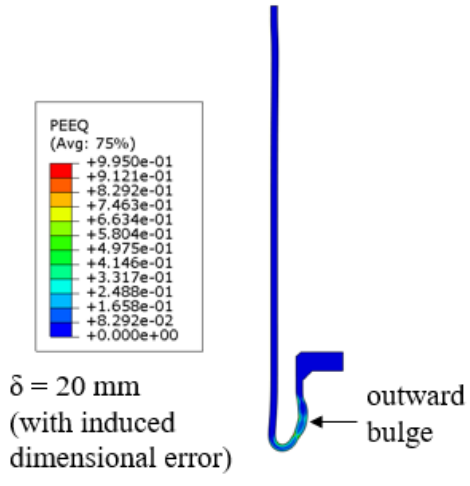


(c) Deformation of specimen with induced dimensional error at 20 mm of inversion from FEA

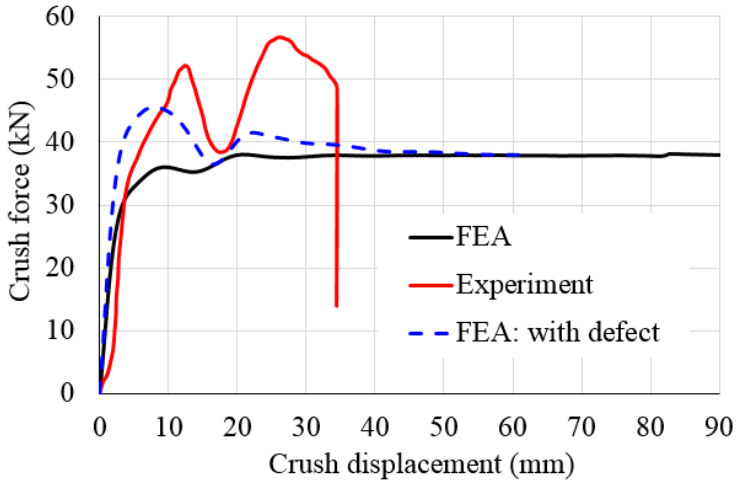


(d) Crush force versus axial displacement

Figure 6.10. Inversion deformation of Variant – 3: a) FEA, b) experiment, c) deformation pattern from FEA with induced dimensional inaccuracy, and d) crush force-axial displacement

The FEA prediction is similar to that of Variant-2, but the experimental trend showed an extension to that of Variant-2. But the effect of outward bulging was a little more severe in this variant. To further study this effect of outward bulging, FEA is repeated by inducing a small dimensional inaccuracy in the groove region simulating a little deviation from the original radius of curvature in the groove region. Updated FEA with this induced defect showed a deformation trend similar to that of the experiment as observed in the Figure 6.10(c), but the magnitude of inversion forces are still offset. A comparison of crush behaviors between FEA and experiment is shown in Figure 6.10(d). From FEA, it is understood that the bottom groove did not follow the intended circular path for straightening during inversion. The groove tried to move outward as a unit due to slight ovality in the contour resulting in an outward bulge. This observation further stresses on the importance of dimensional accuracy of the initial triggers for inversion. However, irrespective of these dimensional inaccuracies, this combination of $t/R$ ratio and initial knuckle radius proved to be unfavourable for inversion from both FEA and experimental perspectives.

### 6.5.4 Variant - 4

Based on observations from the earlier three variants with respect to the effect of initial knuckle radius in the preformed geometry, it may be understood that the tube geometric parameters have little effect on the decreasing tendency of knuckle radius which is a natural deformation phenomenon and yet a vital factor for tube inversion. In Variant-4, the cross

section of the tube is simplified in the shape of English alphabet ‘L’ instead of a reversed ‘J’ in previous variants, as shown in Figure 6.11 (a). This change is introduced with a view that an ‘L’ configuration offers more freedom for the tube profile to attain its own radius than following an enforced path. After a series of iterations in FEA, the profile for this new configuration is finalized with tube thickness of 1.3 mm and initial mean radius of 28.5 mm with $t/R$ ratio of 0.04. Smaller $t/R$ ratio is maintained here due to an observation that the thicker sections face difficulty in continuing with the inversion after the initial stages due to involvement of higher inversion forces and the natural knuckle radius at the stabilized state not being adequate for free bending. At the base of the ‘L’ section, a fillet radius of 5.5 mm is introduced for initiation of a smoother inversion process. The fabricated tube specimen of Variant-4 is shown in Figure 6.11(b). In this, the concept of initial knuckle radius doesn’t come into picture in the initial stages as the profile is left free to attain its own natural knuckle radius after the deformation pattern settles down and the gap between the original radius and the final radius converges to a constant value.

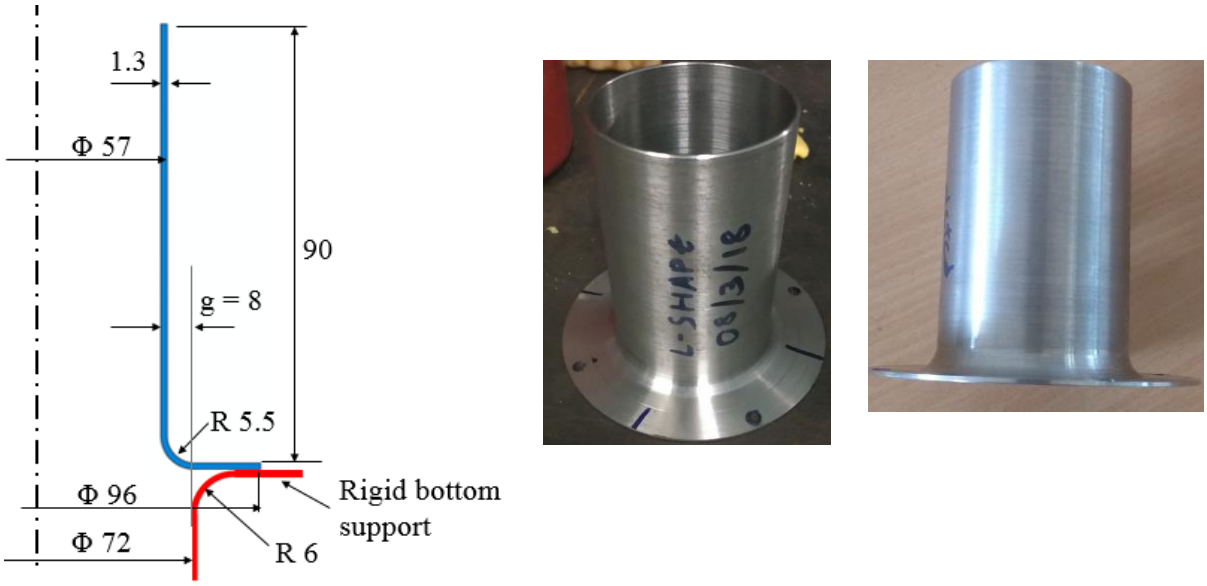


a) Cross section profile b) Test specimen

Figure 6.11. Inversion tube geometry and test specimen of Variant - 4 (dimensions in mm)

Instead of the induced knuckle radius, a simple new parameter ‘g’ is introduced as the gap between the initial mean radius $R$ of the tube and inner radius of the bottom fixture as shown in Figure 6.11(a) which guides the initial deformation vector for inversion. From the preliminary FEA simulations on this variant, this parameter ‘g’ is observed to have some influence on the path of deformation process in the early stages of inversion which eventually

controls the final gap between initial and inversed radii of the tube. In this variant, this gap 'g' is maintained at 8 mm (seen in Figure 6.11(a)). If this gap is smaller than the threshold value required for tube inversion, bending deformation process becomes difficult as observed in the earlier versions. FEA of the finalized version predicted an average inversion force of 30 kN with a stabilized bend radius (natural knuckle radius) of 1.65 mm (annular gap of 3.3 mm), which is still less than 1.5 times the sheet thickness for free bending [113]. However, higher plastic strains were observed in the later stages of inversion process making the FEA observations beyond 25 mm of inversion travel insignificant. Progress of deformation predicted by FEA is shown in Figure 6.12(a).

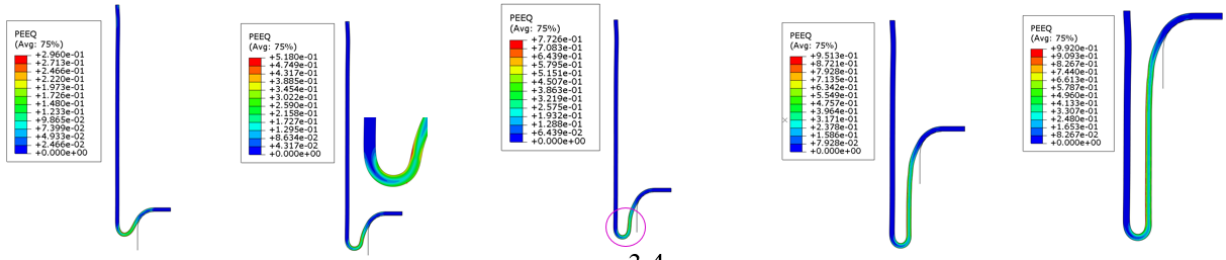


(a) Progress of inversion deformation predicted from FEA simulation

(b) Deformed test specimen


(c) Deformation predicted by FEA (at 34 mm of inversion) with an induced dimensional error

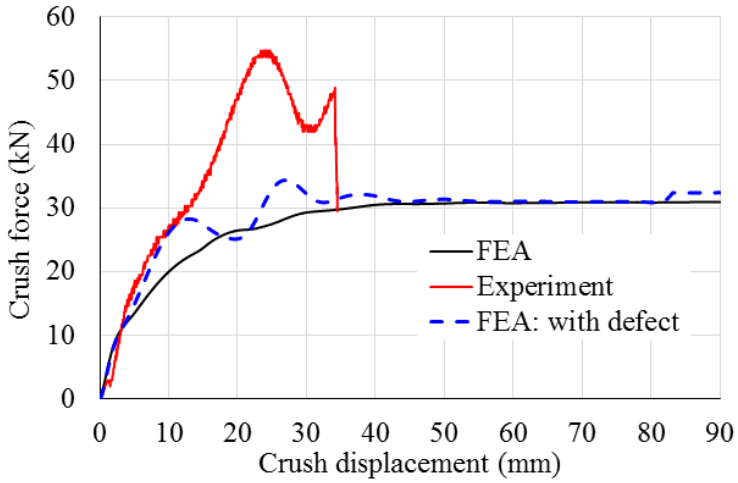


(d) Crush force versus axial displacement

Figure 6.12. Inversion deformation of Variant – 4: a) FEA, b) experiment, c) deformation pattern from FEA with induced dimensional inaccuracy, and d) crush force-axial displacement

The finalized dimension of tube profile is machined out of SS304 rod of 100 mm diameter and experimented as per experimental set up shown in Figure 6.4(b) in order to understand the deformation behavior of new geometry and to get some clues for ideal plastic deformation. The initiation of inversion process is observed to be smooth in comparison to the previous variants. The path of inversion bending pattern appeared to be in agreement with that of FEA simulations. After a steady inversion for about 10 mm, the tube profile is observed to have developed an outward bulge similar to that of Variant-3. This folding altered the path of bending process forcing the start of a new inversion process and eventually closing the gap between inner and inversed radii leading to the similar failure pattern by cracking due to localized axial stretch as observed in the earlier variants. Failed specimen is shown in Figure 6.12(b).

After a detailed study on observations from FEA and experiment, it is understood that the transition between the base fillet arc (5.5 mm radius) and the straight portion of the tube profile during the bending process is disturbing the progress of inversion process. This factor appeared to be more dominant as the FEA also predicted a sudden rise in plastic strains at the end of bending of fillet arc and at the beginning of straight portion of the tube profile. This is observed to be due to the sudden change in curvature of profile that forces the bending pattern to quickly find a new path enforcing the start of a secondary inversion pattern. Similar observation was also found in the earlier variants, but it is more pronounced here without the influence of a preformed knuckle radius. In this variant also, dimensional inaccuracies in machining were suspected to be a contributing factor for the outward bulging effect of the cross section. To confirm this, another round of FEA is conducted by assuming some deviations in the curvature in the fillet radius at the base of L-section. Deformation pattern predicted by FEA with the inaccurate profile is shown in Figure 6.12(c). A comparison of crush force versus crush displacement between FEA and experiment is shown in Figure 6.12(d). FEA with the assumption of dimensional error correlates well with experiment up to a stroke of around 12 mm while the FEA with ideal dimensions agreed well with the experiment only up to a stroke of 6 mm. Though the investigations on this Variant-4 also failed, they provided some crucial clues on the importance of tube profile for achieving an ideal tube inversion.

### 6.5.5 Variant - 5

#### 6.5.5.1 Preliminary profiles of tube geometry

The Variant -5 is developed after taking vital clues from Variant-4, and is focused principally on the transition between the fillet radius and straight portion of the tube profile. As this sudden change of curvature is imposing secondary inversion process with high plastic strains, a new profile is proposed. Initially, a profile with a continuous arc from the base of ‘L’ till the top end of the tube is planned. To achieve this, a quarter section of an ellipse with the total length of the tube as the semi-major axis and width of the profile as the semi-minor axis is tried in the preliminary studies for this variant as shown in Figure 6.13(a). FEA on this profile predicted an improved performance in terms of deformation pattern with the knuckle radius conducive for tube inversion. This is due to the changed profile which increases the distance between the undeformed and the deformed portions of the profile as the inversion progresses and also due to continuity in curvature of the tube profile. As a result, bending of tube profile

becomes easier with the increasing gap aiding the inversion process. However, plastic strains cross the limit of elongation at an inversion travel of around 45-48 mm and a steep rise is observed thereafter. This is still a major improvement in active crush stroke in comparison to the earlier variants. As the second alternative, tube profile based on the parabolic curve is tried with the open end towards the top with different focal widths and heights of parabola as shown in Figure 6.13(b). Parabolic profiles also depicted the deformation pattern similar to that of ellipse.

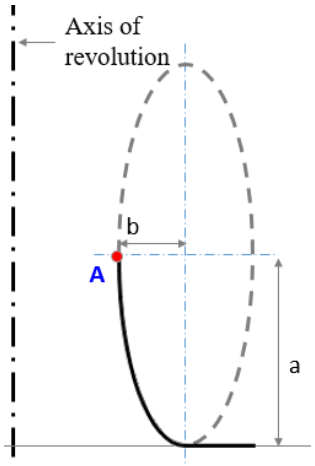


a) Profile construction - Ellipse

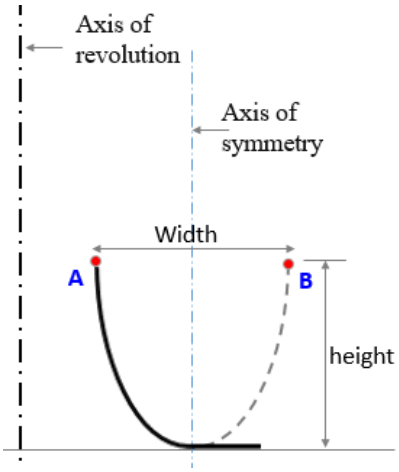


b) Profile construction – Parabola

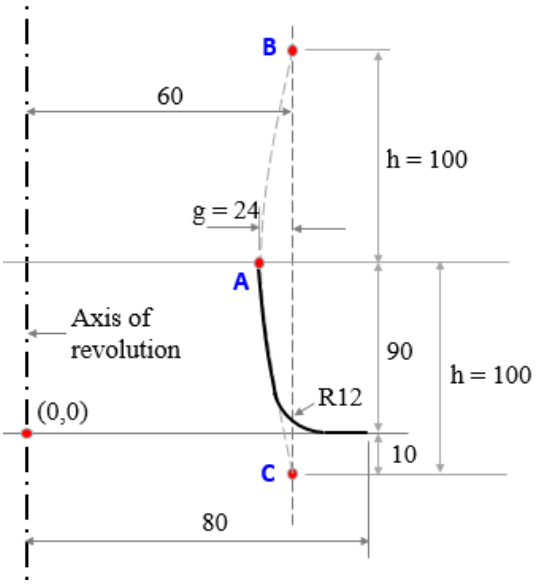


c) Profile construction

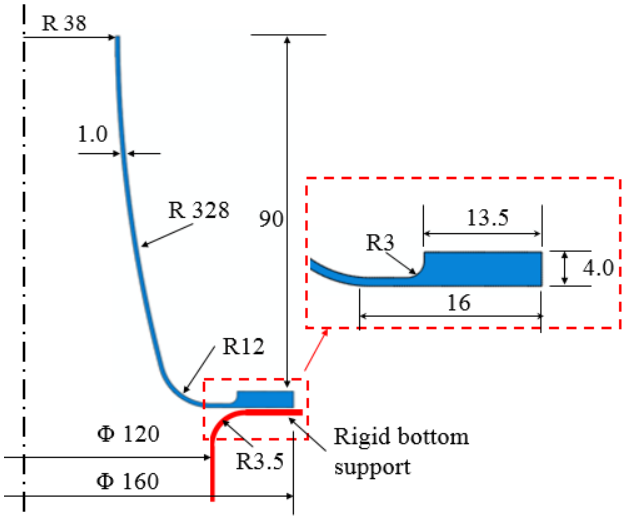


d) Cross section profile

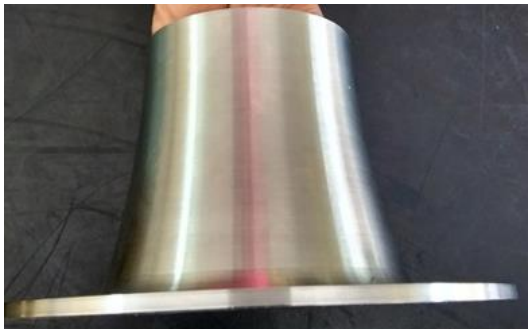

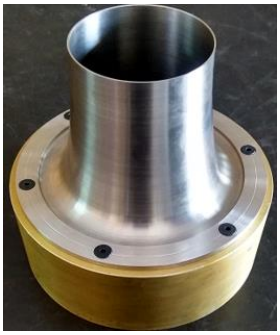

e) Test specimen

Figure 6.13. Inversion tube geometry and test specimen of Variant - 5 (dimensions in mm)

6.5.5.2 Final profile of tube geometry

In the next attempt, another profile with a simple circular arc with a very large radius is tried. This arc is drawn using the 3-point method with point A at the top end of the specimen (90 mm mark of the total axial length of the specimen from the bottom datum line). The other two points B and C are placed symmetrically above and below point A by varying the parameters ‘g’ and ‘h’ along the horizontal and vertical directions respectively. Construction of this arc is shown in Figure 6.13(c). After a series of iterations by varying the parameters ‘g’ and ‘h’, the arc has been constructed with ‘g’ as 24 mm and ‘h’ as 100 mm. A fillet arc of radius 12 mm is introduced between the base horizontal line and the 3-point arc for a smoother initiation of inversion process. The thickness of the tube profile is changed to 1.0 mm. A strip of 13.5 mm at the outer end of the profile has been thickened to 4.0 mm for fastening the specimen to the bottom fixture. Finalized profile of Variant-5 is shown in Figure 6.13(d).

6.5.5.3 FEA simulations

FEA simulation on this profile predicted an ideal inversion pattern without any secondary inversions due to change of deformation path and no closing-in effects of knuckle radius. Resulting plastic strains were under the material’s failure limits. Progress of inversion of this profile is shown in Figure 6.14(a). The inversion process progressed steadily without any locking as the total profile is almost a single arc. No secondary inversions are observed as the profile is a continuous arc without transition between arc and line segments. No problems are observed due to closing-in effect of knuckle radius because the optimum gap between the profile and the support ensured adequate space for transfer of material between inner and outer radii. In this variant, geometry is arrived carefully to keep the induced plastic strains

within the material's limit of elongation at break. As a result $t/R$ is reduced to 0.01 with thickness coming down to 1.0 mm, but the tube profile ensured a certain inversion and free from failures due to problems associated with the earlier variants.

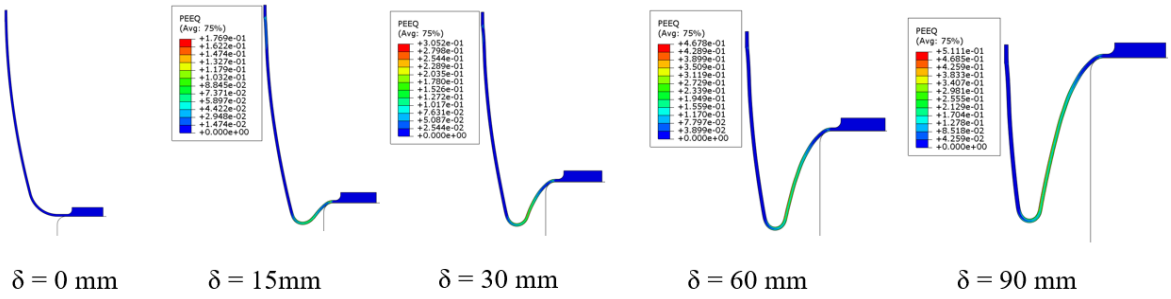

δ = 0 mm  δ = 15mm  δ = 30 mm  δ = 60 mm  δ = 90 mm

(a) Progress of inversion deformation predicted from FEA simulation

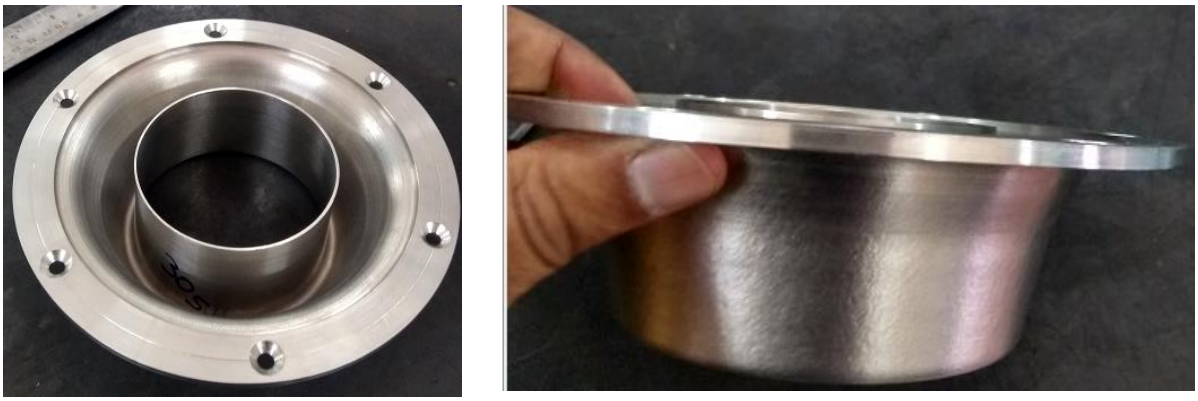

(b) Deformed test specimen

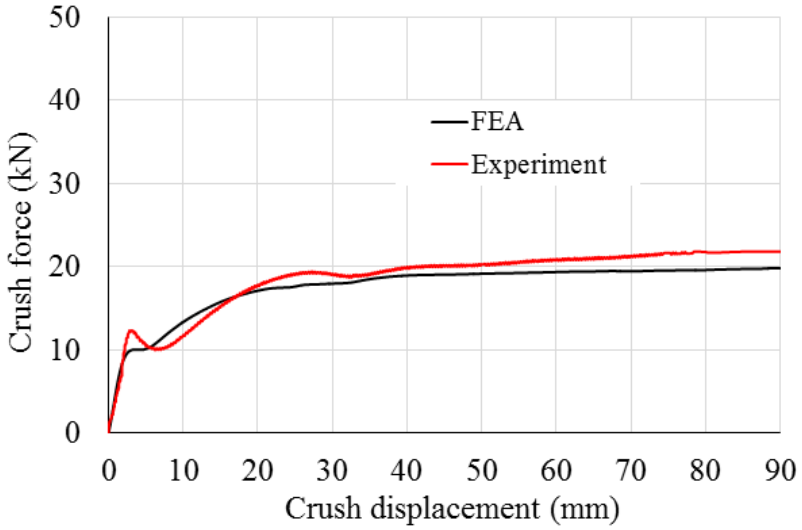


(c) Crush force-axial displacement

Figure 6.14. Inversion deformation of Variant – 5: a) FEA, b) experiment, and c) crush force-axial displacement

#### 6.5.5.4 Fabrication and experiment

Fabrication of this specimen was a challenging task from many perspectives. It is machined out of an SS304 rod of 160 mm diameter. The machining was performed on a CNC lathe as the profile is not linear and the inversion deformation was also suspected to be sensitive to dimensional inaccuracies i.e. imperfections. In the first phase, inner profile is machined to final dimensions with a smoother surface finish. In the second phase, as the profile thickness is very small at 1.0 mm, support fixtures made of mild steel and specially prepared for the inner profile were inserted in the inner profile to provide support for machining the outer profile. Outer profile is finished within 0.01mm of profile deviation. The machined profile is shown in Figure 6.13(e). The specimen is bolted to the bottom fixture using six numbers of M6 screws.

The specimen assembly is placed on UTM and crushed under axial compressive load similar to that shown in Figure 6.4(b). The inversion travel and deformation progressed in exact accordance with FEA simulations. Axial crush progressed for the entire stroke of 90 mm without any premature failures. The major factor for this successful inversion is the tube profile with continuous arc which aided continuous single inversion which also avoided the accumulation of high plastic strains. Completely inversed specimen is shown in Figure 6.14(b). A comparison of crush force versus crush displacement between FEA and experiment is shown in Figure 6.14(c). Average inversion force from FEA is about 95% of that obtained from experiment which strongly endorses the accuracy of the FEA approach. A comparison between FEA and experiment on the total energy absorbed by Variant-5 is shown in Figure 6.15.

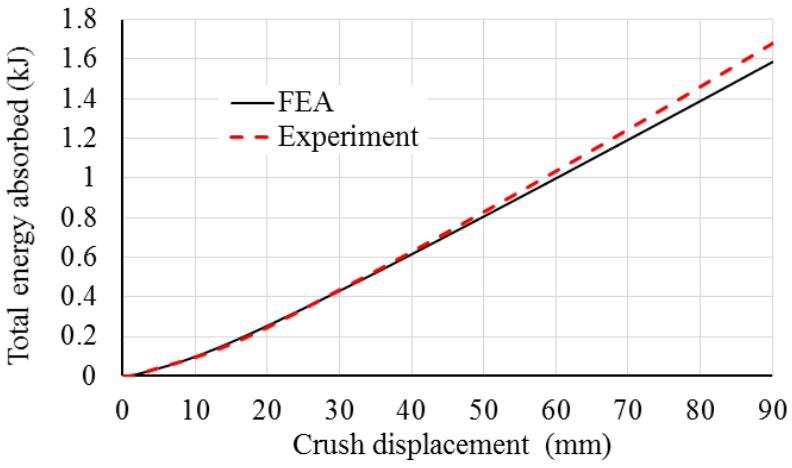

Figure 6.15. Comparison of energy absorption of Variant – 5: FEA and experiment

Successful inversion of tubes using a reasonably high strength material may be considered in designing EA structures to achieve ideal crashworthiness in terms of major parameters such as stroke efficiency and crush force efficiency. Though the final measure of specific energy absorption is a little low in comparison to standard geometries from the previous literatures [39, 86, 92, 101], this research offers a lot of clues to improve the overall crashworthiness. But this approach can be upgraded further to improve the SEA factor. Table 6.1 provides a comparative summary of assessment of crashworthiness between FEA and experimental methods for Variant-5 based on the standard parameters.

Table 6.1: Crashworthiness of Variant-5 invertube: Comparison between FEA and experiment

| Configuration | Mass (kg) | Peak force (kN) | Mean force (kN) | TEA (kJ) | Crush stroke (mm) | CFE (%) | SE (%) | SEA (kJ/kg) |
|---|---|---|---|---|---|---|---|---|
| FEA | 0.16 | 17.0 | 17.9 | 1.6 | 90 | 105 | 100 | 10.0 |
| Experiment | 0.16 | 17.0 | 18.8 | 1.7 | 90 | 110 | 100 | 10.6 |
| % deviation w.r.t experiment | 0 | 0 | 4.8 | 5.8 | 0 | 4.5 | 0 | 6.0 |

## 6.6 Observations, Results and Discussions

Comparison of crush force versus crush displacement of all the five variants is shown in Figure 6.16. In the present study, stainless steel SS304 material having reasonably high strength and good ductility is used in order to maximize the benefits of tube inversion phenomenon in the energy absorption process. Numerical and experimental studies are conducted on circular tube geometries with the preformed trigger of inversed 'J' shape with different $t/R$ ratios (0.1, 0.06 and 0.04). Numerical simulations using FEA predicted a similar deformation trend on the first three variants with a steep rise in plastic strains at the onset of secondary inversion which is driven by the *closing-in* effect of knuckle radius as the tube profile attempted to find an equilibrium position between inner and outer radii. Further, the quasi-static experiments complemented the FEA predictions with cracking failure due to severe localization of strains as the deformed segment of the profile started moving towards the main cylindrical portion in pursuit of finding an equilibrium position thereby decreasing

the knuckle radius. At this stage, plastic bending between inner and outer radii became impossible causing localized axial stretch in the recent deformed segment leading to failure by cracking.

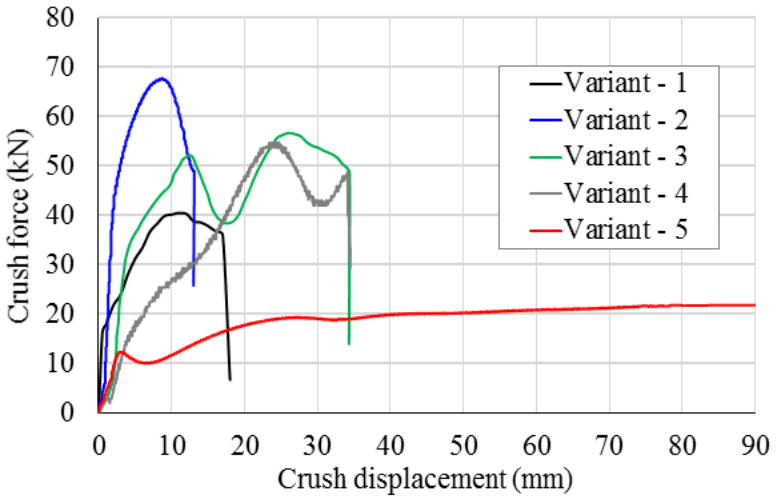


Figure 6.16. Experimental crush force-displacement curves of all five variants

The fourth variant with an 'L' shaped profile without any initial knuckle radius offered more freedom for the profile to find its own natural knuckle radius that suits its combination of *t* and *R* values. Though this variant also failed to achieve the inversion up to the entire length, there was an improvement in the crush stroke up to 34 mm. It failed while trying to find continuity of inversion during the transition between the fillet arc and the straight cylindrical segment. This observation contributed significantly in finding a suitable geometric profile for inversion.

The fifth variant with a continuous arc as the tube profile was successful in achieving the inversion for the entire length of the specimen. This further reinforces the fundamental requirement for a carefully engineered profile for achieving the inversion and it is free from anomaly of gaps existing between theoretical and practical values of knuckle radius which was a major obstacle in the inversion process. An optimum combination of tube profile in tune with the material behavior is the key to achieve a successful inversion of tubes and there is no single profile that suits all materials. Based on FEA results from all the variants, it is observed that the changes to the tube thickness are insignificant and their effects are also negligible. According to the observations from previous research [107], tube inversion involving metals such as SS304 with low $E_p/\sigma_o$ values necessitates the need for very low initial knuckle radii which are not practical from the manufacturing perspective. Adopting the

appropriate numerical simulations with FEA in the early stages of design opens the door for high strength materials for use in the inversion process thereby contributing to improvements in the specific energy absorption factor.

## 6.7 Summary

This chapter brought out some observations related to knowledge gaps between theory and experiments with respect to inversion of tubes through numerical and experimental investigations. These observations are summarized as follows:

1. Initial knuckle radius which is an inherent feature in the pre-formed tube geometry is of theoretical importance. It is observed that it is not having a direct influence on the inversion force as it cannot be retained throughout the inversion process. However, it has influence on the pattern of plastic deformation which is a decisive factor in the inversion process.
2. Natural knuckle radius which evolves during the inversion process prevails over the initial knuckle radius is of practical importance. The pattern of inversion deformation is a result of combination of geometric and material parameters.
3. 'L' shaped pre-formed tube profiles are more favourable for inversion deformation than those of reversed 'J' shaped profiles as the former ones possess the freedom to achieve the equilibrium value of knuckle radius naturally in a progressive manner. Tube profile with a single continuous arc doesn't impose secondary inversion in the deformation process and is a major enabling factor for achieving the inversion.
4. Axial stretch is a critical aspect of failure during the inversion deformation and it can be addressed only by appropriate tube profiles with proper control on the deformation pattern. Materials with low $E\text{p}/\sigma_0$ ratios are also suitable for inversion with properly engineered tube profiles unlike observations in previous research.
5. FE based numerical methods can be effectively utilized for careful optimization of tube profiles by considering high strength materials and combination of multiple materials for improving SEA factor.

# Chapter 7

# Enhancement in Specific Energy Absorption (SEA) of Invertubes

This chapter proposes invertubes with multi-material structural configurations to achieve higher SEA. Initially, a base monolithic configuration of invertube made of SS304 has been studied numerically and validated by experiment. Subsequently, a few invertube configurations have been proposed over this base configuration by combination of different metals and composites. Relative merits and limitations of each variant (configuration) have been discussed in detail with a specific relevance to enhancement in SEA. This chapter 1) presents an introduction to multi-material designs for energy absorbing structures, 2) explains the validation of FEA procedures for simulation of composite materials, 3) gives a brief overview of invertubes for energy absorption, 4) brings out the options for improving SEA factor, 5) explains the different structural arrangements for enhancing the SEA of invertubes, and 6) finally gives an overall comparative summary of all the configurations.

## 7.1 Introduction

Specific energy absorption (SEA) is an important parameter in assessing the crashworthiness of an energy absorbing (EA) structure. The SEA gained importance in the recent times as it has become an environmental imperative for the transportation industry to look for weight reduction opportunities to improve energy (fuel) efficiency of road vehicles and thereby reduce emissions. Inversion of circular tubes may be considered as an inevitable and a practical choice for EA applications that yield nearly 100 % crush force efficiency (CFE) and stroke efficiency (SE) which are major enablers for effective crashworthiness. The recent work on inversion of circular tubes involving SS304 [118] demonstrated that only a certain combination of optimized tube profile and a material with a good degree of ductility can

achieve a proper inversion of tube; and the inversion mode of deformation results in moderate SEA factors. Due to this atypical mode of deformation which is driven by a specific combination of tube profile and material grade, increasing the grade of material or thickness of tube profile are not straight-forward options to improve the SEA factor of invertubes.

In the recent years, multi-material designs involving metals and composites are increasingly finding applications in the transportation industry because of their superior strength to weight ratio. Carbon/epoxy based cone shaped structure for rear impact attenuation device on a formula race car [119], carbon fiber reinforced polymer (CFRP) based L-strut half-tube crash absorbers as part of the frame work for absorbing crash energy in the fuselage of an aircraft [120], thin-walled square frustum based energy absorbing front module of a special purpose electric vehicle [121] and thermo-plastic composite based main frame structure for mass transit vehicle [122] are some of the case studies that demonstrate the effectiveness of multi-material combinations in EA structures. Taking motivation from the current material trends, a few multi-material structural configurations (variants) that work in combination with the experimentally validated invertube [104] are proposed using numerical studies, in this chapter.

The central objective of the present work is to enhance the SEA factor of tube-inversion based EA structure from the recent work [118] by combining with low density materials such as magnesium and fiber reinforced polymer (FRP) composites. The performance of the proposed multi-material invertube structural configurations is assessed using finite element analyses (FEA). This work is divided into two major parts. In the first part, the adopted FEA methodology for simulation of axial crush of two existing EA structures made of composite materials is validated with experimental results available in Luo *et al* [123] and Kathiresan *et al* [124]. In the second part, the established FEA methodology is used to develop a few multi-material based invertube EA structural configurations keeping the monolithic invertube [118] as the base configuration.

The research work focusses on new invertube configurations for enhancing the SEA parameter. This research is not intended for analyses on sensitivity studies on ply orientations, material characterization of composites, adhesive bonding between plies and delamination effects which are available in many literature [125-128] such as study on the delamination behavior of a hybrid structure made of metallic shell, composite skeleton and metallic foam under an axial crushing [129], study of delamination effects and axial crush force trends of a fiber metal top hat structure for energy absorbing applications [125], high-

fidelity FE modeling for study of damage mechanisms of thermoplastic composites under axial crushing [126], crashworthiness studies on aluminum-CFRP hollow square section beam [127] and study of influence of ply orientations on the axial crushing and energy absorption capabilities of a hybrid aluminum-CFRP circular tube [128].

## 7.2 Validation of FEA Methodologies for Composite EA Structures

FEA of invertubes with monolithic configuration using ductile metals is relatively simpler because material is isotropic and its deformation is elasto-plastic and studied extensively in Reddy *et al* [118]. In the present work, metal and FRP composite materials are proposed for use in invertubes. The FRP composite materials with orthotropic properties when combined with metals having elasto-plastic behavior pose a lot of challenges in building proper FE models and comprehending the results. To establish and validate the FEA methodology in numerically analyzing the proposed multi-material based hybrid EA invertube concepts to be discussed in the second part of this chapter, two axial crushing experiments on composite specimens from the literature: (1) a standard circular composite tube from Luo *et al* [123] and (2) a fiber metal laminate (FML) from Kathiresan *et al* [124] are simulated in present FEA and their results are compared. The FEA approach is tuned to get matching results between FEA simulation and experiments.

### 7.2.1 FEA of FRP composite circular tube – validation with experiment

#### 7.2.1.1 Specimen geometry and experimental setup

An experiment conducted by Luo *et al* [123] for investigating the progressive failure of a standard circular tube made of G803/5224 carbon/epoxy material for EA application is considered for establishing and validating the FEA methodology. The tube is 125 mm long with an internal diameter of 50 mm. The total specimen thickness is 3.0 mm with bi-directional layup of 30 layers with a layer thickness of 0.1 mm. The ply sequence is $[(\pm 45^0)_{15}]$ with the axial direction of the tube as the longitudinal direction ($0^0$). The top end of the tube is featured with a $45^0$ chamfer to control the initial peak crush forces. This specimen is tested on a drop hammer impact test setup with a drop mass of 81.5 kg falling on the specimen with an initial velocity of 10.2 m/s. The test specimens and schematic of

experimental layout is shown in Figure 7.1. Mass of the specimen as per FE model is about 0.098 kg.

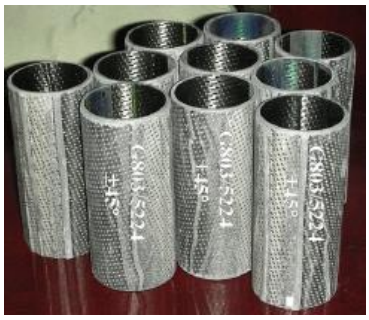


a) FRP composite tubes

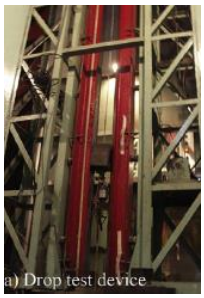


b) Experimental setup

Figure 7.1: FRP composite EA specimens and experimental setup [123]

7.2.1.2 FEA of FRP composite specimens

Single layer shell type of idealization for composite tube is adopted here for simplicity and to save computational time. This is in line with a few previous studies which followed similar approach for axial crushing of tubes [102, 131-133] as they proved to be adequate enough for prediction of axial crush forces. The circular tube is discretized using first order 4-noded S4R type shell elements compatible with explicit dynamic solution methodology in ABAQUS/Explicit [116] with an average element edge length of 1.2 mm. The shell section is defined as a union of 30 layers of plies with layer thickness of 0.1 mm and each layer is defined by the entries of thickness, ply orientation, material and the number of integration points. Each layer is specified with 7 integration points across the thickness. The top trigger with $45^0$ chamfer is approximated with shell elements of different thicknesses over a tube length of 3.0 mm. Six different sets of elements with thickness varying from 0.4 mm to 3.0 mm are modeled as an approximate representation of the top trigger zone as shown in Figure 7.2(a). The orthotropic material of GFRP layer is modeled using linear elastic material behavior until failure with Hashin's [134, 135] criteria for damage initiation and evolution. Material properties of G803/5224 carbon/epoxy considered for the FEA are provided in Table 7.1 [123]. The bottom surface of the tube is fixed to a rigid ground surface and the reference node of this surface is completely fixed in all degrees of freedom. An impactor with a mass of 81.5 kg impacts the top part of the composite tube in the axial direction of the tube and the impactor is restrained in all other degrees of freedom. General contact algorithm is activated to capture all possible contact kinematics and behavior. The reaction forces in the axial

direction at the ground rigid surface are measured as the axial crush forces. FE model setup is shown in Figure 7.2(b).

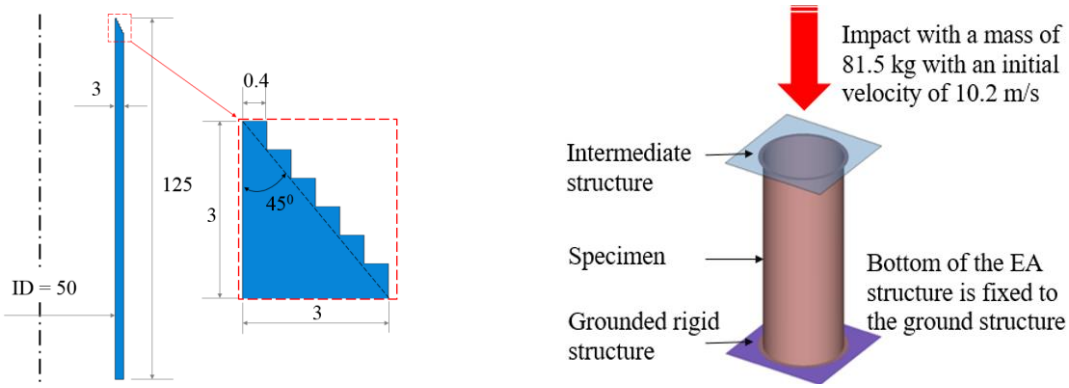


a) FE modeling details b) FEA setup

Figure 7.2: FE modeling details and analysis setup

Table 7.1. Material properties of G803/5224 carbon/epoxy material [123]

| Property | Description | Value |
|---|---|---|
| Density (kg/m$^3$) | ρ | 1560 |
| Modulus (GPa) | $E_1$ | 65.10 |
| | $E_2 = E_3$ | 64.40 |
| | $G_{12}$ | 4.5 |
| | $G_{13} = G_{23}$ | 4.5 |
| Strength (MPa) | $X_T$ | 573 |
| | $X_C$ | 693 |
| | $Y_T$ | 573 |
| | $Y_C$ | 693 |
| | $S_{12}$ | 94.1 |
| Poisson's ratio | $\upsilon_{21}$ | 0.056 |

7.2.1.3 Assessment of crash performance of FRP composite tube

The crushing deformation process of the FRP composite tube starts with a high initial peak force of 122 kN to induce deformation in the tube. As the crush travel a progresses, the crush force drops down drastically to 24 kN as the initial segment of deformation is completed. As the crushing progresses, cracking due to circumferential stretch is observed as stresses in the radial directions cross the material's failure limits which are defined by damage criterion of the FRP composite material. This deformation pattern proceeds along the length of the tube and forms fronds in the radially outward direction. Progressive crushing of the tube continues towards the bottom of the tube as the crush travel progresses. The crush force continues to

sway between 24 kN and 65 kN levels until a crush stroke of 45 mm. Afterwards, as the deformation pattern is stabilized, fluctuations in the crush force also subside and settle around a magnitude of 45 kN. Comparison of deformation patterns, crush force versus crush displacement and total energy absorbed (TEA) versus crush displacement of FRP composite tube as predicted from present FEA simulation and observed in experiment [123] are shown in Figure 7.3. Mean crush forces from the experiment and FEA are observed to be 51.7 kN and 44.8 kN respectively, while the area under the crush force versus crush displacement curves (TEA) from the experiment and FEA for a crush stroke of 85 mm sum up to 4.4 kJ and 3.8 kJ respectively. The present FEA simulation correlates with the experimental results with a difference of 13.3% for mean crush force and 13.6% for TEA respectively. It may be noted here that the FEA simulation over predicted the initial peak crush force and under predicted the crush forces after the initial peak. The crush force behavior in general was also fluctuating with a wide range about a mean value. This may due to the approximate idealization of material with a single shell layer without accounting for the delamination effects. Detailed comparison of experimental and present FEA results on the fundamental crashworthiness parameters is given in Table 7.2.

Table 7.2. Comparison of axial crash performance parameters between experiment [123] and present FEA of FRP composite tube

| FRP specimen | $F_{max}$ (kN) | $F_{mean}$ (kN) | TEA (kJ) | CFE (%) | SE (%) | SEA (kJ/kg) |
|---|---|---|---|---|---|---|
| Experiment [123] | 109 | 51.7 | 4.4 | 47.43 | 68.00 | 45.36 |
| Present FEA | 122 | 44.8 | 3.81 | 36.72 | 72.00 | 39.27 |
| % Difference in FEA *w.r.t.* Experiment [6] | 11.9 | 13.3 | 13.6 | 22.58 | 5.88 | 13.40 |

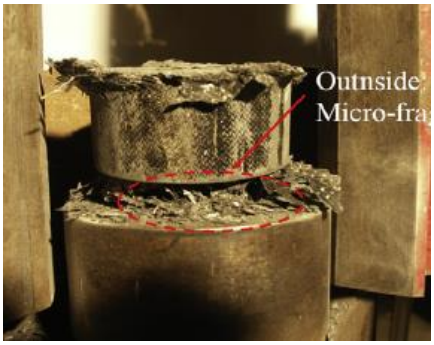


a) Deformation from experiment [123]

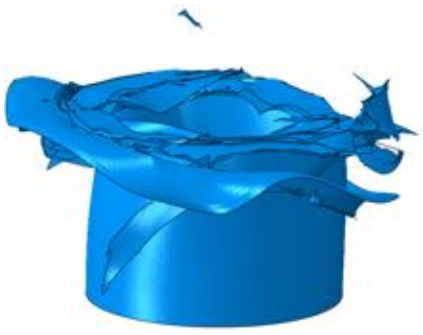

b) Deformation from present FEA simulation

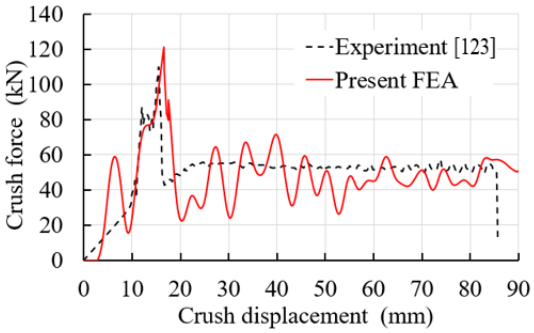


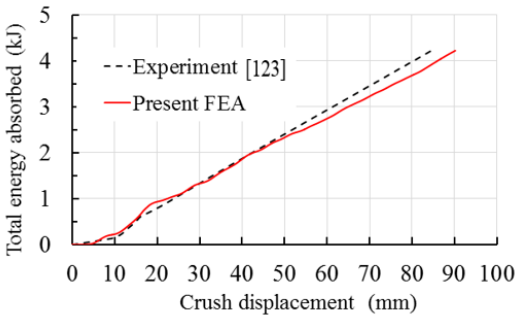


c) Crush force versus crush deformation d) TEA versus crush deformation

Figure 7.3: Comparison of present FEA with experiment [123] on axial crush behaviour of composite tube

### 7.2.2 FEA of FML conical tube – validation with experiment

7.2.2.1 Specimen geometry and experimental setup

The second experiment on a composite EA specimen is taken from Kathiresan *et al* [124] and simulated in present FEA under a low velocity axial impact. The specimen named as CWAC-2 [124] is a fiber metal laminate (FML) based conical tube i.e. a conical frusta made of an aluminium alloy sheet externally wrapped over by a layer of FRP composite (E-glass fiber/epoxy) material. This is analyzed in ABAQUS/Explicit [116]. This FML conical frusta specimen has 94 mm and 144 mm as top and bottom internal diameters respectively with a semi-conical angle of $21^0$. The total wall thickness is 3.20 mm with 0.87 mm for aluminum shell and 2.33 mm for GFRP layer and the height of the specimen is 65 mm. The composite layer has 9 layers of each 0.258 mm thickness with the ply sequence $[0^0/45^0/90^0]_3$ with the axial direction of the tube as the longitudinal direction ($0^0$). The experimented specimen [124] and the cross-section of the FML composite frusta are shown in Figure 7.4.

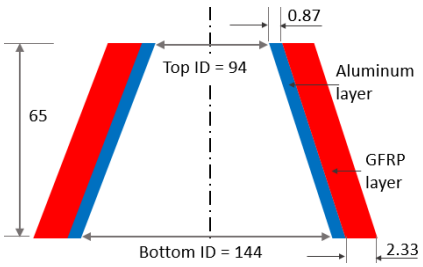


a) FML specimen [124] b) Cross-sectional details

Figure 7.4: FML specimen and its cross-sectional details (all dimensions in mm)

7.2.2.2 FEA of FML composite specimen

Single layer shell model approach is followed for modeling the FML conical tube using S4R elements in ABAQUS/Explicit [116]. The shell layers are created at the mid-surfaces of aluminum and GFRP layers. The orthotropic material of GFRP layer is modeled using linear elastic behavior until failure. Hashin's criteria [134, 135] is followed for specifying the damage initiation and damage evolution. The average element edge length is maintained at 1.0 mm. Detailed material specifications are provided in Table 7.3. Composite layer is modeled with 9 plies of GFRP fibers with the specified orientation sequence. Each GFRP layer is defined with the details of thickness, ply orientation, material and the number of integration points. Each layer is specified with 7 integration points across the thickness. Metal layer is represented with an aluminum alloy with Young's modulus of 70 GPa, Poisson's ratio of 0.33, yield strength of 55 MPa and ultimate strength of 113 MPa. Average element edge length is maintained similar to that of the composite layer. The interface between aluminum and composite layer is modeled using the contact based cohesive zone model in [17] with fracture energies as $G_I$ = 4 kJ/m$^2$ and $G_{II}$ = 4 kJ/m$^2$. These interface properties are taken from a similar work [136] as these values are not available in the reference literature [124].

In accordance with the impact test setup, the surface with the larger diameter of the frusta is fixed to a rigid base plate modeled using rigid R3D4 elements which is completely fixed in all degrees of freedom. A flat rigid impactor plate which is also modeled with R3D4 elements is used to strike the conical frusta at top. A mass of 83 kg is attached to the impactor rigid plate. An initial velocity of 5.4 m/s is applied to the impactor plate along the axial direction of conical frusta and is constrained in all other degrees of freedom. Reaction forces in the axial direction at the reference node of the bottom ground plate are recorded as the crush forces. The original impact test setup and the present FEA setup are shown in Figure 7.5. Mass of the specimen as measured from present FE model is about 0.172 kg.

Table 7.3. Material properties of E-glass fibre/epoxy material [124]

| **Property** | **Description** | **Value** |
|---|---|---|
| Density (kg/m$^3$) | $\rho$ | 1800 |
| Modulus (GPa) | $E_1$ | 30.90 |
| | $E_2 = E_3$ | 8.30 |
| | $G_{12}$ | 2.80 |
| | $G_{13} = G_{23}$ | 3.00 |
| Strength (MPa) | $X_T$ | 798 |
| | $X_C$ | 480 |
| | $Y_T$ | 40 |
| | $Y_C$ | 140 |
| | $S_{12}$ | 70 |
| Poisson's ratio | $\upsilon_{21}$ | 0.0866 |

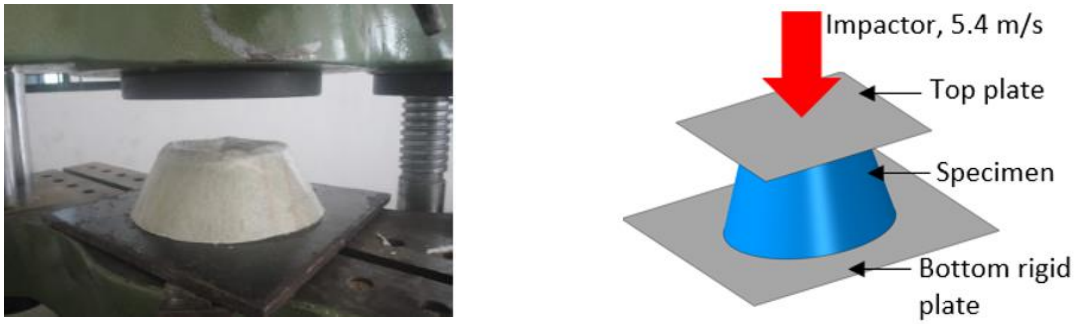


a) Experimental setup [7] b) Present FEA setup

Figure 7.5: Experimental [124] and FEA setups

7.2.2.3 Assessment of crash performance of FML composite specimen

Deformation patterns of FML composite frusta from present FEA simulation and from the experiment are shown in Figures 7.6(a-b). It is observed from FEA that the composite structure required a crush force of about 38.5 kN to initiate plastic deformation followed by a drop to about 22 kN at a crush stroke of 5 mm as the first folding of the hybrid tube is initiated. Further axial crushing densifies the structure until the next plastically deformed configuration is achieved and the crush force reaches a maximum value of 47 kN followed by a gradual fall before settling at a nearly uniform force of 26 kN. The hybrid frusta continues to deform progressively from the top with inward bending at the beginning. Metal and composite layers begin to separate from each other as the axial deformation progresses. Metal layer continues to deform in the diamond fold pattern while the composite layer deforms progressively with failure and fracture modes which is governed by the damage criterion.

Crush force versus crush displacement curves from experiment [124] and present FEA are shown in Figure 7.6(c). The experimental and FEA based mean crush forces are observed to be 29.5 kN and 33.3 kN respectively. Total energy absorbed (TEA) for a crush stroke of 30 mm is measured as 878 J and 992 J from experiment [124] and FEA respectively as shown in Figure 7.6(d). It may be noted that the present FEA simulation method correlates with the experiment with a difference of 13 % for the mean force.

a) Deformation from Experiment [124]

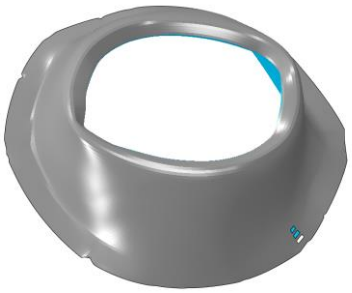

b) Deformation from present FEA simulation

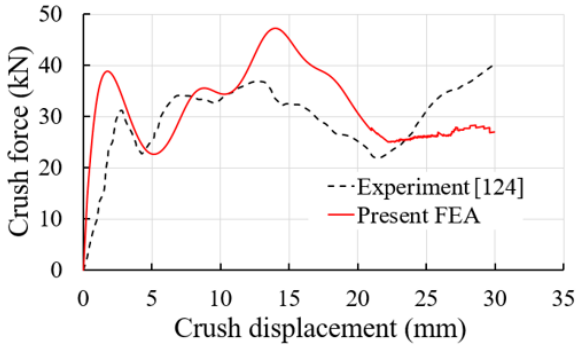


c) Force versus crush displacement

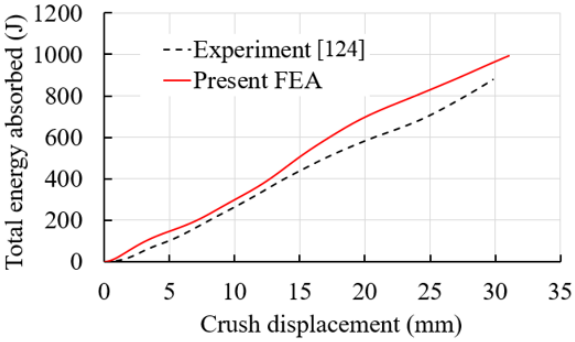


d) TEA versus crush displacement

Figure 7.6: Comparison of present FEA with experiment [124] on axial crush behaviour of FML composite specimen

The present FEA reasonably agree with the trend of experimental results in terms of the deformation pattern and crush force behavior. The stiffer behavior of FE model may be due to the inaccuracies in the assumption of material and interface strengths and difference in the specimen loading conditions in the experiment and present FEA setups. Detailed comparison of experimental [124] and present FEA on the fundamental crashworthiness parameters is shown in Table 7.4.

Table 7.4. Comparison of axial crash performance parameters between experiment [124] and present FEA of FML composite specimen

| FML Specimen | $F_{max}$ (kN) | $F_{mean}$ (kN) | TEA (kJ) | CFE (%) | SE (%) | SEA (kJ/kg) |
|---|---|---|---|---|---|---|
| Experiment [124] | 31.00 | 29.50 | 0.88 | 95.16 | 46.15 | 5.10 |
| Present FEA | 38.50 | 33.30 | 0.99 | 86.49 | 46.15 | 5.77 |
| % Difference in FEA *w.r.t.* Experiment [124] | 24.20 | 12.90 | 12.98 | 9.11 | 0 | 13.13 |

### 7.2.3 Summary of validation of FEA methodology for composite EA structures

Based on the present FEA simulations of axial crush behavior of two composite EA structures and their comparison with two experimental results available from two previous researches [123,124], it may be concluded that the adopted FEA simulation methodology closely represents the trend of crushing patterns and crush force behaviors at large. Therefore, the same FEA methodology will be used for developing the FML based EA structural concepts for enhancing the SEA in composite invertubes.

## 7.3 Invertubes for Crash Energy Absorption

In chapter 7, evolution of new tube profile for proper tube inversion has been discussed. The decisive factors that influence the tube inversion process such as basic dimensions of the tube, initial pre-formed knuckle radius, choice of material and most importantly the cross-section profile of tube have been understood in detail. The key enabler for this successful inversion of circular tube appeared to be the new 3-point arc based cross-section profile of the tube which ensured a smooth progressive deformation without premature failures. It demonstrates the sensitivity of the geometry on the inversion process. The unique unidirectional plastic deformation pattern associated with inversion process outscores the conventional plastic deformation patterns associated with regular geometries in major crashworthiness assessment parameters. The invertube thus discussed is taken as the basis for all the multi-material concepts to be discussed henceforth.

### 7.3.1 Need for enhancing SEA alone in invertube

It is observed that the major drawback of this invertube concept is the SEA factor. This is due to underutilization of the material in plastic deformation. It has also been understood that a successful combination of geometric parameters which enable the successful tube inversion using a certain grade of material may not hold good for the other grade of material. This

interaction between many parameters and the degree of sensitivity makes this tube inversion process enhance its specific energy absorption factor. Further analysis on the deformation mode depicts another peculiarity in the inversion that only 50% of the axial length of the structure is utilized in plastic deformation as observed in Figure 7.7, in contrast to 70-80% of crushed length in conventional EA structural configurations [39, 72, 86, 92]. This is despite scoring 100% in SE and CFE where the conventional EA configurations lag behind. This underutilization of material in plastic deformation is observed to be one of the key factors behind the low SEA factor in invertubes. In the subsequent part of this chapter, a few structural configurations are proposed to improve the SEA factor of invertube based EA configurations.

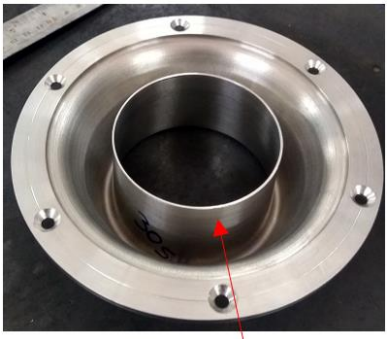


Figure 7.7: Underutilization of material in tube inversion process

## 7.4 Options for Enhancement of SEA in Invertube

To enhance the SEA factor of the invertube thus discussed, available options may be (i) upgrading (choice of higher grade of material), (ii) up-gauging (increasing the thickness of the tube), and (iii) extending the stroke length.

i) *Upgrading:* Theory of tube inversion demonstrated that it is not feasible to employ materials i.e. steels with high strength as the inversion mode is completely governed by the higher degree of ductility of the material. There are not many known grades of steel [137] that exhibit a degree of ductility comparable to that of the reference material SS304. Furthermore, plasticity mechanisms of inversion deformation will be different with different degree of ductility. Going for high strength material may not work unless it possesses high degree of ductility.

ii) *Up-gauging:* Increasing SEA factor by providing higher thickness of the tube demands larger diameter of the tube making it difficult for EA applications due to packaging challenges.

iii) *Increasing the axial length:* This is a practical option subject to the availability of axial space. Increasing the stroke length covers more area under the crush force-displacement curve, resulting in more energy absorption.

In the base version of invertube thus discussed, axial length of the invertube is 90 mm. Even when the axial length is increased to 150 mm in base version of invertube, it enhances the TEA but the increase in SEA is only marginal because the stroke length is increased by adding the mass in lesser proportion. Detailed development of structural configurations for improving the SEA factor of the invertube is discussed in the subsequent sections in this chapter.

## 7.5 Invertube Structural Configurations for Enhancing SEA

### 7.5.1 Variant-1: Base version of invertube with increased stroke length

Based on the observations thus discussed in base version of invertube, in Variant-1, the axial length (crush stroke) is increased from 90 mm to 150 mm. But this will add an additional mass of about 66 % to the existing structure for an equal amount of increase in the area under the crush force–crush displacement curve i.e. the TEA. As the crush force is proven to be uniform through the entire crush stroke, these linear calculations suggest an increase of 66% in TEA, but with almost the same SEA factor, with the same material grade. Thus, using the same material grade alone doesn't bring any improvements in the SEA factor. Hence, a synergistic combination of different materials is being proposed to improve the SEA factor.

In order to further improve the SEA factor, it is proposed to use a low-density and optimally strong material for the extended top portion of the invertube. In this case, a tube made of magnesium alloy AZ61 A-F [138] with mass density of 1.8 kg/m$^3$ which is less than a quarter of steel's density of 7.85 kg/m$^3$, is attached to the top end of the base invertube as shown in Figure 7.8. Top part of the base invertube and bottom part of the magnesium tube are provided with flanges for joining purpose. Steel and Mg tubes can be simply fastened together by bolts or by any advanced joining methods. The total stroke length of the resultant invertube structure is now 150 mm. The cross-section of layout of steel and magnesium tubes is shown in Figure 7.8. The mass of the resultant structure is 0.23 kg. The thickness of magnesium tube is assumed as 4.2 mm such that it is stable enough under the applied axial

crash impact load and doesn't initiate buckling before the initiation of triggering of inversion deformation of bottom steel structure whose peak inversion force is around 20 kN. The mechanical properties of Mg alloy AZ61 A-F [138] are Young's modulus, $E$ = 45 GPa, Poission's ratio = 0.33, tensile yield strength = 230 MPa and ultimate tensile strength = 310 MPa.

The buckling load for a cylindrical tube as given by Wierzbicki *et al* [117] is expressed as

$$F_{mean} = 7.935\ \sigma_p D^{0.5} t^{1.5} \quad (7.1)$$

where $D$ and $t$ are diameter and thickness of tube and $\sigma_p$ is the flow stress of the material.

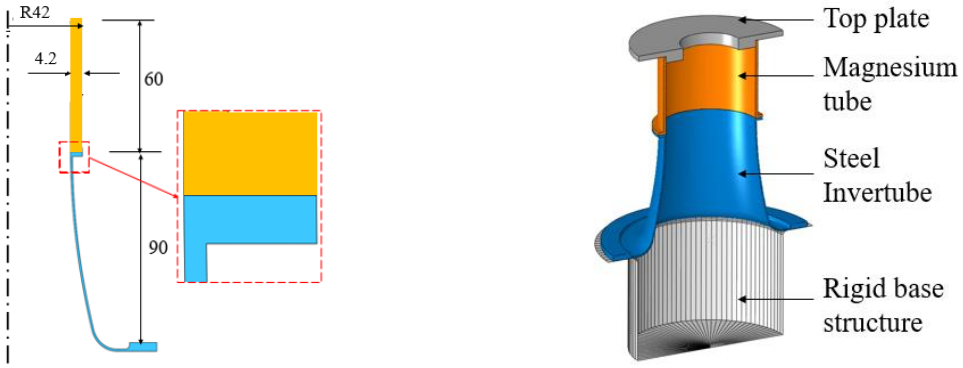


a) Cross section layout b) Final assembly: cut-section view (half model)

Figure 7.8: Basic layout and construction of Variant-1 (all dimensions in mm)

Substituting the corresponding values of the material, the estimated buckling force is approximately 140 kN. Thus it is ensured that the buckling force of supplemental Mg tube is far above the experimentally obtained 20 kN peak inversion force of the base steel invertube [118].

FEA simulation is performed on this Variant-1 of invertube configuration according to the same set up which is followed for the base version of invertube discussed in Sec-7.3. In this variant, the additional magnesium member is attached to the base steel invertube member by defining a *tie* connection [116] between the two members at their respective interfacing surfaces. FEA on this variant illustrates that inversion deformation progresses beyond the original length of 90 mm and continues till the targeted stroke of 150 mm without any premature failures in the base steel invertube. The plastic strains were observed to be within the material's limit of elongation as proved experimentally. The inversion force is stabilized at around 20 kN at a crush travel of 24 mm and continues with the same magnitude for the entire travel of 150 mm, thus simply extending the area under crush force vs crush

displacement graph by 60 mm. This is a simple and direct addition of around 66% to the total energy absorbed in comparison to the base variant with proportionately lesser addition of mass thus enhancing the SEA factor by 25 % from 10.6 kJ/kg (base version) to 12.5 kJ/kg (Variant-1). Progress of inversion deformation and crush force vs crush displacement graph is shown in Figure 7.9. This Variant-1 is taken as the reference for the next two variants proposed subsequently in this paper.

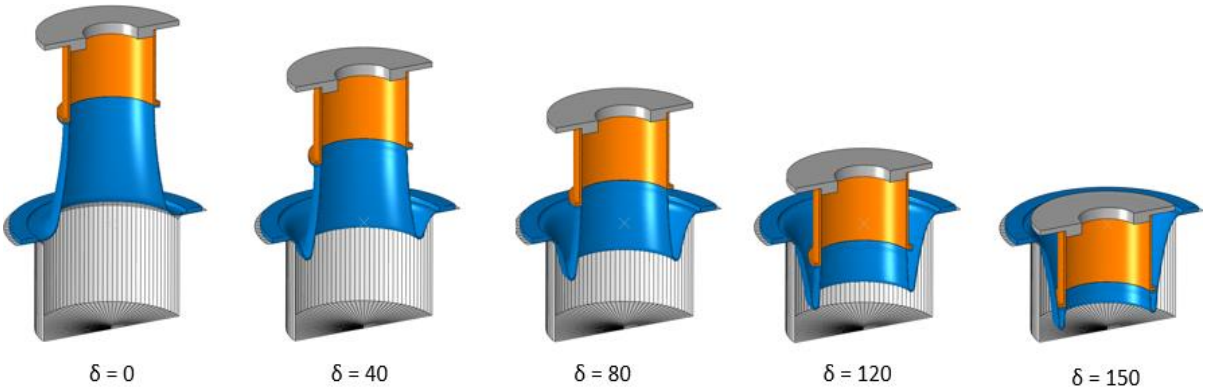


a) Progress of inversion deformation

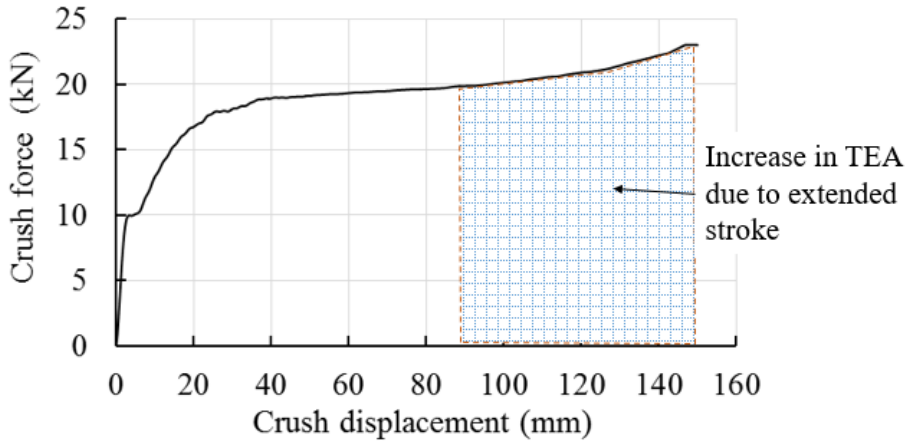


b) Crush force versus crush displacement

Figure 7.9: Deformation and crush force behavior: Variant-1

### 7.5.2 Variant-2: FML

#### 7.5.2.1 Structural configuration

To exploit the benefits of superior strength to weight ratio of composite materials, the second concept in this work is proposed in the form of a fiber metal laminate (FML). With the technological advances in the manufacturing sector, FML are gaining acceptance for primary

structural applications. Teng *et al'*s [139] research work on steel-FRP hybrid laminates for constructions of massive structures, Sinke's [140] work on overview of design and development process of FML based fuselage and Ahmed *et al*'s [141] work on development of hybrid composite tubes for energy absoprption applications provided the stimulus for this Variant-2. Further, Salve *et al* [142] presented a comprehensive review of FML structrures on their applications, manufacturing routes, test methods and numerical modeling procedures for a deeper understanding. This variant is formed by converting the base steel invertube of Variant-1 into a FML consisting of layers of steel-GFRP-aluminium. This FML is proposed to be formed by wrapping up the base steel invertube externally by a layer of composite material and then covering it up with another aluminium metal layer for a better structural integrity. Composite layer with superior strength-to-weight ratio is for adding more strength and boost the SEA factor. This secondary metal layer is added for binding the composite layer and to guide the composite layer during the inversion process and aluminum is proposed here for weight saving.

Kathireesan's *et al*'s [143, 144] works on FML in the form of conical shells provided the clues on the manufacturing feasibility of this variant. The structural configuration in this work was formed by external wrapping of composite layer made of GFRP on a conical aluminum shell by a hand lay-up process. This was accomplished by preparing a composite layer as a sheet in the shape of the developed surface of conical frusta and draping it up externally over the aluminum tube using an appropriate adhesive.

Similar preparation process is being proposed for the Variant-2 with a slight modification to that of Kathiresan *et al*'s [144] specimens, where the current composite specimen is provided with a slight outward radius to fit into the base fillet radius of base steel invertube. For simplicity in fabrication of this FML, the composite layer is made as a simplified version of the base invertube profile. It follows the base arc portion with a slight outward flange radius such that it ends at the middle of the base fillet of the 3-point arc of the base steel invertube. The thickness of the composite layer is taken as 1.2 mm. The steel invertube thickness is maintained at 1.0 mm. The bottom flanged portion of the steel invertube is provided with a stepped boss-like feature with a height of 1.2 mm which is equal to the thickness of the composite layer. This step is provided to maintain uniform thickness of the combined section of steel and composite layers. Another layer of aluminum with a uniform thickness of 1.0 mm is placed on the composite layer. Total thickness of this FML is 3.2 mm. Cross-sectional layout of the individual layers and the FML assembly is shown in Figure 7.10. The composite layer is made up of GFRP with 6 plies with a thickness of 0.2 mm for each ply and with

layup sequence of $[0^0/45^0/90^0]_2$. The total mass of the resulting configuration of Variant-2 is around 0.32 kg.

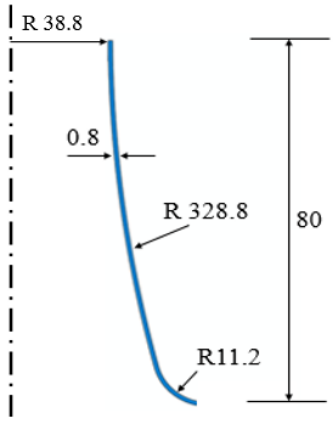


a) Dimensions of GFRP layer

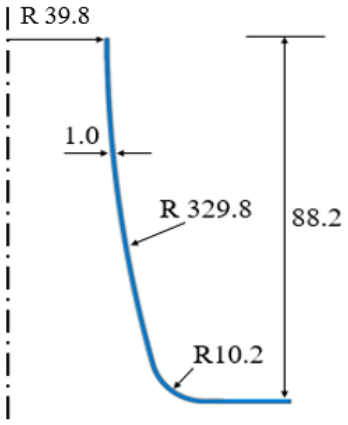


b) Dimensions of Aluminum layer

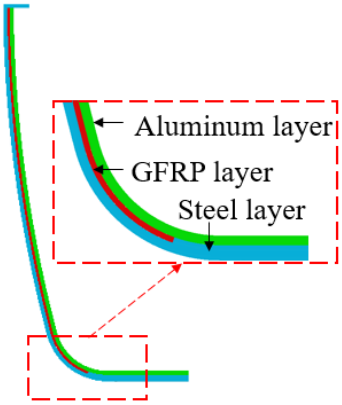


c) Cross-sectional details

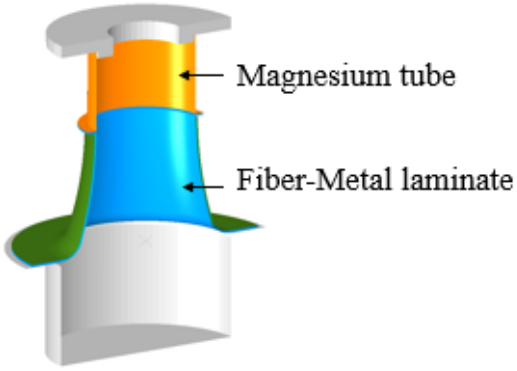


d) Final assembly (sectional view)

Figure 7.10: Constructional and assembly details of Variant-2

7.5.2.2 FE modelling and analysis

As followed in Sec-7.2.2 of this chapter, the GFRP composite layer is modeled as a single layer shell model with first order 4-noded shell S4R type elements for compatibility with ABAQUS/Explicit [116] solution methodology. This idealization is appropriate here because the focus is on investigating the structural concept from the viewpoint of magnitude of axial crush force and the total energy absorbed. The other two layers of steel and aluminum are also represented using the same type of elements. The average size of elements is maintained at 1.2 mm. Material properties considered for GFRP layer are same as given in Table 7.3. Elastic-plastic isotropic material formulation is considered for the aluminum layer with Young's modulus $E$ = 70 GPa, Poisson's ratio = 0.33, tensile yield strength = 55 MPa and the

ultimate tensile strength = 113 MPa. The interface between the three material layers is modeled using the contact based cohesive zone model with Hashin's fracture criterion with fracture energies as $G_I$ = 4 kJ/m$^2$ and $G_{II}$ = 4 kJ/m$^2$. These interface properties are taken from a similar research work [136]. The FEA setup is same as that adopted in Variant-1.

#### 7.5.2.3 Analysis of deformation and crash performance

Numerical analysis on this Variant-2 depicts an inversion deformation pattern similar to that discussed so far with a moderate start of crush force which stabilized at an equilibrium value. Some delay is observed in reaching the equilibrium value and the inversion crush force is stabilized at a crush stroke of around 40 mm as compared to 25 mm in the base version and Variant-1. This is because the GFRP layer is initially not contributing in the entire cross section and it comes into effect after the major part of the base trigger fillet radius portion is inversed. Delamination between layers which is governed by the interface definition is observed after an inversion stroke of around 22 mm, but it is not discussed here as the scope of this work is limited to crush force and deformation behaviors only.

As noticed in the experimental validation of base version of invertube, steel tube being the primary member, leads the inversion process. Addition of GFRP layer gives more resistance in the hoop direction leading to a higher inversion force in comparison to Variant-1, as the expansion of diameter is central to the inversion process. As a result, inversion force is more than doubled with a combined inversion force magnitude of around 45 kN against the inversion force of 20 kN in the base version with proportionately smaller addition to the mass of the EA structure. Failure of GFRP layer as governed by the material definition in longitudinal and transverse directions is observed with cracks initiating due to circumferential stretching. These cracks are observed to propagate in the longitudinal direction at multiple locations along the circumference of the composite layer thus maintaining the progressive failure and the crush force at a nearly constant magnitude. Progress of inversion of FML in Variant-2 is shown in Figure 7.11.

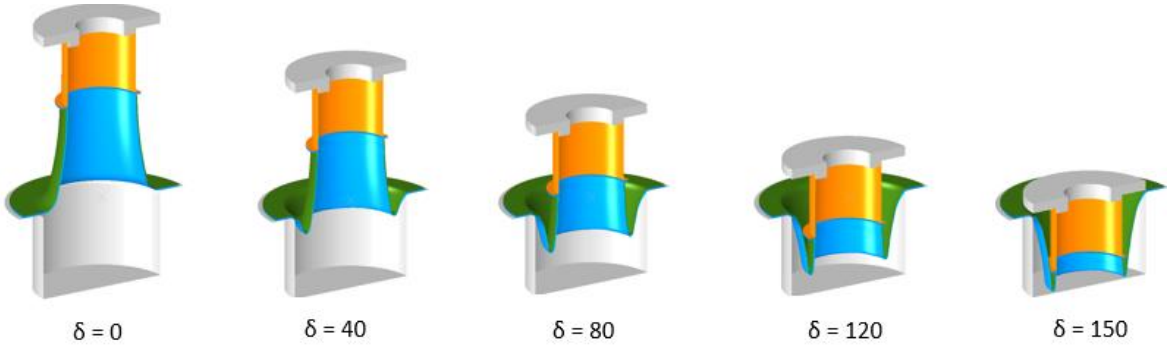


a) Progress of deformation: combined configuration

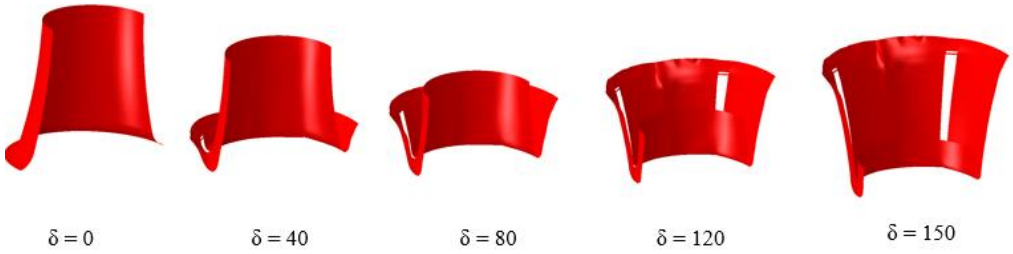


b) Progress of deformation: GFRP layer

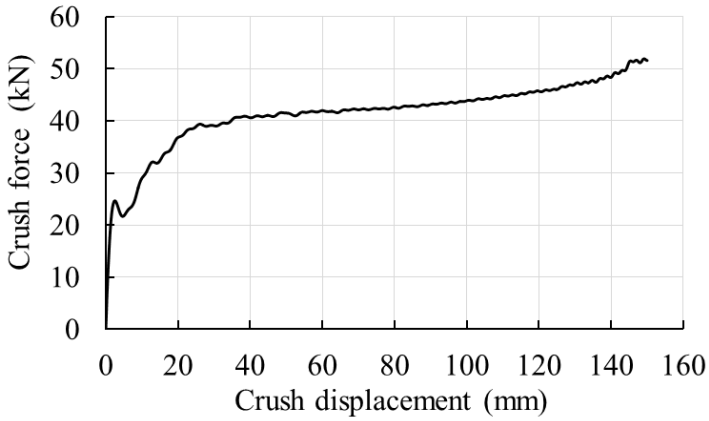


c) Crush force versus crush displacement

Figure 7.11: Deformation and crush force behavior: Variant-2

Detailed analysis of deformation of GFRP layer suggests that cracking in the axial direction is initiated at an inversion stroke of 22 mm and the crack elongates longitudinally as the inversion progresses. Plastic strains in the steel tube are within the limit of elongation at break and no failures are observed. External layer made of aluminum plays a supporting role for the GFRP layer and has not contributed appreciably to the inversion crush force. Inversion deformation process is observed to be smooth for the entire intended stroke of 150 mm similar to that of the Variant-1 with the magnitude of inversion crush force settling around 45 kN. Progress of inversion deformation process and force-displacement graph are

shown in Figure 7.11(a-c). There is an increase in inversion force and TEA by more than two folds whereas the increase in mass is only 50% in comparison to Variant-1. The TEA for this variant is around 6.2 kJ against 2.8 kJ for Variant-1 and also the SEA factor is increased to 20.7 kJ/kg.

### 7.5.3 Variant-3: Independent composite tube in the middle of Variant-1

#### 7.5.3.1 Structural configuration

In literature, numerous investigations have been made on the axial crushing behavior of composite tubes for EA applications including light weight design of a front nose cone's EA member of a formula race car [145], a CFRP based multi-cornered configuration with induced geometric imperfections for controlling the initial peak crush forces and mean crush forces [102], foam-filled hybrid composite structures for higher SEA factor [146] and many more. One common feature among such configurations is the progressive failure behavior of the tubes which is governed by an optimum combination of longitudinal, transverse and interface strengths and all of these configurations demonstrate nearly uniform crush forces. However, most of these structures work independently and may pose structural integrity issues due to failure-induced detachments when assembled in the vehicle. When they are combined with configurations such as invertubes that exhibit uniform crush forces, structural integrity issues associated with composite tubes can be addressed without compromising on the SEA factor and fundamental crashworthiness parameters.

Taking motivation from these observations, Variant-3 is arrived at by supplementing the Variant-1 with an independent composite circular tube. The objective of adding this composite tube as a parallel arrangement is to boost the crush force levels with proportionately smaller addition of mass. This tube is circular in cross section with a thickness of 2 mm. The length of the tube is 165 mm to account for the total crush stroke of 150 mm. The bottom surface of the tube is fixed to the bottom ground rigid structure. The tube is provided with an outward flange of radius 8 mm at the top to act as the initial crush trigger. The tube is also tapered from top to bottom (bigger radius at the top and smaller radius at the bottom) with a semi-conical angle of $1^0$. This taper is provided to ensure progressive crushing of the tube and to avoid catastrophic mode of failure at the mid length of the tube. The dimensions of crush trigger radius and taper angle are arrived at after a series of FEA iterations. Cross-sectional dimensions and assembly of the tube into the main invertube Variant-1 is shown in Figure 7.12.

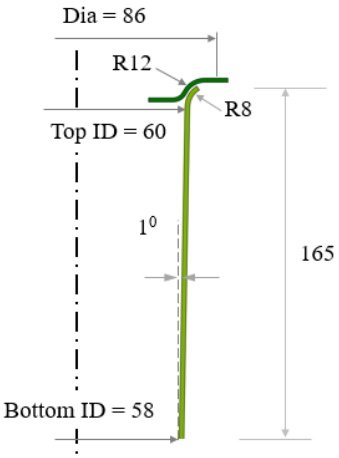


a) Cross section of composite tube and crush trigger

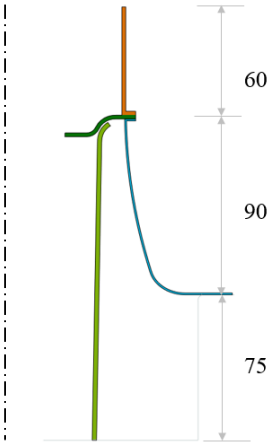


b) Cross-section of assembly

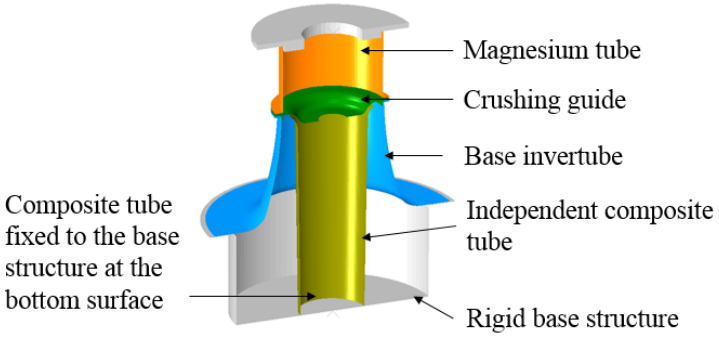


c) Final assembly (sectional view)

Figure 7.12: Constructional details of Variant-3

The composite tube is proposed to be made of CFRP/epoxy combination with 9 plies with the layup sequence of $[0^0/45^0/\text{-}45^0]_3$. The material properties considered for this tube are given in Table 7.5 [147]. Single shell layer idealization is adopted in FEA as the focus of this work is on the combination of structural configurations and the resulting crush force patterns and not on the detailed inter-laminar behavior, failure mechanisms and delamination phenomenon. A guide plate made of the same magnesium alloy which is used for top guiding tube is inserted between base steel invertube and the guiding magnesium tube as shown in Figure 7.12. This insert guides the flanged trigger radius of the composite tube and also helps in progressive crushing of the tapered portion of the tube. Resulting hybrid structure is shown in Figure 7.12(b). Total mass of the hybrid structure in Variant-3 is 0.36 kg.

Table 7.5. Material properties of CFRP tube [147]

| Property | Description | Value |
|---|---|---|
| Density (kg/m$^3$) | $\rho$ | 1560 |
| Modulus (GPa) | $E_1$ | 65.1 |
| | $E_2 = E_3$ | 64.4 |
| | $G_{12} = G_{13} = G_{23}$ | 4.5 |
| Strength (MPa) | $X_T$ | 776 |
| | $X_C$ | 704 |
| | $Y_T$ | 760 |
| | $Y_C$ | 698 |
| | $S_{12}$ | 95 |
| Poisson's ratio | $\upsilon_{21}$ | 0.037 |
| Fracture energies (kJ/m$^2$) | $G_{fc}^{1+}$ | 125 |
| | $G_{fc}^{1-}$ | 250 |
| | $G_{fc}^{2+}$ | 95 |
| | $G_{fc}^{2-}$ | 245 |

7.5.3.2 FE modelling and analysis

FEA simulation is performed on this hybrid structure very similar to the methodology adopted for the previous two variants. Due to the presence of composite tube, the initial part of the crush force curve is different with a slightly high initial peak force of 121 kN followed by a gradual drop to 60 kN at a crush stroke of 21 mm signifying the completion of crushing of trigger part. The crush then picks and settles around a magnitude of 84 kN for the reminder of the crush travel with minor fluctuations. The opening tendency of the composite tube due to its downward taper towards the bottom aids the guide plate to form the outward fronds due to the adopted damage evolution criterion. The formation of outward fronds helps in stabilizing the deformation and breaking pattern in a controlled manner with nearly uniform crush force in a controlled progressive mode. This progressive crush continues for a total intended travel of 150 mm without unwanted failure modes. The average crush force for this variant is around 82 kN and the TEA by this structure is around 12.3 kJ with more than

fourfold increase as compared to Variant-1. The deformation process of the main invertube at base is the same as observed in the experiment [118] because the additional composite tube is an independent addition and there is no interaction between the deformation mechanisms of these two entities. Progress of plastic deformation process of this Variant-3 is shown in Figures 7.13(a-b) and crush force versus crush displacement is shown in Figure 7.13(c).

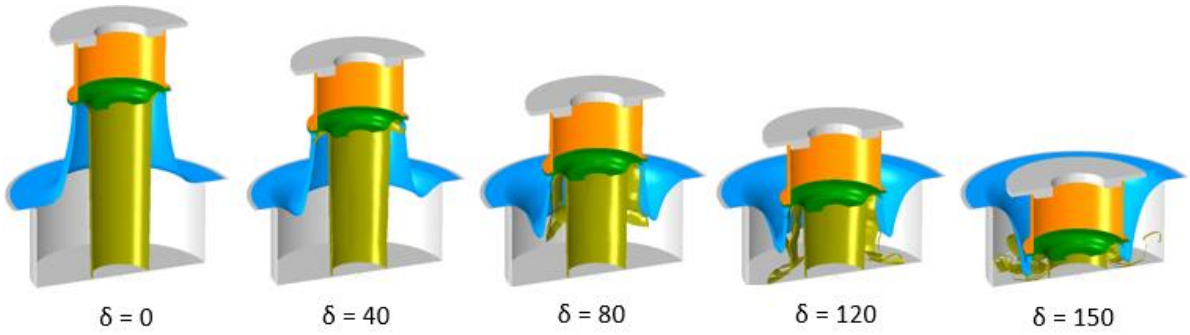


a) Progress of deformation: Combined configuration

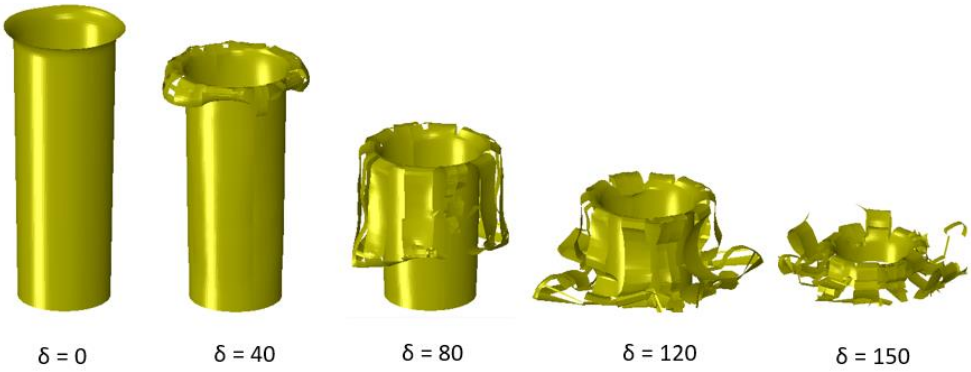


b) Progress of deformation: Composite tube

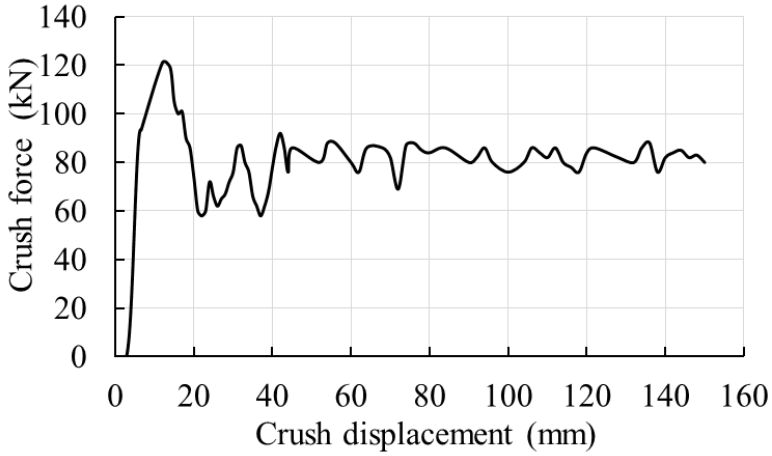


c) Crush force versus crush displacement

Figure 7.13: Deformation and crush force behavior: Variant-3

### 7.5.4 Results, Observations and Discussions

Crush force versus crush displacement and TEA versus crush displacement of all the three variants including the base version of invertube is shown in Figure 7.14(a-b). Detailed crashworthiness assessment of all the four invertube structural configurations is provided in Table 7.6. Variant-1 is simply an extension of crush stroke of the base version [118] for the same levels of crush force. Due to the peculiar deformation process associated with invertubes, the deformed volume of invertube material is generally low at 50% proving detrimental to SEA factor. Variant-1 is developed to address this issue by trying to maximize the volume under plastic deformation. Extended stroke is featured with a low density material (magnesium) allowing the base invertube to utilize its maximum volume in inversion deformation. This approach helped in improving the TEA by 65 % (1.7 kJ to 2.8 kJ) and SEA factor by 20% in comparison to the base variant [118] as the 66 % increase in stroke extended the area under crush force versus crush displacement curve in the same proportion.

Table 7.6: Assessment of crashworthiness of all invertube variants

| Invertube configuration | Mass (kg) | $F_{max}$ (kN) | $F_{mean}$ (kN) | TEA (kJ) | Crush stroke (mm) | CFE (%) | SE (%) | SEA (kJ/kg) |
|---|---|---|---|---|---|---|---|---|
| Base version | 0.16 | 17.0 | 17.9 | 1.7 | 90 | 105 | 100 | 10.6 |
| Variant-1 | 0.22 | 17.0 | 18.8 | 2.8 | 150 | 110 | 100 | 12.7 |
| Variant-2 | 0.32 | 35 | 41.3 | 6.2 | 150 | 118 | 100 | 20.6 |
| Variant-3 | 0.36 | 121 | 82 | 12.3 | 150 | 70 | 100 | 34.2 |

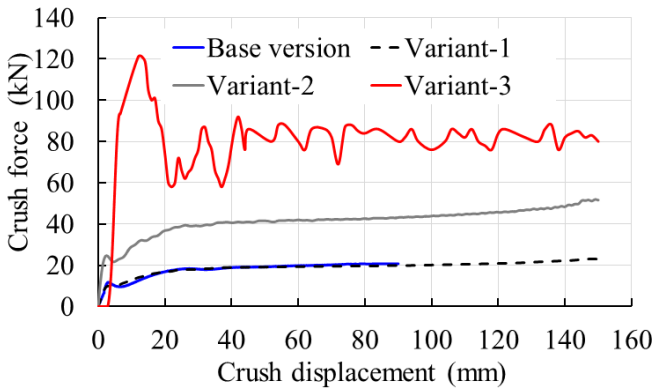


a) Crush force versus crush displacement curves of all variants

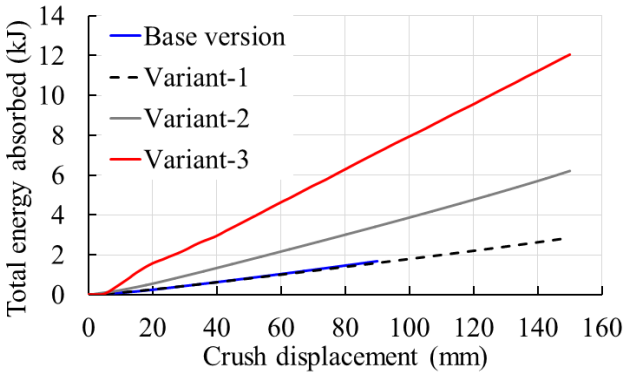


b) TEA versus crush displacement curves of all variants

Figure 7.14. Crush forces and energy absorption summary of all variants

Variant-2 is a further improved version of Variant-1 with an FML configuration with combination of steel, GFRP and aluminum layers. Notwithstanding the challenges in manufacturing this FML specimen, from the numerical study perspective, subjecting the FML to a unique inversion-deformation process helped in achieving the higher magnitudes of uniform crush forces with proportionately lesser addition of mass. Significant feature from this Variant is 121% increase in TEA and 50 % increase in SEA factor in comparison to Variant-1.

Variant-3 is another improved version of Variant-1 with a hybrid, yet simple configuration from the manufacturing perspective. Prominent feature of this variant is optimization of geometry (trigger radius and taper angle) of the composite tube for a crush force behavior which exhibits uniform crush forces throughout the crush stroke (with moderate initial peak crush force) in accordance with the distinctive deformation pattern of invertube. This synergistic tuning of composite tube helped in achieving exceptional crush forces in the inversion-based deformation process. This concept absorbed a total energy of 12.3 kJ and yielded an SEA factor of 34.2 kJ/kg.

Variant-3 with a relatively easier route of manufacturing and superior crashworthiness stands out as the best variant amongst all variants discussed so far. Thus it has been observed that SEA factor which was a major drawback in the pure invertube based EA configurations can be addressed with a synergistic combination of materials with high specific strength.

## 7.6 Summary

This part of research attempted to provide possibilities for enhancing SEA in invertube based crash energy absorbers. The adopted FEA simulation methodology has been validated with

experiments. Three new invertube structural configurations that can be adopted over and above the base invertube configuration have been proposed with a detailed analysis of their crash performances. The following conclusions can be drawn from this chapter.

1. Though invertubes outperform other conventional EA structural configurations in crash performance based on fundamental crashworthiness parameters, they fall behind in SEA factor due to certain limitations associated with the peculiar deformation pattern such as i) inadequate volume of the material undergoing plastic deformation, and ii) limitation on the feasibility of inversion, only for a certain selected combination of geometry and ductile materials.
2. Fiber metal laminates which are generally confined to standard geometric shapes can be floated as a choice for mainstream EA applications by tuning them to tube inversion-amenable shapes in combination with optimum grades of materials.
3. Invertubes when combined with independent composite crush tubes which are characterized by progressive failure modes can achieve a combined and compounding merits of invertubes (with high SE, CFE and structural integrity) and composite tubes (with high SEA). Limitations of both these members when they work in isolation can be counterbalanced.
4. As the industry is encouraging the practice of multi-material designs for weight savings, composite materials with their distinctive feature of producing direction-specific strength hold a lot of promise for future and may be utilized for impact energy absorption purposes in collaboration with the conventional metal-based structural configurations. To further strengthen the case of invertubes, numerical methods can be exploited to achieve inversion-conducive geometries for high strength materials.

# Chapter 8

# Bending-Based Aluminium Foam Sandwich Structures for Impact Energy Applications

Considerable research is reported in literature with the combination of conventional sheet metal structure and aluminium foam to explore the axial compression and lateral bending behavior of aluminum foams. In this chapter, inversion of aluminium foam sandwich structural configurations under lateral bending is investigated numerically using ABAQUS/Explicit [116] for impact energy absorption. This chapter presents 1) an introduction to metal foams, 2) scope of current work, 3) validation of FEA procedures for metal foam based structures, 4) new configurations, 5) research results, and 6) finally, the summary of observations.

## 8.1 Introduction

Recently, several researchers have investigated the application aluminium and various polymer foams for impact energy absorption through numerical and experimental studies. Literature reveals that most of these studies were directed at understanding the energy absorption characteristics by axial crushing of foams. It is observed that axial crushing of foams limit the active crush stroke owing to densification of the structure during progress of crushing, which is not an encouraging feature of an EA structure as it limits the opportunity for absorption of energy by plastic deformation [148-150]. Previous literature report the key findings of investigations on three point bending tests involving various foam materials; Santosa *et al* [101] presented the improvements in bending resistance of thin-walled tubes when filled with foams and also reasonable weight savings with partial foam filling. Zhang *et al* [151] from their numerical studies on foams with multi-cornered cross sections brought forth some observations on interactions between thin sheets and foams during 3-point bending and proposed some empirical formula for bending of certain cross sections. Wang *et al* [152] presented their findings on bending behaviour of aluminium foam sandwich structures with different types of bonding between foam and metal laminates and the related improvements in bending resistance. These investigations presented deformation behaviour of foams in bending in cylindrical and plate configurations and in combination with metallic skins. However, there is no clear evidence on the application of this bending mode of

deformation of foams for energy absorption purposes. Tube inversion based plastic deformations being investigated since 1960s have exhibited plastic deformations with a nearly uniform crush force utilizing the entire available crush stroke in the plastic deformation process leading to improved energy absorption for the same available stroke [104, 153].

In this chapter, inversion-based bending of sandwich structural configurations made of aluminium foam as the core with aluminium sheets have been studied numerically using the FEA code ABAQUS/Explicit [116] for the purpose of impact energy absorption. The crashworthiness of these configurations has been assessed based on the standard parameters such as: (1) initial peak force ($F_{peak}$, the maximum crush force that is required to cause plastic deformation in the EA structure), (2) crush force efficiency (CFE, the ratio of mean force $F_{mean}$ to $F_{peak}$), (3) stroke efficiency (SE, ratio of crushed distance to the total available length), and (4) specific energy absorption (SEA, ratio of total energy absorbed to the mass of EA structure). An ideal EA structure should have low initial peak force and high TEA, SE, CFE and SEA [104].

## 8.2 Scope of current work

This chapter presents the studies in two parts. The first part presents the numerical analysis of a 3-point bending (3PB) of aluminium foam and its comparison with published experimental result from literature [101] to validate and establish confidence in the FEA methodology. The simulation procedure thus validated is adopted in second part of this chapter in developing three structural configurations with aluminium foam that undergo inversion based plastic deformation. Crashworthiness of these two structural configurations has been assessed based on the standard parameters aforementioned and the better one has been recommended for further investigations.

## 8.3 FEA of a 3-Point bending specimen and its validation with experimental result

### 8.3.1 Specimen geometry

The specimen used in the experimental study was a thin-walled steel square tube of length 470 mm with a square cross section of 50 mm and thickness of 1.5 mm. An aluminium foam block of length 400 mm with a square cross section of 47 mm was loosely fitted into the hollow square tube with equal spacing at both the ends. No adhesive bonding was used in the experiment. Specimen details and experimental setup are shown in Figure 8.1.

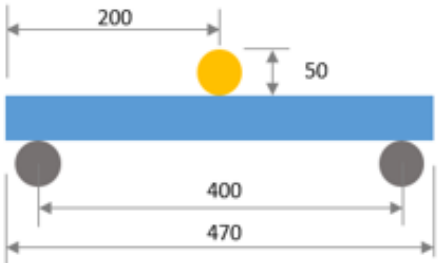


a) 3PB specimen

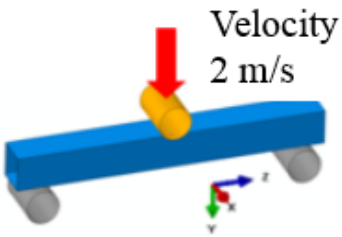


b) Loading setup

Figure 8.1. 3PB specimen with boundary conditions and loading setup [101]

### 8.3.2 Materials

The outer steel tube was made of Cr18Ni8 stainless steel with the mechanical properties: Young's Modulus = 210 GPa, Poisson's ratio = 0.3, initial yield stress = 507.6 MPa and ultimate tensile strength = 698.6 MPa. Engineering stress-strain curve of Cr18Ni8 is shown in Figure 8.2(a). The filler was made of aluminium foam IFAM with a relative density of 0.7 gm/cc and Young's modulus of 6.345 GPa. Stress-strain curve of IFAM foam is shown in Figure 8.2(b).

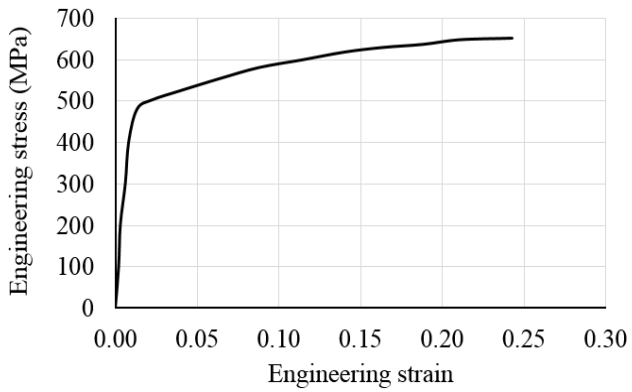


a) Cr18Ni8 steel

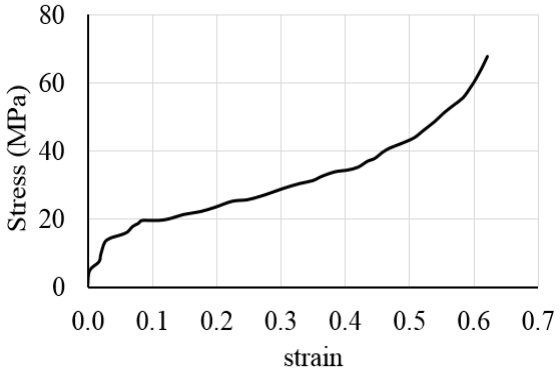


b) Aluminum foam IFAM

Figure 8.2. Stress-strain curves of steel and aluminum foam [101]

### 8.3.3 Test setup

The square steel tube which is partially filled with aluminium foam was placed on two rigid rollers of 50 mm diameter with a centre-to-centre distance of 400 mm. The punch which is also a rigid roller of 50 mm diameter was placed on top of the steel tube at the middle of the

span. The rigid punch was forced to bend the tube with a velocity of 2 m/s (as seen in Figure 8.1(b)).

### 8.3.4 FEA idealization and setup

The outer steel tube was modelled with 4-noded shell elements (S4R) and the foam block with 8-noded hexahedral elements (C3D8R) in ABAQUS [116] with an average element length of 1.6 mm. The stainless steel was represented with elastic-plastic material formulation and IFAM aluminium foam was represented with *crushable foam* and crushable foam hardening options [116]. The two rollers and the punch were represented as non-deformable rigid bodies. General contact algorithm in ABAQUS/Explicit has been activated to capture all the contact interface effects between foam, tube and rollers. The steel tube and the aluminium foam block are not glued together as they were not bonded together in the experiment [101]. The two support rollers were constrained in all degrees of freedom. The punch was allowed to move transversely along y-axis and constrained in all other degrees of freedom. A velocity of 2 m/s was applied to the punch along y-axis. Displacement of punch and the corresponding force along y-direction were recorded in FEA and compared with those from the experiment [101].

### 8.3.5 Analysis of results

As the punch presses the tube, the bending force ramps up till 25 kN as the aluminium foam offers support to the tube. The force stabilized at around 30 kN in present FEA and starts falling from a displacement of 40 mm, while the bending force stabilized in the experiment was at around 28 kN. Comparison of force-displacement curves from FEA and experiment is shown in Figure 8.3(a). Further, the energy absorbed during this deformation is determined for both the cases by calculating the area under these two curves until a displacement of 45 mm and energy absorbed versus punch displacement is shown in Figure 8.3(b). Comparison of deformation modes between the present simulation study and the experiment [101] is shown in Figure 8.4.

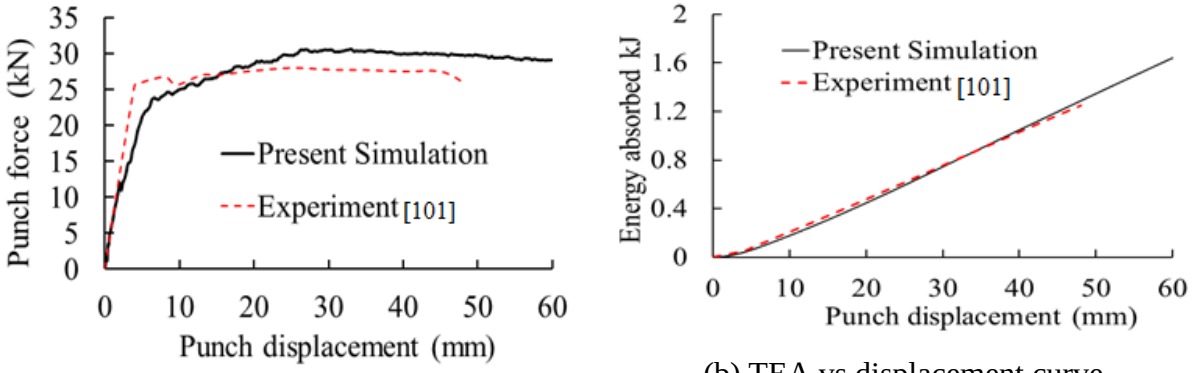


(a) Force vs displacement

(b) TEA vs displacement curve

Figure 8.3: Comparison of results - Present simulation and experiment [101]

From the experimental data, the energy absorbed was 1.11 kJ for a displacement of 45 mm while it is 1.23 kJ from the present simulation with a deviation of 11% from the experiment. It may be understood that this simulation approach reasonably represents the experiment with an acceptable degree of accuracy and may adapted for developing new EA structural configurations.


a) Present simulation

(b) Experiment [101]

Figure 8.4. Comparison of deformation modes

## 8.4 Proposed EA structures and performance analysis

It is understood from the previous literatures [104, 153] that tube-inversion type of plastic deformation modes are effective and ideal for energy absorptions due to their higher CFE, SE and uniform crush forces. In the present study, EA sandwich structural configurations with similar type of inversion based plastic deformations have been proposed and investigated using FEA code ABAQUS [116].

These configurations have been assessed on the aforementioned crashworthiness parameters when subjected to an axial impact scenario where a rigid mass of 100 kg impacts the EA structure with an initial velocity of 15.5 m/s (56 kmph), in line with the standard FMVSS 208 specifications. A schematic of the impact setup is shown in Figure 8.5. Aluminium alloy AA7005-T6 grade [94] was considered for face sheets of sandwich structures while the

IFAM aluminium foam used in the experiment [101] in the first part of this chapter was considered as the foam core material in the proposed EA structural configurations.

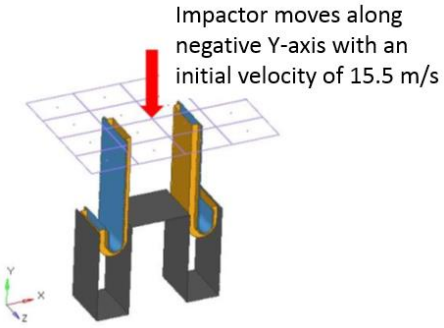


Figure 8.5. Simulation setup of proposed EA structure

### 8.4.1 Configuration-1

This configuration consists of a plain aluminum sheet of thickness 1.6 mm bent into the shape of English letter 'J'. This member is reinforced by another opposing member with the same thickness, also bent into the shape of 'J' with a 'C' shaped hat section. These two members are joined together to form a closed hat section as shown in Figure 8.6. The smaller end face of 'J' is fixed to the support structure by bolted fasteners. The other end of the EA structure is firmly attached to a rigid intermediate structure to provide an active crush stroke of 90 mm. These two sheet members are represented using first order 4-noded shell elements (S4R) in ABAQUS [116]. In order to capture the finer details of plastic deformation of structural members, an average element size of 1.5 mm is considered after a few iterations. General contact algorithm has been activated to capture contact interaction effects between all the interacting surfaces during the axial crushing. This configuration weighs around 0.16 kg. Supporting structure and impacting body are represented as non-deformable rigid bodies. Support structure is completely constrained in all degrees of freedom. Impacting body is provided with an initial velocity of 15.5 m/s in the axial direction and is constrained in all other directions in order to ensure pure axial impact. The FEA simulation setup of impact scenario is shown in Figure 8.5. Reaction forces in the axial direction at the reference node of the ground structure were recorded as the crush force against the axial displacement of the impacting body.

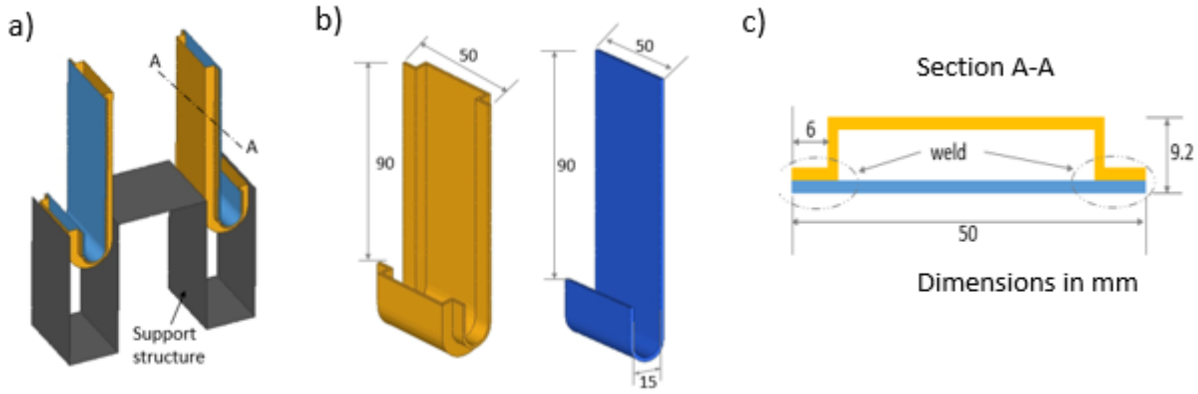


Figure 8.6. (a) Geometric details of configuration-1 of proposed EA structure, (b) separated view of left side J-type structure and (c) cross section.

8.4.1.1 Performance analysis

Different stages of plastic deformation of configuration-1 are shown in the Figure 8.7. The structure with its preformed ‘J’ configuration being conducive to inversion type of plastic deformation starts inverting as the impacting body strikes the intermediate structure in the axial direction. The longer end of ‘J’ continues to travel steadily in the axial direction aiding the inversion process without high initial peak crush force and fluctuations in the crush force after stabilization. This inversion continues for the entire crush stroke of 90 mm utilizing the entire available stroke. Initial peak force is around 28 kN and the average crush force after stabilization was observed to be around 36.5 kN. This axial crushing process with nearly uniform crush force with the entire stroke involved in the crushing is in contrast to the commonly observed plastic deformation modes associated with the standard thin-walled configurations. Crush force versus crush displacement graph of this configuration is shown in Figure 8.8(a). The total energy absorbed by this configuration is 3.0 kJ and total energy absorbed versus crush displacement graph is shown in Figure 8.9. Improvements to this performance with foam as the core material between the two sheet members are discussed in configuration-2.

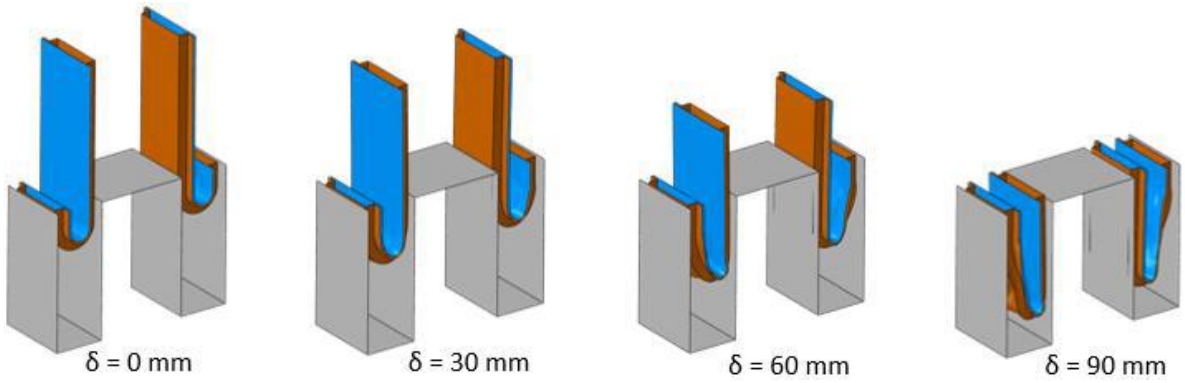


Figure 8.7. Progress of plastic deformation of configuration-1

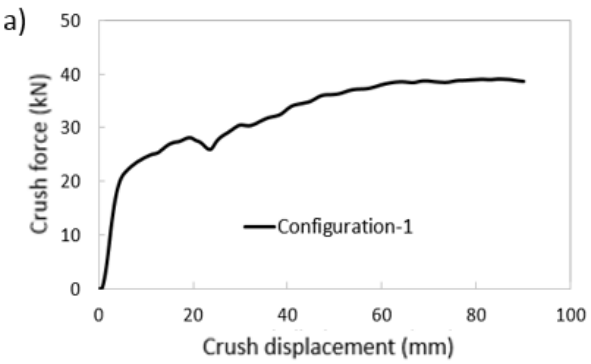


(a) Configuration-1

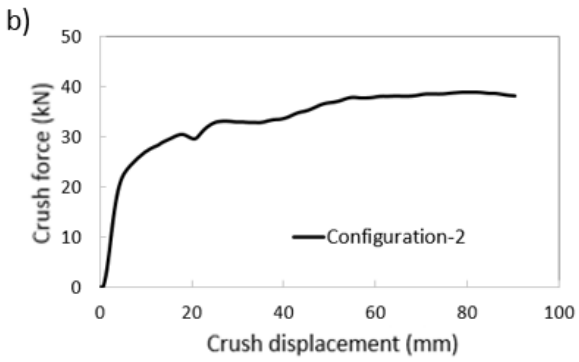


(b) Configuration-1

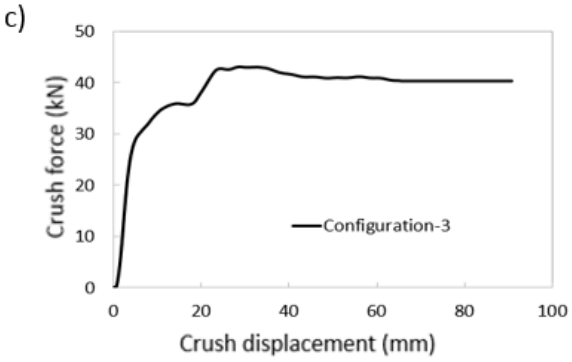


(c) Configuration - 3

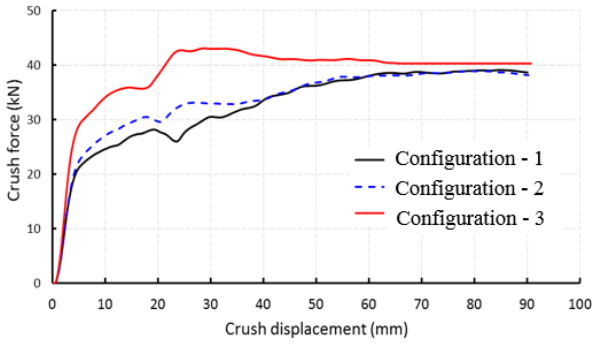


(d) All configurations

Figure 8.8. Force versus displacement curves for all the three proposed configurations

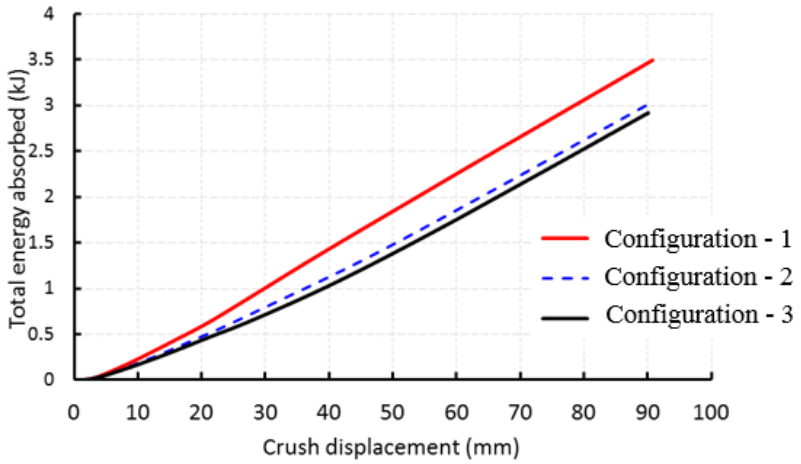


Figure 8.9: TEA vs crush displacement curves for all the three configurations

### 8.4.2 Configuration-2

As the crush force is observed to be nearly constant in the configuration-1, aluminium foam in the shape of 'J' is inserted between flat and C-sections forming a sandwich configuration. The thickness of foam member is kept at an optimum 6 mm after a series of iterations to check the plastic deformation process. Smaller thickness of foam doesn't contribute to improvements in crashworthiness in proportion to its mass. Higher thickness of foam disturbs the inversion process due to uneven deformation resistances between sheet members and foam. To maintain the mass of the whole structure to be comparable to that of the base version, the thicknesses of the sheet members is reduced to 1.40 mm. Aluminium foam is considered to be adhesively bonded to the base 'J' member using *tie* option in ABAQUS and the other side of the foam is not bonded. Configuration-2 is shown in Figure 8.10.

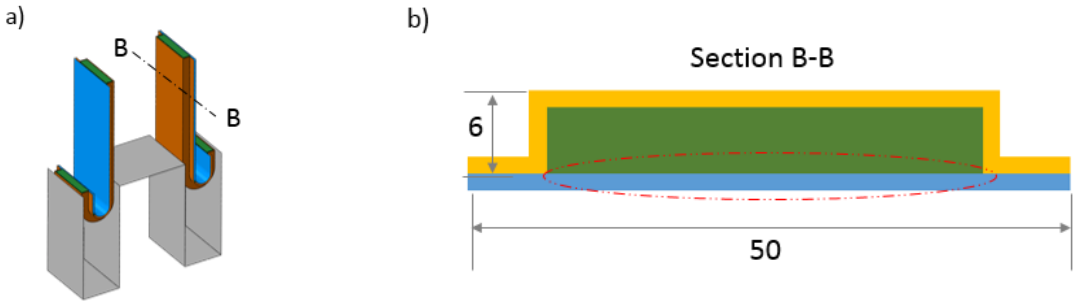


Figure 8.10. Geometric details of configuration-2 (all dimensions in mm)

8.4.2.1 Performance analysis

As the foam contributes to higher initial stiffness, initial peak force increases to 31 kN and the crush force continues at a slightly higher plateau at 33 kN in comparison to the empty hat section, until a crush stroke of 40 mm and stabilizes at around 38 kN from a crush stroke of 60 mm. The total energy absorbed improved to 3.2 kJ. To summarize, this foam sandwich configuration with similar mass as that of the base configuration gives clues for improving crashworthiness. Different stages of plastic deformation of configuration-2 are shown in Figure 8.11. Crush force versus crush displacement and TEA versus crush displacement are shown in Figures 8.8(b) and 8.9 respectively. Further improvements of this foam core sandwich version are discussed in configuration-3.

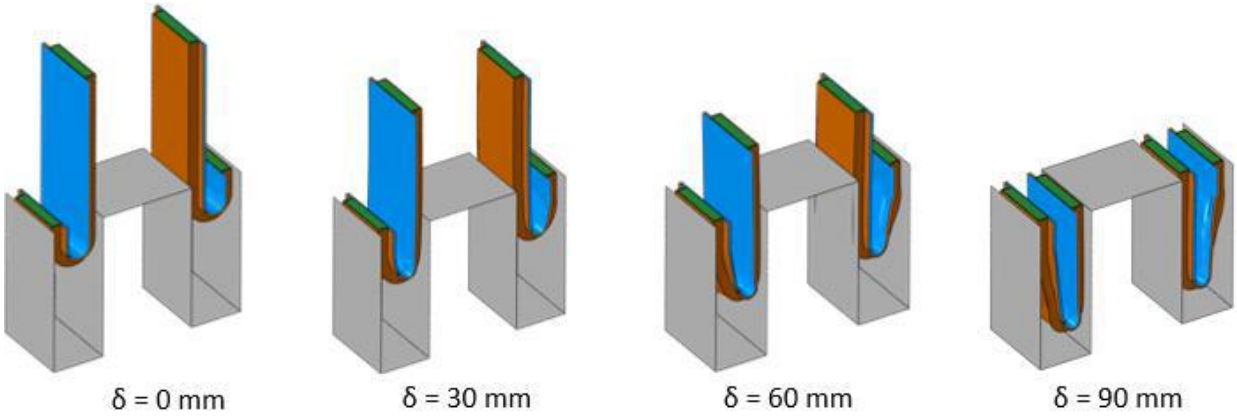


Figure 8.11. Progress of plastic deformation of configuration-2

### 8.4.3 Configuration-3

To maximize the bending resistance of foam and hence to improve the overall crush force, its cross-section is changed from rectangular section to ‘T’ section as shown in Figure 8.12. The base ‘J’ member in the hat section is split into two ‘L’ shaped members to accommodate the new cross section of aluminum foam. The thicknesses of hat section members are reduced to 1.40 mm to maintain the mass consistent with the previous two configurations. Modified aluminum foam is adhesively bonded to the two ‘L’ members while it is left free to interact with ‘C’ member of hat section.

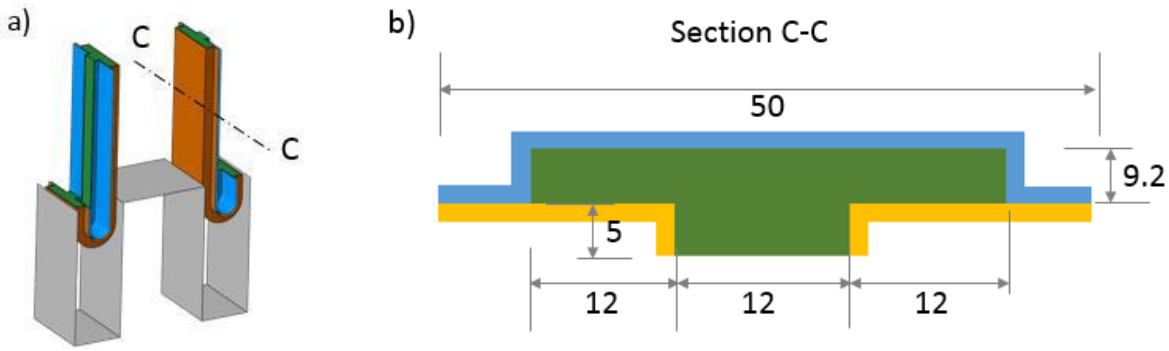


Figure 8.12. Geometry details of configuration-3 (all dimensions in mm)

8.4.3.1 Performance analysis

In comparison to configuration-2, the initial peak crush force increased to 36 kN due to initial high bending stiffness offered by the 'T' cross-section of aluminum foam. The bending resistance further increases continuously to 43 kN to a crush stroke of 30 mm until the inversion process stabilizes as shown in the crush force versus crush displacement in Figure 8.8(c). The crush force stabilizes at around 41 kN from a crush stroke of 40 mm onwards and the inversion of the sandwich configuration continues at the same crush force for the remaining crush stroke until 90 mm. As evident from the trend of crush force with an improvement over the first two configurations, this configuration of EA structure covers more area under the crush force versus displacement curve measuring the total energy absorbed as 3.6 kJ which is 12.5 % more than that of configuration-2 for the same mass. TEA versus crush displacement graph is shown in Figure 8.9. Progress of plastic deformation is shown in Figure 8.13. Detailed comparison of crashworthiness of all the three configurations on the standard parameters is shown in the Table 8.1.

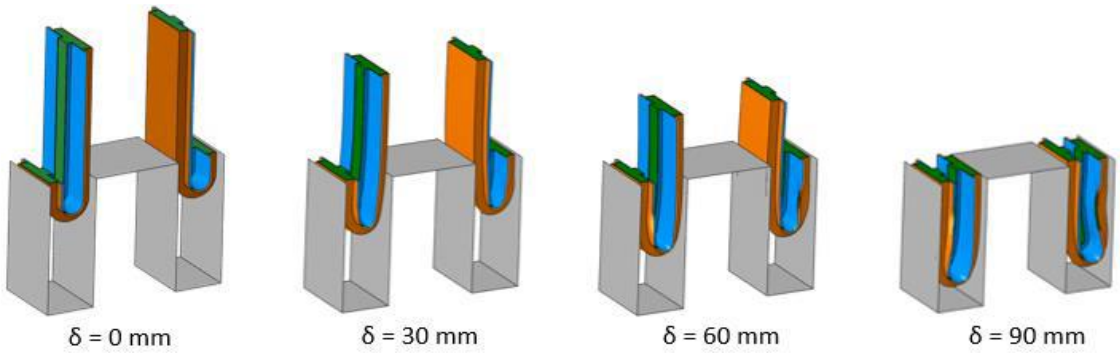


Figure 8.13. Progress of plastic deformation of configuration-3.

Table 8.1. Crashworthiness assessment summary of all the three configurations

| Configuration | Mass kg | Peak force kN | Mean force kN | TEA kJ | Crush stroke mm | CFE % | SE % | SEA kJ/kg |
|---|---|---|---|---|---|---|---|---|
| *1* | 0.16 | 28 | 33.3 | 3.0 | 90 | 119 | 100 | 18.8 |
| *2* | 0.16 | 31 | 35.6 | 3.2 | 90 | 115 | 100 | 20 |
| 3 | 0.16 | 36 | 40.0 | 3.6 | 90 | 111 | 100 | 22.5 |

## 8.5 Discussion of Results

The numerical simulations of three proposed EA structures and assessment of their crashworthiness reveal that inversion based plastic deformation effectively utilizes the entire material in plastic deformation process resulting in the complete utilization of crush stroke and assertion of nearly uniform crush forces throughout the stroke thereby maximizing the total energy absorbed. Configuration-2 with introduction of aluminum foam as the core material with rectangular cross-section in the sandwich configuration shown a marginal improvement in crashworthiness for the same mass. Configuration-3 with 'T' shaped cross-section of foam core with improved bending resistance proved to be a better choice among the current sandwich configurations with improved crashworthiness. It is understood that the optimum cross-section of foam core has a significant influence on the overall crashworthiness in bending dominant plastic deformations.

## 8.6 Summary

This chapter discussed the application of bending of aluminum foam sandwich structural configurations for energy absorption purposes based on the principles of tube inversion. This study revealed that the configuration-3 with exhibited a superior crash performance. This numerical study is limited to bending of sandwich structures involving extrudable shapes of aluminum foams as the core material. It has been understood that core foam shapes with properly engineered cross sections that exhibit optimum bending resistance may be a proper choice for impact energy absorption applications.

# Chapter 9

# Effect of Damage Modelling in Numerical Simulation of Crash Energy Absorption Behaviour of Crush Tubes and Validation with Experiments

Crush tubes are employed as frontal energy absorbing structures in road vehicles and they absorb crash energy by plastic deformation. Finite element analysis (FEA) is being used extensively in the early stages of crush tube design to study the method and magnitude of plastic deformation precisely ahead of prototyping and testing. Accurate definition of crush tube's material including its post-yield and damage/failure behaviors forms a fundamental part of FEA for a realistic prediction of crush tube's response to crash impact loads. Often, for the sake of simplicity or unavailability of data, it is a common practice in numerical simulations to ignore the damage criterion which leads to substantial differences between FEA predictions and experiments. Therefore, this chapter demonstrates the importance and effect of damage modelling in numerical simulation (FEA) of crash energy absorption behavior of crush tubes. This chapter introduces fundamentals of material behavior, introduces crush tube specimens and material properties, explains FEA without damage definitions, explains material and damage modeling in FEA, explains FEA with damage criteria, and finally summarizes the observations.

## 9.1 Introduction

It has been understood from the previous chapters that plastic deformation is the most widely practiced method of impact energy absorption (EA) in road vehicles and an effective EA structure should attenuate the impact-induced decelerations by absorbing the maximum possible kinetic energy in a regulated manner by controlled plastic deformation [104]. This requires a combination of well optimized geometric configuration and a material with a long post-yield behavior. For these applications, materials with high degree of ductility which exhibit a constant plateau of stress over a range of high strains are generally preferred. This is generally expressed as a strain hardening parameter or index [154] which is represented as the ratio of strain hardening modulus or the tangent modulus $E_p$ to the initial yield stress $\sigma_0$ of the material as shown in Figure 9.1. These two parameters are expressed as:

Strain hardening index $= \frac{E_p}{\sigma_0}$ (9.1)

Strain hardening modulus $E_p = \frac{\sigma_u - \sigma_0}{\varepsilon_u - \varepsilon_y}$ (9.2)

where $\sigma_u$, $\varepsilon_y$, and $\varepsilon_f$ are ultimate tensile strength, yield strain and failure strain respectively.

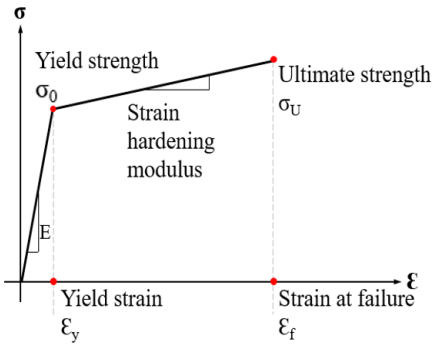


Figure 9.1: Elasto-plastic material behavior [1]

In the quest for designing EA structures with compliance to safety standards, a variety of structural configurations with standard geometric shapes and non-standard shapes have been proposed in the literature. Reddy *et al's* [92] EA configuration with twelve-cornered cross-section, Zhang *et al's* [72] novel kagome type concept and Chen *et al's* [86] multi-cell configurations with foam filling are some of the examples. Most of these structural concepts have been developed based on the FEA procedures. But all these and most other numerical studies related to crashworthiness predictions of crush tubes neglected damage initiation and evolution during crash loadings. Their predictions remain valid as long as the cracks are not initiated. Post crack initiation, the numerical predictions become totally unreliable and do not reveal the real crash behavior and do not match with experimental results. The perfect translation of these virtual concepts based on FEA into realistic and practical designs, requires appropriate modelling of material and its damage behaviour and proper interpretation of simulation results. Inadequate representation of material behavior and inappropriate interpretation of numerical results mislead the designer and the predictions do not capture the true behaviour of EA structure's response to the given crash loading.

In existing literatures on axial crushing of tubes, considerable gaps have been observed with respect to crush forces and plastic deformation modes between FEA predictions and experimental results. These differences and anomalies can be clearly noticed in Sun *et al's* [85] work on multi-cornered sections, Duarte *et al's* [155] thin-walled foam-filled aluminum

tube, analyses on bending behavior of foam-filled beams [156], axial crushing investigation of square tube with novel origami patterns [157], etc. It may be noted that these differences are largely due to incomplete representation of materials in numerical models. One major observations from these studies is that cracking was observed in the crush tubes during the experiment while it was not noticed in the corresponding FEA studies. It is generally due to simplified modelling of material behaviour and non-inclusion of damage in numerical simulations. If the material had been defined in a comprehensive manner in FE model with respect to material's plastic behavior with failure/damage criteria, FEA would have predicted failure of the crush tube in the early stages of design saving prototype development and testing costs and cycle times.

Cracking is not a desired phenomenon in EA structures as it compromises the structure's resistance to crushing leading to a drop in the crush forces and hence the energy absorbed, which is not the objective of an EA structure. It should be ensured that the EA structure do not undergo cracking during plastic deformation process of energy absorption. As the energy absorption process is driven by plastic deformation and high-magnitude plastic strains are involved, a material with higher degree of ductility should be chosen. An optimum balance should be ensured between geometry, gauge (thickness) and grade (material) for effective design of EA structures for their intended purpose. In this chapter, investigations based on numerical simulations in ABAQUS/Explicit [116] FEA code and experiments on axial crushing of cylindrical crush tubes made of aluminum alloy H30 in WP condition and stainless steel SS304 are performed. The results of numerical simulation of crush tubes with and without consideration of proper damage model are compared with carefully conducted axial crush experiments. These numerical studies with and without inclusion of damage criterion help to understand their influence on FEA results in terms of plastic deformation patterns and crush force behaviors. The predictions from numerical simulations are correlated and validated with the experimental results.

## 9.2 Crush tube specimens and material property

### 9.2.1 Crush tube specimens

The crush tube specimens as shown in Figure 9.2 are prepared by machining the rods made of aluminum alloy H30 grade in WP condition and stainless steel SS304 grade. The length of

both the tubes is 90 mm. Each tube has an external diameter of 50 mm and a thickness of 3.0 mm.


a) Aluminium H30 in WP condition b) Stainless steel SS304

Figure 9.2: Crush tube test specimens (all dimensions in mm)

### 9.2.2 Material properties

The tensile tests according to ASTM standard [114] are conducted on standard test specimens shown in Figure 9.3. The tensile test setup, specimen dimensions and true stress-plastic strain curves are shown in Figure 9.3. Observations from the tensile tests are tabulated in Table 9.1.

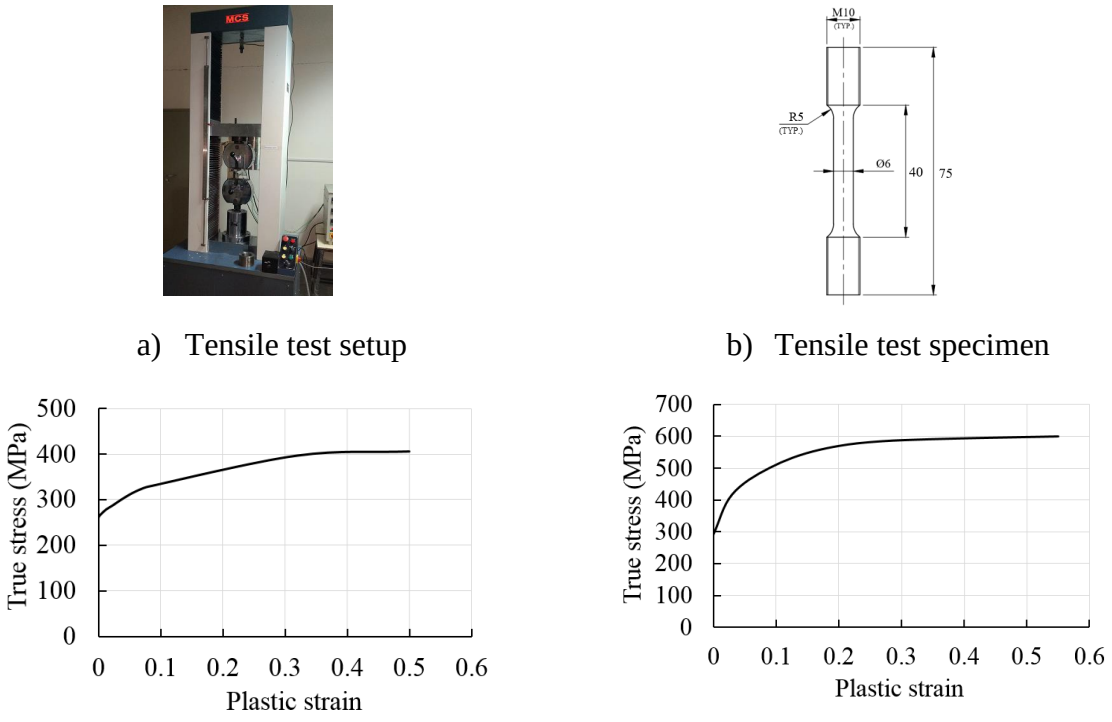


a) Tensile test setup b) Tensile test specimen

c) Stress-strain response of aluminium alloy H30-WP d) Stress-strain response of stainless steel SS304

Figure 9.3: Tensile test setup, tensile specimen and stress-strain behavior of crush tube materials (all dimensions in mm)

Table 9.1. Material properties of aluminum alloy H30-WP and stainless steel SS304

| Material | Young's modulus (MPa) | Tensile yield strength (MPa) | Ultimate tensile strength (MPa) | % Elongation at break |
|---|---|---|---|---|
| Aluminium alloy H30 – WP | 70000 | 280 | 355 | 12 |
| Stainless steel SS304 | 210000 | 290 | 600 | 55 |

## 9.3 Numerical Simulations without Damage and Experiments

### 9.3.1 FEA setup

The crush tube at its mid-surface is discretized using first order 4-noded S4R type shell elements in compliance with the FEA solver ABAQUS/Explicit [116] with an average element edge length of 1.0 mm. The bottom surface of the tube is fixed to the bottom rigid surface which is represented with R3D4 type of rigid shell elements using *tie* option in [116]. The crush tube material is modeled with isotropic elastic-plastic formulation with details of initiation of yielding and the post-yield behavior in the form of true stress versus plastic strain shown in Figure 9.4. An intermediate top surface represented using S4R type shell elements is placed at the top of the crush tube to transfer the impact load to the tube. An impactor which is modeled using R3D4 type of rigid shell elements is used to impact the intermediate plate. A mass of 250 kg is attached to the reference node of the impactor. General contact algorithm is activated to capture all possible contact kinematics and behavior. Reference node at the bottom rigid surface is fixed in all degrees of freedom. Reference node of the impactor is left free in the axial direction of the tube and fixed in all other degrees of freedom. An initial velocity of 0.1 m/s is applied to the reference node of the impactor in the axial direction towards the crush tube specimen. The reaction forces in the axial direction at the ground rigid surface are measured as the axial crush forces. The FEA setup is shown in Figure 9.4(a).

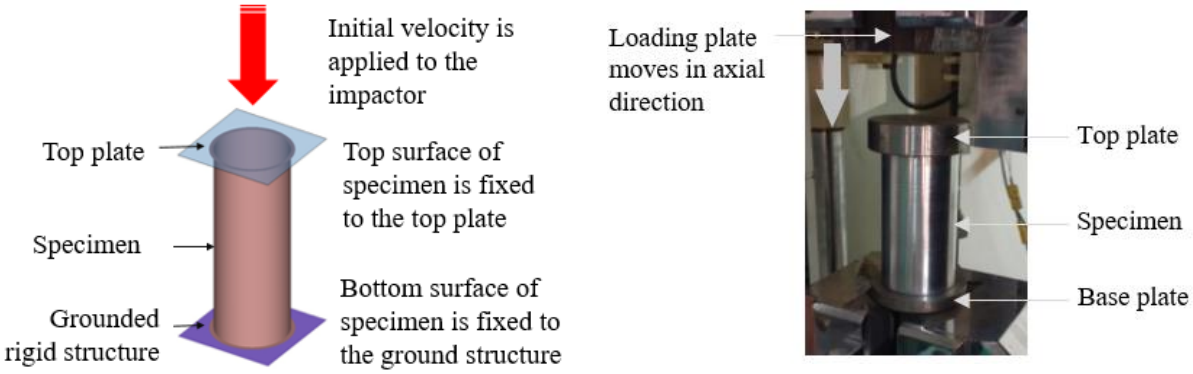


a) FEA setup b) Experimental setup

Figure 9.4: FEA and experimental setups

### 9.3.2 Experimental setup

The experimental setup consists of a universal testing machine (UTM) with a load capacity of 250 kN. The tube specimen is kept on the rigid surface of the test bed and the compressive load is applied through the intermediate loading plate at a quasi-static loading rate of 5 mm/min i.e. at 0.1m/s. The onboard computer which is integrated to the UTM gives the real-time record of axial crush forces against the crush displacement. The experimental setup is shown in Figure 9.4(b).

### 9.3.3 Observations from FEA and experiments

#### 9.3.3.1 Aluminium H30-WP crush tube

The FEA simulation of aluminium H30-WP predicted that the crush tube under the axial compressive load undergoes a standard concertina type of plastic deformation with a series of concentric ring folds. This is characterized by an initial peak crush force of 184 kN to initiate the plastic deformation followed by a gradual fall to 78 kN until a crush stroke of 26 mm marking the completion of first loop of plastic folding. Thereafter the crush force fluctuates between 80 kN and 120 kN with an interval of about 10 mm until a stroke of 50 mm. Crush force tries to stabilize with a downward trend of 80 kN until a stroke of 60 mm and picks up again as the next folding is initiated. Simulation is performed for a crush stroke of 60 mm only. Progress of plastic deformation from FEA and experiments are shown in Figure 9.5(a-b) and crush force versus crush displacement predicted from FEA simulation and experiment is shown in Figure 9.5(c).

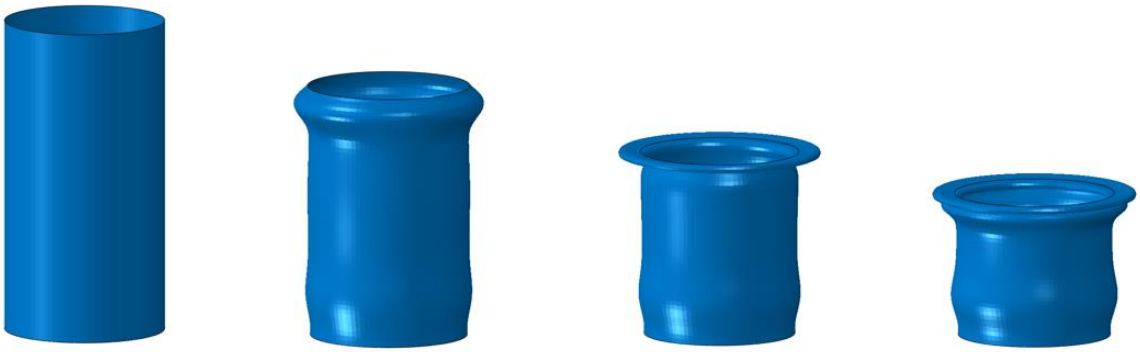


a) Progress of deformation from FEA simulation

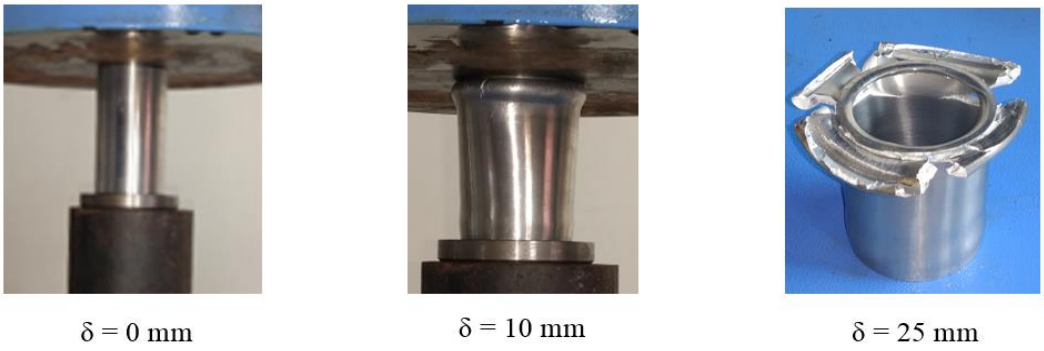


b) Progress of deformation from experiment

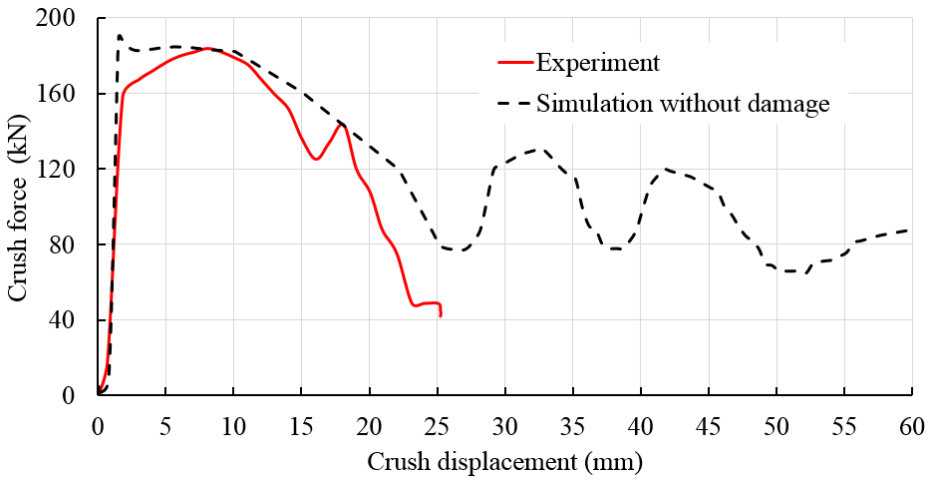


c) Crush force versus crush displacement

Figure 9.5: Deformation and crush force behavior of aluminium alloy H30-WP crush tube - Comparison of FEA simulation and experiment

The axial crushing experiment on the same specimen revealed a different picture with the initial crush force peaking up to 165 kN at a crush stroke of 2 mm and then following a smooth rise to 184 kN at a crush stroke of 8 mm followed by a continuous fall to 50 kN till a stroke of 24 mm. During this period, the tube exhibited a completely different deformation

pattern with small cracks on the first concertina fold along the axial direction. These cracks propagated further in the axial and circumferential directions resulting in a complete failure of the specimen as the stroke reaches 24 mm. The loading was aborted at this instance as the specimen failed completely. Progress of deformation, cracking and the crush force behavior from experiment are shown in Figure 9.5(b-c).

9.3.3.2 Stainless steel SS304 crush tube

The FEA simulation on this crush tube predicted an almost a similar trend of plastic deformation mode as observed in the case of aluminium tube. The crushing process starts with a high crush force for 190 kN to initiate the plasticity effects followed by a gradual drop to 100 kN at a stroke of 32 mm marking the formation of a concertina ring. The plastic deformation process continues as a series of concentric ring folds with an interval of about 30 mm for each ring. In contrast to the observation made in the case of aluminum tube, plastic strains are within the material's limit of elongation. Progress of deformation and crush force versus crush displacement from FEA simulation are shown respectively in Figures 9.6(a) and 9.6(c).

The experiment on this specimen brought out the deformation mode which closely resembles the FEA prediction in terms of deformation patterns (Figure 9.6(b)). The crush force behaviors of experiment and simulation match at a macro level, the difference being the secondary folds observed in the case of experiment. Initial crush force is observed as 192 kN in the experiment. No cracks are noticed in the specimen agreeing the simulation's prediction of plastic strains within the allowable limits. It may be observed that the FEA method largely represents the experimental crushing in terms of deformation and crush force behaviors. Comparison of deformation and crush force behaviors between simulation and experiment are shown in Figure 9.6(a-b).

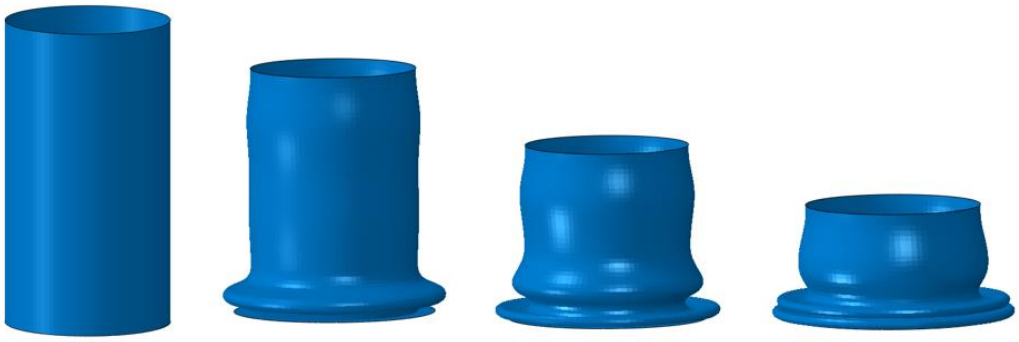


a) Progress of deformation from FEA simulation


b) Progress of deformation from experiment

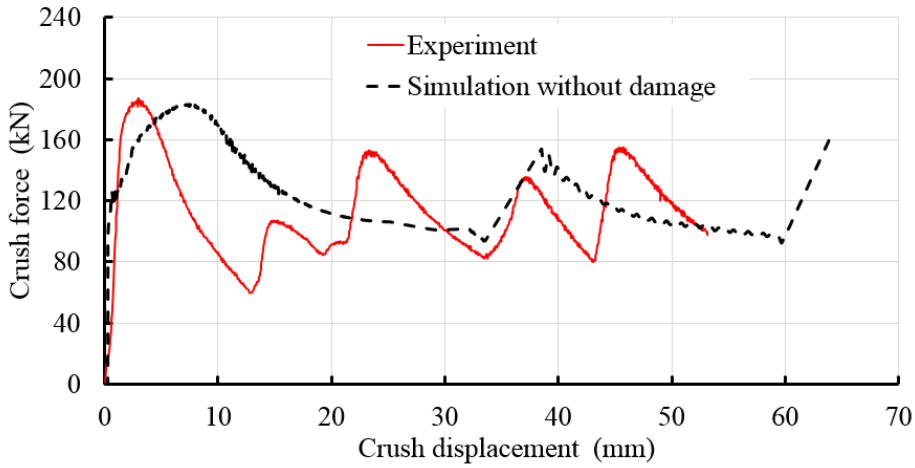


c) Crush force versus crush displacement

Figure 9.6: Deformation and crush force behavior of stainless steel SS304 crush tube - Comparison of simulation and experiment

## 9.4. Material and damage modelling in FEA

### 9.4.1 Material modelling

Material modelling collectively represents the constitutive or material models, equation of states (EOS) and failure or damage models as discussed in detail in Rao *et al* [93]. Basically, the equations in these models are numerically solved both in space and time by a FEA code in any commercially available FEA software like ABAQUS, Autodyne, etc., to describe the behavior of a continuum i.e. an EA structure like a crush tube. This FEA code solves a set of conservation equations for mass, momentum and energy subjected to certain initial and boundary conditions that characterises the physical crash impact event. They make up the required numerical input and implemented in the numerical formulations for the simulation of

vehicular crash impacts, either individually or in combinations depending upon the material, impact velocity, impact characteristics, etc. These numerical codes are continually updated for the relevant parameters in EOS, material models and damage models for many materials and are in fact essential to obtain good agreement with crash impact experiments.

The vehicular crash impacts are relatively complex at a fundamental level although they are not as complex as ballistic impacts. They depend on a number of variables. Therefore, modelling of deformation and failure must capture complex responses of materials such as non-linear constitutive (i.e. stress-strain) behavior involving strain hardening, strain rate hardening (occurs in few materials), pressure hardening, thermal softening (temperature rise may occur depending on geometry of crush tube and crash impact velocity), compaction (in porous materials like polyurethane foams used inside crush tubes), orthotropic response (composites), crushing damage, tensile failure, etc. Material modelling relates stress to deformation and internal energy which are then coupled with the damage characteristics. In general, the stress tensor is decomposed into a hydrostatic pressure (hydrostatic stress) and a deviatoric stress tensor [93]. The deviatoric stress tensor is associated with the resistance of material to shear distortion and is accounted by a strength or material model. Relating hydrostatic pressure, local density and local specific energy in materials is called an EOS which accounts for material compression at high contact-impact pressures and temperatures (if developed). The material model accounts for the strength characteristics and the damage model for failure characteristics of the materials involved.

### 9.4.2 Damage model

The failure, fracture or damage models predict the damage occurring in the EA material during crash impact as a result of the creation of new free surfaces. The damage in material depends on several factors like crash loading time, local stress, temperature and microstructure. The crush tube material is selected such that the crash impact induces ductile fracture which is characterised by the absorption of a large deformational energy and preceded by experiencing large plastic strains. The ductile fracture occurs either under tension or shear when a certain threshold strain is reached. Fracture under tension occurs as a result of the coalescence of small voids, forming macroscopic free surfaces (i.e. cracks) inside the specimen. The processes of void nucleation and growth in ductile materials, under dynamic loading conditions, have been studied in detail by many researchers [93].

In numerical simulations, the failure is shown by means of elements removal or disintegration from the crush tube. Failure models are proposed based on the concept of *continuum damage mechanics* (CDM). In CDM, micro-cracks and micro-voids, which grow, coalesce and initiate cracks, are modeled with a continuous damage variable *D*. In the majority of the damage models, this dimensionless damage variable is defined as a ratio between the damaged surface area or volume and the total surface area or volume. From the definition, it follows that *D* is bounded between 0 (undamaged) and 1 (fully broken or cracked). Many damage models are available and reported in literature for ductile fracture involved in crush tubes. They are the void growth model of McClintock [158] and Rice and Tracey [159], fracture strain model of Hancock and Mackenzie [160], void growth and fracture strain model of Johnson and Cook [161], composite damage model of Chang-Chang [162], orthotropic damage model of Clegg *et al* [163]., and material stress and strain limit damage models [114]. In this chapter, the damage is modelled in ABAQUS [116] using Johnson-Cook (J-C) failure model [161] and is briefly introduced here.

9.4.2.1 Johnson–Cook failure model

Johnson and Cook [161] proposed a failure criterion based on the fracture strain model of Hancock and Mackenzie [160] which is based on CDM. This failure model is generally considered as a fracture criterion for ductile materials and is especially suited for numerical codes. This criterion is based on the maximum strain to fracture i.e., the failure strain $\varepsilon_f$ of an element, which depends on its strain path, strain-rate, and temperature. The J-C failure criterion assumes a damage parameter *D* which represents a continuous degree of damage in the element under consideration and is given by

$$D = \frac{\bar{\varepsilon}_p}{\varepsilon_f} \tag{9.3}$$

where

$$\varepsilon_p = \int_{t=0}^{t} \dot{\bar{\varepsilon}}_p \, dt \tag{9.4}$$

$$\dot{\bar{\varepsilon}}_p = \sqrt{\frac{2}{3} D_p : D_p} \tag{9.5}$$

$$\varepsilon_f = \left[D_1 + D_2 \exp\left(D_3 \sigma^*\right)\right] \left[1 + D_4 \ln\left(\dot{\varepsilon}^*\right)\right] \left[1 + D_5 T^*\right] \tag{9.6}$$

$$\dot{\varepsilon}^* = \frac{\dot{\bar{\varepsilon}}_p}{\dot{\varepsilon}_0} \tag{9.7}$$

$$\sigma^* = \frac{\sigma_m}{\sigma_{eq}} \quad . \tag{9.8}$$

Here, $\varepsilon_f$ = equivalent plastic strain at fracture; $\bar{\varepsilon}_p$ = effective plastic strain; $\dot{\bar{\varepsilon}}_p$ = effective plastic strain rate; $\dot{\varepsilon}^*$ = ratio of effective plastic strain rate to reference strain rate; $\dot{\varepsilon}_0$ = user defined reference strain rate (normally taken as 1.0 $s^{-1}$); $\sigma^*$ = stress triaxiality; $\sigma_m$ = mean stress or the local hydrostatic pressure ($\sigma_m = \sigma_h$) as calculated by the average of the three principal stresses in each element; $\sigma_{eq}$ = effective or the equivalent stress (von-Mises stress); $D_p$= plastic deformation rate tensor; and $D_1,...,D_5$ are empirical material parameters which have to be calibrated for each material. In FEA simulations, an element is supposed to fail if the damage parameter $D$ reaches the value of 1.

### 9.4.3 Damage modelling in FEA

A typical stress-strain response of a metal under uniaxial loading is explained in Figure 9.7(a). The curve ***a-b*** represents linear elasticity, followed by yielding and strain hardening represented by the curve ***b-c***. Beyond point ***c***, load carrying capacity decreases until rupture as marked by the curve ***c-d***. Point ***c*** denotes the onset of damage which is governed by the damage initiation criterion and the response beyond this point which is denoted by the curve ***c-d*** is governed by the evolution of the degradation of the stiffness. The curve ***c-d'*** represents the behavior of the material in the absence of damage criterion.

The stress tensor, $\boldsymbol{\sigma}$ at any point of loading is expressed by the scalar damage equation

$$\boldsymbol{\sigma} = (1-D)\,\boldsymbol{\sigma}` \tag{9.9}$$

where $D$ is the overall damage variable and $\boldsymbol{\sigma}`$ is the effective (undamaged) stress tensor.

Figure 9.7(b) illustrates the typical stress-strain behavior of a material undergoing damage. According to plasticity and damage mechanics, damage occurs in two dimensions - softening of yield stress and degradation of elastic stiffness in unloading and reloading. In Figure 9.7(b), $\sigma_{y0}$ and $\bar{\varepsilon}_0^{pl}$ are the yield stress and equivalent plastic strain at the onset of damage, $\bar{\varepsilon}_f^{pl}$ is the equivalent plastic strain at failure when the overall damage variable $D$ reaches the

value $D$ = 1. The damage variable $D$ captures the combined effect of all active damage mechanisms. Continuum damage mechanics offers multiple mechanisms to define the initiation and evolution of damage based on various parameters of material non-linearity, ductile failure, shear failure, damage evolution by fracture energy and so on [163].

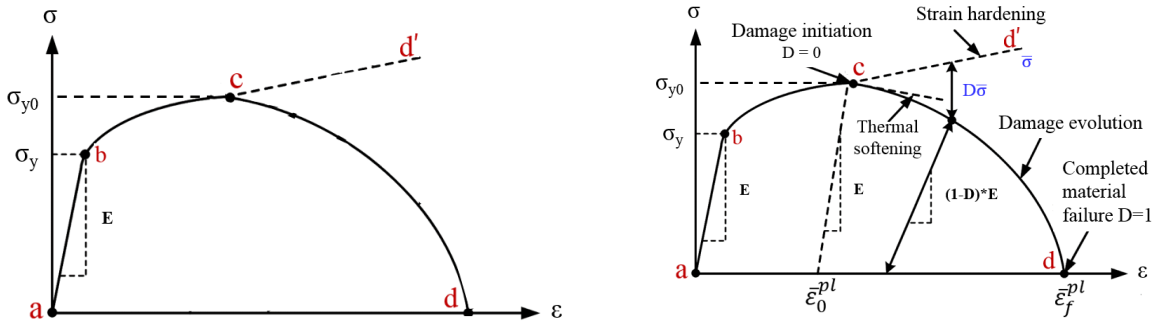


a) **Uniaxial stress-strain response** b) **Stress-strain curve with progressive damage**

Figure 9.7: Typical stress-strain response of a metal – a) without damage and b) with damage evolution [116]

## 9.5 FEA Simulations with damage / failure criterion

The numerical simulation in case of aluminium crush tube clearly exhibits its inadequacy in numerical modelling and predicting crush behavior when compared with results from crush experiment (as seen in Figure 9.5). One major source of inadequacy is the incomplete material definition. The material grade considered is aluminium alloy H30 in WP condition which is hardened and tends to exhibit strong and brittle behavior with vulnerability to crack when loaded beyond the limits of elongation. But the material definition considered in the FEA simulation was a simple isotropic elastic-plastic formulation without any reference to initiation and evolution of damage. Without the specification of damage criterion, the FE model continues to extrapolate its plastic behavior without leading to any failure. This phenomenon gives a deceptive picture of EA structure's response to the given loading if the results are not evaluated properly. In this case, inclusion of damage and failure criterion would have enabled FEA simulation to result a better correlation with the experiment.

There are certain evidences from little literature on crashworthiness [164-166] and many on ballistic impacts [93], where damage/failure criterion had been included in the FEA simulations for better correlation with the experimental results. An investigation on low velocity axial crushing response of a fiber-metal laminate [164], crashworthiness assessment

of an extruded aluminum square tube [165] and experimental-numerical study on the axial crushing of a composite tube [166] included damage in limited extent in their numerical simulations to improve the predictions but the importance of damage model and its effect when neglected in FEA simulations were not brought out and studied in detail. To improve the accuracy of FEA simulation and to demonstrate its reliability, FEA simulations on the two crush tubes, aluminum H30-WP and stainless steel SS304 are repeated by considering the damage criterion.

### 9.5.1 Aluminum alloy H30-WP crush tube

The isotropic elastic-plastic material model definition shown in Figure 9.3(c) which was used in the earlier FEA study is coupled with Johnson-Cook's damage model for damage initiation [116, 161] which is defined with the constants $D_1$ to $D_5$ which are given by $D_1$ = 0.125, $D_2$ = 0.135, $D_3$ = -1.5, $D_4$ = 0.015, and $D_5$ = 0 for aluminum alloy H30-WP [93]. Damage evolution has been defined with fracture energy which is arrived as 88 kJ/m$^2$ after a series of iterations.

Numerical simulation of axial crush with the aforementioned damage criterion resulted in significant differences in plastic deformation mode and axial crush force behavior. As the stresses in the tube cross the point of damage initiation as explained in Figure 9.7, the plasticity mechanics is completely altered as the yield stress softens and stiffness is degraded. The crushing resistance of the tube is no longer the same as observed in the case of the earlier version of FEA simulation without damage (as seen in Figure 9.5) with isotropic elastic-plastic material formulation. Due to the damage model, the plastic strains are governed by the softening yield stress and the failure becomes inevitable. Deformation pattern and crush forces simulated with inclusion of damage correlate with previous simulations neglecting damage only until a stroke of 12 mm. Cracking is observed in the crush tube due to failure along circumferential and axial directions. Though the plastic deformation mode did not entirely correlate with that from the experiment as shown in Figure 9.98(a), there was reasonably a good agreement between present FEA simulation considering damage and experiment with respect to crush force behaviors as seen in Figure 9.8(b). Comparison of deformation modes and crush force behaviors between FEA simulation and experiment is shown in Figure 9.8.

Experiment FEA Simulation

a) Comparison of deformation modes at a crush stroke of 25 mm

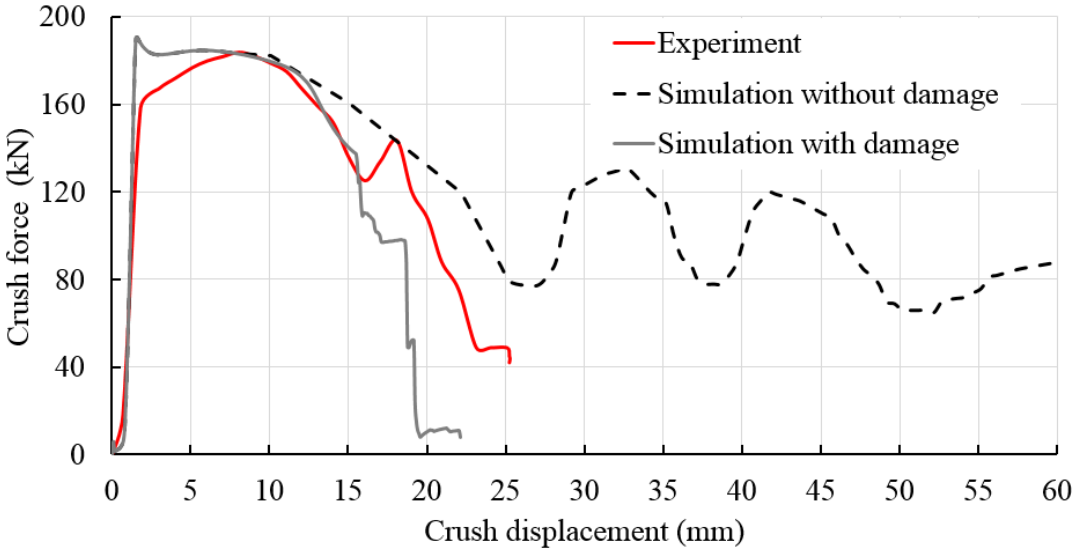


b) Crush force versus crush displacement

Figure 9.8: Deformation and crush force behavior of aluminium alloy H30-WP crush tube - Comparison of numerical simulation and experiment

### 9.5.2 Stainless steel SS304 crush tube

The isotropic elastic-plastic material model definition shown in Figure 9.3(d) which was used in the earlier FEA study is coupled with Johnson-Cook's damage model for damage initiation [116, 161] which is defined with the constants $D_1$ to $D_5$ given by $D_1$ = 0.8, $D_2$ = 2.1, $D_3$ = -0.5, $D_4$ = 0.002, and $D_5$ = 0.61 for stainless steel SS304 crush tube [93]. Damage evolution has been defined with fracture energy arrived as 110 kJ/m$^2$ after a series of iterations.

Simulation of axial crushing of SS304 tube with inclusion of damage model did not exhibit any difference. It may be noted here that the plastic strains from the earlier FEA simulation without considering damage model (as seen in Figure 9.6) were within the material's limit of elongation and the experiment also did not reveal any failure initiation or cracking. Earlier FEA simulation without any damage criterion demonstrated a reasonably good correlation with the experiment. This is primarily because the material has not been loaded beyond its allowable plasticity and hence the inclusion of damage criterion did not make any difference in the predicted simulation results. The earlier FEA simulation without damage definition was adequate enough to replicate the experimental results. But this is not always true as it is entirely dependent on magnitude of loading.

### 9.5.3 Observations and Discussions

The aforementioned analyses and their experimental comparison demonstrate that in design of energy absorbing structures undergoing large plastic deformation and plastic strains, using an appropriate damage model along with material model in numerical simulations can always predict the experimental results more accurately irrespective of any amount of loading and its loading rate. Proper material modelling helps in precise estimation of an EA structure's response to the given loading conditions. Johnson-Cook [161] damage model with the appropriate damage parameters helps in improving the accuracy of prediction of post-yield behavior of crush tube material.

## 9.6 Summary

This chapter presented the effect of damage modelling in FEA based numerical simulation of crash energy absorption behavior of crush tubes. The results of numerical simulation of crush tubes with and without consideration of proper damage model were compared with axial crush experiments on crush tubes made of aluminium alloy H30-WP and stainless steel SS304 materials. The following important conclusions can be drawn from this chapter.

1. In design of energy absorbing structures undergoing large plastic deformation and plastic strains, using an appropriate material (strength) model along with damage model in numerical simulations can predict the experimental results more accurately irrespective of any amount of crash impact loading and its loading rate.

2. Depending upon the geometry and material of crush tube and if the magnitude of crash impact loading induces plastic deformation only within the material's limit of elongation without exceeding failure strain, the numerical simulations considering only the material model and even neglecting damage model can produce reliable crush deformation and crush force behaviors matching experimental results.
3. Further, it may also be noted that for the energy absorption applications, materials with higher degree of ductility and moderate strength shall be given preference over materials with high strength and low ductility.
4. The appropriate material and damage model formulation that matches well with the dominant mode of deformation and failure mode of the structure is recommended for accurate prediction of the structure's response to crash impact loading.
5. Energy absorbing structures made of ductile metals should be designed such that the plastic strains during the deformation should be within the allowable plasticity range and below the damage initiation levels as the onset of damage alters the deformation mechanisms and crush force behavior compromising the amount of crash energy absorbed.

# Chapter 10

# Conclusions and Future Work

## 10.1 Introduction

The concept of automotive crashworthiness has gained importance and priority due to the evolving and stringent statutory requirements on passenger safety since 1950s and has become an integral part of vehicle engineering. Since then, several scenarios of vehicular road accidents have been studied in detail with attention to probability and intensity of injuries in each collision. Injury criteria have been developed for several vital parts of the body and limits have been set for the allowable levels of vehicular crash impact-induced decelerations. The concept of controlled energy absorption has been introduced as a part of impact mitigation and crash energy management. Automotive industry is on a continuous mission to offer the safest possible means of road transport. Frontal energy absorbing structures attracted a special attention as the frontal collision is the most common mode of vehicular road accidents. Till now, a lot of research efforts have gone towards developing frontal energy absorbing structures that attenuate the intensity of impact-induced decelerations. However, a few gaps exist in the existing crash energy absorbing (EA) structural configurations from the passenger safety perspective.

## 10.2 Summary

In the present research, an attempt has been made to understand the intrinsic geometrical and material features and develop few energy absorbing structural configurations for overall enhancement of vehicular crashworthiness. This research is summarized as given below.

1. Developed and established the methodologies for non-linear explicit finite element analysis based numerical simulation of crash energy absorption behaviour of EA structures and validated them by comparison with experimental results available in literature for certain standard EA structures.

2. Investigated the crush force behaviour of crush tubes having basic geometric cross-sections through established FEA simulations before attempting to develop novel EA structural configurations in the next phase.
3. Proposed various EA structural configurations through numerical simulations based on two different approaches such as i) circular tube-in-tube, and ii) hybrid cross-sections and evaluated their relative crash performance.
4. Evolved a new invertube's geometric profile and cross-section with stainless steel SS304 material and achieved desirable inversion characteristics for near-ideal crush force behaviour based on numerical simulations and experiments.
5. Underutilization of material in the plastic inversion deformation adversely limited the specific energy absorption (SEA) in invertubes. Therefore, developed invertubes with multi-material using hybrid composites and fibre metal laminates and achieved higher SEA and improved the overall crash performance of invertube based EA structural arrangements.
6. Proposed few more EA structural concepts through unique bending and inversion deformation mode with multi-material combinations involving conventional steel/aluminium sheets sandwiching aluminium foams and increased the total crash energy absorption.
7. Finally, demonstrated the importance and effect of damage modelling in numerical simulation of crash EA structures.

### 10.3 Specific Research Contribution

This research on structural configurations for vehicular crash energy absorption led to the following specific contributions.

1. Provided a comprehensive understanding of the influence of geometric cross-sections and topology of EA structures on their plastic deformation patterns which are directly related to the crush force behaviors.
2. Proposed a few geometric configurations that maximized the energy absorption by utilizing the crush forces that are within the human tolerance limits which are critical to the passenger safety.

3. Developed an invertube geometry and profile using medium strength stainless steel SS304 that exhibited a near-ideal plastic inversion.
4. Clarified the anomalies existing in the conventional invertubes and demonstrated that the materials with low $E_p/Y_0$ ratios are also suitable for inversion with properly engineered tube profiles unlike observations in previous research.
5. Shown that the low SEA in invertubes is due to underutilization of material in plastic inversion and proposed different methods to improve this limitation and enhance overall crashworthiness of invertubes.
6. In vehicular crash simulations, modelling of material damage is often ignored assuming that the crash energy is absorbed mostly through plastic deformation. But shown that the damage modelling improves the accuracy of predictions irrespective of the magnitude of loading, loading rates and plastic strains in crush tubes.

## 10.4 Conclusions

The major conclusions that can be drawn from this research are as outlined below.

1. **Assessment of crashworthiness***:* The amount of total energy absorbed alone is not measure of crashworthiness of an energy absorbing structure. The energy should be maximized only by maintaining the crush force levels uniform throughout the crush stroke.
2. **Role of geometry***:* Cross-section of the energy absorbing structure plays a pivotal role in the energy absorption. No cross-section with a standard geometric shape is suitable for efficient crash energy absorption. Cross-sections made of curved geometric entities exhibit high stroke efficiency but fail to maintain uniformity in the crush force levels. Cross-sections made of straight segments (polygons) exhibit uniformity in crush forces but show relatively poor stroke efficiency. Cross-sections with an optimized combination of arcs and line segments are favourable for enhanced crush force behavior.
3. **Deformation mode:** Tube inversion mode of plastic deformation shows better performance in all the crashworthiness assessment parameters. However, the process of inversion is limited to a certain optimized combination of geometric parameters of tube, its cross-section and the material involved. Successful tube inversion requires an

optimum balance of **G**eometry, **G**auge (thickness) and **G**rade (material). The existing theory of tube inversion appears to have limitations in applicability to all metals but for metals with high degree of ductility with optimum balance between aforementioned parameters.

4. **Improvements in SEA:** SEA of invertubes can be enhanced by combining ductile materials with materials having high specific strength such as composites in the form of hybrid composite structures or fiber metal laminates (FML). Composites with their progressive deformation and failure modes can maintain uniformity in crush force levels without diluting the unique and uniform crush force trend associated with invertubes.
5. **FEA methods:** With the growing acceptance and reliability, non-linear FEA based numerical simulations are promisingly applied to design non-conventional structural configurations. However, comprehensive methodology involving geometric, material and damage modelling ensures accuracy in numerical simulations.
6. **Materials:** High tensile strength is not the criteria for selection of material for energy absorption applications. Materials with high degree of ductility are favourable as the energy absorption involves large plastic deformation. Materials with high strength and moderate ductility are prone to premature failure by cracking leading to lower crush forces which defeats the holistic objective of energy absorption.

## 10.5 Scope for Future

The topic of present research is related to human safety in vehicular crashes and it is always encouraging and inspiring to continue the research in designing structures that are ideal for impact energy absorption as contribution to the mission of road safety.

The following options may be recommended for future research.

1. Tapered and /or lofted crush tubes with basic geometric shapes as cross-sections can be explored as they can be manufactured easily.
2. Adopting variable thickness sections, tailor welded blanks and other forms of inversion such as *outside-in* methods helps to extend the inversion-based deformation to high strength materials.

3. Investigations on adaptive hydraulics-based closed-loop energy absorption system for (i) precise control on crush forces and (ii) effective protection of occupants in oblique and offset crashes.
4. Combination of bending and inversion mode of deformation together with multi-material configuration can be explored.
5. Invertubes filled with low density metallic foams can be studied to develop compact crash energy absorbers.

# REFERENCES


[1] Safety companion 2018, Gesellshaft fur numerische Simulation mbH, Braunschweig, Germany https://www.carhs.de/en/companion-poster/product/safetycompanion-2018-digital-pdf.html

[2] World Health Organization. “Violence, Injury Prevention, and World Health Organization. Global status report on road safety 2013: supporting a decade of action”. World Health Organization, 2013.

[3] World Health Organization. *Global status report on road safety 2015*. World Health Organization, 2015.

[4] ITF (2017), *Road Safety Annual Report 2017*, OECD Publishing, Paris

[5] Lu, Guoxing, and T. X. Yu. *Energy absorption of structures and materials*. Elsevier, 2003. CRC Press

[6] National Center for Statistics and Analysis. (2017, March). Children: 2015 data. (Traffic Safety Facts. Report No. DOT HS 812 383). Washington, DC: National Highway Traffic Safety Administration

[7] Adolph, T., H. Schwedhelm, I. Lazaro, T. Versmissen, M. Edwards, R. Thomson, and H. Johannsen. "Development of compatibility assessments for full-width and offset frontal impact test procedures in FIMCAR." International Journal of Crashworthiness 19, no. 4 (2014): 414-430.

[8] Brumbelow, Matthew L., and David S. Zuby. "Impact and injury patterns in frontal crashes of vehicles with good ratings for frontal crash protection." In 21st ESV Conference, no. 09-0257. 2009

[9] Hollowell, William T., Hampton C. Gabler, Sheldon L. Stucki, Stephen Summers, and James R. Hackney. "Updated review of potential test procedures for FMVSS No. 208." Office of Vehicle Safety Research, NHTSA (1999).

[10] CARNEY III, J. F. "Motorway impact attenuation devices: past, present and future." In Structural Crashworthiness and Failure: Proceedings of the Third International Symposium on Structural Crashworthiness held at the University of Liverpool, England, 14-16 April 1993, p. 366. CRC Press, 2010.

[11] Leonardi, Paul M. "From road to lab to math: The co-evolution of technological, regulatory, and organizational innovations for automotive crash testing." *Social studies of science* 40, no. 2 (2010): 243-274.

[12] O'Neill, Brian. "Preventing passenger vehicle occupant injuries by vehicle design—a historical perspective from IIHS." Traffic injury prevention 10, no. 2 (2009): 113-126.

[13] Mark, Steve. "Effect of frontal crash pulse variations on occupant injuries." In Proceedings: International Technical Conference on the Enhanced Safety of Vehicles, vol. 2003, pp. 7-p. National Highway Traffic Safety Administration, 2003.

[14] Huang, X., Guoxing Lu, and Tong X. Yu. "On the axial splitting and curling of circular metal tubes." International journal of mechanical sciences 44, no. 11 (2002): 2369-2391

[15] Fan, H., B. Wang, and G. Lu. "On the tearing energy of thin sheet." International journal of mechanical sciences 44 (2002): 407-421

[16] Witteman, W., “Adaptive frontal structure design to achieve optimal deceleration pulses”. In Proceedings of the 19th International Technical Conference on the Enhanced Safety of Vehicles (ESV) (2005), Vol. 1, pp. 1108-1), 2005

[17] Eppinger, Rolf, Emily Sun, Faris Bandak, Mark Haffner, Nopporn Khaewpong, Matt Maltese, Shashi Kuppa et al. "Development of improved injury criteria for the assessment of advanced automotive restraint systems–II." National Highway Traffic Safety Administration (1999): 1-70

[18] Newman, James A. "Head injury criteria in automotive crash testing." SAE Transactions (1980): 4098-4115.
[19] Takhounts, Erik G., Matthew J. Craig, Kevin Moorhouse, Joe McFadden, and Vikas Hasija. "Development of brain injury criteria (BrIC)". No. 2013-22-0010. SAE Technical Paper, 2013.
[20] Takhounts, Erik G., Vikas Hasija, Stephen A. Ridella, Steve Rowson, and Stefan M. Duma. "Kinematic rotational brain injury criterion (BRIC)." In Proceedings of the 22nd enhanced safety of vehicles Conference. Paper, no. 11-0263, pp. 1-10. 2011.
[21] Boström, Ola, Rikard Fredriksson, Yngve Håland, Lotta Jakobsson, Maria Krafft, Per Lövsund, Markus H. Muser, and Mats Y. Svensson. "Comparison of car seats in low speed rear-end impacts using the BioRID dummy and the new neck injury criterion (NIC)." Accident Analysis & Prevention 32, no. 2 (2000): 321-328.
[22] Wood, Denis P., Nicolas Veyrat, Ciaran Simms, and Colin Glynn. "Limits for survivability in frontal collisions: Theory and real-life data combined." Accident Analysis & Prevention 39, no. 4 (2007): 679-687.
[23] Iwamoto, Masami, Yoshikatsu Kisanuki, Isao Watanabe, Katsuya Furusu, Kazuo Miki, and Junji Hasegawa. "Development of a finite element model of the total human model for safety (THUMS) and application to injury reconstruction." In Proceedings of the international IRCOBI Conference. 2002.
[24] Mohan, Dinesh, Geetam Tiwari, and K. S. Bhalla. "Road safety in India status report, 2015." Transportation Research & Injury Prevention Programme (TRIPP). New Delhi, India
[25] National Highway Traffic Safety Administration. "Final regulatory impact analysis: amendment of FMVSS No. 208-Passenger car front seat occupant protection." Washington DC: US Department of Transportation (1984).
[26] Du Bois, P., C. Chou, B. Fileta, T. Khalil, A. King, H. Mahmood, H. Mertz, and J. Wismans. "Vehicle Crashworthiness and Occupant Protection. (2004)." Southfield, MI, USA: American Iron and Steel Institute.
[27] Huang, Matthew. *Vehicle crash mechanics*. CRC press, 2002.
[28] Giancoli, Douglas C. *Physics: principles with applications*. Boston: Pearson, 2016.
[29] Perrone, N., "Biomechanical problems related to vehicle impact, in Biomechanics: Its Foundations and Objectives", Prentice Hall, Englewood Cliffs, NJ, 1972.
[30] Chou, Clifford C., R. J. Howell, and B. Y. Chang. *A review and evaluation of various HIC algorithms*. No. 880656. SAE Technical Paper, 1988.
[31] Kuppa, Shashi M., and Rolf H. Eppinger. *Development of an improved thoracic injury criterion*. No. 983153. SAE Technical Paper, 1998.
[32] Hackney, James R., Michael W. Monk, William T. Hollowell, Lisa K. Sullivan, and Donald T. Willke. *Results of the national highway traffic safety administration's thoracic side impact protection research program*. No. 840886. SAE Technical Paper, 1984.
[33] Clemens, H. J., and K. Burow. *Experimental investigation on injury mechanisms of cervical spine at frontal and rear-front vehicle impacts*. No. 720960. SAE Technical Paper, 1972.
[34] Gabauer, Douglas, and Robert Thomson. "Correlation of vehicle and roadside crash test injury criteria." In *19th International Technical Conference on the Enhanced Safety of Vehicles (ESV)-Washington DC June*, pp. 6-9. 2005.
[35] Ambrosio, Jorge AC, ed. *Crashworthiness: energy management and occupant protection*. Vol. 423. Springer, 2014.
[36] Salehghaffari, S., M. Tajdari, M. Panahi, and F. Mokhtarnezhad. "Attempts to improve energy absorption characteristics of circular metal tubes subjected to axial loading." *Thin-Walled Structures* 48, no. 6 (2010): 379-390.
[37] Andrews, K. R. F., G. L. England, and E. Ghani. "Classification of the axial collapse of cylindrical tubes under quasi-static loading." *International Journal of Mechanical Sciences* 25, no. 9-10 (1983): 687-696.

[38] Tvergaard, Viggo. "On the transition from a diamond mode to an axisymmetric mode of collapse in cylindrical shells." *International Journal of Solids and Structures* 19, no. 10 (1983): 845-856.
[39] Abramowicz, W. "Thin-walled structures as impact energy absorbers." *Thin-Walled Structures* 41, no. 2-3 (2003): 91-107.
[40] Alexander, J. M. "An approximate analysis of the collapse of thin cylindrical shells under axial loading." *The Quarterly Journal of Mechanics and Applied Mathematics* 13, no. 1 (1960): 10-15.
[41] Johnson, W. "Metallic energy dissipating systems." *Applied Mech. Review* 31 (1978): 277-287.
[42] Pugsley, Alfred. "The large-scale crumpling of thin cylindrical columns." *The Quarterly Journal of Mechanics and Applied Mathematics* 13, no. 1 (1960): 1-9.
[43] Alghamdi, A. A. A. "Collapsible impact energy absorbers: an overview." *Thin-walled structures* 39, no. 2 (2001): 189-213.
[44] Aljawi, A. A. N., and A. A. Alghamdi. "Investigation of axially compressed frusta as impact energy absorbers." *WIT Transactions on Engineering Sciences* 24 (1970).
[45] Aljawi, A. A. N., and A. A. Alghamdi. "Inversion of frusta as impact energy absorbers." In *Current advances in mechanical design and production VII*, pp. 511-519. 2000.
[46] Alghamdi, A. A. A., A. A. N. Aljawi, T. M. N. Abu-Mansour, and R. A. A. Mazi. "Axial crushing of frusta between two parallel plates." *Structural failure and plasticity* (2000): 545-550.
[47] Huang, Xiaodong, Guoxing Lu, and Tong Xi Yu. "Energy absorption in splitting square metal tubes." *Thin-walled structures* 40, no. 2 (2002): 153-165.
[48] Reddy, T. Y., and S. R. Reid. "Axial splitting of circular metal tubes." *International Journal of Mechanical Sciences* 28, no. 2 (1986): 111-131.
[49] Yang, Jialing, Min Luo, Yunlong Hua, and Guoxing Lu. "Energy absorption of expansion tubes using a conical–cylindrical die: Experiments and numerical simulation." *International Journal of Mechanical Sciences* 52, no. 5 (2010): 716-725.
[50] Abdul-Latif, Akrum. "Comparative Study of Several Energy Dissipating Devices." *Journal of materials engineering and performance* 20, no. 8 (2011): 1392-1400.
[51] Abramowicz, Wlodzimierz, and Norman Jones. "Dynamic axial crushing of square tubes." *International Journal of Impact Engineering* 2, no. 2 (1984): 179-208.
[52] Reid, S. Reddy, T. Y. Reddy, and M. D. Gray. "Static and dynamic axial crushing of foam-filled sheet metal tubes." *International Journal of Mechanical Sciences* 28, no. 5 (1986): 295-322.
[53] Reddy, T. Y., and S. T. S. Al-Hassani. "Axial crushing of wood-filled square metal tubes." *International journal of mechanical sciences* 35, no. 3-4 (1993): 231-246.
[54] Abbasi, Milad, Sekhar Reddy, Ali Ghafari-Nazari, and Mohammad Fard. "Multiobjective crashworthiness optimization of multi-cornered thin-walled sheet metal members." *Thin-walled structures* 89 (2015): 31-41.
[55] Liu, Wangyu, Zhenqiong Lin, Jiayue He, Ningling Wang, and Xiaolin Deng. "Crushing behavior and multi-objective optimization on the crashworthiness of sandwich structure with star-shaped tube in the center." *Thin-Walled Structures* 108 (2016): 205-214.
[56] Mahmoodi, A., M. H. Shojaeefard, and H. Saeidi Googarchin. "Theoretical development and numerical investigation on energy absorption behavior of tapered multi-cell tubes." *Thin-Walled Structures* 102 (2016): 98-110.
[57] Goel, Manmohan Dass. "Deformation, energy absorption and crushing behavior of single-, double-and multi-wall foam filled square and circular tubes." *Thin-Walled Structures* 90 (2015): 1-11.
[58] Najafi, Ali, and Masoud Rais-Rohani. "Mechanics of axial plastic collapse in multi-cell, multi-corner crush tubes." *Thin-Walled Structures* 49, no. 1 (2011): 1-12.
[59] Wu, Suzhen, Gang Zheng, Guangyong Sun, Qiang Liu, Guangyao Li, and Qing Li. "On design of multi-cell thin-wall structures for crashworthiness." *International Journal of Impact Engineering* 88 (2016): 102-117.

[60] Chen, Weigang, and Tomasz Wierzbicki. "Relative merits of single-cell, multi-cell and foam-filled thin-walled structures in energy absorption." *Thin-Walled Structures* 39, no. 4 (2001): 287-306.
[61] Zhang, Xiong, Gengdong Cheng, and Hui Zhang. "Theoretical prediction and numerical simulation of multi-cell square thin-walled structures." *Thin-Walled Structures* 44, no. 11 (2006): 1185-1191.
[62] Nagel, Gregory M., and David P. Thambiratnam. "Dynamic simulation and energy absorption of tapered thin-walled tubes under oblique impact loading." *International Journal of Impact Engineering* 32, no. 10 (2006): 1595-1620.
[63] Nia, Ali Alavi, and Jamal Haddad Hamedani. "Comparative analysis of energy absorption and deformations of thin walled tubes with various section geometries." *Thin-Walled Structures* 48, no. 12 (2010): 946-954.
[64] Hou, Shujuan, Xu Han, Guangyong Sun, Shuyao Long, Wei Li, Xujing Yang, and Qing Li. "Multiobjective optimization for tapered circular tubes." *Thin-Walled Structures* 49, no. 7 (2011): 855-863.
[65] Kavi, Halit, A. Kaan Toksoy, and Mustafa Guden. "Predicting energy absorption in a foam-filled thin-walled aluminum tube based on experimentally determined strengthening coefficient." *Materials & design* 27, no. 4 (2006): 263-269.
[66] Hussein, Rafea Dakhil, Dong Ruan, Guoxing Lu, Stephen Guillow, and Jeong Whan Yoon. "Crushing response of square aluminium tubes filled with polyurethane foam and aluminium honeycomb." *Thin-Walled Structures* 110 (2017): 140-154.
[67] Azarakhsh, Sajad, and Ali Ghamarian. "Collapse behavior of thin-walled conical tube clamped at both ends subjected to axial and oblique loads." *Thin-Walled Structures* 112 (2017): 1-11.
[68] Li, Zhibin, Jilin Yu, and Liuwei Guo. "Deformation and energy absorption of aluminum foam-filled tubes subjected to oblique loading." *International Journal of Mechanical Sciences* 54, no. 1 (2012): 48-56.
[69] Jones, N., and R. S. Birch. "Dynamic and static axial crushing of axially stiffened square tubes." *Proceedings of the Institution of Mechanical Engineers, Part C: Mechanical Engineering Science* 204, no. 5 (1990): 293-310.
[70] Zhang, Xiong, and Hoon Huh. "Energy absorption of longitudinally grooved square tubes under axial compression." *Thin-Walled Structures* 47, no. 12 (2009): 1469-1477.
[71] Eyvazian, Arameh, Meisam K. Habibi, Abdel Magid Hamouda, and Reza Hedayati. "Axial crushing behavior and energy absorption efficiency of corrugated tubes." *Materials & Design (1980-2015)* 54 (2014): 1028-1038.
[72] Zhang, Zonghua, Shutian Liu, and Zhiliang Tang. "Crashworthiness investigation of kagome honeycomb sandwich cylindrical column under axial crushing loads." *Thin-Walled Structures* 48, no. 1 (2010): 9-18.
[73] Yang, Kai, Shanqing Xu, Shiwei Zhou, Jianhu Shen, and Yi Min Xie. "Design of dimpled tubular structures for energy absorption." *Thin-Walled Structures* 112 (2017): 31-40.
[74] Zahran, M. S., P. Xue, and M. S. Esa. "Novel approach for design of 3D-multi-cell thin-walled circular tube to improve the energy absorption characteristics under axial impact loading." *International Journal of Crashworthiness* 22, no. 3 (2017): 294-306.
[75] Esa, Moustafa, Pu Xue, Mohamed Zahran, Mostafa Abdelwahab, and Mohamed Khalil. "Novel strategy using crash tubes adaptor for damage levels manipulation and total weight reduction." *Thin-Walled Structures* 111 (2017): 176-188.
[76] Xu, Fengxiang, Guangyong Sun, Guangyao Li, and Qing Li. "Experimental study on crashworthiness of tailor-welded blank (TWB) thin-walled high-strength steel (HSS) tubular structures." *Thin-Walled Structures* 74 (2014): 12-27.
[77] Yan, Libo, Nawawi Chouw, and Krishnan Jayaraman. "Effect of triggering and polyurethane foam-filler on axial crushing of natural flax/epoxy composite tubes." *Materials & Design (1980-2015)* 56 (2014): 528-541.
[78] Mahdi, E., AMS and Hamouda, and T. A. Sebaey. "The effect of fiber orientation on the energy absorption capability of axially crushed composite tubes." *Materials & Design (1980-2015)* 56 (2014): 923-928.

[79] Kalhor, Roozbeh, and Scott W. Case. "The effect of FRP thickness on energy absorption of metal-FRP square tubes subjected to axial compressive loading." *Composite Structures*130 (2015): 44-50.
[80] Boria, S., A. Scattina, and G. Belingardi. "Axial energy absorption of CFRP truncated cones." *Composite Structures*130 (2015): 18-28.
[81] Wang, Lu, Xueming Fan, Hao Chen, and Weiqing Liu. "Axial crush behavior and energy absorption capability of foam-filled GFRP tubes under elevated and high temperatures." *Composite Structures* 149 (2016): 339-350.
[82] Dlugosch, M., J. Fritsch, D. Lukaszewicz, and S. Hiermaier. "Experimental investigation and evaluation of numerical modeling approaches for hybrid-FRP-steel sections under impact loading for the application in automotive crash-structures." *Composite Structures* 174 (2017): 338-347.
[83] Witteman, W. J., and R. F. C. Kriens. *The necessity of an adaptive vehicle structure to optimize deceleration pulses for different crash velocities*. No. 2001-06-0171. SAE Technical Paper, 2001.
[84] ABAQUS 6.14.3 Documentation, Dassault Systèmes Simulia Corp., Providence, RI, USA, 2014
[85] Sun, Guangyong, Tong Pang, Jianguang Fang, Guangyao Li, and Qing Li. "Parameterization of criss-cross configurations for multiobjective crashworthiness optimization." *International Journal of Mechanical Sciences* 124 (2017): 145-157.
[86] Chen, Weigang, and Tomasz Wierzbicki. "Relative merits of single-cell, multi-cell and foam-filled thin-walled structures in energy absorption." *Thin-Walled Structures* 39, no. 4 (2001): 287-306.
[87] Hanssen, Arve Grønsund, Magnus Langseth, and Odd Sture Hopperstad. "Static and dynamic crushing of square aluminium extrusions with aluminium foam filler." *International Journal of Impact Engineering* 24, no. 4 (2000): 347-383.
[88] Langseth, M., O. S. Hopperstad, and A. G. Hanssen. "Crash behaviour of thin-walled aluminium members." *Thin-walled structures* 32, no. 1-3 (1998): 127-150.
[89] Abramowicz, W., and T. Wierzbicki. "Axial crushing of multicorner sheet metal columns." *Journal of Applied Mechanics* 56, no. 1 (1989): 113-120.
[90] Zhang, Xiong, and Hui Zhang. "Energy absorption of multi-cell stub columns under axial compression." *Thin-Walled Structures* 68 (2013): 156-163.
[91] Zhang, Xiong, Gengdong Cheng, and Hui Zhang. "Theoretical prediction and numerical simulation of multi-cell square thin-walled structures." *Thin-Walled Structures* 44, no. 11 (2006): 1185-1191.
[92] Reddy, Sekhar, Milad Abbasi, and Mohammad Fard. "Multi-cornered thin-walled sheet metal members for enhanced crashworthiness and occupant protection." *Thin-Walled Structures* 94 (2015): 56-66.
[93] Rao, C. Lakshmana, V. Narayanamurthy, and K. R. Y. Simha. *Applied impact mechanics*. John Wiley & Sons, 2016.
[94] Simhachalam, Bade, C. Lakshmana Rao, and Krishna Srinivas. "The effect of holes on the dynamic behavior and energy absorption of aluminum alloy AA7005 tube." In *Applied Mechanics and Materials*, vol. 446, pp. 325-328. Trans Tech Publications, 2014.
[95] Applications: Car body - Crash management systems, *The Aluminium Automotive Manual*; European Aluminium Association, Ver 2013
[96] Zhang, Xiong, and Hui Zhang. "Axial crushing of circular multi-cell columns." *International Journal of Impact Engineering* 65 (2014): 110-125.
[97] Reid, S. R. "Plastic deformation mechanisms in axially compressed metal tubes used as impact energy absorbers." *International Journal of Mechanical Sciences* 35, no. 12 (1993): 1035-1052.
[98] Qiu, X. M., and T. X. Yu. "Some topics in recent advances and applications of structural impact dynamics." *Applied Mechanics Reviews* 64, no. 3 (2011): 030801.
[99] Costas, M., J. Díaz, L. E. Romera, S. Hernández, and A. Tielas. "Static and dynamic axial crushing analysis of car frontal impact hybrid absorbers." *International Journal of Impact Engineering* 62 (2013): 166-181.

[100] Tarlochan, F., and F. Samer. "Design of thin wall structures for energy absorption applications: design for crash injuries mitigation using magnesium alloy." *International Journal of Research in Engineering and Technology* 2, no. 7 (2013): 24-36.
[101] Santosa, Sigit, John Banhart, and Tomasz Wierzbicki. "Bending crush behavior of foam-filled sections." *Metal foams and porous metal structures. Bremen: Verlag-MIT* (1999): 337-45.
[102] Liu, Qiang, Jingbo Ma, Xiyu Xu, Yinghan Wu, and Qing Li. "Load bearing and failure characteristics of perforated square CFRP tubes under axial crushing." *Composite Structures* 160 (2017): 23-35.
[103] Guist, L. R., & Marble, D. P. "Prediction of the inversion load of a circular tube". NASA TN D-3622. (1966). NASA, Washington D.C., USA
[104] Reddy, T. J., Y. V. D. Rao, and V. Narayanamurthy. "Thin-walled structural configurations for enhanced crashworthiness." *International journal of crashworthiness* 23, no. 1 (2018): 57-73.
[105] Zhang, Xiong, Gengdong Cheng, and Hui Zhang. "Numerical investigations on a new type of energy-absorbing structure based on free inversion of tubes." *International Journal of Mechanical Sciences* 51, no. 1 (2009): 64-76.
[106] Kinkead, A. N. "Analysis for inversion load and energy absorption of a circular tube." *The Journal of Strain Analysis for Engineering Design* 18, no. 3 (1983): 177-188.
[107] Reddy, T. Y. "Guist and Marble revisited—on the natural knuckle radius in tube inversion." *International journal of mechanical sciences* 34, no. 10 (1992): 761-768.
[108] Colokoglu, A., and T. Y. Reddy. "Strain rate and inertial effects in free external inversion of tubes." *International journal of crashworthiness* 1, no. 1 (1996): 93-106.
[109] Qiu, Xin Ming, Liang Hong He, Jie Gu, and Xiao Huan Yu. "An improved theoretical model of a metal tube under free external inversion." *Thin-Walled Structures* 80 (2014): 32-37.
[110] Qiu, XinMing, LiangHong He, Jie Gu, and XiaoHuan Yu. "A three-dimensional model of circular tube under quasi-static external free inversion." *International Journal of Mechanical Sciences* 75 (2013): 87-93.
[111] Yu, XiaoHuan, XinMing Qiu, and T. X. Yu. "Analysis of the free external inversion of circular tubes based on deformation theory." *International Journal of Mechanical Sciences* 100 (2015): 262-268.
[112] Qiu, XinMing, XiaoHuan Yu, YiLiang Li, and T. X. Yu. "The deformation mechanism analysis of a circular tube under free inversion." *Thin-Walled Structures* 107 (2016): 49-56.
[113] Tool and Manufacturing Engineers Handbook, Volume 2, Forming, 4th Edition, Society of Manufacturing Engineers, 1984
[114] ASTM E8/E 8M-08, Standard Test Methods for Tension Testing of Metallic Materials, American Soceity for Testing Materials, 2008
[115] Altair HyperMesh user guide, 2016, "Altair HyperWorks," Altair, Troy, MI, http://www.altairhyperworks.com
[116] ABAQUS Analysis User's Manual, ABAQUS Version 2017, Dassault Syste`mes, 2017(Dassult Systèmes, Providence, RI, USA, 2015)
[117] Wierzbicki, Tomasz, Shankar U. Bhat, Wlodzimierz Abramowicz, and D. Brodkin. "Alexander revisited—a two folding elements model of progressive crushing of tubes." *International Journal of Solids and Structures* 29, no. 24 (1992): 3269-3288.
[118] Reddy TJ, Naarayanamurthy V, Rao YVD. "Evolution of a new geometric profile for an ideal tube inversion for crash energy absorption". International Journal of Mechanical Sciences 2018; under review.
[119] Feraboli, Paolo, Chris Norris, and Doug McLarty. "Design and certification of a composite thin-walled structure for energy absorption." *International Journal of Vehicle Design* 44, no. 3-4 (2007): 247-267.
[120] Waimer, M., M. H. Siemann, and T. Feser. "Simulation of CFRP components subjected to dynamic crash loads." *International journal of impact engineering* 101 (2017): 115-131.

[121] Boria, S., S. Pettinari, F. Giannoni, and G. Cosimi. "Analytical and numerical analysis of composite impact attenuators." *Composite Structures* 156 (2016): 348-355.
[122] Ning, Haibin, Uday Vaidya, Gregg M. Janowski, and George Husman. "Design, manufacture and analysis of a thermoplastic composite frame structure for mass transit." *Composite Structures* 80, no. 1 (2007): 105-116.
[123] Luo, Haibo, Ying Yan, Xiangji Meng, and Can Jin. "Progressive failure analysis and energy-absorbing experiment of composite tubes under axial dynamic impact." *Composites Part B: Engineering* 87 (2016): 1-11.
[124] Kathiresan, M., K. Manisekar, and V. Manikandan. "Performance analysis of fibre metal laminated thin conical frusta under axial compression." *Composite Structures* 94, no. 12 (2012): 3510-3519.
[125] Subbaramaiah, R., B. G. Prusty, G. M. K. Pearce, S. H. Lim, and R. S. Thomson. "Crashworthy response of fibre metal laminate top hat structures." *Composite Structures* 160 (2017): 773-781.
[126] Tan, Wei, and Brian G. Falzon. "Modelling the crush behaviour of thermoplastic composites." *Composites Science and Technology* 134 (2016): 57-71.
[127] Kim, Hee Chul, Dong Kil Shin, Jung Ju Lee, and Jun Beom Kwon. "Crashworthiness of aluminum/CFRP square hollow section beam under axial impact loading for crash box application." *Composite Structures* 112 (2014): 1-10.
[128] Reuter, Corin, and Thomas Tröster. "Crashworthiness and numerical simulation of hybrid aluminium-CFRP tubes under axial impact." *Thin-Walled Structures* 117 (2017): 1-9.
[129] Zhu, Guohua, Zhen Wang, Xintao Huo, Aiguo Cheng, Guangyao Li, and Chenyu Zhou. "Experimental and numerical investigation into axial compressive behaviour of thin-walled structures filled with foams and composite skeleton." *International Journal of Mechanical Sciences* 122 (2017): 104-119.
[130] Liu, Qiang, Yongzhou Lin, Zhijian Zong, Guangyong Sun, and Qing Li. "Lightweight design of carbon twill weave fabric composite body structure for electric vehicle." *Composite Structures* 97 (2013): 231-238.
[131] Pervaiz, Muhammad, Suhara Panthapulakkal, K. C. Birat, Mohini Sain, and Jimi Tjong. "Emerging trends in automotive lightweighting through novel composite materials." *Materials Sciences and Applications* 7, no. 01 (2016): 26.
[132] Boria, S., J. Obradovic, and G. Belingardi. "Experimental and numerical investigations of the impact behaviour of composite frontal crash structures." *Composites Part B: Engineering* 79 (2015): 20-27.
[133] Bussadori, B. P., K. Schuffenhauer, and A. Scattina. "Modelling of CFRP crushing structures in explicit crash analysis." *Composites Part B: Engineering* 60 (2014): 725-735.
[134] Hashin, Zvi, and Assa Rotem. "A fatigue failure criterion for fiber reinforced materials." *Journal of composite materials* 7, no. 4 (1973): 448-464.
[135] Hashin, Zvi. "Failure criteria for unidirectional fiber composites." *Journal of applied mechanics* 47, no. 2 (1980): 329-334.
[136] Lapczyk, Ireneusz, and Juan A. Hurtado. "Progressive damage modeling in fiber-reinforced materials." *Composites Part A: Applied Science and Manufacturing* 38, no. 11 (2007): 2333-2341.
[137] Keeler, Stuart, and Menachem Kimchi. *Advanced high-strength steels application guidelines V5*. WorldAutoSteel, 2015.
[138] Yokoyama, T. "Impact tensile stress–strain characteristics of wrought magnesium alloys." *Strain* 39, no. 4 (2003): 167-175.
[139] Teng, J. G., T. Yu, and D. Fernando. "Strengthening of steel structures with fiber-reinforced polymer composites." *Journal of Constructional Steel Research* 78 (2012): 131-143.
[140] Sinke, J. "Development of fibre metal laminates: concurrent multi-scale modeling and testing." *Journal of Materials Science* 41, no. 20 (2006): 6777-6788.
[141] Ahmad, Zaini, Muhammad Ruslan Abdullah, and Mohd Nasir Tamin. "Experimental and numerical studies of fiber metal laminate (FML) thin-walled tubes under impact loading."

In *Mechanical and Materials Engineering of Modern Structure and Component Design*, pp. 433-443. Springer, Cham, 2015.
[142] Salve, Aniket, R. R. Kulkarni, and Ashok Mache. "A review: Fiber metal laminates (FML's)-Manufacturing, test methods and numerical modeling." *International Journal of Engineering Technology and Sciences (IJETS)* 6, no. 1 (2016): 71-84.
[143] Kathiresan, M., K. Manisekar, and V. Manikandan. "Crashworthiness analysis of glass fibre/epoxy laminated thin walled composite conical frusta under axial compression." *Composite Structures* 108 (2014): 584-599.
[144] Kathiresan, M., and K. Manisekar. "Axial crush behaviours and energy absorption characteristics of aluminium and E-glass/epoxy over-wrapped aluminium conical frusta under low velocity impact loading." *Composite Structures* 136 (2016): 86-100.
[145] Obradovic, Jovan, Simonetta Boria, and Giovanni Belingardi. "Lightweight design and crash analysis of composite frontal impact energy absorbing structures." *Composite Structures*94, no. 2 (2012): 423-430.
[146] Sun, Guangyong, Shunfeng Li, Qiang Liu, Guangyao Li, and Qing Li. "Experimental study on crashworthiness of empty/aluminum foam/honeycomb-filled CFRP tubes." *Composite Structures* 152 (2016): 969-993.
[147] Zhu, Guohua, Guangyong Sun, Guangyao Li, Aiguo Cheng, and Qing Li. "Modeling for CFRP structures subjected to quasi-static crushing." *Composite Structures* 184 (2018): 41-55.
[148] Barnes, A. T., K. Ravi-Chandar, S. Kyriakides, and S. Gaitanaros. "Dynamic crushing of aluminum foams: Part I–Experiments." *International Journal of Solids and Structures*51, no. 9 (2014): 1631-1645.
[149] Found, M. S., A. M. Robinson, and J. J. Carruthers. "The influence of FRP inserts on the energy absorption of a foam-cored sandwich panel." *Composite structures* 38, no. 1-4 (1997): 373-381.
[150] Ahmad, Zaini, and D. P. Thambiratnam. "Crushing response of foam-filled conical tubes under quasi-static axial loading." *Materials & design* 30, no. 7 (2009): 2393-2403.
[151] Zhang, Junyuan, Linan Wu, Guang Chen, and Hao Zhou. "Bending collapse theory of thin-walled twelve right-angle section beams." *Thin-Walled Structures* 85 (2014): 377-387.
[152] Wang, Ning-zhen, C. H. E. N. Xiang, L. I. Ao, Yan-xiang Li, Hua-wei Zhang, and L. I. U. Yuan. "Three-point bending performance of a new aluminum foam composite structure." *Transactions of Nonferrous Metals Society of China* 26, no. 2 (2016): 359-368.
[153] Niknejad, Abbas, Golam Hosein Liaghat, and Majid Moeinifard. "Experimental investigation of the rubber-filled tubes in the tube inversion process." In *Advanced Materials Research*, vol. 445, pp. 33-38. Trans Tech Publications, 2012.
[154] Shibanuma, Kazuki, Fuminori Yanagimoto, Tetsuya Namegawa, Katsuyuki Suzuki, and Shuji Aihara. "Brittle crack propagation/arrest behavior in steel plate–Part I: Model formulation." *Engineering Fracture Mechanics* 162 (2016): 324-340.
[155] Duarte, Isabel, Matej Vesenjak, and Lovre Krstulović-Opara. "Dynamic and quasi-static bending behaviour of thin-walled aluminium tubes filled with aluminium foam." *Composite structures* 109 (2014): 48-56.
[156] Zarei, H. R., and M. Kröger. "Bending behavior of empty and foam-filled beams: Structural optimization." *International Journal of Impact Engineering* 35, no. 6 (2008): 521-529.
[157] Albert, Prescilla Christy, Amir Radzi Ab Ghani, Mohd Zaid Othman, and Ahmad Mujahid Ahmad Zaidi. "Axial Crushing Behavior of Aluminum Square Tube with Origami Pattern." *Modern Applied Science* 10, no. 2 (2016): 90-98.
[158] McClintock, Frank A. "A criterion for ductile fracture by the growth of holes." *Journal of applied mechanics* 35, no. 2 (1968): 363-371.
[159] Rice, J. R_, and Dennis Michael Tracey. "On the ductile enlargement of voids in triaxial stress fields∗." *Journal of the Mechanics and Physics of Solids* 17, no. 3 (1969): 201-217.
[160] Hancock, J. W., and A. C. Mackenzie. "On the mechanisms of ductile failure in high-strength steels subjected to multi-axial stress-states." *Journal of the Mechanics and Physics of Solids*24, no. 2-3 (1976): 147-160.

[161] Johnson, Gordon R. "A constitutive model and data for materials subjected to large strains, high strain rates, and high temperatures." *Proc. 7th Int. Sympo. Ballistics* (1983): 541-547.
[162] Chang, Fu-Kuo, and Kuo-Yen Chang. "A progressive damage model for laminated composites containing stress concentrations." *Journal of composite materials* 21, no. 9 (1987): 834-855.
[163] Clegg, R. A., D. M. White, W. Riedel, and W. Harwick. "Hypervelocity impact damage prediction in composites: Part I—material model and characterisation." *International Journal of Impact Engineering* 33, no. 1-12 (2006): 190-200.
[164] Zhu, Shengqing, and Gin Boay Chai. "Low-velocity impact response of fibre–metal laminates–Experimental and finite element analysis." *Composites Science and Technology* 72, no. 15 (2012): 1793-1802.
[165] Qiao, J. S., J. H. Chen, and H. Y. Che. "Crashworthiness assessment of square aluminum extrusions considering the damage evolution." *Thin-walled structures* 44, no. 6 (2006): 692-700.
[166] Huang, Jiancheng, and Xinwei Wang. "Numerical and experimental investigations on the axial crushing response of composite tubes." *Composite Structures* 91, no. 2 (2009): 222-228.

# PUBLICATIONS

## Summary

| | |
|---|---|
| International Journals | Published = 2<br>Review completed = 2<br>Under review = 2<br>Under preparation = 1 |
| International Conferences | Presented = 3 |

## International Journals

### Published

1. T.J. Reddy, Y.V.D. Rao, and V. Narayanamurthy, **"Thin-walled structural configurations for enhanced crashworthiness",** ***International Journal of Crashworthiness,*** **2017, pp 1-17,** (http://dx.doi.org/10.1080/13588265.2017.1306824).

2. T.J. Reddy, Y.V.D. Rao, and V. Narayanamurthy, "**Analysis of structural configurations for assessment of crashworthiness",** ***In Proceedings of 11th International Symposium on Impact and Plasticity, IMPLAST – 2016, Elsevier – Procedia Engineering,*** **173 ( 2017), 1357 – 1364.** (http://dx.doi.org/ 10.1016/j.proeng.2016.12.180).

### Working on revision

3. T. J. Reddy, V. Narayanamurthy and Y.V.D. Rao, **"Evolution of a new geometric profile for an ideal tube inversion for crash energy absorption",** ***International Journal of Mechanical Sciences,*** **2018.** Submission number: SUBMIT2IJMS_2018_2549

   Received positive comments on 27-11-2018 and Working on review comments

### Decision pending

4. T. J. Reddy, V. Narayanamurthy and Y.V.D. Rao, **"Enhancement in Specific Energy Absorption of Invertubes", Thin-walled Structures, 2018.** Submission number: TWST_2018_1256

   Review completed and Editor's decision pending.

**Under review**

5. T. J. Reddy, V. Narayanamurthy and Y.V.D. Rao, **"Energy absorbing structures for reduced acceleration levels and improved crash performance in frontal collision of vehicles",** ***International Journal of Vehicle Safety,*** **2018.** Reference number: IJVS-213518.

6. T. J. Reddy, V. Narayanamurthy and Y.V.D. Rao, **"Effect of damage modelling in numerical simulation of crash energy absorption behaviour of crush tubes and validation with experiments",** ***International Journal of Crashworthiness (Taylor & Francis*****), 2018.**

**Under preparation**

7. T. J. Reddy, V. Narayanamurthy and Y.V.D. Rao, **"Crush behaviour of EA structures with basic geometric shapes and their enhancements"**

## Publications in International conference proceedings

1. T.J. Reddy, Y.V.D. Rao, and V. Narayanamurthy, "**Analysis and validation of an energy absorbing structure",** ***In Proceedings of NAFEMS-India International Conference 2016*** - *Engineering Modeling, Analysis, Simulation and 3D Printing*, Aug 29-31, 2016, Bangalore. Paper No. NI3D029. ***(Accepted & Presented).***

2. T.J. Reddy, Y.V.D. Rao, and V. Narayanamurthy, "**Development of deformable members for energy absorption",** ***3rd Indian Conference on Applied Mechanics, INCAM-2017,*** MNNIT- Allahabad, July 5-7, 2017. Paper No. 36 ***(Accepted & Presented).***

   Awarded **First Prize** in Solid Mechanics stream of INCAM-2017 out of 140 papers.

3. T.J. Reddy, V. Narayanamurthy, and Y.V.D. Rao, "**Bending-based aluminium foam sandwich structures for impact energy applications"** ***International Conference on Composite Materials and Structures (ICCMS) -2017, IIT-Hyderabad,*** **(Accepted and Presented).** Paper No: 323

## BIOGRAPHY OF THE CANDIDATE

| | |
|---|---|
| Name of the candidate | Janardhana Reddy T |
| ID. No. | 2013PHXF0117H |
| Experience | Over 18 years of CAE experience in automotive industry |
| Academic credentials | • Pursuing Ph D from BITS-Pilani, Hyderabad Campus<br>• M.E. in Mechanical Engineering (OU, Hyderabad)<br>• B.Tech in Mechanical Engineering (SKU, Anantapur)<br>• Intermediate in M.P.C (Coles Junior College, Kurnool)<br>• SSC, Chinmaya Mission Vidyalaya, Kurnool |
| Career achievements | Developed CAE teams for simulation of static and dynamic loading scenarios of various automotive systems |
| Professional memberships | • Life Member of Indian Society for Indian Society for Applied Mechanics (ISAM) |
| Personal details | Residential address: Flat-301, Navkar's Prathul Residency, Premsai Sagar Enclave, Adj. to Manasarovar heights-2, Old Bowenpally, Hyderabad – 500009<br>Contact Number: +919908148149<br>Email address: janardhan.tjr@gmail.com |

## BIOGRAPHY OF THE SUPERVISOR-1

| | |
|---|---|
| Name of the Supervisor | Dr. VENKATA DASESWARA RAO YENDLURI |
| Designation and address | Associate Professor<br>Room: E 108, Mechanical Engineering Department,<br>BITS Pilani Hyderabad Campus, Jawaharnagar, Shameerpet, Hyderabad- 500078, Telangana State, India.Tel: LL: 0091-40-66303551<br>Email: email: yvdrao@hyderabad.bits-pilani.ac.in |
| Experience (years) | 33 years of academic experience |
| Number of publications | Journals: Published = 12; Under review = 4<br>Conferences: 30 |
| Professional memberships | 1. Member of American Society for Mechanical Engineering, USA.<br>2. Fellow of Institute of Engineers (IND), Kolkata, India.<br>3. Life Member of Indian Society for Technical Education (ISTE), New Delhi. |
| No. of Ph.D.s Completed | 1 |
| No. of Ph.D. students under supervision | 4 |

## BIOGRAPHY OF THE SUPERVISOR-2

| | |
|---|---|
| Name of the Supervisor | Dr. VIJAYABASKAR NARAYANAMURTHY |
| Designation and address | Scientist-'E'<br>Directorate of Systems Integration (Mechanical)<br>Research Centre Imarat, Vignyanakancha P.O., Hyderabad – 500 069.<br>Tel: LL: 0091-40- 2430-6416; M: 949-398-5044<br>Email: vbnarayanamurthy@gmail.com/ v.narayanamurthy@rcilab.in |
| Experience (years) | 19 years in R&D of Flight structures and mechanisms |
| Number of publications | Patents = 4<br>Books: Authored =1; Edited = 2; Chapters = 3<br>Journals: Published = 14; Under review = 4<br>Conferences: International = 23 ; National = 18<br>Technical Documents in DRDO = 52 |
| Projects undertaken | 1. Research and development on flight vehicle interface structures and mechanisms (confidential from Nation's Security):<br>• Designed and proven sabots for flight release from canister;<br>• Designed and developed novel airframe structure and mechanisms for launch tube actuation – ejection - restraint and hold-release for mother flight launched sub-flights;<br>• Designed, developed and qualified a quick fastening intersection joint for flights; Designed and realised novel external gimbal and interface structure and to conduct live stage test of air defence flight; Designed, developed and realised two different antennae manipulators and novel umbilical release mechanisms; Designed several new handling systems; Designed and commissioned an indigenous mass property measurement system for slender flights.<br><br>2. Modeling of interfacial stresses and debonding failures in plated beams (2008-2011), University of Edinburgh, UK:<br>Developed a novel interfacial stress solution applicable for arbitrary loading; Evaluated the effect of shear deformation and derived a rigorous solution employing Timoshenko's beam theory; Devised new technique for deduction of interfacial stresses from experiments; Formulated structural |

| | |
|---|---|
| | mechanics analysis for characterization of intermediate crack induced interfacial debonding; and Developed a first interfacial fracture mechanics based flexural plate end debonding model for design applications. |
| No. of Ph.D. students under supervision | 4 |